ELECTROOSMOTIC FLOW IN A MICROCHANNEL PACKED WITH MICROSPHERES

KANG YUEJUN

SCHOOL OF MECHANICAL & AEROSPACE ENGINEERING

NANYANG TECHNOLOGICAL UNIVERSITY

2005

Electroosmotic Flow in a Microchannel Packed with Microspheres

Kang Yuejun

School of Mechanical & Aerospace Engineering

A Thesis Submitted to the Nanyang Technological University

In fulfillment of the requirement for the degree of

Doctor of Philosophy

2005

This work is dedicated with affection to my wife

Ranran, whose care, courage, and patience

have been an inspiration to me,

and to my dear grandparents, parents, and younger brother,

whose love, support, and encouragement

have put me where I am now.

Abstract

The electrokinetic (EK) micropump, which employs electroosmosis rather than hydrostatic pressure, is a rapidly emerging pumping technique to transport reagents and electrolytes through microchannel networks. Due to many advantages such as no moving parts, low solvent and sample consumption, and precise control, it has been favored in developing the advanced microfluidic devices which can perform total biochemical analysis on a single fabricated chip. Use of porous structures greatly enlarges the interfacial area, and thus significantly enhances the pressure-building capacity of the EK micropump. Although electroosmosis in porous media has been widely practiced as a kinetic pumping source in many electro-separation techniques (e.g., Capillary Electro-Chromatography), the theoretical investigations on the underlying mechanism still remain limited. In light of this, this dissertation provides a fundamental, systematic and in-depth exploration on the electroosmosis in porous microstructures and its dynamic nature.

The theoretical development in this dissertation mainly comprises three aspects. Firstly, a mathematical model is developed to describe the electroosmotic flow in a microcapillary packed with microspheres under electrokinetic wall effect. The model is based on the *Carman-Kozeny theory*, also known as capillary model. The Darcy velocity of the electroosmotic flow in the porous media is obtained using volume averaging method, taking into consideration of the porosity and tortuosity of the porous packing. And a velocity correction due to the electrokinetic wall effect is included by analytically and numerically solving the modified Brinkman's macroscopic momentum equation.

Secondly, motivated by potential application in electrokinetic micro-actuators, this

study also presents an analysis on AC electroosmotic flow in both open-end and closed-end microcapillaries packed with microspheres. The oscillating Darcy velocity in an open-end capillary in response to an AC electric field is obtained using Green's function formulation. The backpressure associated with the counter-flow in a closed-end capillary is obtained by solving the modified Brinkman's momentum equation.

Thirdly, a systematic numerical simulation is carried out to evaluate the Joule heating effect on the electroosmotic flow in a packed microcapillary. Specifically, the non-uniform electric field resulted from the temperature gradient is analyzed. It is also found that an induced pressure field presents in the capillary due to the velocity variation caused by the temperature elevation.

In addition, the dynamic electroosmotic flows in simple geometries, such as cylindrical and annular microcapillaries, under the time-dependent electric field are analyzed. The analytical solutions are derived as a basis of model development for the electroosmosis in porous media using capillary model.

As the other essential part of this dissertation, an experimental study on electroosmosis in a packed microcapillary is conducted. Electrokinetic micropumps are fabricated using high pressure driven slurry packing technique. Two different methods to characterize the fabricated micropumps are employed and compared under the influences of the capillary size, particle size, solution concentration and type of the electrolyte solutions, and the capillary length. It is found that the experimental data are generally in reasonable agreement with the predictions by the model developed in this study. However, deviation is observed under the condition of high electric field strength.

Acknowledgements

The work presented in this thesis was conducted between June 2001 and July 2004 in the research group led by Dr Yang Chun, Charles. As my principal supervisor, Dr Yang opened the door of the world of scientific research for me and taught me how to enjoy the pleasure at every stage. The first contact between Dr Yang and me began even one year before I joined NTU when I was still a final year undergraduate in USTC. He wanted to take in some graduate students shortly after he joined NTU faculty. However due to many reasons I could not manage to join his group right after I graduated. Although I began to work as an engineer in an IT company, my long-term career remained misty. In my second trial of application, Dr Yang contacted me again and gave me a lot of good suggestions and help. Finally, I was fortunate enough to become his first PhD student in summer of 2001. During the three years at NTU, I have very clear direction under the close supervision of Dr Yang. He always gave me inspiring suggestions and shared me with his rich research experience through our frequent discussions. Most importantly, he gradually helped me build up my confidence for a successful academic career. I also appreciated very much the care extended to my family by Dr Yang and his wife, Mrs Xu Li.

The completion of this work is also owed to my co-supervisor Dr Huang Xiaoyang. Although my interaction with Dr Huang is not so much, it has always been stimulating and thought provoking. Especially his very practical suggestions on my each presentation have helped me improve my communication and presentation skill to a more effective and efficient way. Dr Huang also helped me get some part-time teaching jobs, which gave me some relief from the pressure of living expenses.

My sincere gratitude should also be extended to some of my colleagues and friends. Actually part of this work would not be finished without their contributions. Mr Tan Say Chong, who was a final year undergraduate student, had spent almost one year working closely with me on the experiment. No one has experience on this experiment before thus we had to start from scratch. We had many sleepless nights when it was difficult. But finally it was done after so many trial and errors, and we all learned much during the entire course of experiment. Mr Marcos, whose is a very smart guy doing his master study, had happily cooperated with me in some projects. His unconditional help in my modeling and experiments was always greatly appreciated. My fellow research students, Mr. Tang Gongyue, Mr. Liu Yue, and Mr. Chen Xuyang gave me a lot of advices on numerical simulations.

I would also thank the technician officer Mr. Yap Pow Khim Eric in Fluid Dynamics Lab and Mr. Yuan Kee Hock in Thermal and Fluids Research Lab for their technical assistance. Senior clerical officer Mrs Soh Meow Chng in general office of the School of MAE greeted me when I first joined NTU and continued to advice me for varied administrative issues during my study here. I am also grateful for many other people, without producing a long list of them, who have helped me in different ways and made my three years at NTU memorable.

I would like to thank the direct support for three years from Nanyang Technological University through a research scholarship, without which I would not have a chance to work with so many smart and brilliant people.

Vita

Kang Yuejun was born on March 24, 1977, in Xiangfan, Hubei, People's Republic of China. He obtained Bachelor of Engineering degree in July 2000 after five years undergraduate study at University of Science and Technology of China, Hefei, Anhui, China. After that he had worked as a Product Specialist for a year in Acer Communication & Multimedia Co. Ltd., Suzhou, China. In June 2001, he joined Nanyang Technological University as a postgraduate research student for a PhD degree in Mechanical and Aerospace Engineering.

List of Publications

Refereed Journals:

1) **Yuejun Kang**, Chun Yang, and Xiaoyang Huang. "Joule Heating Effects of Electroosmotic Flow in Microcapillaries Packed with Microspheres" *Langmuir* (under review, 2005)

2) **Yuejun Kang**, Chun Yang, and Xiaoyang Huang. "Analysis of Electroosmotic Flow in a Microchannel Packed with Microspheres" *Journal of Microfluidics and Nanofluidics* **1**, 168-176 (2005)

3) Marcos, **Yuejun Kang**, Kim Tiow Ooi, Chun Yang, and Teck Neng Wong "Frequency Dependent Velocity and Vorticity Fields of Electroosmotic Flow in a Closed-End Cylindrical Microchannel". *Journal of Micromechanics and Microengineering* **15**, 301-312 (2005)

4) **Yuejun Kang**, Chun Yang, and Xiaoyang Huang. "Analysis of the Electroosmotic Flow in a Microchannel Packed with Homogeneous Microspheres under Electrokinetic Wall Effect ". *International Journal of Engineering Science* **42**, 2011-2027 (2004)

5) **Yuejun Kang**, Chun Yang, and Xiaoyang Huang. "AC Electroosmosis in Microchannels Packed with a Porous Medium". *Journal of Micromechanics and Microengineering* **14**, 1249-1257 (2004)

6) **Yuejun Kang**, Chun Yang, and Xiaoyang Huang. "Modelling of the Capillary Electrochromatography with Application in BioMEMS". *International Journal of Computational Engineering Science*, Vol. **4**, No. 2, 261-264 (2003)

7) **Yuejun Kang**, Chun Yang, and Xiaoyang Huang. "Dynamic aspects of electroosmotic flow in a cylindrical microcapillary". *International Journal of Engineering Science* **40**, 2203-2221 (2002)

8) **Yuejun Kang**, Chun Yang, and Xiaoyang Huang. "Electroosmotic Flow in a Capillary Annulus with High Zeta Potentials". *Journal of Colloid and Interface Science* **253**, 285-294 (2002)

Conference papers:

1) Chun Yang, **Yuejun Kang**, and Xiaoyang Huang. "AC Electrokinetic Micropump Using Packed Microcapillaries" *3rd International Conference on Materials for Advanced Technologies & IUMRS - International Conference in Asia 2005*, 3-8 July, 2005, Singapore (accepted).

2) **Yuejun Kang**, Chun Yang, and Xiaoyang Huang. "Transient Joule Heating and its Effects on Electroosmotic Flow in a Microcapillary Packed with Microspheres" *The 3rd International Conference on Microchannels and Minichannels*, 13-15 June, 2005, Toronto, Canada (accepted).

3) **Yuejun Kang**, Chun Yang, and Xiaoyang Huang. "Analysis of Electroosmotic Flow in a Microchannel Packed with Microspheres" *The 2nd International Conference on Microchannels and Minichannels*, 17-19 June, 2004, Rochester, New York, USA.

4) **Yuejun Kang**, Chun Yang, and Xiaoyang Huang. "Frequency Dependent Electroosmotic Flow in a Capillary Packed with Microspheres" *The 1st International Symposium on Micro & Nano Technology*, 14-17 March, 2004, Honolulu, Hawaii, USA.

5) **Yuejun Kang**, Chun Yang, and Xiaoyang Huang. "Modelling of the Capillary Electrochromatography with Application in BioMEMS". *2nd International Conference on Materials for Advanced Technologies & IUMRS – International Conference in Asia 2003*, 7-14 December, 2003, Singapore

6) **Yuejun Kang**, Chun Yang, and Xiaoyang Huang. "Modelling of the Capillary Electrochromatography with Application in BioMEMS". *5th IFAC Symposium on Modelling and Control in Biomedical Systems,* 21-23 August 2003, Melbourne, Australia.

Table of Contents

List of Tables

List of Figures

Nomenclature

A	cross-sectional area of the specified geometry [m^2]
a	cylindrical capillary radius, or the outer radius of annular capillary [m]
C_n	integration defined by $C_n = \int_{\xi=0}^{1} \xi J_0(\lambda_n \xi) \sinh[\Psi(\xi)]\, d\xi$
C_p	Heat capacity [J kg^{-1} K^{-1}]
D_i	diffusion coefficient of the type-i ion [m^2 s^{-1}]
d	diameter of the cylindrical geometry [m]
E	external applied electric field [V m^{-1}]
E_0	the magnitude of the electric field [V m^{-1}]
e	exponential function, same as exp(x)
e_0	elementary charge, 1.602×10^{-19} [C]
e_z	flowing axial coordinate direction
F	force [N]
f	frequency of the applied sinusoidally alternating electric field [s^{-1}]
f_i	hydrodynamic resistance coefficient [J m^{-2} s]
G	Green's function; or ratio of the mean electrostatic potential across the annulus region to the zeta-potential of the outer charged wall
H	Heaviside step function
I_0, I_1	zero-order and first-order of the first kind modified Bessel function, respectively
i	unit imaginary number
J	a correction factor to the Smoulochowski equation
J_0, J_1	zero-order and first-order of the first kind Bessel function, respectively.
K	Darcy permeability of the porous media [m^2]
K_0, K_1	zero-order and first-order of the second kind modified Bessel function, respectively
k	thermal conductivity [W m^{-1} K^{-1}]
k_b	Boltzmann constant, 1.381×10^{-23} [J K^{-1}]

L	length of the microcapillary
N_0	zero-order Bessel function of the second kind
n_0	ionic number concentration in the bulk phase [m^{-3}]
n_i	local number concentration of the type-i ion [m^{-3}]
P	pressure gradient [Pa m^{-1}]
p	pressure [Pa]
$\overline{Q}_V$	dimensionless total volumetric net flow quantity
q	heat production per unit volume [J m^{-3}]
R	dimensionless spatial variable defined as $R = \kappa r$ in the non-dimensional P-B equation
r	channel radius [m]
$\overline{r}$	dimensionless radius
$\overline{r}_0$	dimensionless radius of the zero-velocity plane
T	absolute temperature [K]
t	time [s]
$\overline{t}$	dimensionless time
$\underline{U}$	velocity vector [m s^{-1}]
u_z, u_r, u_θ	velocity components [m s^{-1}]
u_s	reference velocity [m s^{-1}]
$\overline{u}$	dimensionless velocity as defined by Eq. (3.2.3)
$\overline{u}_m$	dimensionless mean velocity
$\overline{u}_t$	dimensionless transient part of the total velocity $\overline{u}$
$\overline{u}_\infty$	dimensionless steady limiting velocity of the total velocity $\overline{u}$
$\langle u_z \rangle$	average velocity of the fluid across the annulus cross-section [m s^{-1}]
Q_V	volumetric flow rate [m^3 s^{-1}]
$\overline{V}$	velocity vector in Navier-Stokes equation [m s^{-1}]
z_i	valence of the type-i ion

Greek Symbols

α	ratio of the inner radius to the outer radius of the annular capillary walls
α_m	thermal diffusivity
β	aspect ratio of the capillary radius, a to the Stokes penetration depth, δ_s
β	ratio between the zeta potential of the inner and outer radii of the annulus
β_0	characteristic zeta potential ratio when the zero flow rate occurs
δ	time duration when the constant electric field is switched on [s]
$\overline{\delta}$	dimensionless time duration, defined as $\overline{\delta} = \frac{\mu}{\rho a^2}\delta$
δ_s	Stokes penetration depth [m]
ε_0	permittivity of vacuum, 8.854×10^{-12} [C V^{-1} m^{-1}]
ε_r	dielectric constant of the electrolyte
Φ	electric field potential
ϕ	porosity of the porous media
κ	Debye-Hückel parameter, defined as $\kappa = (\frac{2n_0 e_0^2}{\varepsilon_r \varepsilon_0 k_b T})^{\frac{1}{2}}$ [m^{-1}]
λ_f	electric conductivity of the electrolyte solution
λ_n	positive roots of the zero-order Bessel function $J_0(\lambda_n) = 0$, or $J_0(\lambda_n)N_0(\alpha\lambda_n) - J_0(\alpha\lambda_n)N_0(\lambda_n) = 0$
μ	dynamic viscosity [N s m^{-3}]
ξ	dummy spatial variable in the Green's function
ρ	mass density [kg m^{-3}]
ρ_e	net charge density [C m^{-3}]
τ	dummy time variable in the Green's function; tortuosity of the porous media
Ω	viscous dissipation function of the fluid in the energy equation
ω	angle frequency of the sinusoidally alternating electric field [s^{-1}]
Ψ	dimensionless electrical potential of the EDL field, $\Psi = \frac{e_0\zeta}{k_b T}$
ψ	electrical potential of the EDL field [V]

ζ	zeta potential of the specified surfaces [V]

Subscripts

D	with reference to Darcy parameter
diff	with reference to viscous diffusion
e	with reference to electrical charge
eff	with reference to effective parameter
H	with reference to high EDL potential regime
i	with reference to type-*i* ion species, in this work *i* = +, -; value at inner wall of the annulus
L	with reference to low EDL potential value
m	with reference to the mean value
max	maximum value
o	value at outer wall of the annulus or the wall of a cylinder
p	with reference to the packing particles
pore	with reference to the pore in the porous media
r	value at radius coordinate direction
ref	reference value
rev	with reference to the representative elementary volume in the porous media
s	with reference to Stokes layer; reference slip velocity; with reference to capillary inner surface
t	value of transient aspect
V	with reference to volumetric quantity
z	value at axial coordinate direction
θ	value at angle coordinate direction
∞	value at steady state

Superscripts

$n+1$	the value for n obtained in the previous iteration

*	with reference to characteristic value or eigenvalue
′	dimensionless variable in figures

Abbreviations

AC	Alternating Current
CEC	Capillary Electro-Chromatography
DC	Direct Current
DI	Deionised
EDL	Electric Double Layer
EK	Electrokinetic
EOF	Electroosmotic Flow
HPLC	High-Performance Liquid Chromatography
LTE	Local Thermal Equilibrium
ODS	Octyldecyl Silica
REV	Representative Elementary Volume
SEM	Scanning Electron Micrograph

Chapter 1

Introduction

1.1 Background and Motivation

Miniaturization and automation have revolutionized the world of micro-electronics. In recent decades these cutting-edge engineering technologies have been applied to the needs of the biomedical industry, giving rise to a brand new interdisciplinary area – Microfluidics. Microfluidic devices hold great promise for biomedical applications. They consume sample material and reagents in extremely low volumes. Individual microfluidic device can be inexpensive and disposable. The process time from sampling to result tends to be very short. And the most advanced chip designs can perform all analytical functions, including sample manipulation (Minerick *et al.*, 2003), sample pretreatment (Peled, 1996), separation, dilution, mixing (Ben and Chang, 2002; Takhistov *et al.*, 2003), ejection (Thamida and Chang, 2002), chemical reactions (Northrup *et al.*, 1995), and detection (Meinhart *et al.*, 1998), in a single integrated microfluidic circuit.

As a kernel component in the microfluidic devices, micropump provides the kinetic source to route the liquid through microchannel networks. Micropumps are categorized into two major types (Nguyen *et al.*, 2002): mechanical and non-mechanical pumps. The former often involves moving parts such as check valves, microturbines, or oscillating membranes. When devices are miniaturized to microscale, the surface-to-volume ratio becomes very large and the surface forces, such as surface tension may dominate in the microsystem. Thus the mechanical micropump often cannot provide enough power to overcome the high fluidic impedance due to the size scaling down. In

addition, since the mechanical pumps only generate a constant fluid volume in each pump cycle, it is difficult to accurately control a very fine amount of fluids. In contrast, the non-mechanical micropump creates momentum in the fluid by converting other forms of energy into kinetic energy. For instance, the electrokinetic (EK) micropump is solely dependent on the interaction between the fluid the applied electric field. And it has many advantages over other types of micropumps. First, EK micropumps have no solid moving parts and have much simpler designs. Secondly, EK micropumps can transport working fluids of a wide range of conductivity, even non-electrolyte liquid samples (Takhistov *et al.*, 2002), which is essential for biological and medical applications. Thirdly, precise amount of liquid can be maneuvered by easily controlling external electric field.

The physical mechanism underlying the electrokinetic pumping capability is electroosmosis, which together with electrophoresis constitute the basic interfacial electrokinetic phenomena. Electroosmosis was first investigated by researchers in geophysical sciences, who found water migration through porous clay diaphragms under an applied electric field (Reuss, 1809). It is only in recent decades that electroosmosis has found a variety of practical applications in geophysical or environmental industries, such as dewatering of soils for construction purpose, and removing contaminants or waste sludges from soils (Hunter, 1981). With the rapid development of microfluidics in the past few years, electroosmosis has drawn wide attention due to its pressure-building ability. Extensive theoretical and experimental works on electroosmosis have been reported to further the physical understanding and realize the most advanced application of this basic phenomenon. For instance, it has been employed as a basic manipulation to transport and control liquid samples of nanovolumes in microdevices used for chemical and biological analysis and medical diagnosis (Bousse *et al*., 2000).

After a broad review of the currently available literature on electroosmosis, it can be concluded that most of the studies done so far in this area mainly focus on the electroosmosis in simple geometries, such as parallel slits, cylinders, or rectangular channels. Since electroosmosis is an interfacial phenomenon, to maximize interfacial effects, some complex and non-continuous geometries are applied in order to increase the effective interface area, such as the stationary porous structure used in electro-separation. However, the reported studies on electroosmosis in porous media are limited. And majority of them are either experimental investigation with simple extensions of the basic theory, or complicated statistical model which ignores the contact of the stationary phase. Furthermore, the insight to the dynamic nature of the electroosmosis can provide guidance on the design for precision control of the electrokinetic micropump or other micromixing instruments. Theoretically, the works reported in the literature are based on numerical method, or simplified theoretical analysis, and mainly focus on the parametric studies without further concerning of the kernel causes of the dynamic electroosmosis. To the best of the author's knowledge, there is still no study reported on the dynamic electroosmosis in porous media. In addition, there is still much scope to explore the electroosmosis in porous structures.

Thus this study serves as an attempt to fulfill the present void by carrying out a fundamental, systematic and in-depth exploration on the electroosmosis in porous microstructures and its dynamic nature from both hydrodynamic and thermal aspects.

1.2 Objectives

Electroosmosis is an interfacial phenomenon in nature. The momentum acquired by polar fluid originates from the interaction between the electric field and an extremely thin layer of fluid close to the liquid-solid interface. Therefore the electroosmosis in

porous media and in unpacked microcapillary share the same fundamental mechanism. In order to further understand more complicated physics of electroosmosis in porous media, it is a prerequisite that one should investigate the dynamic nature of electroosmosis in simple structures, such as cylindrical geometry that is widely applied in electro-separation technology. Use of porous structures greatly enlarges the interface area. Consequently the active region where the electrokinetic driving force is present gets maximized and the pressure building capacity is significantly enhanced. But the fluid flow inside porous structures are scattered and intertwined. The fluid domain is not continuous due to the presence of stationary phase. Therefore the analysis becomes more difficult. It is expected that the theoretical findings obtained by simple geometry analysis should be improved by accounting for the geometrical and electrokinetic complexity in porous media. The other important objective of this study is to provide the extensive experimental data on the electroosmosis in porous media as validation of current models and guidance of electrokinetic micropump development. In summary, the objectives of this thesis are highlighted as following:

(1) Study electroosmotic flow through cylindrical microcapillary, and a more general micron-sized annular geometry, and investigate the dynamic responses under the time-dependent electric field and other important working parameters;

(2) Characterize static and dynamic aspects of the electroosmotic flow in a microcapillary packed with microspheres, taking into consideration of the boundary wall effect and the Joule heating effect;

(3) Conduct an experiment to design, fabricate, and characterize an electrokinetic micropump using packed microcapillaries. Extensive experimental data under a wide variety of hydrodynamic and physicochemical conditions will be accumulated.

Although majority of this study is theoretical in nature, the information uncovered by the modeling and experimental results can be of great importance to the development and optimization of the electrokinetic micropump or microactuator.

1.3 Outline of the Thesis

The overall thesis comprises five major parts summarized as following:

Chapter 1 serves as an introduction to the background and motivation of this work. The applications and latest development of microfluidics are presented and the objectives of this thesis are outlined. Following is a brief of the electric double layer (EDL) theory. In the end the literature of existing studies on the electroosmotic flow in microchannels is thoroughly reviewed and remarked.

The second part includes chapters 2 and 3, in which the complete models for dynamic aspects of the electroosmotic flow in a cylindrical and annular capillary with high zeta potentials are presented. Analytical solutions of the Poisson-Boltzmann equation for the EDL potential distribution and the Navier-Stokes equation for the electroosmotic flow field in microcapillaries are obtained, and the results under influences of the EDL, external electric field, and geometric parameters are presented. Specifically, as a major contribution of this part, the dynamic electroosmotic flow under AC electric field is analytically solved using Green's function formulation.

The third part comprises chapters 4, 5, and 6, in which a systematic study of the electroosmotic flow in a microcapillary packed with microspheres is conducted based on the capillary model. The electrokinetic wall effect is included by analytically solving the modified Brinkman's equation in chapter 4. The dynamics of the AC electroosmotic flow in a packed capillary is studied in chapter 5. Specifically, the backpressure occurring in a packed capillary with closed-ends is discussed. The Joule heating effect associated with

use of high voltages, concentrated electrolytes, or large capillary size is numerically solved in chapter 6. The transient development of the temperature field inside the packed capillary and its effect on electroosmotic velocity is analyzed in details.

The fourth part is the experimental investigation on the electroosmotic flow in a microcapillary packed with microspheres. In chapter 7, electrokinetic micropumps are fabricated using high pressure driven slurry packing technique. The electroosmotic velocity inside the packed capillary is measured under different physicochemical conditions. The influences of the capillary and particle size, the concentration and the type of the electrolyte solutions are presented. Two different methods to measure the flow velocity are employed for different voltage conditions. The experimental results are compared with the predictions by the theoretical model developed in chapter 4.

Finally, Chapter 8 provides major results and findings from this thesis. The contributions made by this thesis are highlighted and some possible directions for further studies are briefly outlined.

1.4 The Electric Double Layer and the Electroosmotic Flow

Generally, most surfaces will acquire a certain amount of electric charges when they are brought into contact with an aqueous (polar) medium. Some of the charging mechanisms are ionization, ion adsorption, and ion dissolution. The surface charge, in turn, will influence the distribution of nearby ions in the solution. Ions of opposite charge (counter-ions) to that of surface are attracted towards the surface while ions of like charge (co-ions) are repelled from the surface. This electrostatic interaction together with the mixing tendency resulted from the random thermal motion of the ions, leads to the formation of an *electric double layer* (EDL): a compact layer and a diffuse layer. The electric double layer is a region close to the charged surface in which there is an excessive

of counter-ions over co-ions to neutralize the surface charge, and these ions are distributed in a "diffuse" manner. Evidently there is no charge neutrality within the double layer because the number of counter-ions is more than the number of co-ions.

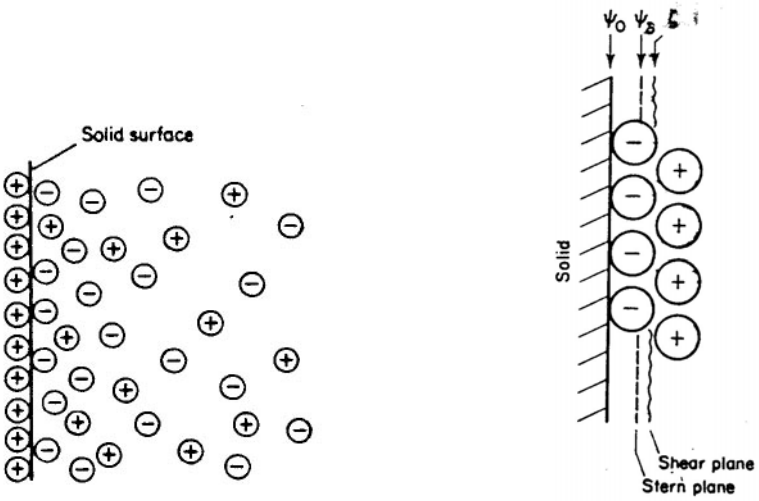

Figure 1-1 (a) Schematic representation of the ionic distribution close to a positively charged surface in the Gouy-Chapman model (Hiemenz, 1986). (b) The region very close to the solid, showing the Stern plane where the potential is ψ_B and the shear plane where the potential is ζ (Probstein, 1994).

The theory for the *diffuse* double layer was first developed independently by Gouy and Chapman (Hiemenz, 1986). According to this model, one layer of charge is assumed to be smeared out uniformly over a plane surface immersed in an electrolyte solution as illustrated in Figure 1-1(a). This surface has an electrostatic potential, ψ_0. Based on the assumption that the compensating ions are regarded as point charges immersed in a continuous dielectric medium, Gouy-Chapman model indicates that the concentration of the ions in the sheath follows the Boltzmann distribution.

However, the ions are of finite size and thus limits the inner boundary of the diffuse part of the double layer, since the center of an ion can only approach the surface to within its hydrated radius without becoming specifically adsorbed. To take this effect into

account, the Gouy-Chapman model was later modified by Stern (Probstein, 1994) who introduced an inner part of the double layer immediately next to the charged surface. The inner layer, the outer boundary of which is approximately a hydrated ion radius from the surface (usually of several Angstroms), contains a layer of counter-ions that are strongly attracted to the surface and are immobile. This compact layer is also called the *Stern layer*. The plane separating the inner compact layer and the outer diffuse layer is called the *Stern plane* as shown in Figure 1-1(b). Ions whose centers are located beyond the Stern plane form the diffuse mobile part of the double layer. The thickness of the diffuse double generally ranges from several to a few hundreds of nanometers, depending upon the bulk ionic concentration and other physicochemical properties of liquid.

As shown in Figure 1-2, the electrical potential changes from the surface potential, ψ_0, to the Stern plane potential, ψ_B, within the Stern layer, and decays to zero far away from the Stern plane. The potential at the Stern plane, ψ_B is close to the *electrokinetic potential* or *zeta potential*, ζ, which is defined as the potential at the shear surface between the charge surface and electrolyte solution and is measurable from experiments.

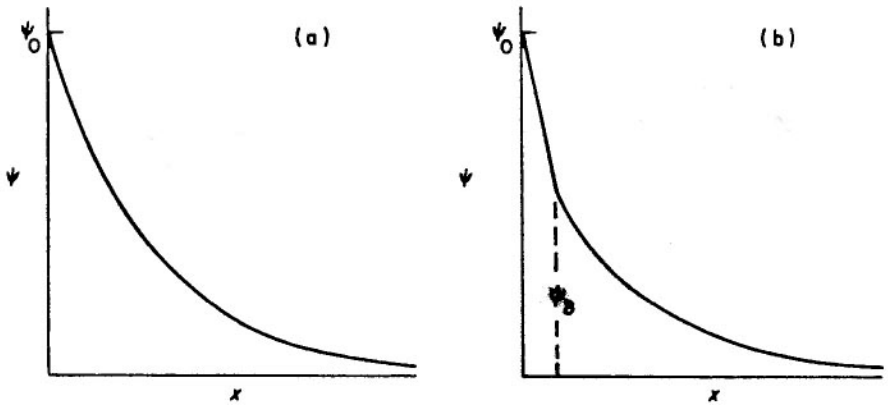

Figure 1-2 Electrical potential (a) for the Gouy-Chapman diffuse region (b) for the Stern model showing expontential decay from the Stern plane. (Probstein, 1994)

Electroosmosis arises when the mobile portion of the diffuse double layer interacts with an external applied electric field in the viscous shear layer near the charged surface. Within the diffuse layer, due to the presence of EDL, the counter-ions predominate and the local net charge density is not zero. If an electric field is applied tangentially along a charged surface, then the electric field will exert a coulombic force on the ions in the diffuse layer. The migration of the mobile ions will carry the adjacent liquid with them leading to an *electroosmotic flow* (EOF). Due to viscous forces, the flow is carried through beyond the EDL region to the rest of the liquid in the microchannel. This electrokinetic phenomenon was first investigated by Reuss (1809), who demonstrated that under the influence of an applied electric field water migrated through porous clay diaphragms towards the cathode. This fact can be well understood today in that the clay, sand and other mineral particles usually carry negative surface charges when in contact with water; the water normally contains small quantities of dissociated salts. As described above, electroosmotic flow is induced through the porous medium in the clay, upon application of electric field.

1.5 Literature Review

In the literature, numerous theoretical and experimental studies have been reported on the electroosmotic flow in fine capillaries. A detailed review of the literature will be presented in the following, focusing on five major aspects: steady-state EOF, dynamic EOF, EOF in porous media, Joule heating on EOF, and the design and fabrication of electrokinetic micropump.

1.5.1 Steady-state electroosmotic flow

The steady state electroosmosis has been well studied decades before. The classical model for electroosmosis is attributed to Smoluchowski (Hiemenz, 1986) on the

consequences of applying pressure and potential gradients across capillaries filled with an electrolyte. His formulation of the problem is based on the assumption of large electrokinetic diameter; the contribution due to the EDL thickness is neglected. Despite that his classical results for EOF plug velocity and streaming potential are still frequently employed in routine experimental works on EOF.

Burgreen and Nakache (1964) formulated a mathematical model for the electroosmotic flow in an ultrafine slit. From the analytical solution obtained they discussed the possible effect of the electrokinetic radius on the electroosmotic flow through the microchannel.

Rice and Whitehead (1965) calculated analytically the correction factors that must be applied to the Smoluchowski's results when dealing with narrow capillaries having arbitrary electrokinetic diameters. However the Rice and Whitehead theory itself is subject to the severe restriction that the zeta potential be sufficiently low to permit the Debye-Hückel approximation, effectively limiting the application of their predictions in $\zeta \leq 25\,\mathrm{mV}$ for an 1-1 electrolyte.

Levine *et al.* (1975) extended the Rice and Whitehead model to high zeta-potentials for the electrokinetic flow in cylindrical capillaries. They developed an analytical approximation to solve the Poisson-Boltzmann (P-B) equation within the capillary, in a fashion similar to the method used by Philip and Wooding (1970) who solved the P-B equation outside a charged cylindrical particle immersed in an electrolyte. And it was shown by Philip and Wooding that the yielded result differs only slightly from those by numerical method.

Keh and Liu (1995) analytically studied the steady EOF in a long uniform circular capillary bearing a solvent-permeable and ion-penetrable layer of adsorbed poly-electrolytes on its inside wall. They obtained the electrical potential and space charge

density distribution by solving the linearized P-B equation. Their results on the EOF demonstrated that the structure of the surface charge layer can result in an augmented or diminished EOF relative to that in a capillary with bear walls, depending on the characteristics of the electrolyte solution, surface charge layer, and capillary.

Koh and Anderson (1975) experimentally investigated the electroosmotic flow in charged microcapillaries of ellipse shape. They compared the data with numerical calculations and showed that adsorption of the potential determining ion is dependent on electrostatic potential at the pore wall.

Mala *et al.* (1997a) investigated the interfacial electrokinetic effects on characteristics of liquid flow and heat transfer between two parallel plates. Experiments were conducted to study the effect of EDL on flow characteristics with different ionic concentrations and plate materials. A mathematical model was developed for a steady-state liquid flow with consideration of the EDL effects. The predicted flow rate agrees well with the measured data.

Recently, due to the relevance to microfluidics fabricated by micromachining technology, electrokinetic flows in rectangular microchannels have been studied by Yang *et al*. (1997, 1998), Arulanandam and Li (2000), and Yang and Huang (2001). In these studies a two dimensional electrokinetic model has been proposed to account for the "corner effect". Based on the Debye-Hückel approximation, an analytical solution of the linearized two-dimensional P-B equation is presented to describe the EDL potential distribution in the cross-section of a rectangular channel. By using the Green's function method, they also obtained an exact solution for the EOF velocity.

Patankar and Hu (1998) developed a numerical scheme to simulate steady-state electroosmotic flows in complicated geometry. Their results agree with the experiment on electroosmotic injection at the intersection of a cross-channel done by Fan and Harrison

(1994). The results show that application of electric field can be used to control the shape of injected fluid.

Mitchell *et al*. (2000) simulated a steady-state electro-osmotic flow on three different geometries by using meshless analysis based on Finite Cloud Method (FCM). Their results show that linear approximation of Poisson-Boltzmann equation for large zeta potential can predict the plug velocity accurately but fails to predict the velocity variation close to the walls.

Bianchi *et al*. (2000) studied electroosmotic flow at a T-junction by using finite element simulation. Their results indicate that relative zeta potential and channel widths are two predominant parameters affecting the distribution of flow at the intersection.

Cummings *et al*. (2000) examined the conditions for similitude between the fluid velocity and electric field in electroosmotic flow. They showed that the conditions necessary are a steady electric field, uniform fluid and electrical properties, a relative thin Debye layer compared to the physical dimensions, and fluid velocities on all inlet and outlet boundaries that satisfy the Helmholtz-Smoluchowski relation.

Tsao (2000) studied the electroosmosis flow through an annulus under the Debye-Hückel linear approximation, indicating that his work is valid only for the case of low zeta potentials (e.g., $\zeta \le 25 mV$ for an 1-1 electrolyte). He introduced a geometry-dependent correction factor electroosmotic mobility described by the Helmholtz–Smoluchowski equation. He also found there exist net flows even for zero area-averaged surface charge density due to the curvature differences between the inner and outer walls. Under certain circumstances the flow direction in an annulus is opposite to that in a capillary with the same sign of the net charge.

Herr *et al*. (2000), Ren and Li (2001), and Gleeson (2001, 2002) investigated the characteristics of the EOF in a cylindrical microchannel with non-uniform zeta potential.

Their theoretical and numerical results show the distorted electroosmotic velocity profiles resulted from the axial variation of the zeta potential. Also, the influences of the unequal section size and the direction of the zeta potential change on the velocity profile, the induced pressure distribution, and the volumetric flow rate are discussed. The simulation results revealed possible effects of bio-adhesion in microchannels on the electroosmotic flow in biochip devices.

Erickson and Li (2002) studied the effects of surface electrokinetic heterogeneity on the electroosmotic flow and mixing efficiency of a T-shaped micromixer through 3D numerical simulations. While all cases of surface heterogeneity were shown to enhance species mixing, they found that the greatest improvements can be achieved when the zeta potential of the heterogeneous surface is of opposite sign to that of the homogeneous surface, resulting in localized circulation zones within the bulk flow field. They also showed that the mixing efficiency improved in general method, such as decreasing applied voltage and the channel size, can be enhanced by the introduction of surface heterogeneity, in some cases resulting in a 70% reduction in the required mixing length.

1.5.2 Dynamic electroosmotic flow

Compared with the static nature, the dynamic aspects of the EOF have received relatively less intention. However, the study on the unsteady EOF not only can provide more insight into the characteristics of the EOF but also is important to the development and precise control of the EOF based microfluidic device.

Lopez-Garcia *et al*. (2000) who have done an analysis of the dynamics of EDL in both time and frequency domain provide some insights into the transient behavior of potential, velocity, and ion concentration profiles. They analyzed how potential and ion concentration profiles, particle or fluid velocity evolve in the nanosecond to microsecond

time range after the application of an electric field. A network method is proposed to gain information about the evolution with time of the potential, the counter-ion, and co-ion perturbations, the particle velocity, and the fluid velocity profile.

Yang *et al*. (2002) developed an exact solution for the transient electroosmotic flow in a slit microchannel. Exact solutions for the electrical potential profile and the transient electroosmotic flow field are obtained by solving the complete Poisson–Boltzmann equation and the Navier-Stokes equation under an analytical approximation for the hyperbolic sine function.

Santiago (2001) studied the effects of fluid inertial and pressure on the transient velocity and vorticity fields of electroosmotic flow in a two-dimensional microchannel. His work is based on the classical Debye-Hückel linear approximation in solving the P-B equation to obtain the electric double layer potential distribution and a validated slip velocity condition. In typical on-chip electrokinetics applications, the flow field can be separated into an inner flow region dominated by viscous and electrostatic forces and an outer flow region dominated by inertial and pressure forces. These two regions are separated by a slip velocity condition determined by the Helmholtz-Smoluchowski equation. The validity of this assumption is investigated by analyzing the velocity field in a pressure-driven, two-dimensional flow channel with an impulsively started electric field. The regime for which the inner/outer flow model is valid is described in terms of non-dimensional parameters derived from the example problem.

Without assumption of thin double layer thickness, Keh and Tseng (2001) analytically studied the transient response of electrolyte solutions in a narrow capillary tube and slit to a step change in the applied electric field and pressure gradient by solving the linearized P-B equation. Their results demonstrated that the behavior of the transient electrokinetic flow in a capillary tube and in a capillary slit is similar; however, the rate of

evolution of the flow in a tube with time is faster by a factor of about 2 than that in a slit with its half thickness equal to the tube radius.

By numerically solving the combination of the Poisson, the Nernst-Planck, and the Navier-Stokes equations, Yang *et al.* (2001) investigated the time and space development for the entry region of an electroosmotic flow through microchannels between two parallel plates. They discussed the effects of the entrance region on the fluid velocity distribution, charge density boundary layer, entrance length, and shear stress. They found the entrance length of the electroosmotic flow is longer than that of classical pressure-driven flow. The thickness of the electrical double layer (EDL) in the entry region is thinner than that in the fully developed region. The change of velocity profile is apparent in the entrance region, and the axial velocity profile is no longer flat across the channel height when the Reynolds number is large.

Static electric fields are usually used in above research work on the unsteady electroosmotic flow. However, in recent years, the use of time dependent electric fields has proved another practical and useful technique in maneuvering the electroosmotic flow. For instance, Söderman and Jönsson (1996) developed a theoretical framework for the description of the time and spatial resolution of electroosmosis for both planar and cylindrical geometries under the effect of pulsed electric fields. Specifically, sinusoidally alternating (AC) electric fields are more often applied to investigate the frequency dependent nature of the fluid velocity or the motion of the nano-particles, whose mechanism in the literature is termed as *AC electroosmosis* (Ramos *et al.*, 1999). Due to potential applications in micromixing and microactuators, AC electroosmosis has drawn much more research intention.

Barragán and Bauzá (2000) performed electroosmosis experiments through a cation-exchange membrane and showed that the presence of AC perturbation affects the

electroosmotic flow, depending on the frequency of AC signal and on the solution stirring conditions. In the frequency range studied, two regions have been observed where the electroosmotic flow reaches a maximum value: one at low frequencies (~Hz); the other at frequencies of the order of kHz. These regions could be related to membrane relaxation phenomena.

In a recent work on electrokinetic instability micromixing, Oddy *et al*. (2001) developed an electrokinetic process to rapidly stir micro-and nano liter volume solutions for microfluidic bioanalytical applications. They rapidly stirred micro flow streams by initiating a flow instability, which they observed in sinusoidally oscillating, electroosmotic flows. As the effect occurs within an oscillating electroosmotic flow, they refer to it as an electrokinetic instability (EKI). They obtained the electroosmotic velocity profile in a micromixer by using slip velocity approximation, in which the velocity on the outskirts of the flow field is bounded by the "slip velocity". The slip velocity model was first proposed by Overbeek (1952) who showed that for micro-channels with relatively thin electrical double layers, the flow field outside the double layer is an irrotational flow with a slip velocity boundary condition determined by the well-known Helmholtz-Smoluchowski equation.

1.5.3 Electroosmotic flow through porous media

As in above discussion, the electroosmosis is an interfacial phenomenon. Use of porous structures can greatly enlarge the interfacial area, and thus significantly enhance the pressure-building capacity of the EK micropump. Therefore the mechanism of the EOF in porous media is deserved for further research input.

Rathore and Horváth (1997) presented two models in their review paper on the theories of the EOF in porous media. The first is based on Smoluchowski's work as

adapted and extended by Overbeek (1952). It deals with the EOF through packed capillaries under a condition of low electric field strength where the EOF varies linearly with the field strength because there is no polarization of the double layer. The second model proposed by Dukhin (1991) predicts the EOF of at least an order of magnitude higher than that expected by classical theories. It was concluded that there had not yet been established a solid theoretical understanding of the EOF in capillary chromatography (CEC). They strongly indicated that the construction and solution of the mathematical model that could properly describe the electrokinetic phenomena underlying the EOF in packed beds could have the potential to develop the CEC into a powerful separation process.

Liapis and Grimes (2000) constructed a mathematical model to describe quantitatively the profiles of the electrostatic potential, pressure, and velocity of the EOF in charged cylindrical capillaries and in the CEC systems. They compared their theoretical results of the EOF velocity with the experimental values of the EOF velocity obtained from a fused-silica column packed with charged porous silica particles; the agreement between the theoretical results and the experimental data is good. Also, the results from model simulations indicated the conditions that permit high values for the average velocity of the EOF to be obtained, for a given operationally permissible value of the applied electric field.

As a continue work, Grimes *et al*. (2000) employed the pore network theory and the model constructed by Liapis and Grimes (2000) together to estimate the magnitudes of the intraparticle EOF flow rate, velocity in the pores of the charged porous silica particles.

Tallarek *et al*. (2001) studied the macroscopic heterogeneities in electroosmotic and pressure-driven flow through fixed beds at low column-to-particle diameter ratio and

demonstrated that a significantly superior performance, which has been shown for the EOF through packed capillaries compared to pressure-driven flows, can be obstructed by wall effects, and it is difficult trace back remaining differences in the asymptotic dispersion observed for these types of fluid flow to an inherent performance concerning intraparticle and film mass transfer or a macroscopic flow heterogeneity.

Blokhra and Joshi (1999) investigated the effects of the magnetic field on the electrokinetic transport coefficients of electrolyte at different potentials, concentrations, and magnetic fields. The phenomenological coefficients characterizing the EOF and the membrane characteristics are also estimated for the various solutions with the object of determining the efficiencies of electrokinetic energy conversion and zeta potentials.

Lee *et al*. (2000) theoretically modeled the EOF of a general electrolyte solution through a fibrous medium, taking effect of the EDL polarization into account. It was shown that if the effect of EDL polarization is neglected using the linearized P-B equation will underestimate the electroosmotic velocity. The deviation becomes inappreciable if the electrokinetic diameter is either very large or very small.

Coelho *et al*. (1996) developed a general theory of electroosmotic phenomena in porous media possessing spatially periodic structure. General expressions for the electric conductivity, permeability, and coupling electroosmotic tensor coefficients are obtained in terms of solutions of several transport unit cell problems, posed for the linearized electrokinetic equations.

Marino *et al*. (2000) extended the results by Coelho *et al*. (1996) to the important case of deterministic sinusoidal and random self-affined fractures in the linear limit for various double layer thickness. Their numerical results showed a definite influence of the surface amplitude on electroosmotic processes. And in a more recent paper, Marino *et al*.

(2001) further extended their work to include the effects of macroscopic concentration gradients, in addition to the influence of electrical and pressure gradients.

1.5.4 Thermal effects in electroosmotic flow systems

Since the electroosmosis is electric field driven flow, the Joule (resistive) heat generation is inevitable due to the electric current incurred. This effect becomes significant for large capillary size (due to decreased surface-area-to-volume ratio) or high electrolyte concentration (due to high electric conductivity). In application of electrokinetic separation, the temperature rise due to Joule heating will in turn affect the electroosmotic flow and the separation efficiency. The significant temperature rise may even damage the thermal labile sample and cause vapor bubbles. Due to its importance, the Joule heating problem has drawn wide attention of the researchers.

Based on Poisson-Boltzmann model for electric double layer, Tang et al. (2004a, 2004b) presented numerical models to evaluate the Joule heating effect on the electroosmotic flow and mass transfer in *non-packed* microcapillaries for steady sate and transient situations. Their numerical simulations showed the significant radial and axial temperature rise. And they also compared the simulation results based on P-B equation and Nernst-Planck equation respectively (Tang *et al.*, 2003). They pointed out the two models gives the same results for the solution ionic concentration in the fully-developed flow region or in case of large electrokinetic diameter. In their calculation, they assumed uniform electric field strength, which in effect ignores the continuity of the electric current. Considering the temperature-dependent electric conductivity, however, the electric field strength should be strongly coupled with the temperature field.

Xuan et al. (2004a) numerically investigated the thermal end effects on the electroosmotic flow in a *non-packed* microchannel. Their model includes the coupling

electric field strength which is subject to local change due to the non-uniform electric conductivity. And as a continual work, they use fluorescence-based techniques to measure the liquid temperature variation and the electroosmotic velocity profile along a microchannel (Xuan et al., 2004b). Their experimental results were found to agree well with the predictions of the numerical model.

Knox (1988) pointed out that Joule heating causes the main limitation of performance of four capillary electro-separation methods. One of them is capillary electrochromatography in which the capillaries packed with microparticles are used as separation media. The separation efficiency is greatly affected because of the peak dispersion arising from Joule heating. He found the heat is generated homogeneously over the central region and the temperature variation across the bore of the cylindrical capillary is parabolic. The thermal gradient is largest in the air zone and least in the tube wall. In addition, he derived simple analytical expression of the cross-stream temperature excess within the core region and the capillary wall at steady state. But his model is too simple because he did not consider the temperature dependence of the liquid properties as well as the non-uniform electric field.

Keim and Ladisch (2003) developed a two-dimensional transient temperature model for electrochromatography. Their model accounts the temperature dependence of the physical properties of the stationary and mobile phase. Their model also included the temperature dependence of the electric conductivity and thus the non-uniform electric field strength. The modeling results were compared with experiment data. The prediction was found to be within 3 ^{o}C of the actual temperature. In addition they reported there was a transient voltage drop at the column outlet due to uniform electric field. However they did not further discuss the Joule heating effects on the electroosmotic flow though the packed capillary.

1.5.5 Deign and fabrication of electrokinetic micropump

Due to the advantages of the EK micropump and its potential of delivering liquid in high flow rate and generating high pressure, the development of the actual EK micropump have become an area of intense research during recent years.

The first effort made to design an electrokinetic micropump may attribute to Paul *et al*. (1998) who reported the ability to generate high pressures using electrokinetic pumping of liquid through porous media. Pressures in excess of 8000 psi have been achieved using silica capillaries packed with micron-size silica beads.

Chen *et al.* (2000) developed a preliminary model of planar EK micropump to characterize the flow rate, pressure capacity, and thermodynamic efficiency of the pump. The pump was fabricated on a 50 × 75 × 1.2 mm glass substrate using standard micro lithography and chemical wet etching techniques. The pump is 1 mm long in the flow direction and 0.9 μm × 38mm in cross-section. DI water was used as working fluid. Their experimental results showed a linear relationship between flow rate and counter pressure. However, their planar EK pump can only generate flow rate up to 15 μl/min and pressure up to 0.3 atm at an applied voltage of 1 kV.

Zeng *et al*. (2001) fabricated an EK pump by packing the 3.5 μm diameter non-porous silica particles into 500-700 μm diameter fused-silica capillaries and using a silicate frit fabrication scheme to hold the particles in place. The pump can generate maximum pressures in excess of 20 atm or maximum flow rates of 3.6 μl/min for a 2 kV applied potential. But they also addressed the limitations associated with electrolytic gases and its negative effect on the long-term performance of the device.

In designing a large flow rate EK micropump, one of the key issues is the fabrication of the robust frits. Zeng *et al.* (2002) reported a novel fabrication technique by

employing photopolymerization method to make frits and by applying a side-bore packing method to produce a bed of 1-3 μm particles. The photopolymer offers significant design flexibility because it can be photopolymerized in varied structures. The maximum flow rates and pressure generated by their pumps are 0.8 ml/min. and 2 atm, at 1.0 kV applied voltage.

Chen *et al.* (2003) developed the EK micropump using single and multiple microcapillaries packed with silica microspheres. Their pump is tested with methanol, phosphate sodium buffer and their mixture, which can generate pressure from 0.1 to 15 MPa and flow rates of tens of nanoliters to several microliters per minute. Specifically, the interruption of the pumping by bubble formation due to Joule heating, vaporization or decompounding of the fluid in side the capillaries was observed, especially for high voltage or large capillary size.

Yao *et al*. (2003a, b) demonstrated an EK pump prototype by modifying a commercially available sintered glass frit. The frits they used were porous cylinders of 40 mm in diameter and 1 to 5 mm thick and provide the high wetted-surface-to-volume ratio. One of their pumps achieved a maximum flow rate of 33 ml/min and a maximum pressure capacity of 1.3 atm at a 100V applied voltage. They also developed a theoretical model to simulate the electroosmotic flow in the pump and compared the results with the experimental data. It is found the model can predict the performance trend and useful for design of EK pump. However, large discrepancy from 21% to 49% between modeling results and experimental data had been found. At least part of the discrepancy, as they said, may be due to the random geometry of the actual porous structure, which is different from the idealized cylindrical pore geometry in their modeling.

Chapter 2

Dynamics of Electroosmotic Flow in a Capillary Cylinder

2.1 Introduction

As discussed in the first chapter, study of unsteady electroosmotic flow not only can provide more insights into the characteristics of electroosmotic flow but also is important to the practical development and operation of microfluidic devices. The current study presents a theoretical analysis of the dynamics of electroosmotic flow in a cylindrical microcapillary. We start with the time evolution of the transient electroosmotic flow motivated by a time dependent electric field, and discuss the flow field oscillations excited by a sinusoidally alternating electric field. Importantly, the complete Poisson-Boltzmann equation governing the EDL electric field is analytically solved with arbitrary zeta potentials under a proposed analytical scheme. Exact solutions for transient velocity distributions and time-dependent mean velocities are obtained using the Green's function method. As a comparison, the solution under slip velocity approximation is also presented.

In the analysis of electroosmosis presented below we have made the following assumptions

(i) The temperature is assumed uniform over the entire sample. Thus we neglect any possible effect due to Joule heating.

(ii) The magnetic field produced by the moving charges is neglected.

(iii) The flow of the liquid is laminar in nature.

(iv) The liquid is assumed to be an incompressible, Newtonian, symmetric electrolyte

of constant viscosity and permittivity over the considered volume.

(v) All the boundary surfaces are assumed to be of uniform charge density.

(vi) The changing frequency of the external electric field is not very high (e.g., less than 1 MHz), so the Poisson-Boltzmann equation is still valid for dynamic electroosmotic flows.

2.2 Problem Formulation

For the case of a forced, laminar flow through a cylindrical microchannel of radius *a*, the equation of motion of an incompressible Newtonian fluid of density, ρ, and viscosity, μ, is given by the Navier-Stokes equation (Probstein, 1994).

$$\rho\frac{\partial \overline{V}}{\partial t}+\rho\left(\overline{V}\cdot\nabla\right)\overline{V}=-\nabla\overline{P}+\overline{F}+\mu\nabla^{2}\overline{V} \tag{2.1}$$

For a fully developed flow in the cylindrical microchannel, the components of velocity $\overline{V}$ satisfy $u_z = u(r,t)$ and $u_r = u_\theta = 0$ in terms of cylindrical coordinates. Thus the inertial term $\left(\overline{V}\cdot\nabla\right)\overline{V}$ vanishes. When an external electric field, $E(t)$ is applied along the axis of the capillary, the liquid starts to move as result of the interaction between the net charge density in the electric double layer (EDL) and the applied electric field. As the flow is not pressure induced, the term $\nabla\overline{P}$ is not present. If the gravity effect is negligible, the body force $\overline{F}$ is only the Coulomb force caused by the action of an applied electric field E on the net charge density $\rho_e(r)$ in the EDL region. With these considerations, Eq. (2.1) is reduced to (Probstein, 1994)

$$\rho \frac{\partial u(r,t)}{\partial t} - \mu \frac{1}{r} \frac{\partial}{\partial r} \left[r \frac{\partial u(r,t)}{\partial r} \right] = E(t) \rho_e(r) \tag{2.2}$$

where $u(r,t)$ is the transient velocity field. $\rho_e(r)$ is the local volumetric net charge density of the electrolyte due to the presence of the EDL.

Consider a fluid phase containing positive and negative ions in contact with a charged capillary wall. An EDL field will be established. Assume the surface bears a uniform zeta potential, ζ_o. We consider a simple fully dissociated symmetrical salt in solution, where far away from the wall, the concentration of the positive and negative are equal, i.e., $z_+ = -z_- = z$ and $n_+ = n_- = n_0$. The electrostatic potential $\psi(r)$, at any point near the surface, is related to the net number of electrical charge per unit volume $\rho_e(r)$, in the neighborhood of the point, which measures the excess of the positive ions over negative ions or vice versa. Accordingly to the theory of electrostatics, the relation between $\psi(r)$ and $\rho_e(r)$ is given by Poisson's equation (Hunter, 1981), which for a cylindrical surface is

$$\frac{1}{r} \frac{d}{dr} \left[r \frac{d\psi(r)}{dr} \right] = - \frac{\rho_e(r)}{\varepsilon_r \varepsilon_0} \tag{2.3}$$

where ε_r is the dielectric constant of the electrolyte and ε_0 is the permittivity of vacuum.

For any fluid consisting of two kinds of ions of equal and opposite charge z_+ and z_-, the number of ions of each type is given by the Boltzmann equation (Hunter, 1981)

$$n_{\pm}(r) = n_0 \exp \left[\mp \frac{z e_0 \psi(r)}{k_b T} \right] \tag{2.4}$$

where e_0 is the elementary charge, n_0 is the ionic number concentration in the bulk phase (i.e., far from the charged surfaces), k_b is the Boltzmann constant, T is the absolute

temperature, and $\psi(r)$ is the electric potential of the EDL. A proof of the validity of the Boltzmann distribution in application of time-dependent electroosmotic flow is presented in the appendix A.

The net charge density in a unit volume of the fluid is given by

$$\rho_e(r) = (n_+ - n_-)ze_0 = -2n_0 ze_0 \sinh\left[\frac{ze_0\psi(r)}{k_b T}\right] \tag{2.5}$$

where z is the valence of the ions. For a monovalence electrolyte considered in this study, $z = 1$.

Substituting Eq. (2.5) into Eq. (2.3), we obtain a non-linear Poisson-Boltzmann equation, which solely determines the EDL potential distribution

$$\frac{1}{r}\frac{d}{dr}\left[r\frac{d\psi(r)}{dr}\right] = \frac{2n_0 ze_0}{\varepsilon_r \varepsilon_0}\sinh\left[\frac{ze_0\psi(r)}{k_b T}\right] \tag{2.6}$$

Introducing the following dimensionless parameters

$$\bar{u} = \frac{u}{u_s} \qquad \bar{t} = \frac{\mu}{\rho a^2}t \qquad \bar{r} = \frac{r}{a} \qquad \Psi = \frac{e_0\psi}{k_b T} \tag{2.7}$$

We can nondimensionlize Eq. (2.2) and Eq. (2.5) respectively as

$$\frac{\partial \bar{u}}{\partial \bar{t}} - \frac{1}{\bar{r}}\frac{\partial}{\partial \bar{r}}\left(\bar{r}\frac{\partial \bar{u}}{\partial \bar{r}}\right) = \frac{a^2}{\mu u_s}\rho_e(\bar{r})E(\bar{t}) \tag{2.8}$$

and

$$\rho_e(\bar{r}) = -2n_0 e_0 \sinh[\Psi(\bar{r})] \tag{2.9}$$

Here u_s is the reference velocity defined as

$$u_s = -\frac{\varepsilon_r \varepsilon_0}{\mu}E_0\zeta_o \tag{2.10}$$

The reference velocity, u_s can also be regarded as the "slip" velocity on the shear plane of the EDL (Overbeek, 1952). Obviously, u_s is proportional to the magnitude of the external field, E_0 and the zeta potential, ζ_o.

Substituting Eq. (2.9) into Eq. (2.8), we obtain an inhomogeneous diffusion equation

$$\frac{\partial \bar{u}}{\partial \bar{t}} - \frac{1}{\bar{r}}\frac{\partial}{\partial \bar{r}}\left(\bar{r}\frac{\partial \bar{u}}{\partial \bar{r}}\right) = \frac{(\kappa a)^2}{\Psi_s E_0}\sinh\left[\Psi(\bar{r})\right]E(\bar{t}) \tag{2.11}$$

where $\Psi_s = \frac{e_0\zeta_o}{k_bT}$ and $\kappa = \sqrt{\frac{2n_0e_0^2}{\varepsilon_r\varepsilon_0k_bT}}$. κ is the Debye-Hückel parameter, and $1/\kappa$ denotes the characteristic thickness of the EDL (Hunter, 1981). Eq. (2.11) is subject to the initial and boundary conditions

$$\bar{t} = 0 \qquad \bar{u} = 0 \tag{2.12a}$$

$$\bar{r} = 0 \qquad \frac{\partial \bar{u}}{\partial \bar{r}} = 0 \qquad \bar{r} = 1 \qquad \bar{u} = 0 \tag{2.12b}$$

2.3 Green's Function Method for Inhomogeneous Diffusion Equation

In Green's function technique, to obtain the field caused by a distributed source (or charge heat generator or whatever it is that causes the field) we calculate the effects of each elementary portion of source and add them all. If $G(x,t\,|\,\xi,\tau)$ is the field at the observer's point **x** at the moment of *t* caused by a unit point source at the source point ξ at the moment of τ, then the field at **x** at the moment of *t* caused by a source distribution $\rho(\xi,\tau)$ is the integral of $G\rho$ over the whole range of space ξ and time τ occupied by the source. The function *G* is called Green's function.

Thus the solution of inhomogeneous diffusion equation

$$\frac{\partial u}{\partial t} - D\nabla^2 u = Q(\mathbf{x}, t) \tag{2.13}$$

is given by (Morse and Feshbach, 1953)

$$\begin{aligned} u(\mathbf{x},t) = & \int_0^t \iiint G(\mathbf{x},t;\xi,\tau) Q(\xi,\tau) d\xi d\tau \\ & + \iiint G(\mathbf{x},t;\xi,0) u(\xi,0) d\xi \\ & + \alpha \int_0^t \oiint \left[G(\mathbf{x},t;\xi,\tau) \frac{\partial u}{\partial n} - u(\xi,\tau) \frac{\partial G}{\partial n} \right] dS d\tau \end{aligned} \tag{2.14}$$

where $G(x,t;\xi,\tau)$ is the Green's function of the specified diffusion equation. The second and third term on the right hand side represent the effects of initial and boundary conditions, respectively.

The sought Green's function $G(r,t \mid \xi,\tau)$ should satisfy (Butkov, 1968)

$$\frac{\partial G}{\partial \bar{t}} - \frac{1}{\bar{r}} \frac{\partial}{\partial \bar{r}} \left(\bar{r} \frac{\partial G}{\partial \bar{r}} \right) = \delta(\bar{r} - \xi)\, \delta(\bar{t} - \tau) \tag{2.15}$$

subject to the initial and boundary conditions

$$G(\bar{r}, 0 \mid \xi, \tau) = 0 \tag{2.16a}$$

$$\frac{\partial}{\partial r} G(0, \bar{t} \mid \xi, \tau) = 0 \tag{2.16b}$$

$$G(1, \bar{t} \mid \xi, \tau) = 0 \tag{2.16c}$$

where $\delta(\bar{r} - \xi)$ and $\delta(\bar{t} - \tau)$ are Dirac delta functions. We can see that the source is an impulse at $\bar{t} = \tau$, located at $\bar{r} = \xi$. G then gives the description of effect of this impulse as it propagates away from $\bar{r} = \xi$ in the course of time.

Taking Hankel transform with respect to $\bar{r}$ ($G_H = \mathcal{H}\{G\}$) and using the boundary

conditions Eqs. (2.16b)-(2.16c), we obtain

$$\frac{dG_H}{d\bar{t}} + \lambda_n^2 G_H = \xi J_0(\lambda_n \xi)\delta(\bar{t} - \tau) \tag{2.17}$$

where λ_n are the positive roots of the zero-order Bessel function $J_0(\lambda_n) = 0$.

Now, we take the Laplace transform with respect to $\bar{t}$ ($G_{HL} = \mathcal{L}\{G_H\}$) and use the initial condition Eq. (2.16a) to obtain

$$s\,G_{HL} + \lambda_n^2 G_{HL} = \xi J_0(\lambda_n \xi) e^{-s\tau} \tag{2.18}$$

We solve for G_{HL} and get

$$G_{HL} = \frac{\xi J_0(\lambda_n \xi)}{s + \lambda_n^2} e^{-s\tau} \tag{2.19}$$

taking inversive Laplace transform

$$G_H = H(\bar{t} - \tau)\xi J_0(\lambda_n \xi) e^{-\lambda_n^2(\bar{t} - \tau)} \tag{2.20}$$

where $H(\bar{t} - \tau)$ is the Heaviside step function. The inversion with respect to Hankel transform leads to

$$G(\bar{r}, \bar{t} \mid \xi, \tau) = H(\bar{t} - \tau) \sum_{n=1}^{\infty} \frac{2 J_0(\lambda_n \bar{r})}{J_1^2(\lambda_n)} \xi J_0(\lambda_n \xi) \exp[-\lambda_n^2(\bar{t} - \tau)] \tag{2.21}$$

Hence we obtain the Green's function for inhomogeneous diffusion equation in cylindrical coordinates. Using Green's function method and applying the initial and boundary conditions in Eqs. (2.12), we can show that the solution to Eq. (2.11) is expressed as

$$\bar{u}(\bar{r}, \bar{t}) = \int_{\tau=0}^{\bar{t}} \int_{\xi=0}^{1} G(\bar{r}, \bar{t} \mid \xi, \tau) \left\{ \frac{(\kappa a)^2}{\Psi_s E_0} \sinh[\Psi(\xi)] E(\tau) \right\} d\xi d\tau \tag{2.22}$$

Substituting Eq. (2.21) into Eq. (2.22) leads to

$$\bar{u}(\bar{r},\bar{t}) = \frac{2(\kappa a)^2}{\Psi_s}\sum_{n=1}^{\infty} C_n \frac{J_0(\lambda_n \bar{r})}{J_1^2(\lambda_n)} \int_{\tau=0}^{\bar{t}} \frac{1}{E_0} E(\tau)\exp[-\lambda_n^2(\bar{t}-\tau)]d\tau \tag{2.23}$$

where $C_n = \int_{\xi=0}^{1} \xi J_0(\lambda_n \xi)\sinh\left[\Psi(\xi)\right] d\xi$. Integrating Eq. (2.23) along the radius of the cylinder, we obtain the non-dimensional mean velocity

$$\begin{aligned} \bar{u}_m(\bar{t}) &= 2\int_{\bar{r}=0}^{1} \bar{r}\bar{u}(\bar{r},\bar{t})\, d\bar{r} \\ &= \frac{4(\kappa a)^2}{\Psi_s}\sum_{n=1}^{\infty} C_n \frac{1}{\lambda_n J_1(\lambda_n)} \int_{\tau=0}^{\bar{t}} \frac{1}{E_0} E(\tau)\exp[-\lambda_n^2(\bar{t}-\tau)]d\tau \end{aligned} \tag{2.24}$$

Since the electroosmotic flow velocity is coupled with the EDL potential distribution in Eq. (2.23) by the factor C_n, the EDL potential field should be obtained independently before we solve the flow field. A detailed derivation is presented in appendix B.

2.4 Unsteady and Frequency-dependent Electroosmotic Flow

2.4.1 Sinusoidally alternating electric field

Consider the application of a sinusoidally alternating electric field with an angle frequency ω

$$E(t) = E_0 e^{i\omega t} \tag{2.25}$$

Substituting Eq. (2.25) into Eq. (2.23), we can show next

$$\begin{aligned} \bar{u}(\bar{r},\bar{t}) &= REAL\left[\frac{2(\kappa a)^2}{\Psi_s}\sum_{n=1}^{\infty} C_n \frac{J_0(\lambda_n \bar{r})}{J_1^2(\lambda_n)} \frac{\exp(i\beta^2\bar{t}) - \exp(-\lambda_n^2\bar{t})}{\lambda_n^2 + i\beta^2}\right] \\ &= \frac{2(\kappa a)^2}{\Psi_s}\sum_{n=1}^{\infty} C_n \frac{J_0(\lambda_n \bar{r})}{J_1^2(\lambda_n)} \frac{\lambda_n^2\cos(\beta^2\bar{t}) + \beta^2\sin(\beta^2\bar{t}) - \lambda_n^2\exp(-\lambda_n^2\bar{t})}{\lambda_n^4 + \beta^4} \end{aligned} \tag{2.26}$$

where i is the unit imaginary number. "*REAL*" denotes the real part of the solution. Here a

new parameter β is defined as (Telionis, 1981)

$$\beta = \frac{a}{\sqrt{\mu / \rho\omega}} \tag{2.27}$$

β represents the aspect ratio of the capillary radius a to the Stokes penetration depth δ_s, defined as (Telionis, 1981)

$$\delta_s = \sqrt{\frac{\mu}{\rho\omega}} = \sqrt{\frac{\mu}{2\pi\rho f}} \tag{2.28}$$

where $f = \frac{\omega}{2\pi}$ is the frequency of the applied electric field.

Accordingly, the mean velocity is given by

$$\begin{aligned} \bar{u}_m(\bar{t}) &= 2\int_{\bar{r}=0}^{1} \bar{r}\,\bar{u}(\bar{r},\bar{t})d\bar{r} \\ &= \frac{4(\kappa a)^2}{\Psi_s}\sum_{n=1}^{\infty} C_n \frac{1}{\lambda_n J_1(\lambda_n)} \frac{\lambda_n^2\cos(\beta^2\bar{t}) + \beta^2\sin(\beta^2\bar{t}) - \lambda_n^2\exp(-\lambda_n^2\bar{t})}{\lambda_n^4 + \beta^4} \end{aligned} \tag{2.29}$$

2.4.2 Step change electric field

The external electrical field is applied and remains constant from the time $t = 0$ (i.e., the electrical field follows step function change)

$$E(t) = E_0 H(t) \tag{2.30}$$

where

$$H(t-\delta) = \begin{cases} 1 & (t \geq \delta) \\ 0 & (t < \delta) \end{cases} \tag{2.31}$$

is the well-known Heaviside step function.

Substituting Eq. (2.30) into Eq. (2.23) and Eq. (2.24), we obtain

$$\bar{u}(\bar{r},\bar{t}) = \frac{2(\kappa a)^2}{\Psi_s}\sum_{n=1}^{\infty} C_n \frac{J_0(\lambda_n \bar{r})}{J_1^2(\lambda_n)} \frac{1-\exp(-\lambda_n^2 \bar{t})}{\lambda_n^2} \tag{2.32}$$

and

$$\bar{u}_m(\bar{t}) = \frac{4(\kappa a)^2}{\Psi_s}\sum_{n=1}^{\infty} C_n \frac{1-\exp(-\lambda_n^2 \bar{t})}{\lambda_n^3 J_1(\lambda_n)} \tag{2.33}$$

In fact, we also can derive Eq. (2.32) and Eq. (2.33) by setting the angle frequency of the electrical field ω in Eq. (2.26) and Eq. (2.29) equal to zero, and then $\beta = 0$. Hence Eq. (2.26) and Eq. (2.29) can reduce to Eq. (2.22) and Eq. (2.23), respectively.

2.4.3 Pulsed electric field

For a more general situation when the electric field is switched on at the time $t = 0$ and remains constant until it is switched off at the time $t = \delta$, the electric field is then described by

$$E = E_0 \left[H(t) - H(t-\delta)\right] \tag{2.34}$$

Substituting Eq. (2.34) to Eq. (2.23) and Eq. (2.24), we get

$$\bar{u}(\bar{r},\bar{t}) = \frac{2(\kappa a)^2}{\Psi_s}\sum_{n=1}^{\infty} C_n \frac{J_0(\lambda_n \bar{r})}{J_1^2(\lambda_n)} \frac{\exp[-\lambda_n^2(\bar{t}-\bar{\delta})H(\bar{t}-\bar{\delta})] - \exp(-\lambda_n^2 \bar{t})}{\lambda_n^2} \tag{2.35}$$

and

$$\bar{u}_m(\bar{t}) = \frac{4(\kappa a)^2}{\Psi_s}\sum_{n=1}^{\infty} C_n \frac{\exp[-\lambda_n^2(\bar{t}-\bar{\delta})\cdot H(\bar{t}-\bar{\delta})] - \exp(-\lambda_n^2 \bar{t})}{\lambda_n^3 J_1(\lambda_n)} \tag{2.36}$$

The total volumetric net flow quantity from the electric field is switched on to the termination of the entire flow due to frictional stress can be determined from

$$\overline{Q}_V(\bar{\delta}) = \int_{\bar{t}=0}^{\infty} \bar{u}_m(\bar{t})\, d\bar{t} = \bar{\delta}\, \frac{4(\kappa a)^2}{\Psi_s} \sum_{n=1}^{\infty} C_n \frac{1}{\lambda_n^3\, J_1(\lambda_n)} \tag{2.37}$$

It is obvious that the total net flow quantity is proportional to the duration of time $\bar{\delta}$ (here $\bar{\delta} = \frac{\mu}{\rho a^2}\delta$), during which the electric field is applied.

2.5 Results and Discussion

In calculations, NaCl is used as the electrolyte solution. At room temperature of $T = 298\,K$, the electrolyte properties are dielectric constant $\varepsilon_r = 80$, viscosity $\mu = 0.90 \times 10^{-3}\ kg/sm$, and density $\rho = 998\ kg/m^3$.

2.5.1 Potential profile

Figure 2-1 shows the EDL potential profiles in a cylindrical capillary for two different electrokinetic diameters, κa with a fixed zeta potential, Ψ_s. For comparison, we also include the results obtained from the Debye-Hückel linear approximation and complete numerical method. To exclude the effect of zeta potential on the magnitude of the EDL potential, we choose the arbitrary reference potential, ζ_o. It is shown in Figure 2-1 that the Debye-Hückel linear assumption provides a good approximation for a larger electrokinetic diameter. However, the linearized solution deviates from the complete Poisson-Boltzmann equation for a smaller electrokinetic diameter, i.e., a thicker EDL corresponding to a dilute electrolyte or smaller capillary. Furthermore, it is noted from Figure 2-1 that the difference between the analytical scheme used in the present study and the numerical solution of the Poisson-Boltzmann equation is visually indistinguishable, suggesting an excellent

approximation estimated by Eq. (B.3).

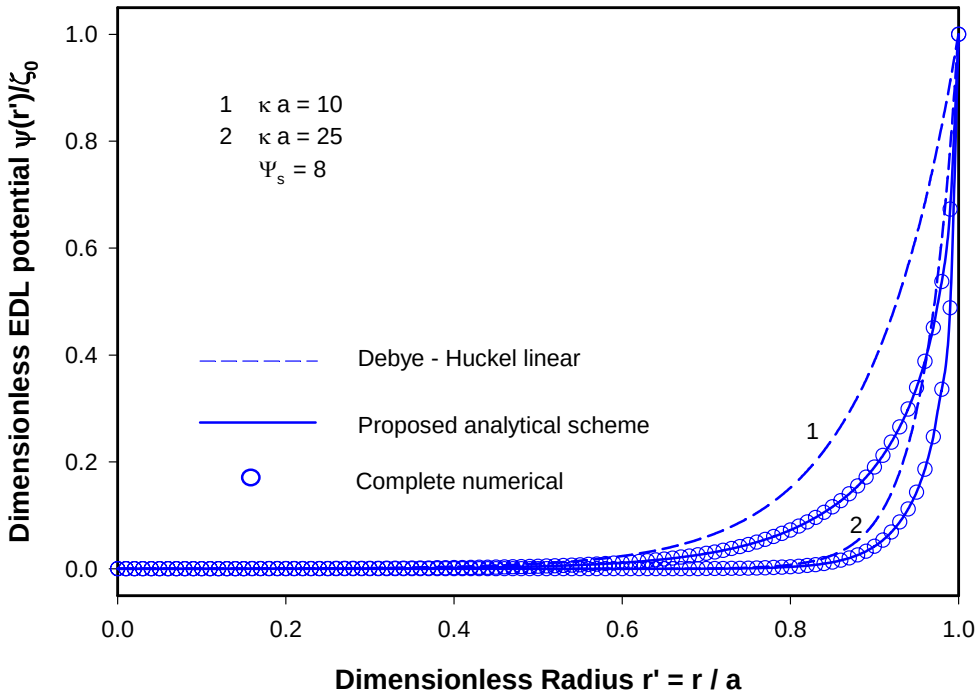

Figure 2-1 Comparison of the results for dimensionless EDL potential, $\psi(r) / \zeta_0$ versus dimensionless radius, r / a, obtained from the Debye-Hückel linear approximation, the analytical scheme proposed in this study, and the numerical integration of the complete Poisson-Boltzmann equation in a cylindrical capillary for two cases: (i) $\kappa a = 10$, and (ii) $\kappa a = 25$, with a fixed dimensionless zeta potential, $\Psi_s = 8$.

2.5.2 Transient velocity profile

Time evolution of the electroosmotic flow field in cylindrical capillaries under a constant electric field is shown in Figures 2-2(a-b). Here the reference velocity is chosen as $u_{s0} = -\frac{\varepsilon_r \varepsilon_0}{\mu} E_0 \frac{k_b T}{e_0}$ so that the zeta potential effect can be shown. According to the results displayed in Figures 2-2(a-b), we can observe that upon the application of an electric field, the flow is activated in a region adjacent to the channel wall and the velocity increases rapidly from zero on the wall to a maximum within the EDL where the driving

force is present. As the time goes, the flow gradually extends to the rest portion of the channel due to hydrodynamic stresses originated from liquid viscosity. When the flow in entire channel becomes steady, the flow velocity across the channel other than the EDL region remains almost a constant value, resembling a plug flow. Furthermore, we can estimate the

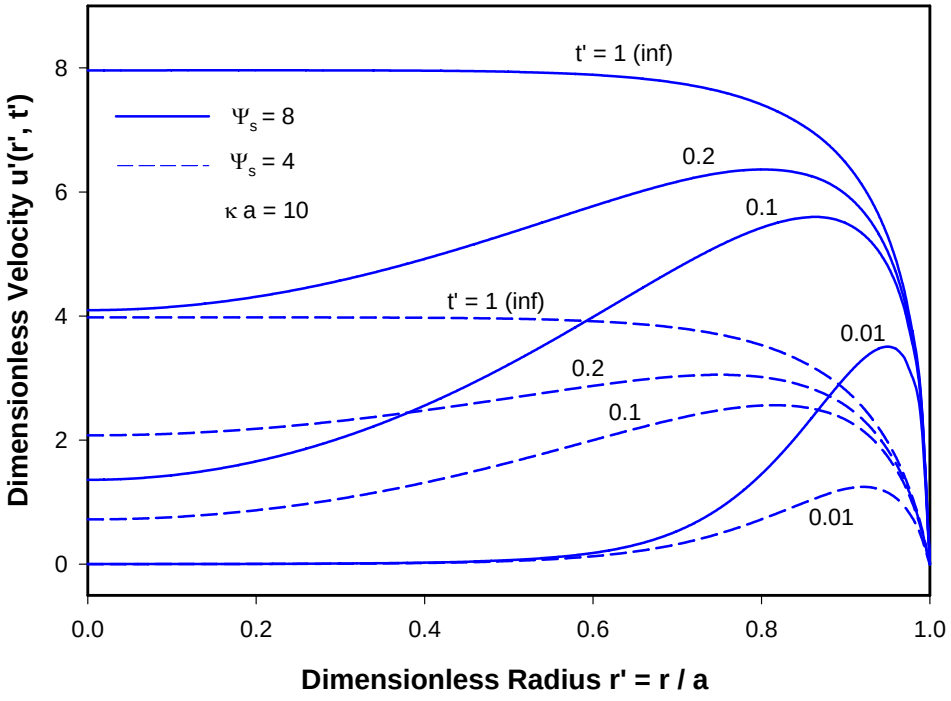

Figure 2-2(a) Time evolution for the case of thick electric double layer with the electrokinetic diameter, κa = 10. The reference velocity is defined as $u_{s0} = -\frac{\varepsilon_r \varepsilon_0}{\mu} E_0 \frac{k_b T}{e_0}$.

characteristic time scale for the electroosmotic flow to reach its steady state from Eq. (2.32) by choosing $\lambda_1^2 \bar{t}^* = \lambda_1^2 \frac{\mu}{\rho a^2} t^* = 1$. Then we can obtain $t^* = \frac{\rho a^2}{\mu \lambda_1^2}$, where $\lambda_1 = 2.405$ determined form $J_0(\lambda_n) = 0$; this shows that the characteristic time, t^* is proportional to the

square of the channel radius, a^2. In addition, it is noted that the velocity increases with the increasing zeta potential, indicating an almost linear relationship between the velocity and the zeta potential.

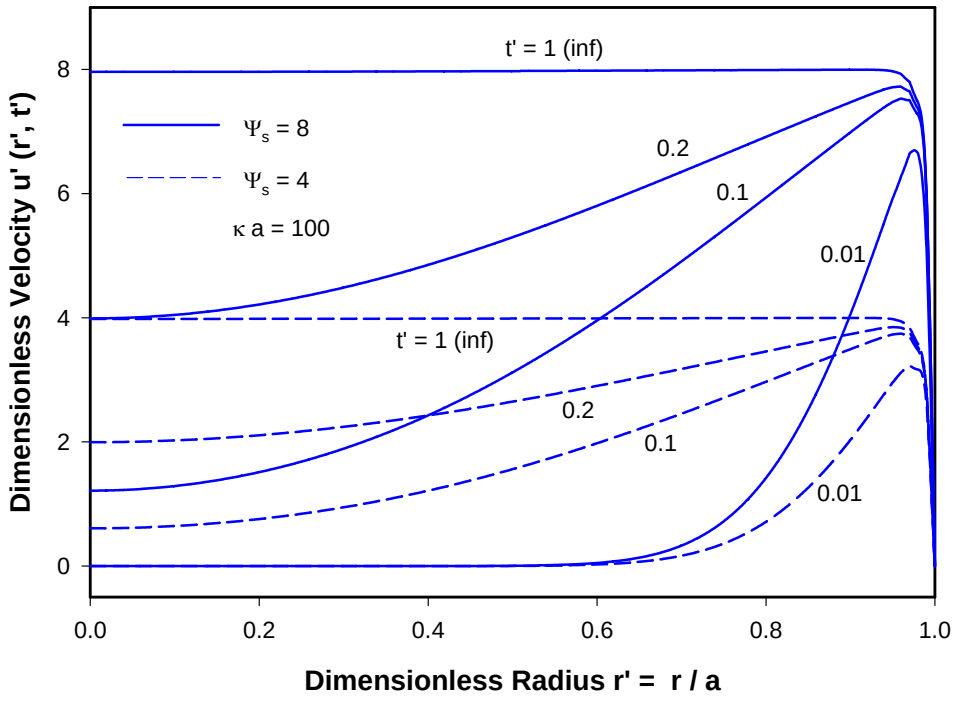

Figure 2-2(b) Time evolution for the case of thin electric double layer with the electrokinetic diameter, κa = 100. The reference velocity is the same as in 2-2(a).

As a comparison, when the electric field is switched off the time devolution of the electroosmotic flow is shown in Figure 2-2(c). It can be seen that the flow decays following a parabolic trend, and is similar to the well-known Stokes first problem, i.e., a streaming flow over a suddenly stopped plate, which was discussed in length by Telionis (1981). However, such a similarity is not coincidence. As pointed out earlier, the electroosmotic flow is activated inside the EDL, which can be considered as the moving plate in the Stokes first problem. Once the "driving force" is removed – the moving plate is suddenly stopped and the

external electric field is turned off, the mechanism governing fluid flow is the same, i.e., hydrodynamic frictional stresses due to liquid viscosity.

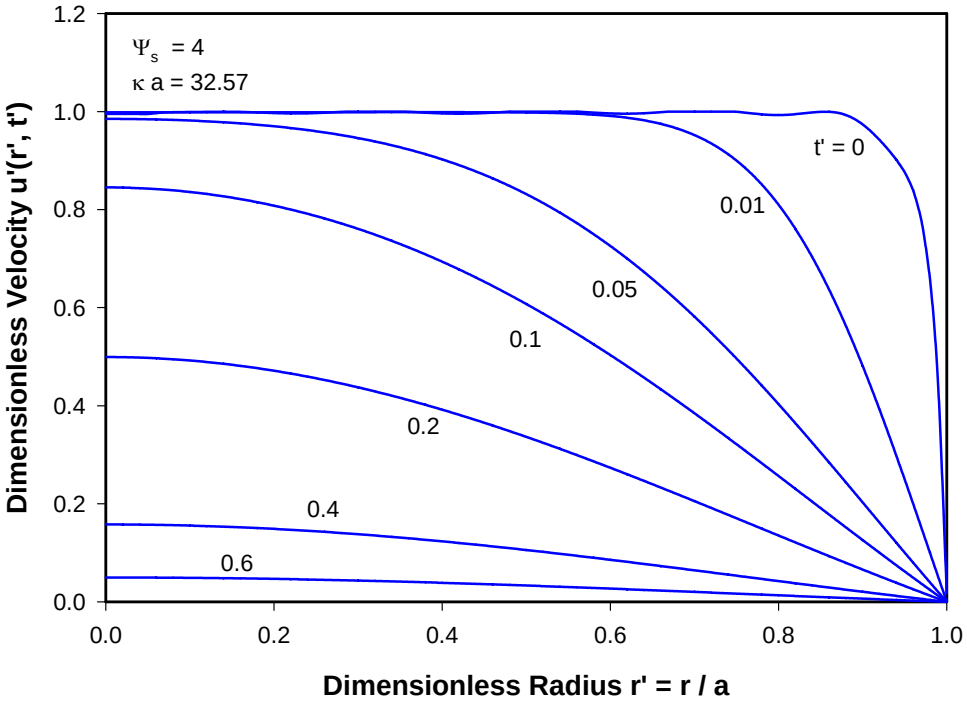

Figure 2-2(c) Time devolution with fixed the electrokinetic diameter, κa = 32.57 and the zeta potential, Ψ_s = 4. The reference velocity is the same as in 2-2(a).

2.5.3 AC perturbation

For a capillary of $a = 10\mu m$ in radius, we can estimate the characteristic time for the electroosmotic flow to reach a steady state is $t^* = \frac{\rho a^2}{\mu \lambda_1^2} = 19.2\mu s$. The corresponding eigenfrequency of the system is $f^* = \frac{1}{t^*} = \frac{\mu \lambda_1^2}{\rho a^2} = 52.25 KHz$. Hence, three different characteristic frequencies of the external electric field, $0.1 f^*$, f^* and $10 f^*$ ($f = \omega / 2\pi$) are chosen to study the characteristic features of the oscillating electroosmotic flow.

The steadily oscillating velocity distributions are shown in Figures. 2-3(a-c) for five different characteristic moments: $\omega t = 0$, $\frac{\pi}{4}$, $\frac{\pi}{2}$, $\frac{3\pi}{4}$, π. It is obvious that the perturbed flow regime becomes smaller with an increase in the frequency of the electric field. This scenario can be logically anticipated because under very high frequencies, the electric field changes its direction so fast that the flow never can get developed across the entire channel. According to Eq. (2.28), the frequency-dependent Stokes penetration depth, δ_s, representing a typical length scale of the oscillatory laminar viscous flows in response to a harmonic external excitation (Telionis, 1981), is inversely proportional to the square root of the frequency, *f*. This specific dependence on frequency agrees well with that for classical Stokes second problem, i.e., the oscillating viscous flow induced by sinusoidally oscillating infinite flat plate (Telionis, 1981). For example, at a very high frequency, e.g., $f = 10 f^*$, the perturbed area is restricted only in a small region near the channel wall, while the fluid in the rest of the channel remains zero velocity, as shown in Figure 2-3(c). In contrast, in Figure 2-3(a), at a very low frequency, e.g., $f = 0.1 f^*$, the flow is extended through the entire capillary.

Furthermore, it also should be noted that, in Figures 2-3(a-c) the magnitude of the maximum velocity decreases as the frequency increases. This can be explained by further examination of the analytical solution derived in the previous section. When the oscillatory flow becomes steady, i.e., $\bar{t} \to \infty$, the exponential term in Eq. (2.26) decays, the value of the maximum velocity should be bounded by

$$\bar{u}_{\max}(\bar{r}) = \frac{2(\kappa a)^2}{\Psi_s} \sum_{n=1}^{\infty} C_n \frac{J_0(\lambda_n \bar{r})}{J_1^2(\lambda_n)} \frac{1}{\sqrt{\lambda_n^4 + \beta^4}} \le \frac{2(\kappa a)^2}{\Psi_s} \sum_{n=1}^{\infty} C_n \frac{J_0(\lambda_n \bar{r})}{J_1^2(\lambda_n)} \frac{1}{\lambda_n^2} \tag{2.38}$$

According to the definition of β given in Eq. (2.27), we can reasonably infer that the

maximum velocity $\bar{u}_{\max}$ increases as the frequency ω decreases. The maximum velocity reaches its peak value when the frequency of the electric field is zero, i.e., $\beta = 0$.

The slip velocity approximation used by Söderman and Jönsson (1996) and Santiago (2001) is rooted from an analogy to the Stokes second problem. To compare the slip velocity approximation with the analytical method used in this work, we also present the results for the electroosmotic flow field under the slip velocity approximation, represented by dashed curves in Figures 2-3(a-c). Detailed derivation of the electroosmotic velocity with the slip velocity approximation is provided in appendix C. It is demonstrated in Figures 2-3(a-c) that at the center region of the capillary, the two methods give nearly the same results for transient velocity distributions, while adjacent to the charged channel wall the discrepancy is observed. Such a discrepancy is due to the assumption of moving boundary condition used in the slip velocity approximation, in which the boundary velocity is assumed to be proportional to the oscillating electric field (refer to Eq. (C.2b)), while the boundary velocity is chosen as zero (non-slip condition) in the analytical scheme used in present study. The slip velocity approximation neglects the velocity profile in the EDL region. Thus the analytical scheme used in this work can present a more accurate and complete scenario for the oscillating electroosmotic flow in the microchannel.

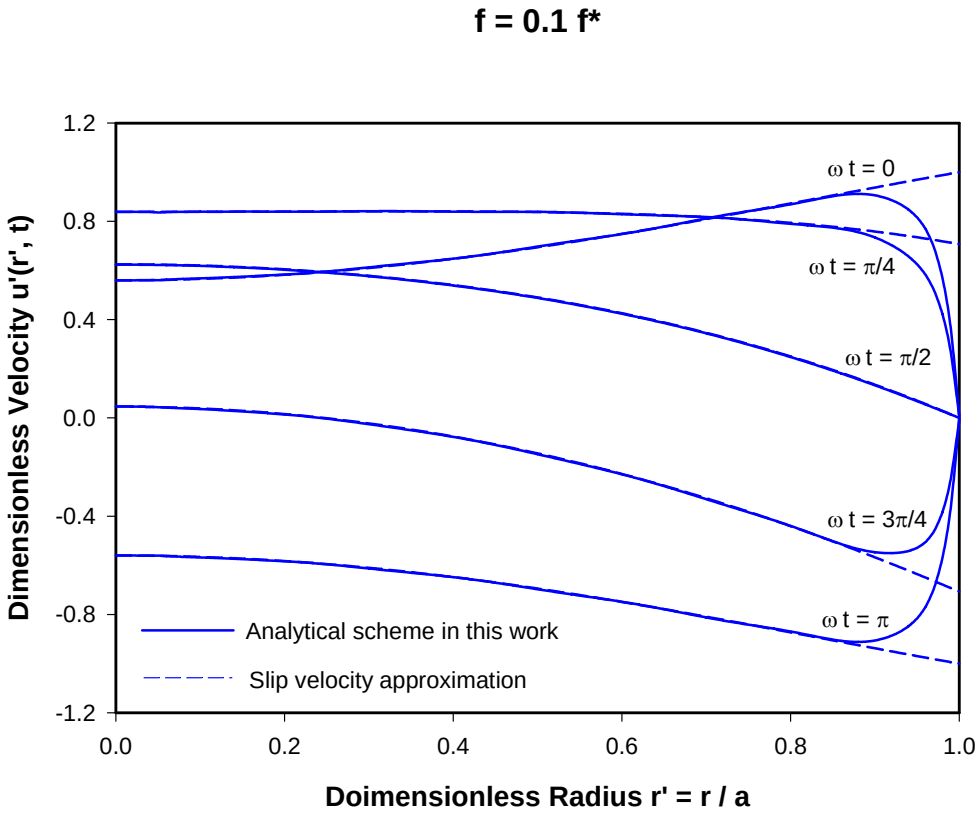

Figure 2-3(a) Low frequency of the external field, $f = 0.1\ f^*$.

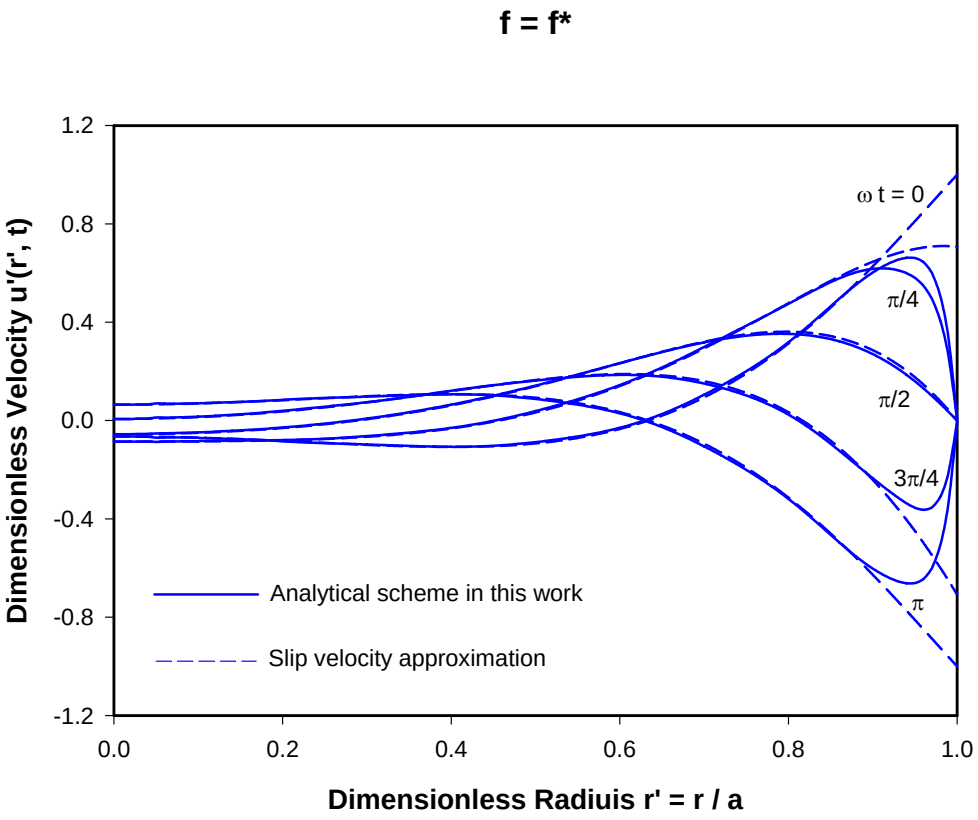

Figure 2-3(b) The eigenfrequency of the external field, $f = f^*$.

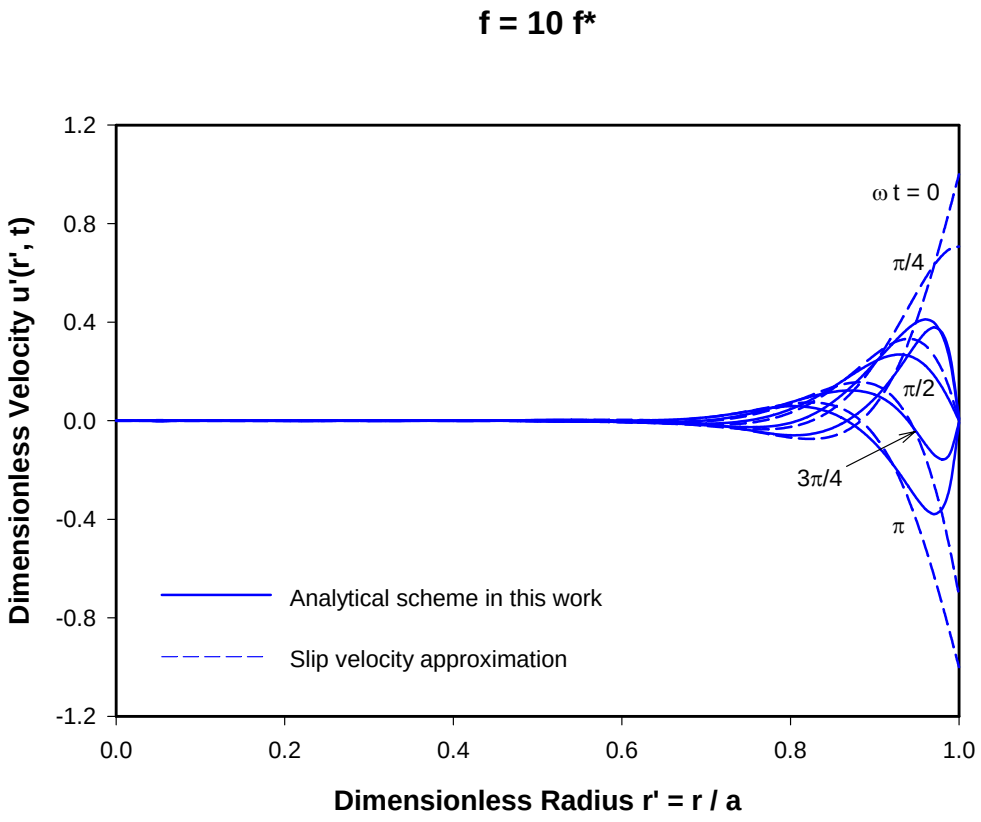

Figure 2-3(c) High frequency of the external field, $f = 10\ f^*$.

Figure 2-3 Steadily oscillating velocity distributions along the dimensionless radius for three different aspect frequencies of the external field, 0.1 f^*, f^* and 10 f^*, with the electrokinetic diameter, κa = 32.57, the zeta potential, Ψ_s = 4 and eigenfrequency, f^*=52.25 KHz. Snapshots are presented at five different characteristic moments: ωt = 0, π/4, π/2, 3π/4, π. Reference velocity is chosen as $u_s = -\frac{\varepsilon_r \varepsilon_0}{\mu} E_0 \zeta_o$. Comparison with the results obtained from slip velocity approximation represented by dashed curves.

In Figure 2-4(a), the time dependent mean velocity is plotted for two-cycle periods of the AC electric field. The flow can follow the sinusoidally oscillation of the electric field, but there exists a phase lag. Furthermore, it can be observed that as increasing frequency the flow lags behind the excitation field with a larger phase lag. From Eqs. (2.26)-(2.28), we can show that the phase lag of the oscillating velocity to the excitation field is expressed as $\theta = \tan^{-1}\left(\frac{\beta^2}{\lambda_n^2}\right) = \tan^{-1}\left(\frac{2\pi\rho}{\mu\lambda_n^2} f a^2\right) = \tan^{-1}\left(2\pi\frac{f}{f^*}\right)$, indicating that the phase lag θ increases monotonically with increasing the excitation frequency *f*. These results are in accord with the findings by Dutta and Beskok (2001) in their studies on AC electroosmosis in microchannels. And it can be further inferred that when the excitation frequency f approaches to zero (DC electric field), the phase lag angle θ approaches to zero, i.e., there is no phase lag. When the excitation frequency remains at very low value (e.g., $f \le 0.05 f^*$), the phase lag is proportional to the excitation frequency and can be simply estimated as $\theta = 2\pi f / f^*$. On the other hand, when the excitation frequency approaches to infinity the phase lag angle approaches to 90 degree. The similar trend exists for the effect of the capillary size, the phase lag increases monotonically with the capillary cross-sectional area, $A = \pi a^2$. This is not surprising because larger channel size requires longer time for the momentum transfer by diffusion. The magnitude of the maximum mean velocity (the amplitude of the velocity fluctuation) is also dependent on the frequency. As shown in Eq. (2.39), the amplitude of velocity fluctuation can reach an asymptote when the frequency is below a critical value. This critical value can be determined by setting $\frac{\beta^4}{\lambda_n^4} = \left(2\pi\frac{f}{f^*}\right)^2 = 0.1$ in Eq. (2.39), one can

get $f = 0.05 f^*$.

$$\bar{u}_{\max} = \frac{4(\kappa a)^2}{\Psi_s} \sum_{n=1}^{\infty} C_n \frac{1}{\lambda_n^3 J_1(\lambda_n)} \frac{1}{\sqrt{1+\beta^4/\lambda_n^4}} \le \frac{4(\kappa a)^2}{\Psi_s} \sum_{n=1}^{\infty} C_n \frac{1}{\lambda_n^3 J_1(\lambda_n)} \tag{2.39}$$

Figure 2-4(b) shows dependence of the mean electroosmotic flow velocity on the time, during which the electric field is powered on. It is shown that the flow cannot reach its steady state until the time is larger than the characteristic time. On the other hand, the flow decays exponentially after the electric field is switched off.

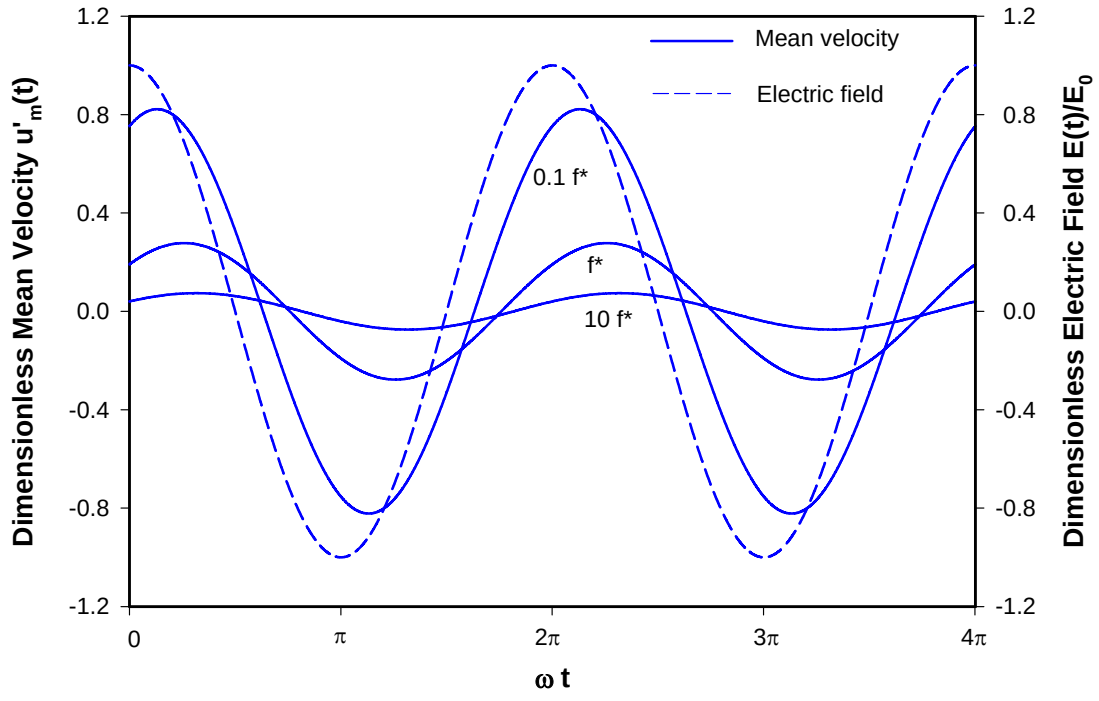

Figure 2-4(a) Steadily oscillating mean velocity for three different aspect frequencies of the external field, 0.1 f^*, f^* and 10 f^*, with the system eigenfrequency of f^*=52.25 KHz.

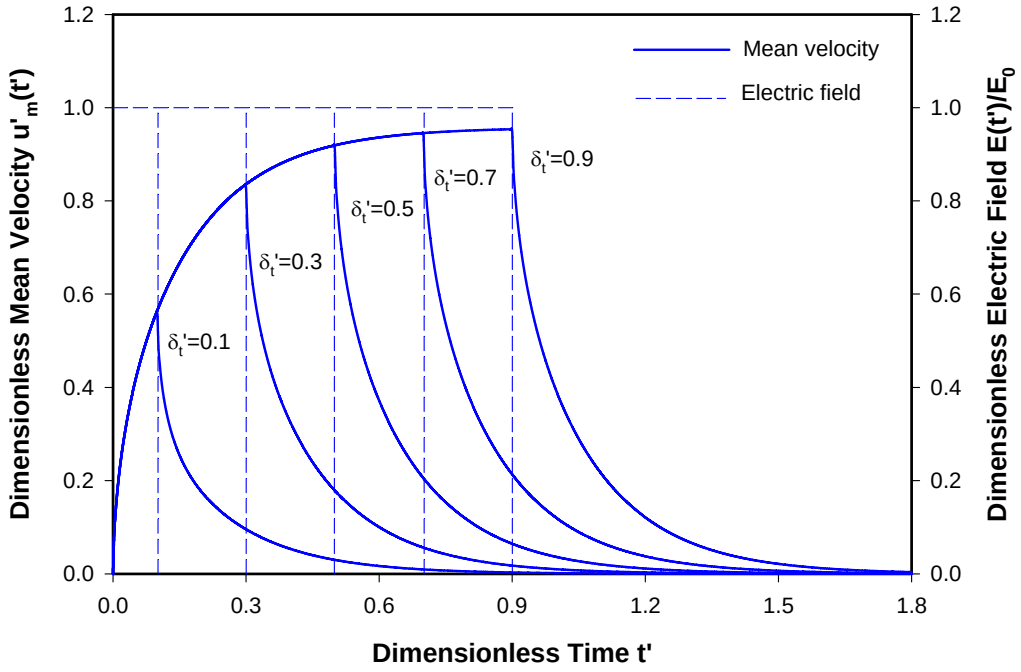

Figure 2-4(b) Evolution and devolution of the mean velocity when the external field is switched on for different duration of time δ_t'.

Figure 2-4 Dimensionless mean velocity versus time with fixed the electrokinetic diameter, κa = 32.57 and the zeta potential, Ψ_s = 4. Reference velocity is chosen as $u_s = -\frac{\varepsilon_r \varepsilon_0}{\mu} E_0 \zeta_o$.

2.6 Summary

An analytical scheme is used to solve the Poisson-Boltzmann equation for study of the dynamics of electroosmotic flow in a cylindrical microcapillary. The results show that the solution of the Poisson-Boltzmann equation based on the analytical scheme is virtually no different from numerical solution. It is demonstrated that the geometry and zeta potential of the channel wall have a strong impact on the electroosmotic flow. The electrokinetic diameter determines the relative thickness of the electric double layer while zeta potential determines the magnitude of the velocity, and hence the flow rate. The characteristic time for the flow to reach its steady state is proportional to the square of the channel radius. The evolution of the electroosmotic flow upon application of a constant electric field exhibits a unique flow profile, which is resulted from the contributions due to the electric body force and hydrodynamic viscous stress. On the other hand, the flow devolution after the external electric field is switched off follows a flow pattern solely controlled by hydrodynamic friction due to liquid viscosity. In addition, it is found that the oscillating electroosmotic flow is strongly dependent on the modulation frequency of the applied sinusoidally alternating electric field, which determines the thickness of unstable Stokes layer, and thus governs the extent of the harmonic oscillation and the velocity distributions of the oscillating electroosmotic flow.

Chapter 3

Analytical Solution of Electroosmotic Flow in a Capillary Annulus with High Zeta Potentials

3.1 Introduction

The annulus model is more general than a model like a cylindrical pore or two parallel plates. When the inner radius of the annulus becomes zero, the annulus acts as a cylindrical pore. The effect associated with the inner cylinder can be ignored. On the other hand, as the inner radius approaches the outer radius, the annulus behaves like two parallel plates, and therefore both cylinders play an equal important role. In practice, the electroosmotic flow in a capillary annulus is related to modelling of the electrokinetic motion of a particle in a polymeric porous membrane, which is important to understanding of electrophoretic separation of proteins (O'Connor *et al.*, 1996). In addition, the annulus geometry is employed as a novel microfluidic mode for the blending of chemical and biological fluids (Andreeev *et al.*, 1999). Recently, Tsao (2000) studied the steady state electroosmosis flow through an annulus under the Debye-Hückel linear approximation, indicating that his work is valid only for the case of low zeta potentials (e.g., $\zeta \le 25\,mV$ for an 1-1 electrolyte). In practical situations, however, the zeta-potentials as high as $100 \sim 200\,mV$ are not uncommonly encountered. Therefore, to circumvent this problem, in this chapter we extend Tsao's model by developing an analytical approximation to obtain the general solution of the complete Poisson- Boltzmann equation with high zeta potentials,

in a fashion similar to the method used by Philip and Wooding (1970). As such, analytical solutions of the Poisson-Boltzmann equation for the EDL potential distribution and the Stokes equation for the transient electroosmotic flow field in the annulus region are obtained, and their results under influences of the EDL and geometric parameters are presented. Specifically, we also discuss the situations when two cylindrical walls are oppositely charged. As another contribution of this chapter, the analytical solutions for the frequency-dependent velocity distributions in a capillary annulus are obtained using Green's function method. The flow field oscillations excited by a sinusoidally alternating electric field is discussed under different modulation frequencies. The generality of the annulus model is also presented.

3.2 Dynamics of the Electroosmotic Flow

Consider an electroosmotic flow in an annular capillary with infinite length between two coaxial circular cylinders of radii, αa and a, as shown in Figure 3-1 (α is the ratio of the inner radius to the outer radius). The annulus is filled with an incompressible, Newtonian, symmetric monovalence electrolyte of constant dielectric constant, ε_r, viscosity, μ and density, ρ. The inner and outer capillary walls are uniformly charged with the zeta-potentials ζ_i and ζ_o, respectively. When an external electric field, E_0 is applied along the axis of the capillary, the liquid starts to move as result of the interaction between the net charge density in the electric double layer (EDL) and the applied electric field. The motion of liquid through the cylindrical microcapillary is governed by the Navier-Stokes equation (Probstein, 1994)

$$\rho \frac{\partial u(r,t)}{\partial t} = \mu \frac{1}{r} \frac{\partial}{\partial r}\left[r \frac{\partial u(r,t)}{\partial r} \right] + E_0 \rho_e(r) \tag{3.1}$$

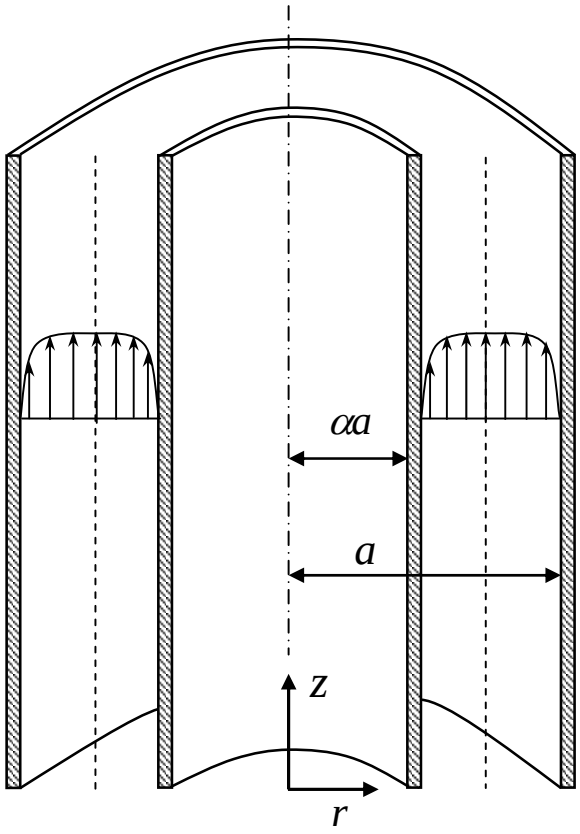

Figure 3-1 Schematic diagram of an annulus. The radii of the inner and the outer cylinders are αa and a, respectively.

Here $u(r)$ is the velocity field. $\rho_e(r)$ is the volumetric charge density due to the presence of the electric double layer (EDL), and it is given by the Poisson equation, which takes the form (Hunter, 1981)

$$\frac{1}{r}\frac{d}{dr}\left[r\frac{d\psi(r)}{dr}\right] = -\frac{\rho_e(r)}{\varepsilon_r\varepsilon_0} \tag{3.2}$$

Substituting Eq. (3.2) into Eq. (3.1), we obtain

$$\rho\frac{\partial u(r,t)}{\partial t}=\mu\frac{1}{r}\frac{\partial}{\partial r}\left[r\frac{\partial u(r,t)}{\partial r}\right]-E_0\varepsilon_0\varepsilon_r\frac{1}{r}\frac{\partial}{\partial r}\left[r\frac{\partial \psi(r)}{\partial r}\right]$$
$$=\mu\frac{1}{r}\frac{\partial}{\partial r}\left\{r\frac{\partial}{\partial r}\left[u(r,t)-\frac{\varepsilon_r\varepsilon_0}{\mu}E_0\psi(r)\right]\right\} \tag{3.3}$$

Introducing dimensionless parameters

$$\bar{u}=\frac{u}{u_s}\qquad \bar{t}=\frac{\mu}{\rho a^2}t\qquad \bar{r}=\frac{r}{a}\qquad \Psi=\frac{e_0\psi}{k_bT} \tag{3. 4}$$

Here u_s is the reference velocity defined by the well-known Smoluchowski equation (Hunter, 1981)

$$u_s=-\frac{\varepsilon_r\varepsilon_0}{\mu}E_0\zeta_o \tag{3.5}$$

Obviously, u_s is proportional to the magnitude of the external field, E_0 and the zeta potential, ζ_o. Eq. (3.3) takes the dimensionless form as

$$\frac{\partial\bar{u}(\bar{r},\bar{t})}{\partial\bar{t}}=\frac{1}{\bar{r}}\frac{\partial}{\partial\bar{r}}\left\{\bar{r}\frac{\partial}{\partial\bar{r}}\left[\bar{u}(\bar{r},\bar{t})+\frac{\Psi(\bar{r})}{\Psi_s}\right]\right\} \tag{3.6}$$

where $\Psi_s=\frac{e_0\zeta_o}{k_bT}$.

The EDL potential Ψ and velocity $\bar{u}$ satisfy the dimensionless initial and boundary conditions

$$\bar{t}=0\qquad \bar{u}=0 \tag{3.7a}$$

$$\bar{r}=\alpha\qquad \bar{u}=0\qquad \Psi=\beta\Psi_s \tag{3.7b}$$

$$\bar{r}=1\qquad \bar{u}=0\qquad \Psi=\Psi_s \tag{3.7c}$$

where $\beta=\zeta_i/\zeta_o$ denotes the ratio between the zeta potential of the inner and outer radii.

Comparing with the results in the previous section, we can infer the system will become steady state when the time goes to infinite, the solution should take the following non-dimensional form

$$\bar{u}(\bar{r},\bar{t}) = \bar{u}_{\infty}(\bar{r}) + \bar{u}_{t}(\bar{r},\bar{t}) \tag{3.8}$$

The steady state limiting solution $\bar{u}_{\infty}(\bar{r})$ can be obtained from Eq. (3.6) by setting $\partial\bar{u}/\partial\bar{t} = 0$, subject to the boundary conditions Eqs. (3.7b) and (3.7c). Hence we can obtain the steady state velocity, which is defined as

$$\bar{u}_{\infty}(\bar{r}) = 1 - \frac{\Psi(\bar{r})}{\Psi_{s}} - \frac{\ln\bar{r}}{\ln\alpha}(1-\beta) \tag{3.9}$$

Substituting Eq. (3.8) into Eq. (3.6), using the solution of Eq. (3.9), we can get the governing equation for the transient velocity $\bar{u}_{t}(\bar{r},\bar{t})$,

$$\frac{\partial\bar{u}_{t}(\bar{r},\bar{t})}{\partial\bar{t}} = \frac{1}{\bar{r}}\frac{\partial}{\partial\bar{r}}\left[\bar{r}\frac{\partial\bar{u}_{t}(\bar{r},\bar{t})}{\partial\bar{r}}\right] \tag{3.10}$$

subject to the initial and boundary conditions

$$\bar{t} = 0 \quad \bar{u}_{t} = -\bar{u}_{\infty}(\bar{r}) \tag{3.11a}$$

$$\bar{r} = \alpha \quad \bar{u}_{t} = 0 \tag{3.11b}$$

$$\bar{r} = 1 \quad \bar{u}_{t} = 0 \tag{3.11c}$$

Using the classical method of separation of variables, the solution of Eq. (3.10) can be given by

$$\bar{u}_{t}(\bar{r},\bar{t}) = -\sum_{n=1}^{\infty} B_{n}\left[J_{0}(\lambda_{n}\bar{r})N_{0}(\alpha\lambda_{n}) - J_{0}(\alpha\lambda_{n})N_{0}(\lambda_{n}\bar{r})\right]\exp(-\lambda_{n}^{2}\bar{t}) \tag{3.12}$$

where

$$B_n = \frac{\int_{\alpha}^{1} r'\left[1-\frac{\Psi(r')}{\Psi_s}-\frac{\ln r'}{\ln\alpha}(1-\beta)\right]\left[J_0(\lambda_n r')N_0(\alpha\lambda_n)-J_0(\alpha\lambda_n)N_0(\lambda_n r')\right]dr'}{\int_{\alpha}^{1} r'\left[J_0(\lambda_n r')N_0(\alpha\lambda_n)-J_0(\alpha\lambda_n)N_0(\lambda_n r')\right]^2 dr'} \tag{3.13}$$

and λ_n are the positive roots of

$$J_0(\lambda_n)N_0(\alpha\lambda_n)-J_0(\alpha\lambda_n)N_0(\lambda_n)=0 \tag{3.14}$$

where J_0 and N_0 are the zero-order Bessel function of the first and second kind, respectively.

The transient aspect is similar to the EOF in cylindrical capillary. So the steady aspect is emphasized here. According to Eq. (3.9), the steady state velocity is

$$u_\infty(r)=u_s\left[1-\frac{\psi(r)}{\zeta_o}-\frac{\ln(r/a)}{\ln\alpha}(1-\beta)\right] \tag{3.15}$$

The average velocity of the fluid across the annulus cross-section is obtained by

$$\langle u_z\rangle=\frac{2}{a^2(1-\alpha^2)}\int_{\alpha a}^{a} ru(r)dr=u_s\,J(G,\alpha,\beta) \tag{3.16}$$

and the volumetric flow rate is expressed as

$$Q_V=2\pi\int_{\alpha a}^{a} ru(r)dr=u_s\pi a^2(1-\alpha^2)\cdot J(G,\alpha,\beta) \tag{3.17}$$

where

$$J(G,\alpha,\beta)=1-G+\frac{1-\beta}{2\ln\alpha}\frac{1-\alpha^2+2\alpha^2\ln\alpha}{1-\alpha^2} \tag{3.18}$$

and

$$G=\frac{2}{\zeta_o a^2(1-\alpha^2)}\int_{\alpha a}^{a} r\psi(r)dr \tag{3.19}$$

J is regarded as a correction factor to the Smoluchowski equation (Hunter 1981) that

assumes a negligible thickness of the EDL, and it depends on the geometry ratio, α and the ratio of zeta-potentials, β. Clearly, the flow direction is also determined by the sign of J. And G is the ratio of the mean electrostatic potential across the annulus region to the zeta-potential of the outer charged wall, representing the effect of the finite EDL thickness.

For a wide capillary (i.e., $\kappa a >> 1$), G is negligibly small, and hence Eq. (3.18) reduces to (Tsao, 2000)

$$J = 1 + \frac{1-\beta}{2\ln\alpha}\frac{1-\alpha^2+2\alpha^2\ln\alpha}{1-\alpha^2} \tag{3.20}$$

By setting $J = 0$ we can obtain the condition that the zero flow rate occurs is (Tsao, 2000)

$$\beta_0(\alpha) = \left(\frac{\zeta_i}{\zeta_o}\right)_0 = 1 + \frac{2(1-\alpha^2)\ln\alpha}{1-\alpha^2+2\alpha^2\ln\alpha} < -1 \tag{3.21}$$

Eq. (3.21) shows that for a given α, the liquid flow due to electroosmosis moves toward one direction when $\beta > \beta_0$, while the flow goes opposite when $\beta < \beta_0$.

Since the electroosmotic flow velocity is coupled with the EDL potential distribution in Eq. (3.15), the EDL potential field should be obtained independently before we solve the flow field. An analytical solution of the EDL potential in a capillary annulus is presented in appendix E.

3.3 Generality of Annulus Model

It has been mentioned that the annulus model is more general than a model like a cylindrical pore or two parallel plates. The generality of annulus model is presented here. The steady state limiting solution $\bar{u}_\infty(\bar{r})$ has been obtained in Eq. (3.9). Actually, the cylindrical capillary model and parallel plates model are two limiting cases of the annulus model.

Limiting Case I: when the inner radius becomes zero (i.e., $\alpha \to 0$), the capillary annulus behaves as a capillary cylinder.

Because $\ln\alpha \to -\infty$ when $\alpha \to 0$, Eq. (3.9) reduces to

$$\bar{u}_{\infty}(\bar{r}) = 1 - \frac{\Psi(\bar{r})}{\Psi_s} \tag{3.22}$$

The result in Eq. (3.22) is consistent with Rice and Whitehead's results for electroosmotic flow in capillary cylinder (Rice and Whitehead, 1965).

Limiting Case II: when the inner radius approaches the outer radius (i.e., $\alpha \to 1$), the capillary annulus behaves as parallel plates.

Introducing new spatial variable between the two parallel slits $\bar{y} = \bar{r} - \alpha$, and because $\lim_{\alpha\to 1} \frac{\ln(\alpha + \bar{y})}{\ln\alpha} = \lim_{\alpha\to 1} \frac{\alpha}{\alpha + \bar{y}} = \frac{1}{1+\bar{y}}$, Eq. (3.9) reduces to

$$\bar{u}(\bar{y}) = 1 - \frac{\Psi(\bar{y})}{\Psi_s} - \frac{1-\beta}{1+\bar{y}} \tag{3.23}$$

If the two slits walls are equally charged, i.e., $\beta = 1$. Eq. (3.23) reduces to

$$\bar{u}(\bar{y}) = 1 - \frac{\Psi(\bar{y})}{\Psi_s} \tag{3.24}$$

The result in Eq. (3.24) is consistent with Yang's results for electroosmotic flow in parallel plates (Yang *et al.*, 2002).

3.4 Results and Discussion

In the previous chapter, basic equations have been derived for the EDL and the electroosmotic velocity distributions in an annulus region. Examination of these equations reveals that the characteristics of the electroosmotic flow in an annulus are

determined by the following non-dimensional parameters: the geometric radius ratio, α, the zeta potential ratio, β, the electrokinetic diameter, κa, and the zeta potential, Ψ_s. In calculations, we consider these parameters bounded by: $\alpha = 0.4$, $\beta = -3 \sim 3$, $\kappa a = 25 \sim 100$, and $\Psi_s = 2 \sim 10$, which are of most practical interests.

3.4.1 Potential profile

Figure 3-2(a) shows the comparison results of the non-dimensional electrical potential profiles obtained from the Debye-Hückel linear approximation, the analytical scheme proposed in this study, and the numerical integration of the complete Poisson-Boltzmann equation in an annulus for two cases: (a) $\kappa a = 10$, and (b) $\kappa a = 25$. It is noted that in either case, use of the Debye-Hückel linear solutions always gives rise to errors in the electrical potential. In contrast, the difference between the analytical scheme proposed in current study and the complete numerical solution of the Poisson-Boltzmann equation is visually indistinguishable, indicating an excellent approximation given in Eq. (E.4).

Figure 3-2(b) presents the profile of the non-dimensional EDL potential for three different values of the electrokinetic diameter, κa. As illustrated in Figure 3-2(b), the EDL potential is symmetrically distributed when the inner and outer walls are equally charged (i.e., $\beta = \pm 1$). It can also be seen that for large electrokinetic diameters, the EDL field exists only in the region close to the wall. However, for small electrokinetic diameters, the EDL potential can extend to a larger portion of the annulus, consistent with previous studies of the electroosmotic flow through microcapillaries of other geometric cross-sectional shapes (Burgreen and Nakache (1964), Levine *et al*. (1975), Koh and Anderson (1975), Yang and

Huang (2001)). It is, therefore, expected that the EDL effect is more significant for small-sized annuluses. In Figure 3-2(c), the EDL potential versus the non-dimensional radius is plotted for three different zeta potentials, Ψ_s. Since the electrokinetic diameter, κa keeps as a constant, the EDL regime in all these three cases remains the same. As such, variation of the zeta potential only results in a change of the magnitude of the EDL potential. It is noted that as the zeta potential increases, the potential drops off more sharply within the EDL regime.

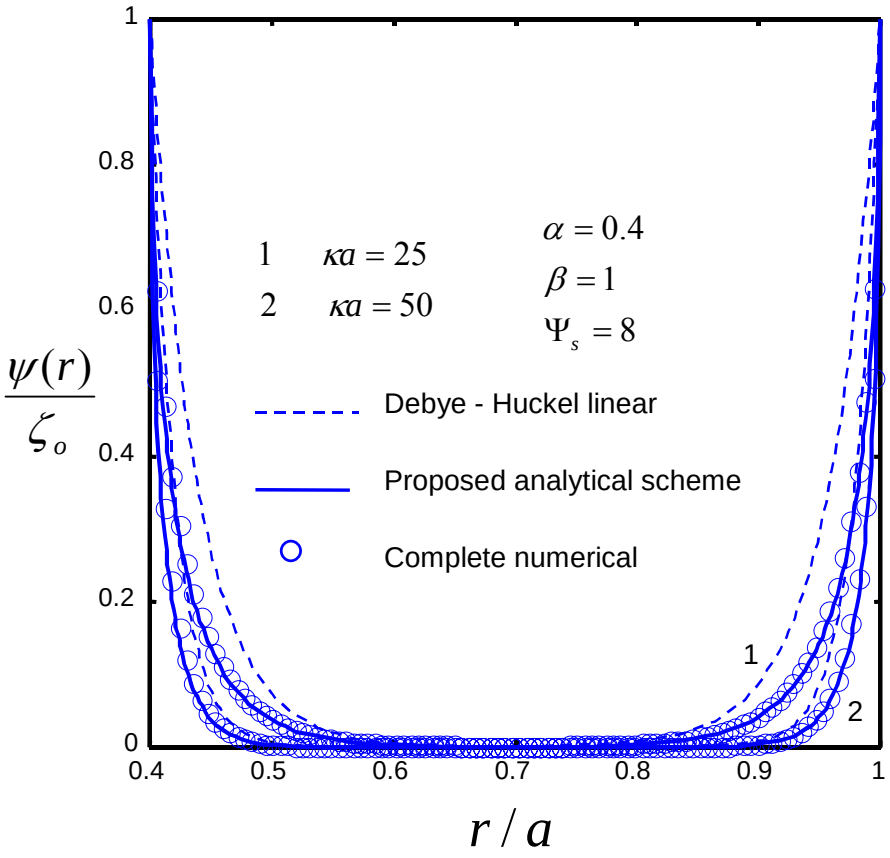

Figure 3-2(a) Comparison of the results obtained from the Debye-Hückel linear approximation, the analytical scheme proposed in this study, and the numerical integration of the complete Poisson-Boltzmann equation in an annulus for two cases: (i) κa = 10, and (ii) κa = 25, with fixed the non-dimensional zeta potential of the outer cylinder, Ψ_s = 8 and the zeta potential ratio of the inner cylinder to the outer cylinder, β = 1.

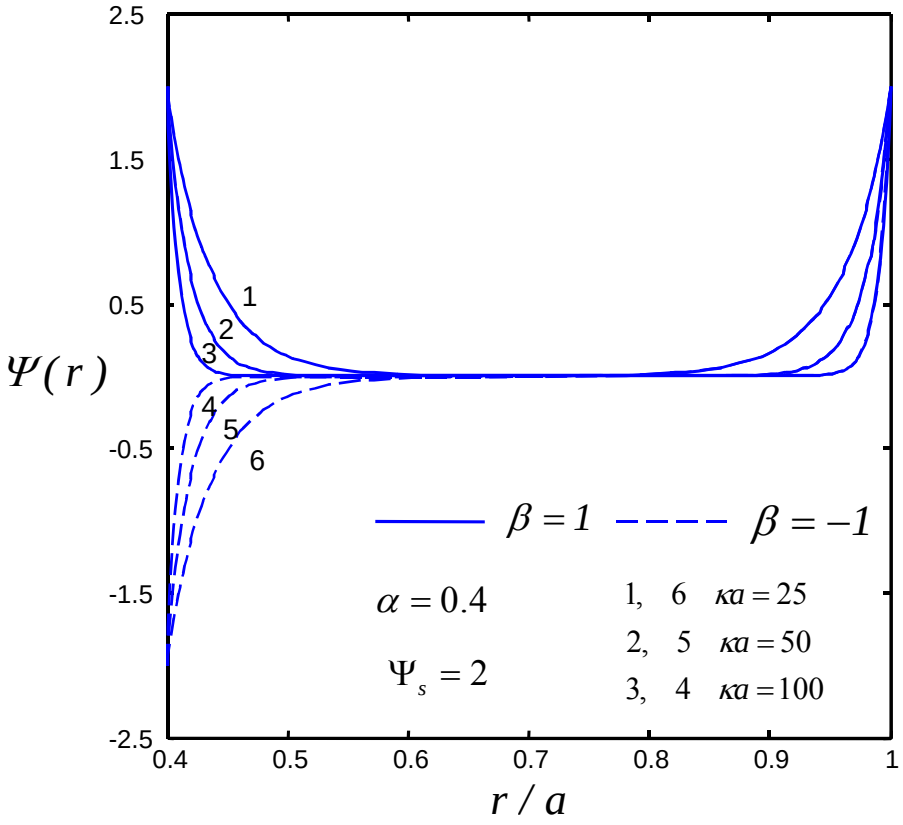

Figure 3-2(b) Effect of the electrokinetic diameter, κa with a fixed non-dimensional zeta potential of the outer cylinder, Ψ_s = 2.

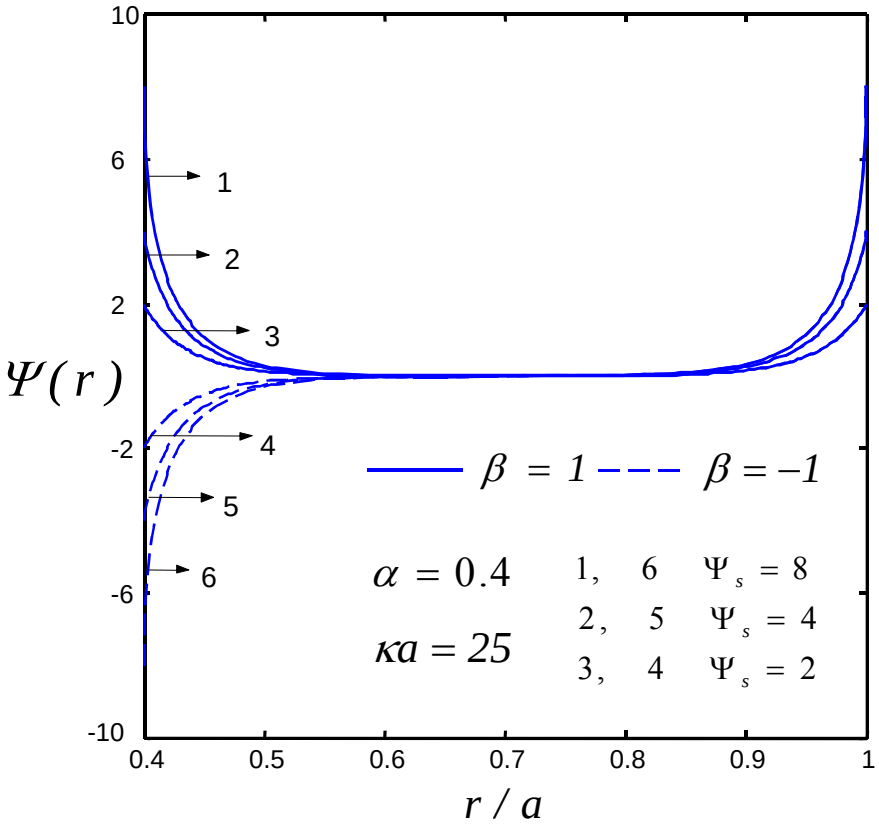

Figure 3-2(c) Effect of the zeta potential, Ψ_s with a fixed electrokinetic diameter, κa = 25.

Figure 3-2 Non-dimensional EDL potential, Ψ (r) versus non-dimensional radius, r / a of the annulus. The geometry ratio of the annular inner radius to outer radius, α = 0.4. The zeta potential ratio of the inner cylinder to the outer cylinder, β = 1 and β = -1, denoting a symmetrically-charged and oppositely-charged annulus, respectively.

3.4.2 Velocity profile

Time evolution of the electroosmotic flow field in annular capillaries under a constant electric field is shown in Figures 3-3(a)~(d). The reference velocity is chosen as $u_{s0} = -\frac{\varepsilon_r \varepsilon_0}{\mu} E_0 \frac{k_b T}{e_0}$. It is obvious that the velocity evolution in annulus is similar to that in cylindrical capillary, which is discussed in detail in chapter 2. Thus only steady-state flow characteristics of EOF in annulus will be discussed in this section.

The non-dimensional steady-state velocity distribution for different electrokinetic diameters, κa, is shown in Figures 3-4(a)~(b). When two cylindrical walls are equally charged (i.e., $\beta = 1$), the velocity field exhibits a profile resembling a plug flow. It can be seen that the velocity increases rapidly from zero on the wall to a maximum velocity within the EDL region that extends about a few Debye-Hückel lengths from the channel wall. Then the velocity remains as a constant through the rest of the channel. This unique profile can be attributed to the fact that the flow is driven by the electrical forces resulted from the interaction of an externally imposed electric field and the EDL field. Such driving forces exist only inside the EDL region where the electrical net charge is not zero. The flow in this region may be viewed as "active". In contrast, the flow outside the EDL region moves due to frictional stresses originated from liquid viscosity, and hence it can be considered as "passive" flow. Furthermore, an examination of Figure 3-4(a) reveals that for a fixed zeta potential, Ψ_s, the magnitude of the maximum electroosmotic velocity is the same, regardless of different values of κa. Taking advantages of the analytical solution for the electroosmotic flow in the annulus, we can interpret this scenario by using Eq. (3.15). According to Eq. (3.15), the maximum electroosmotic velocity, in the case of $\beta = 1$, is given by the

apparent "slip" velocity, u_s (defined in Eq. (3.5)) that is independent of the electrokinetic diameter, κa. Figure 3-4(b) shows the effect of asymmetrically charged walls.

As explained earlier, the electroosmotic flow is the result of the interaction between the applied electric field and the EDL. The zeta potential, Ψ_s, therefore, has a significant influence on the electroosmotic flow, which is amply demonstrated in Figures 3-4(c)~(e) for both symmetrically-charged (i.e., $\beta = 1$) and asymmetrically-charged ($\beta \neq 1$) annuluses. It is noted that the velocity increases with an increase of the zeta potential, indicating a nearly linear relationship between zeta potential and velocity.

Now we consider a situation when the two cylindrical walls are oppositely charged (i.e., $\beta < 0$). As illustrated in Figures 3-4(a)~(e), the direction of the electroosmotic flow in the annulus is directly correlated to the polarity of the charged channel wall. It is observed that there is a cylindrical plane inside the annulus, on which the fluid velocity is zero. The liquids divided by such a plane flow in two opposite directions, undisturbed to each other as if there exists a wall dividing them. Interestingly, an inspection of Figure 3-4(a) and Figure 3-4(c) indicates that given a fixed geometry ratio, α, the location of the zero-velocity plane in an equally-charged annulus remains unchanged despite the difference in the zeta potential and the electrokinetic diameter. In fact, the location of the zero-velocity plane can be predicted from Eq. (3.15). Given the fact that for the case of $\beta < 0$ and large electrokinetic diameters, for example $\kappa a \geq 25$, the electrical potential, ψ at the zero-velocity plane is negligible, i.e., $\psi(\bar{r}_0) \approx 0$. As such, the location of the zero-velocity plane, as shown in Figs. 3-4(a)~(e), can be estimated as $\bar{r}_0 = \sqrt[(1-\beta)]{\alpha}$, which gives the values of $\bar{r}_0 = 0.632$ and $\bar{r}_0 = 0.737$ for $\alpha = 0.4$ and, $\beta = -1$ and $\beta = -2$, respectively.

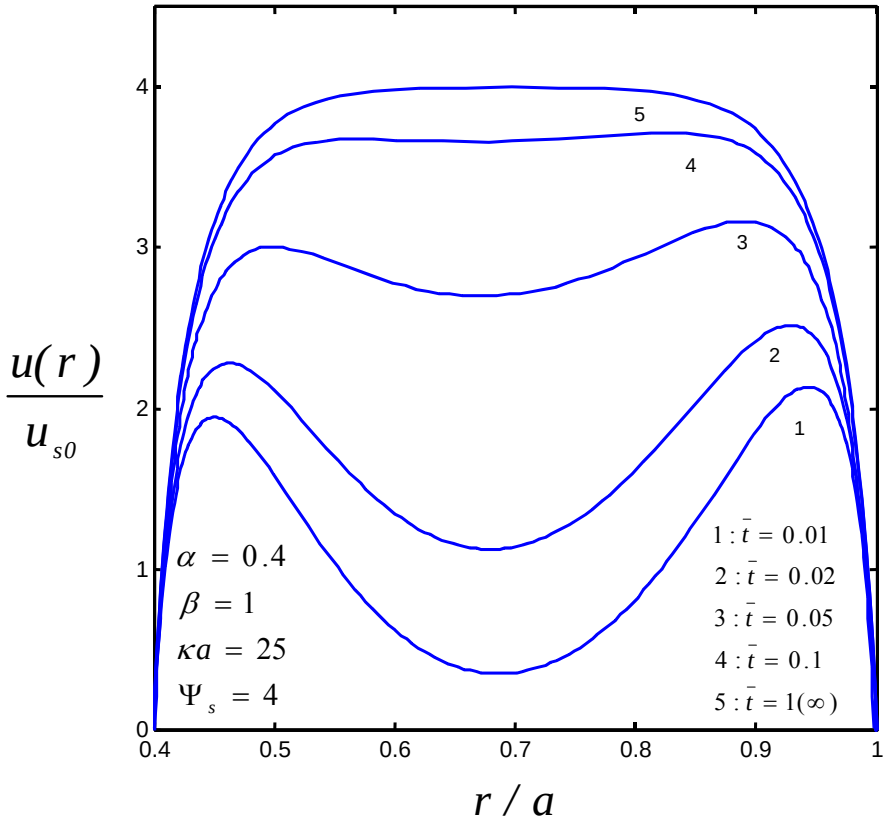

Figure 3-3(a) Time evolution for the case of thick electric double layer with the electrokinetic **diameter, κa = 25 and β = 1.**

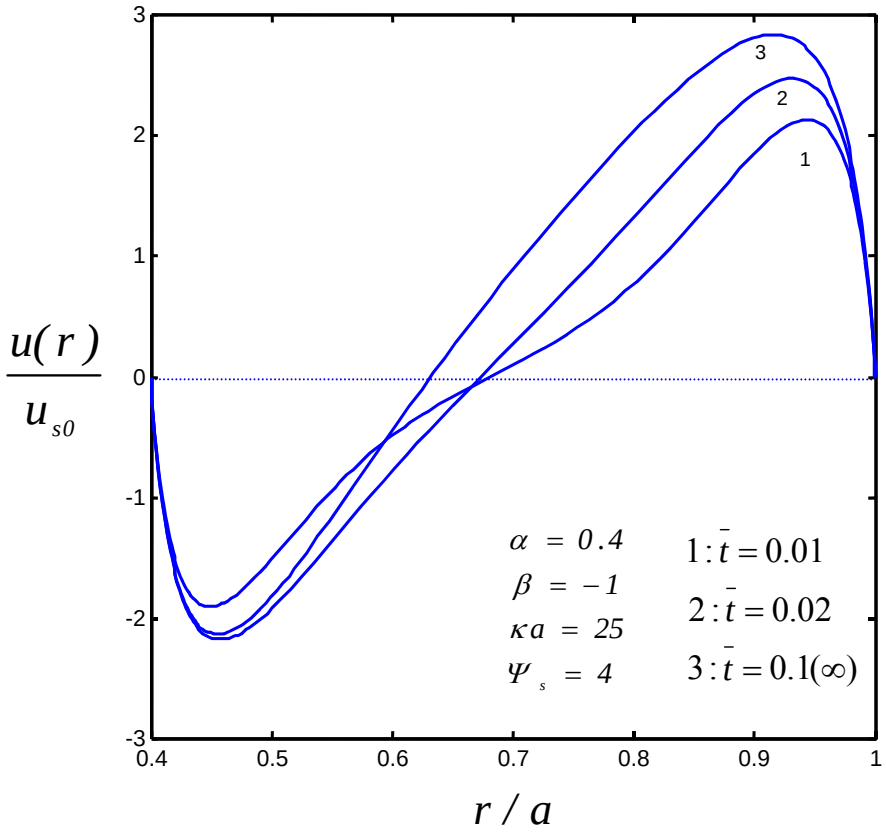

Figure 3-3(b) Time evolution for the case of thick electric double layer with the electrokinetic diameter, κa = 25 and β = -1.

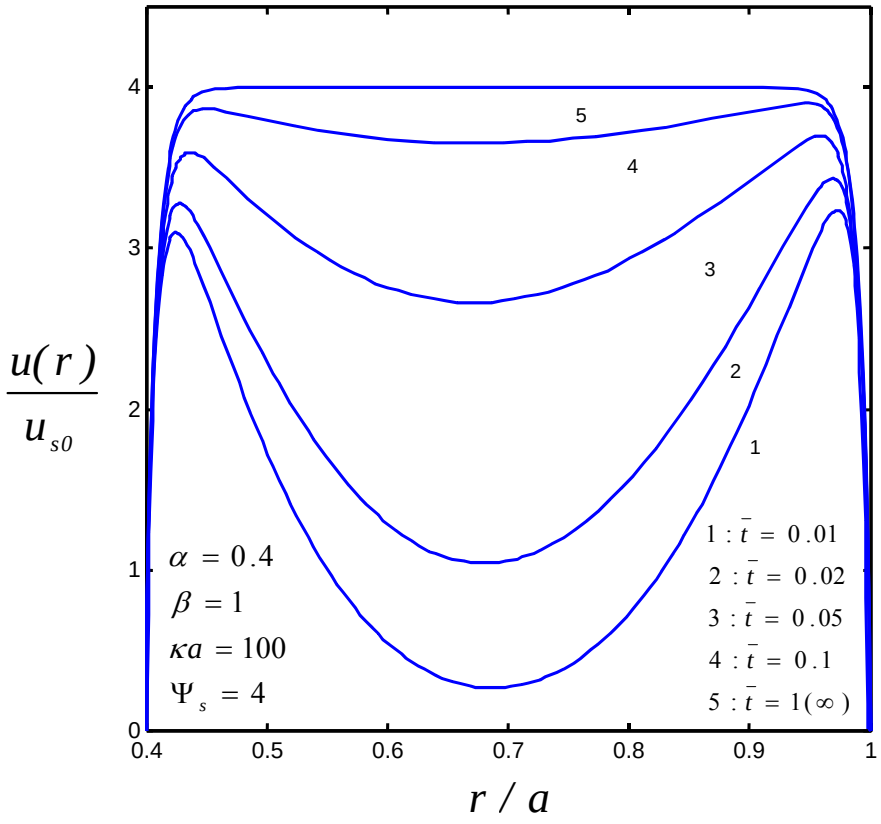

Figure 3-3(c) Time evolution for the case of thin electric double layer with the electrokinetic diameter, κa = 100 and β = 1.

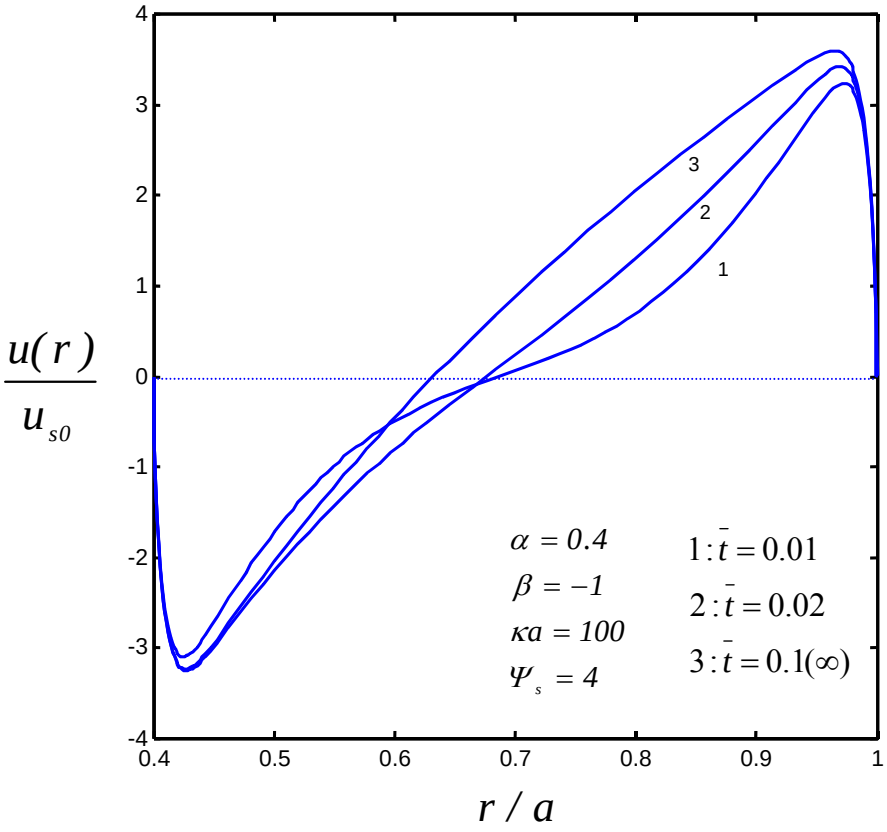

Figure 3-3(d) Time evolution for the case of thin electric double layer with the electrokinetic diameter, κa = 100 and β = 1.

Figure 3-3 Dimensionless transient velocity, $u(r) / u_{s0}$ versus dimensionless radius, r / a for the case of radius ratio, α = 0.4 and the zeta potential Ψ_s = 4. The reference velocity is defined as $u_{s0} = -\frac{\varepsilon_r \varepsilon_0}{\mu} E_0 \frac{k_b T}{e_0}$.

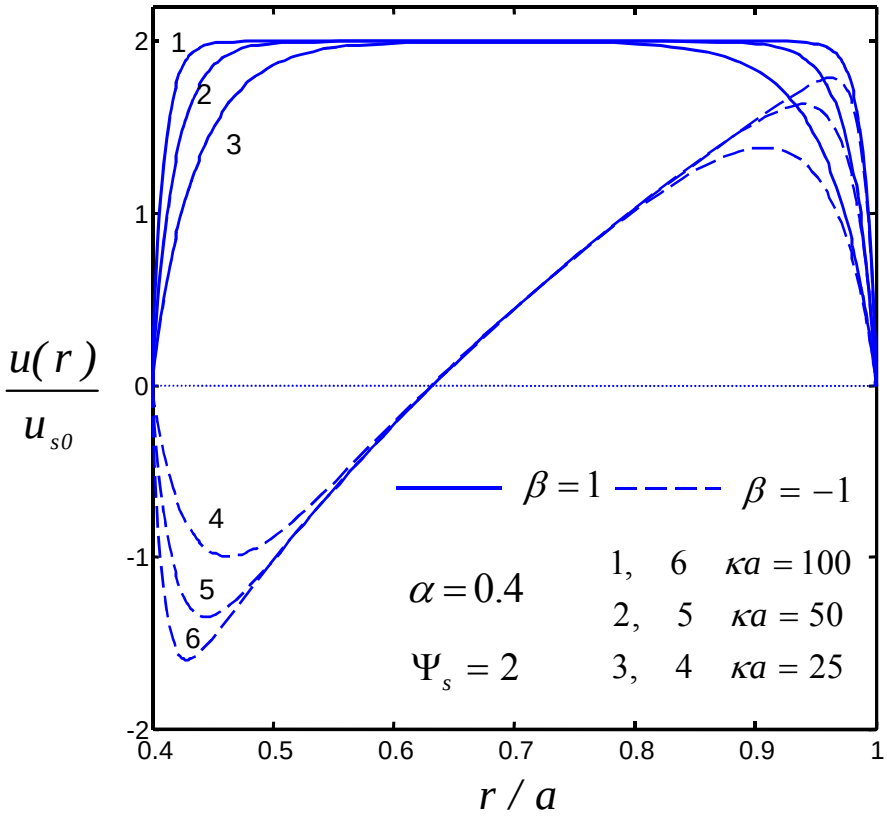

Figure 3-4(a) Effect of the electrokinetic diameter, κa with a fixed non-dimensional zeta potential of the outer cylinder, Ψ_s= 2 and radius ratio $\beta = \pm 1$.

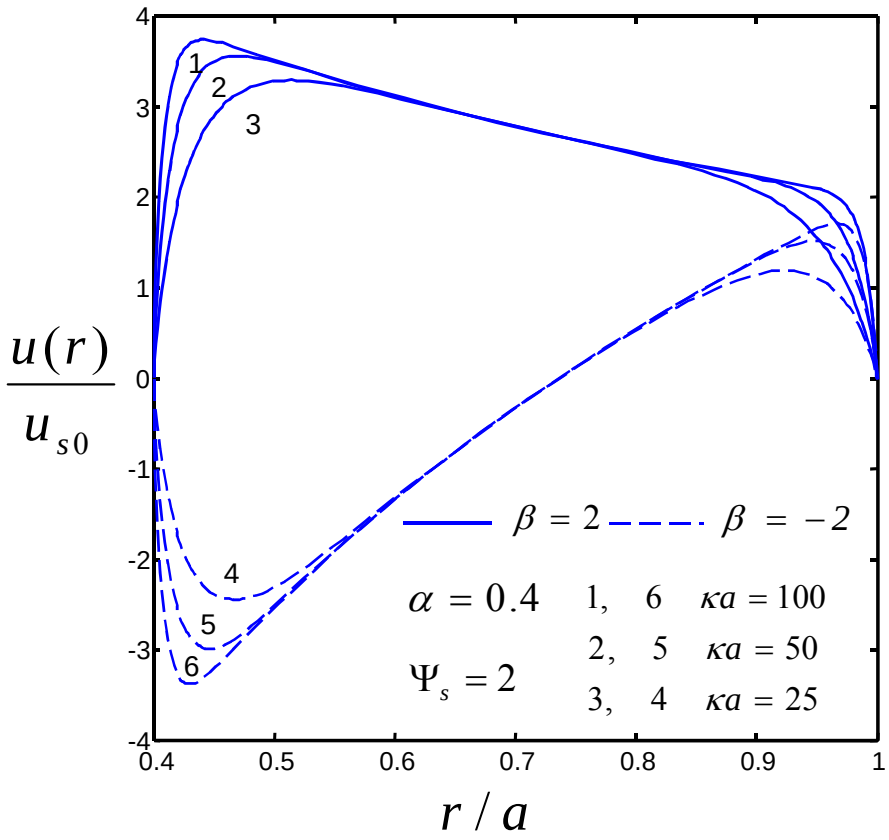

Figure 3-4(b) Effect of the electrokinetic diameter, κa with a fixed non-dimensional zeta potential of the outer cylinder, Ψ_s= 2 and radius ratio $\beta = \pm 2$.

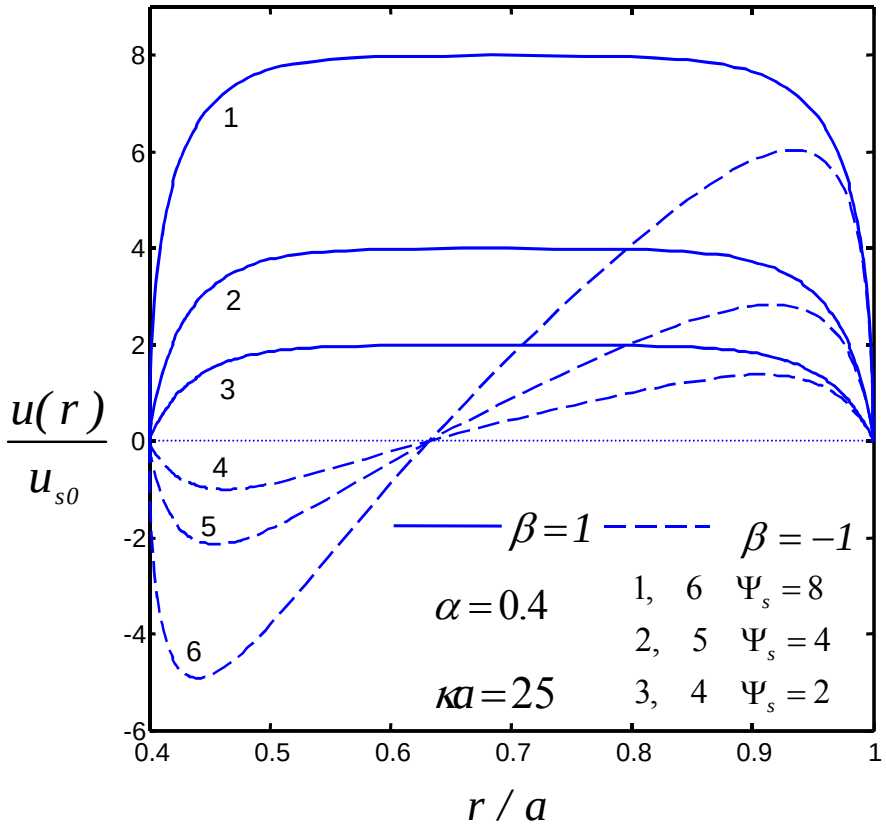

Figure 3-4(c) Effect of the zeta potential, Ψ_s with a fixed electrokinetic diameter, κa = 25 and radius ratio $\beta = \pm 1$.

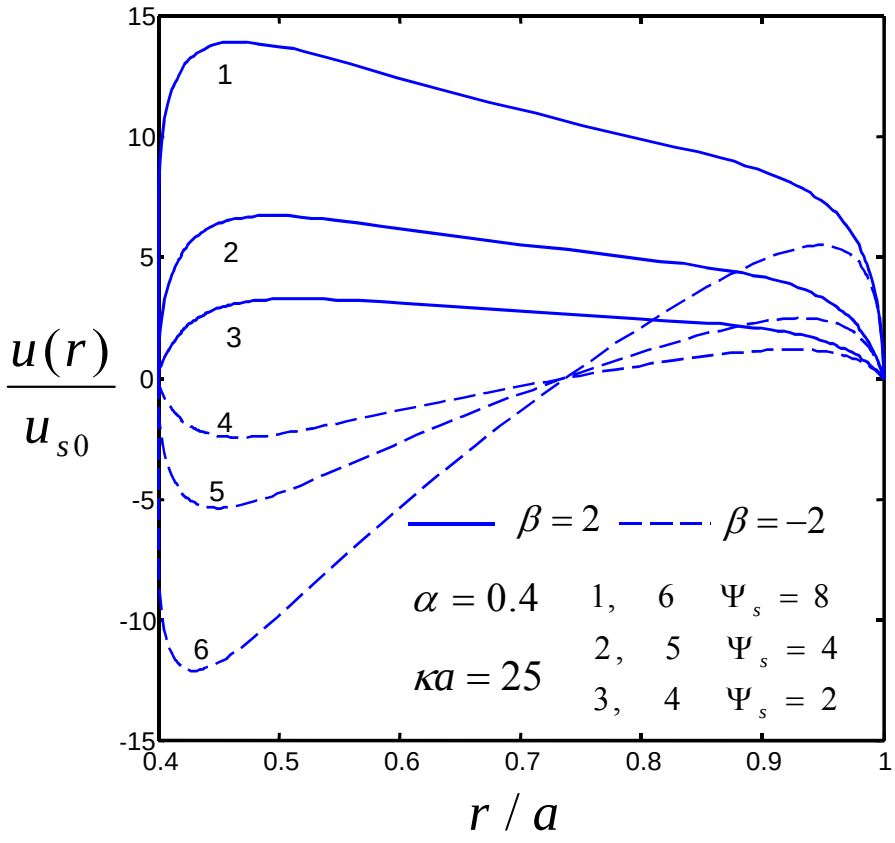

Figure 3-4(d) Effect of the zeta potential, Ψ_s with a fixed electrokinetic diameter, κa = 25 and radius ratio $\beta = \pm 2$.

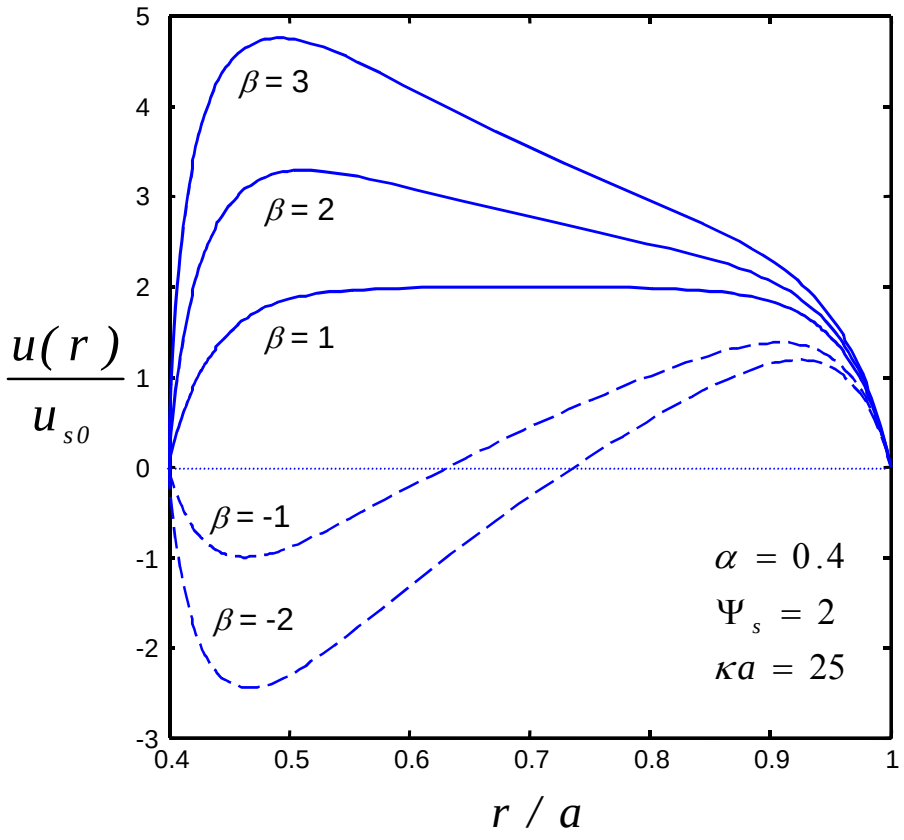

Figure 3-4(e) Effect of the zeta potential ratio, $\beta = \zeta_i / \zeta_0$ with fixed the electrokinetic diameter, $\kappa a = 25$ and the non-dimensional zeta potential of the outer cylinder, $\Psi_s = 2$.

Figure 3-4 Non-dimensional electroosmotic flow velocity, $u(r) / u_{s0}$ versus non-dimensional radius, r / a of the annulus. The geometry ratio of the annular inner radius to outer radius, $\alpha = 0.4$. Reference velocity is chosen as $u_{s0} = -\frac{\varepsilon_r \varepsilon_0}{\mu} E_0 \frac{k_b T}{e_0}$.

3.4.3 Prediction for the EDL-related correction factor, G

The quantity $(1-G)$ is important in a sense that it denotes the effect of the finite EDL thickness. It can be considered as the EDL-related correction factor to the Smoluchowski equation. In Figure 3-5, $(1-G)$ versus κa is plotted for various values of the zeta potential, Ψ_s ($\Psi_s \geq 2$). The predictions display that when the electrokinetic diameter, κa is small, $(1-G)$ is far away from 1, indicating that the impact of the finite EDL thickness on the electroosmotic flow becomes relatively stronger, and hence this correction factor should be taken into account. Furthermore, for a given value of the electrokinetic diameter, κa, $(1-G)$ increases with an increase in the wall zeta potential, Ψ_s. However, with the linear approximation (Rice and Whitehead, 1965), G was reported to be independent of Ψ_s. On the other hand, as κa becomes large, irrespective of Ψ_s all curves for $(1-G)$ are approaching to 1, suggesting that while the capillary electrokinetic diameter is large enough, the effect of the finite EDL thickness, G is negligible.

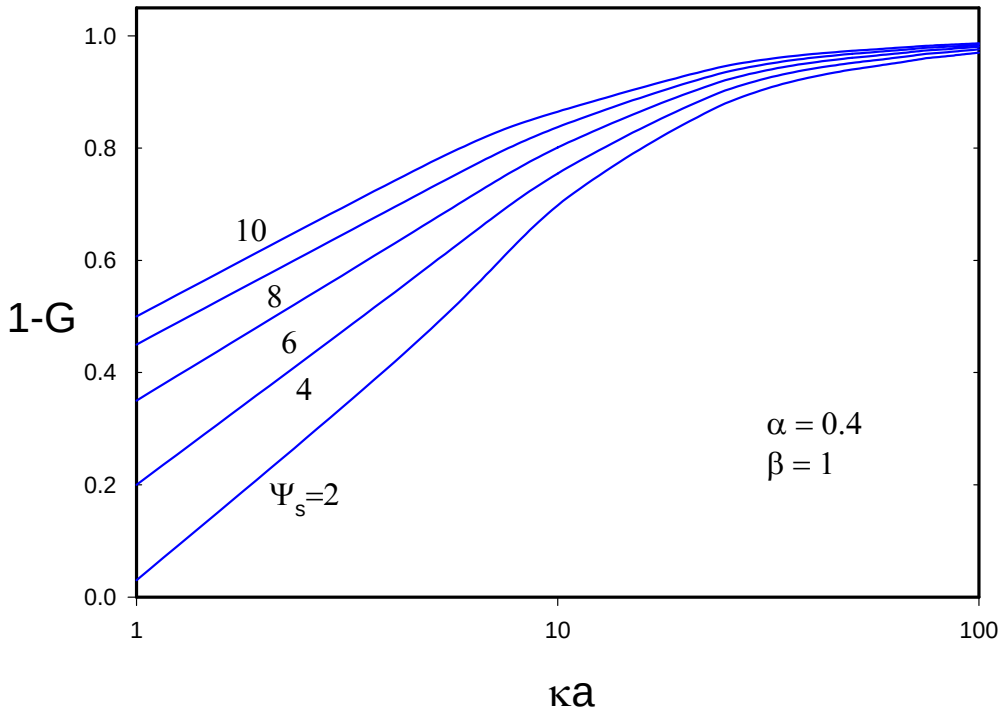

Figure 3-5 Variation of the EDL-related correction factor (1-*G*) with the electrokinetic diameter, κa for various zeta potentials of the outer cylinder, Ψ_s. The geometry ratio of the annular inner radius to outer radius, α = 0.4. The inner and outer annular walls are equally charged, β = 1.

3.4.4 Prediction for the correction factor to the Smoluchowski equation, J

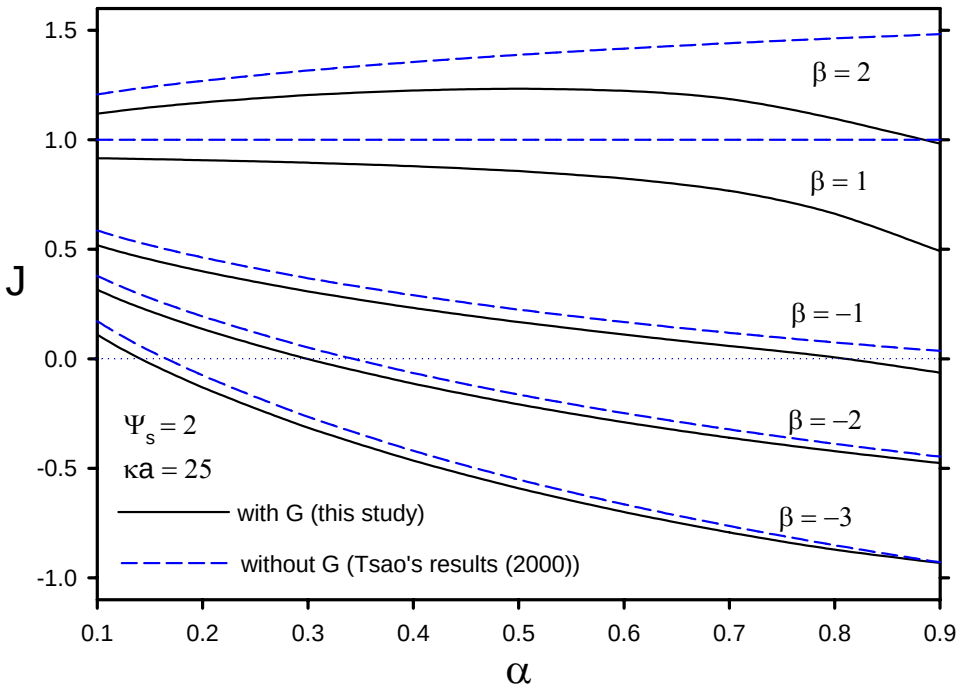

Figure 3-6 Correction factor for the Smoluchowski Equation, J versus the geometric ratio of the annular inner radius to outer radius, α for various values of the zeta potential ratio, $\beta = \zeta_i / \zeta_o$. Without including the EDL-related correction factor, G, we recover Tsao's results (2000) represented by the dashed lines.

According to the definition given in Eq. (3.18), the quantity J represents the correction factor to the Smoluchowski equation, and it takes into account of contributions due to the EDL and the geometric ratio of the annulus. As pointed out by Tsao (2000), physically J also can be considered as the normalized mobility with respect to that of a charged surface with ζ_o (see Eq. (3.16)). The effects of the radius ratio, α and the zeta potential ratio, β on J are shown in Figure 3-6. For a comparison, the results obtained by Tsao (2000) who used the solution of the linearized Poisson-Boltzmann equation and

neglected the EDL-related correction, G are plotted as the dashed lines in Figure 3-6. As expected, the mobility, J predicted from this study is different from that obtained by using Tsao's approach. For instance, Figure 3-6 clearly shows that for $\beta > 1$ Tsao predicted the inner cylinder enhances the fluid mobility that increases with increasing α. While our calculations show a completely different trend of the dependence of J on α. It is anticipated that such discrepancy would become larger for the cases of higher zeta potentials, Ψ_s and smaller electrokinetic diameters, κa, under which the contributions of the non-linear Poisson-Boltzmann equation and the EDL-related correction, G, are more significant.

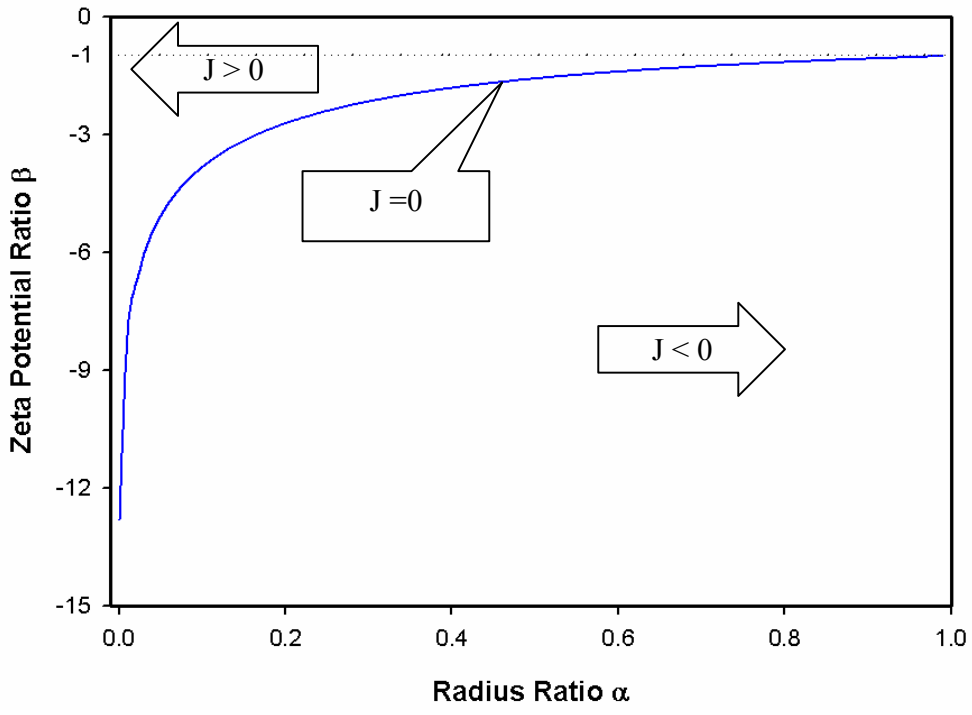

Figure 3-7 Critical value combinations of the radius ratio, α and the zeta potential ratio, β for zero net flow rate.

On the other hand, our calculations based on the approach developed in this work reconfirm the important features of the electroosmotic flow in the annulus when the two cylindrical walls are oppositely charged. As mentioned earlier, reverse of the sign of J from positive to negative implies a change of the net flow direction. The net flow direction change also implies that there exists some combination of α and β when the net flow rate is zero ($J = 0$).Without loss of generality, the α - β combination for zero net flow rate in wide capillary is shown as the solid curve in Figure 3-7, according to Eq. (3.21). Regardless of the value of α, the value of J is found always positive for $\beta > -1$. However, for $\beta \le -1$, J decreases from positive to negative as α increases. The two regions divided by the solid curve denotes two opposite net flow directions. The net flow rate right on this curve is zero. This α-β relationship is very interesting because it is related to the condition corresponds to the electrokinetic displacement of air bubble in a microchannel (Takhistov et al., 2002). The electrokinetic flow between the bubble surface (oppositely charged compared to channel wall) and the channel wall can be modeled as an annular thin film of EOF around the bubble. When the net flow in this annular film is zero, the bubble remains stationary while there is EOF around it. Once net flow exists in the thin film, the fluid behind the bubble accumulates and a pressure gradient is built up to move the bubble forward in order to accommodate the accumulated fluid. Thus the results in Figure 3-7 can predict that when the bubble would begin to translate. The α-β relationship at zero net flow rate is an important threshold condition for transporting bubble (or drop) in microchannels.

3.5 Summary

Analytical scheme is proposed to solve the nonlinear Poisson-Boltzmann equation in an annulus domain. The calculated results show that the difference between the proposed analytical scheme and the complete numerical solution of Poisson-Boltzmann equation is visually indistinguishable, indicating an excellent approximation proposed in this study. An analytical expression for the electroosmotic flow filed in an annulus is derived. The calculations show that for a given zeta potential, the magnitude of the maximum electroosmotic velocity is independent on κa. In the case that the two walls of an annulus are oppositely charged, there exits a zero-velocity plane, which can be estimated by $\bar{r}_o = \sqrt[(1-\beta)]{\alpha}$. In addition, it is found that the correction factor to the Smoluchowski equation for annulus needs to account for both the EDL-related and the geometry-dependent contributions.

Chapter 4

DC Electroosmotic Flow in a Microchannel Packed with Microspheres under Electrokinetic Wall Effect

4.1 Introduction

In this chapter, we attempt to construct a mathematical model for the EOF in a charged microcapillary packed with charged microspheres. Our approach is based on the capillary model and the volume averaging method. Since the packing particles are not neutral but charged with a zeta potential, ζ_p, the local EDL regime will occupy a finite portion of each void space among particles as long as there is an interface between the particle and the fluid. Due to the interaction of the local EDL and the applied electric field, EOF occurs everywhere in the space occupied by fluid phase, including in the void space between the charged packing particles and the charged channel wall. We start with the analysis of the EOF in a microcapillary packed with homogeneously charged microspheres. It is obvious that under the volume averaging method, the macroscopic EOF velocity should be uniform everywhere in a homogeneous (no boundary, uniform particle size) porous medium. However, in this study, the porous medium is bounded by a charged capillary wall. Thus the volume averaging method is employed to obtain the macroscopic EOF velocity distribution, taking into account inhomogeneity due to the geometrical variation of packing porosity. Next, the modified Brinkman momentum equation is solved to obtain the electrokinetic wall effect

which is due to the excessive zeta potentials of the capillary inner surface. The effects of geometrical and electrokinetic parameters on the EOF velocity fields are discussed.

4.2 Method of Volume Averaging

In a natural porous medium, the distribution of pores with respect to shape and size is irregular. On the pore scale (microscopic scale) the flow quantities such as velocity, pressure, etc., are also irregular (Nield and Bejan, 1999). But in typical experiments the quantities of interest are measured over areas that across many pores and such space-averaged (macroscopic) quantities change in a regular manner with respect to space and time and hence are amenable to the theoretical treatment. A macroscopic variable is defined as an appropriate mean over a sufficiently large *representative elementary volume* (REV). It is assumed that the result is independent of the size of the REV. As illustrated in Figure 4-1(a), the length scale of the REV is much larger than the pore scale, but considerably smaller than the length scale of the macroscopic flow domain.

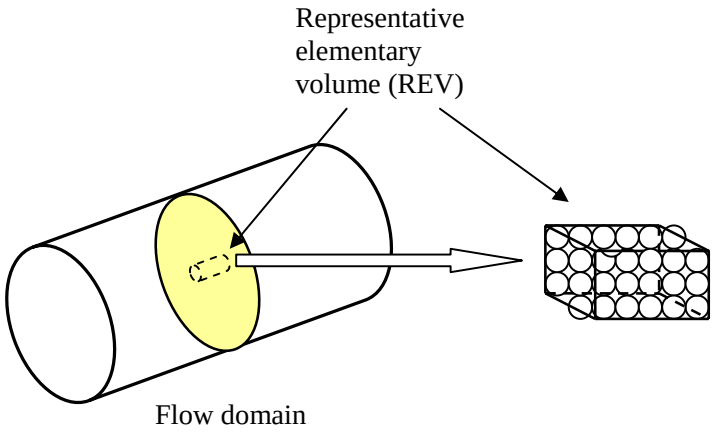

(a)

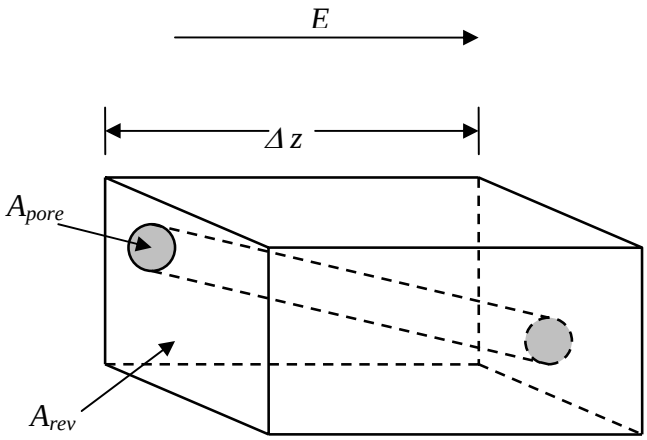

(b) $\phi = V_f / V = A_{pore} / A_{rev}$

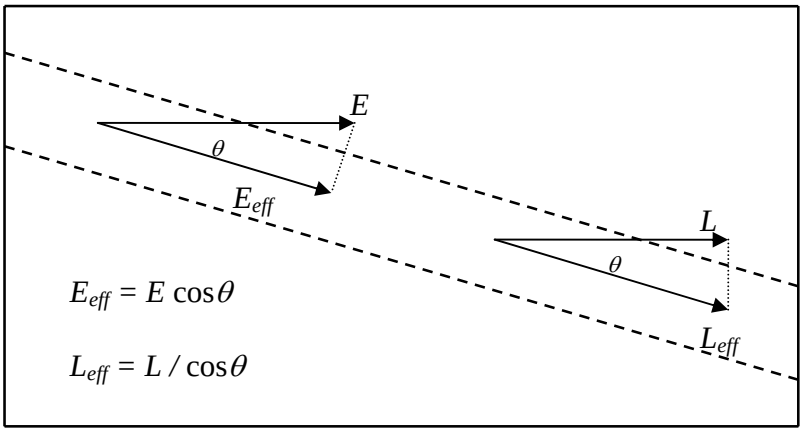

(c) $\tau = 1 / \cos^2 \theta = (L_{eff} / L)^2$

Figure 4-1 Schematic illustration of representative elementary volume (REV): the length scale of the REV is much larger than the pore scale, but considerably smaller than the length scale of the macroscopic flow domain.

Under the volume averaging method, the flow quantity, such as the velocity will be lowered in magnitude in a packed capillary than in an unpacked capillary by some geometric

constraint factors (Remcho and Vallano, 2001). Two major geometric constraint factors to characterize a porous medium are called the porosity and the tortuosity. The porosity is defined as $\phi = V_f / V$, where V_f and V are the void and total volumes of the porous medium, respectively (as illustrated in Figure 4-1(b)). Thus the porosity factor is a volume averaging including the space occupied by the solid packing material. The other factor, as illustrated in Figure 4-1(c), tortuosity includes the non-alignment of most flow channels with the electric field, which is applied along the capillary axis. The fluid flow in a capillary tube packed with solid spherical particles will occur only within the interparticulate spaces. The individual flow channels comprise a highly complex, directionally non-uniform network, of which only a fraction will be aligned axially with the electric field. Most flow channels will be off-axis with respect to the field resulting in a lower effective field strength (decreased by a factor of $\cos\theta$). In addition, the fluid flowing in an off-axis channel must travel a greater distance (increased by a factor of $1/\cos\theta$) for a given displacement along the capillary axis. The tortuosity is defined as $\tau = 1/\cos^2\theta = (L_{eff} / L)^2$, where L_{eff} is the effective length of travel for flow along the pore path and L is the physical length of the porous structure (Kaviany, 1995). Combination of above factors results in the reduction of the velocity component along the axis by a factor of ϕ / τ.

The other two parameters are the pore size, d_{pore}, and the Darcy permeability, K, which will be defined in next section. These structure-related parameters can be determined by experiment.

In this study, we consider a charged cylindrical microcapillary of the radius, R_w packed with charged spherical microparticles of uniform diameter, d_p. The liquid in the microcapillary is

assumed to be an incompressible, Newtonian, monovalence electrolyte of density, ρ, and viscosity, μ. The zeta potentials of the inner wall surface and the particle surface are ζ_w and ζ_p, respectively. When an external electric field, E_0 is applied along the axis of the microchannel, the electrolyte in the microchannel will move due to the electroosmosis resulted from the interaction of the EDL (close to the interface of the particles as well as the channel wall) and the applied electric field. Joule heating effect due to axially imposed electric field is ignored in our model development.

The overall macroscopic EOF velocity in the packed capillary is decomposed into two separate components due to: the contribution from homogeneous densely packed charged microparticles and the contribution from the charged capillary wall with neutral packing, as illustrated in Figure 4-2.

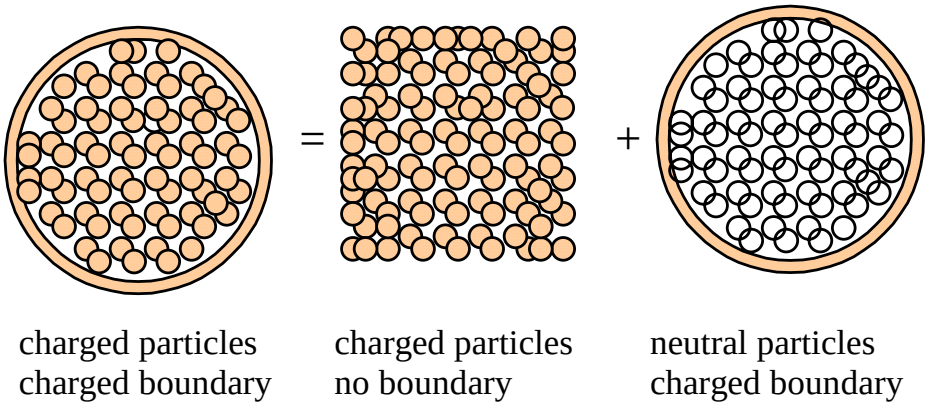

Figure 4-2 Schematic illustration of decomposing the overall macroscopic EOF velocity in a packed capillary into two separate components due to: (i) the contributions from homogeneous (isotropic) densely packed with charged microparticles, and (ii) the contributions from the charged capillary wall with neutral packing.

As mentioned above, the present model is based on the space-averaging method which is

commonly applied in the classical pressure-driven transport phenomena in porous media. This averaging method focuses on the equivalent macroscopic physics without considering the local complexity in the microscale. However, the EOF in porous media is originated from the interaction of the external electric field and the EDL at internal surface of the porous structure. In reality from microscopic viewpoint, the driving force is dependent on the local configuration of the interface and local pressure gradient may be induced because of the complicated geometric structure and overlapped EDLs, which makes the real scenario much more complex. Strictly speaking, a more accurate three dimensional pore-size level modeling instead of space-averaging modeling should be developed to include such effects. However due to the enormous difficulties involved in numerically simulating the true 3-D problem and the time limit for this project, the macroscopic space-averaging model for the EOF in the porous media is applied, as a "first-order" approximation, throughout this thesis.

4.3 Macroscopic EOF in Homogeneous Charged Microspheres

4.3.1 Interstitial EOF velocity

The present work is based on a semi-heuristic model of flow through solid matrices using the concept of hydraulic diameter, which is also known as the *Carman-Kozeny theory* (Probstein, 1994). The theory assumes the porous medium to be equivalent to a series of parallel tortuous tubules. The characteristic diameter of the tubules is taken to be a hydraulic diameter or effective pore diameter. This diameter is conventionally defined as (Kaviany, 1995)

$$d_{pore} = \frac{4 \times Void\ Volume}{Surface\ Area} = \frac{4\phi_\infty}{A_o(1-\phi_\infty)} \tag{4.1}$$

where ϕ_∞ is the average porosity of the porous medium. A_o is the volumetric or specific area based on the solid volume, i.e., A_{fs}/V_s, where A_{fs} is the interfacial area between the fluid and the solid phase and V_s is the solid volume. For spherical particles considered in this work $A_o = 6/d_p$, where d_p is the diameter of spherical particles. So the hydraulic diameter can be expressed as

$$d_{pore} = \frac{2\phi_\infty}{3(1-\phi_\infty)} d_p \tag{4.2}$$

We propose the interstitial tubules to be cylindrical with an effective diameter, i.e., effective pore size, $d_{pore} = 2R_{pore}$. The inner wall of the cylindrical tubules is charged with zeta potential ζ_p. The interstitial EOF velocity $u_i(r)$ in each tubule is governed by the Stokes equation (Probstein, 1994).

$$\mu \frac{1}{r}\frac{d}{dr}\left[r \frac{du_i(r)}{dr} \right] + E_0 \rho_e(r) + P_z = 0 \qquad (0 \le r \le R_{pore}) \tag{4.3}$$

where $P_z = \Delta P/L$ is the global pressure gradient along the flow direction. L is the physical length of the flow domain. In the present study, no global pressure gradient is applied, i.e., $P_z = 0$. As noted in section 4.2, from microscopic point of view, a local back pressure gradient may be induced where the EOF becomes non-uniform due to the complicated geometry and packing conditions. For instance, at narrow constrictions the local electric field strength becomes higher if the porous packing has a lower permittivity than the working fluid. As we know, the EOF velocity is proportional to the electric field strength. Thus the local EOF tends to be strengthened to increase local velocity. When the EOF is non-uniform, local pressure-driven back flow must be induced to maintain the local mass conservation (Tallarek

et al., 2001). However, the geometrical non-uniformity and the induced local pressure are highly random within the bulk packing except at the end of the packed capillary – the interface of the retaining frits, where the flow path may subject to drastic decrease in cross-sectional area, depending on the quality of the frits. In present study the end frit effect is ignored and we focus on the electroosmosis-driven flow through the porous packing. Under the present space averaging method, the overall effect of the random local pressure gradient vanishes. Therefore the porous media is assumed as equivalent parallel tubules of uniform cross-sectional area without global pressure gradient. $\rho_e(r)$ is the local volumetric charge density due to the presence of the EDL inside each interstitial tubule, and it is given by the Poisson equation, which takes the form (Hunter, 1981)

$$\frac{1}{r}\frac{d}{dr}\left[r\frac{d\psi_i(r)}{dr}\right] = -\frac{\rho_e(r)}{\varepsilon_r\varepsilon_0} \qquad (0 \le r \le R_{pore}) \tag{4.4}$$

where ε_r is the dielectric constant of the electrolyte and ε_0 is the permittivity of vacuum. Substituting Eq. (4.4) into Eq. (4.3), and using the following boundary conditions

$$\left.\frac{du_i}{dr}\right|_{r=0} = 0 \qquad \left.\frac{d\psi_i}{dr}\right|_{r=0} = 0 \tag{4.5a}$$

$$u_i\big|_{r=R_{pore}} = 0 \qquad \psi_i\big|_{r=R_{pore}} = \zeta_p \tag{4.5b}$$

we can obtain an analytical expression for the velocity distribution, which takes the form as

$$u_i(r) = -\frac{\varepsilon_r\varepsilon_0}{\mu}E_0\zeta_p\left[1-\frac{\psi_i(r)}{\zeta_p}\right] \tag{4.6}$$

Under the volume averaging method, the macroscopic superficial velocity (also called the Darcy velocity) of the fluid over the representative elementary volume can be expressed by taking into account the tortuosity τ and the porosity ϕ, as

$$u_{Di} = \frac{\phi}{\tau}\langle u_i \rangle = \frac{\phi}{\tau}\frac{2}{R_{pore}^2}\int_0^{R_{pore}} r u_i(r) dr = -\frac{\varepsilon_r \varepsilon_0}{\mu} E_0 \zeta_p \frac{\phi}{\tau}(1-G) \tag{4.7}$$

where

$$G = \frac{2}{\zeta_p R_{pore}^2}\int_0^{R_{pore}} r \psi_i(r) dr \tag{4.8}$$

and $\phi = \phi(r)$ is the local porosity distribution of the porous medium. In the literature, $\phi(r)$ is assumed to take a form of (Nield and Bejan, 1999)

$$\phi(r) = \phi_\infty \left[1 + C_0 \exp\left(-N\frac{R_w - r}{d_p}\right)\right] \qquad (0 \le r \le R_w) \tag{4.9}$$

where ($R_w - r$) is the distance from the microcapillary wall. C_0=1.4 and N=5 are empirical constants (Hsu and Cheng, 1990).

4.3.2 Interstitial EDL potential field

The interstitial EDL potential distribution ψ_i in each tubule is governed by Poisson-Boltzmann (P-B) equation, which is expressed in the normalized form as (Hunter, 1981)

$$\frac{1}{R}\frac{d}{dR}\left[R\frac{d\Psi_i(R)}{dR}\right] = \sinh \Psi_i(R) \qquad (0 \le R \le \kappa R_{pore}) \tag{4.10}$$

where $R = \kappa r$, $\kappa = (\frac{2n_0 e_0^2}{\varepsilon_r \varepsilon_0 k_b T})^{\frac{1}{2}}$, dimensionless EDL potentials $\Psi_i = \frac{e_0 \psi_i}{k_b T}$ and $\Psi_{ip} = \frac{e_0 \zeta_p}{k_b T}$, e_0 is the elementary charge, n_0 is the ionic concentration in the bulk phase (i.e., far from the charged tubular wall), k_b is the Boltzmann constant, and T is the absolute temperature.

The boundary conditions given by Eq. (4.5) can be rewritten as

$$\left.\frac{d}{dR}\Psi_i\right|_{R=0} = 0 \qquad \Psi_i\big|_{R=\kappa R_{pore}} = \Psi_{ip} \tag{4.11}$$

An analytical solution to Eq. (4.10) is provided in appendix B.

4.4 Macroscopic EOF in a Charged Microcapillary Packed with Neutrally Charged Microspheres

4.4.1 EOF velocity field

We consider a charged cylindrical microcapillary of radius R_w, with the inner surface charged with zeta potential ζ_w. Inside the microchannel there are densely packed, neutrally charged spherical microparticles of diameter d_p. The Brinkman momentum equation, which originally was derived for a pressure-driven Darcy flow in porous media, then has been generalized by Brinkman to account for the inertial forces, pressure gradient, body forces, and shear stresses (Kaviany, 1995). In the present situation, no pressure is exerted and hence no pressure gradient is present. Further, due to low Reynolds number flow in micro-sized pores, the macroscopic inertial force is ignored. The body force is the columbic force due to the interaction of the electric double layer (EDL) and the external electric field. Thus the modified Brinkman momentum equation used for describing the macroscopic EOF of an incompressible, Newtonian electrolyte solution in a packed microcapillary under a steady state can be expressed as

$$\mu_{eff}\frac{1}{r}\frac{d}{dr}\left[r\frac{du_{Dw}}{dr}\right] + E_0\phi\rho_{ef}(r) - \left[\frac{\mu\phi u_{Dw}}{K} + \rho\frac{F\phi u_{Dw}^2}{\sqrt{K}}\right] = 0 \qquad (0 \le r \le R_w) \tag{4.12}$$

Here $u_{Dw}(r)$ is the macroscopic EOF velocity (Darcy velocity) field through the neutral

porous medium inside the microcapillary. $\phi = \phi(r)$ is the local porosity distribution of the porous medium, determined by Eq. (4.9). The Darcy permeability K is defined by the *Carman-Kozeny* equation (Probstein, 1994), $K = \phi^3 d_p^2 / a(1-\phi)^2$, and the inertial coefficient $F = b/\sqrt{a}\phi^{3/2}$, with $a = 150$ and $b = 1.75$ being the Ergun constants (Hsu and Cheng, 1990). μ_{eff} is the effective fluid viscosity, a function of the fluid viscosity and the geometry of the permeable medium. For an isotropic porous medium, $\mu_{eff} / \mu = 1/\phi\tau$ (Nield and Bejan, 1999). $\rho_{ef}(r)$ is the average volumetric charge density due to the presence of the EDL, and it is assumed to satisfy the Boltzmann distribution (Hunter, 1981)

$$\rho_{ef}(r) = -2n_0 e_0 \sinh\left[\frac{e_0 \psi_w(r)}{k_b T}\right] \qquad (0 \le r \le R_w) \tag{4.13}$$

Eq. (4.12) is subject to the boundary conditions

$$\left.\frac{du_{Dw}}{dr}\right|_{r=0} = 0 \qquad \left.\frac{d\psi_w}{dr}\right|_{r=0} = 0 \tag{4.14a}$$

$$u_{Dw}\big|_{r=R_w} = 0 \qquad \psi_w\big|_{r=R_w} = \zeta_w \tag{4.14b}$$

4.4.2 EDL potential field

The EDL potential distribution is governed by the Poisson-Boltzmann equation (Hunter, 1981)

$$\frac{1}{R}\frac{d}{dR}\left[R\frac{d\Psi_w(R)}{dR}\right] = \sinh\Psi_w(R) \qquad (0 \le R \le \kappa R_w) \tag{4.15}$$

where $R = \kappa r$, subject to the boundary conditions

$$\left.\frac{d\Psi_w}{dR}\right|_{R=0} = 0 \tag{4.16a}$$

$$\Psi_w\big|_{R=\kappa R_w} = \frac{e_0 \zeta_w}{k_b T} \tag{4.16b}$$

An analytical solution of the Eq. (4.15) is provided in appendix B, and such an analytical solution will be also used when we use the numerical method to solve the non-linear modified Brinkman's momentum equation, Eq. (4.12).

4.4.3 Analytical solution of the modified Brinkman momentum equation, Eq. (4.12)

In general, no analytical solution is available for Eq. (4.12), which can only be solved numerically. However, due to the low Reynolds number laminar flow in microchannels, we can safely ignore the high Reynolds number term, i.e., $\rho F \phi u_{Dw}^2 / \sqrt{K} \approx 0$. And to emphasize only the electrokinetic wall effect, we can further assume that the porosity is uniform in the porous medium, i.e., $\phi = \phi_\infty$. Under these assumptions, we can exclude the geometrical wall effect, and thus Eq. (4.12) can be simplified to

$$\frac{1}{r}\frac{d}{dr}\left(r\frac{du_{Dw}}{dr}\right) - \frac{a\tau(1-\phi_\infty)^2}{\phi_\infty d_p^2} u_{Dw} = -\frac{\phi_\infty^2 \tau E_0}{\mu}\rho_e(r) \qquad (0 \le r \le R_w) \tag{4.17}$$

According to Poisson's equation (Hunter, 1981)

$$-\frac{\rho_e(r)}{\varepsilon_r \varepsilon_0} = \frac{1}{r}\frac{d}{dr}\left[r\frac{d\psi_w(r)}{dr}\right] \tag{4.18}$$

Substituting Eq. (4.18) into Eq. (4.17) gives

$$\frac{1}{r}\frac{r}{dr}\left[r\frac{d(u_{Dw} - \eta\psi_w)}{dr}\right] - \beta^2 u_{Dw} = 0 \tag{4.19}$$

where

$$\eta = \frac{\phi_\infty^2 \tau \varepsilon_r \varepsilon_0 E_0}{\mu} \qquad \beta = \sqrt{\frac{a\tau(1-\phi_\infty)^2}{\phi_\infty d_p^2}} \tag{4.20}$$

Introducing

$$v = u_{Dw} - \eta\psi_w \tag{4.21}$$

Eq. (4.19) becomes

$$\frac{1}{r}\frac{d}{dr}\left(r\frac{dv}{dr}\right) - \beta^2 v = \beta^2 \eta \psi_w \tag{4.22}$$

Under the Debye-Hückel approximation, it has been shown that (Rice and Whitehead, 1965)

$$\psi_w(r) = \zeta_w \frac{I_0(\kappa r)}{I_0(\kappa R_w)} \tag{4.23}$$

Hence Eq. (4.22) can be rewritten as

$$\frac{1}{r}\frac{d}{dr}\left(r\frac{dv}{dr}\right) - \beta^2 v = \beta^2 \eta \zeta_w \frac{I_0(\kappa r)}{I_0(\kappa R_w)} \tag{4.24}$$

This is a non-homogeneous zero-order modified Bessel equation, subject to the boundary conditions

$$\left.\frac{dv}{dr}\right|_{r=0} = 0 \tag{4.25a}$$

$$v\big|_{r=R_w} = -\eta\zeta_w \tag{4.25b}$$

A homogeneous solution and a particular solution to Eq. (4.24) is given respectively by

$$v_0(r) = -\frac{\kappa^2}{\kappa^2 - \beta^2}\eta\zeta_w \frac{I_0(\beta r)}{I_0(\beta R_w)} \tag{4.26a}$$

$$v_p(r) = \frac{\beta^2}{\kappa^2 - \beta^2}\eta\zeta_w \frac{I_0(\kappa r)}{I_0(\kappa R_w)} \tag{4.26b}$$

The general solution to Eq. (4.24) is

$$v(r) = v_0(r) + v_p(r) = -\frac{\kappa^2}{\kappa^2 - \beta^2}\eta\zeta_w \frac{I_0(\beta r)}{I_0(\beta R_w)} + \frac{\beta^2}{\kappa^2 - \beta^2}\eta\zeta_w \frac{I_0(\kappa r)}{I_0(\kappa R_w)} \tag{4.27}$$

Making use of Eq. (4.21) and Eq. (4.23), we can obtain an analytical solution for the EOF velocity distribution in a charged microchannel packed with neutrally charged microspheres

$$u_{Dw}(r) = v(r) + \eta\psi_w(r) = -\frac{\varepsilon_r\varepsilon_0}{\mu}E_0\zeta_w\phi_\infty^2\tau\frac{\kappa^2}{\kappa^2 - \beta^2}\left[\frac{I_0(\beta r)}{I_0(\beta R_w)} - \frac{I_0(\kappa r)}{I_0(\kappa R_w)}\right] \tag{4.28}$$

4.4.4 Slip velocity approximation based solution to the modified Brinkman momentum equation Eq. (4.12)

Considering a large channel size, the momentum equation can be further simplified by applying the slip velocity approximation, in which the EDL thickness is ignored. In this situation the boundary velocity at the channel wall is determined by Smoluchowski equation (Probstein, 1994). Thus Eq. (4.19) is reduced to

$$\frac{1}{r}\frac{r}{dr}\left[r\frac{du_{Dw}}{dr}\right] - \beta^2 u_{Dw} = 0 \tag{4.29}$$

subject to boundary conditions

$$\left.\frac{du_{Dw}}{dr}\right|_{r=0} = 0 \tag{4.30a}$$

$$u_{Dw}\big|_{r=R_w} = -\frac{\varepsilon_r\varepsilon_0}{\mu}E_0\zeta_w \tag{4.30b}$$

Solution to Eq. (4.29) can be readily obtained as

$$u_{Dw}(r) = -\frac{\varepsilon_r\varepsilon_0}{\mu}E_0\zeta_w\frac{I_0(\beta r)}{I_0(\beta R_w)} \tag{4.31}$$

4.5 Overall Macroscopic EOF Velocity

We re-couple the two velocity components from the charged wall and the charged packing particles, and obtain the overall macroscopic EOF velocity in a charged cylindrical microcapillary with charged microsphere packing. The excess zeta potential is taken into account by such a treatment that the zeta potential of the capillary wall is replaced by (ζ_w - ζ_p), which is responsible for the electrokinetic wall effect (Liapis and Grimes, 2001).

$$u_D = u_{Dw}\left(1-\frac{\zeta_p}{\zeta_w}\right)+u_{Di} \tag{4.32}$$

Specifically, in the case when $\zeta_w = \zeta_p$, Eq. (4.32) is reduced to $u_D = u_{Di}$, indicating no electrokinetic wall effect.

4.6 Results and Discussion

The mathematical models governing the EOF in a microchannel packed with microspheres have been developed. In this section we will study how the EOF in a packed microcapillary is affected by the geometrical and electrokinetic parameters. In calculation, the following parameters are bounded as: ionic strength 7.5 μM, fluid viscosity 1.0×10^{-3} kg $m^{-1}s^{-1}$, density 998 kg m^{-3}, dielectric constant 6.9×10^{-10} $CV^{-1}m^{-1}$, and corresponding Debye length, 0.11 μm, ($\lambda_D = 1/\kappa$, $\kappa = \sqrt{\frac{2n_0e_0^2}{\varepsilon_r\varepsilon_0k_bT}}$), which is the characteristic thickness of the EDL regime. Other fixed parameters are: zeta potential –100 mV, porosity 0.37, and tortuosity 1.5. For all of the case studies, the reference velocity is $u_0=-\varepsilon_r\varepsilon_0E_0\zeta_0/\mu$, where E_0=300 V/cm and

$\zeta_0 = -100$ mV.

In the following, the results under three different approaches: the complete numerical solution of Eq. (4.12), the analytical solution based on Eq. (4.28), and the slip velocity approximation based on Eq. (4.31) will be compared.

Figure 4-3(a-c) shows the electrokinetic wall effects for a given particle size d_p = 5 μm under different charge conditions of the capillary wall. The wall zeta potentials are chosen to vary from positive to negative, relative to the polarity of the particle zeta potential. According to Eq. (4.32), it can be readily understood that when the zeta potential ratio, ζ_w/ζ_p=1, there is no electrokinetic wall effect. The velocity distributions exhibit a uniform profile (i.e., a straight horizontal line) along the cross-sectional area. We also can further infer that at such situation, this homogeneous velocity is equal to $u_{Di.}$ The prediction results in Figure 4-3(a-b) show that when the capillary wall is more negatively charged than the particles, i.e., ζ_w/ζ_p >1, the EOF close to the wall is enhanced. In these cases, the EOF velocity starts to increase from u_{Di} on the wall to a maximum velocity, and then decreases to u_{Di} at the location around $0.98R_w$. The local enhancement is due to the interaction between the applied electric field and the excessive EDL potential, which is limited within a region of several Debye lengths from the wall. In our calculation, the portion where the enhanced EOF occurs is limited in an annular region with thickness of around 0.75 μm, i.e., about 7 times of Debye lengths. Beyond this regime, the fluid remains uniform. This velocity enhancement by the channel wall cannot extend to the rest portion of the channel because the presence of packing particles causes the fractional force between the fluid and the surface of packing particles. This trend was experimentally verified by Tallarek *et al*. (2001). They used the pulsed field gradient nuclear magnetic resonance (PFG-NMR) and NMR imaging techniques to study the electroosmotic

flow in packed capillaries. It was reported that higher EOF close to the capillary wall is detected when the channel wall is more negatively charged than the particles. Furthermore, it can be predicted on the basis of the present model that when the capillary wall is less negatively charged than the particles ($0<\zeta_w/\zeta_p<1$), neutral ($\zeta_w=0$), or positively charged ($\zeta_w>0$), the EOF close to the capillary wall becomes weakened, even leading to change of flow direction.

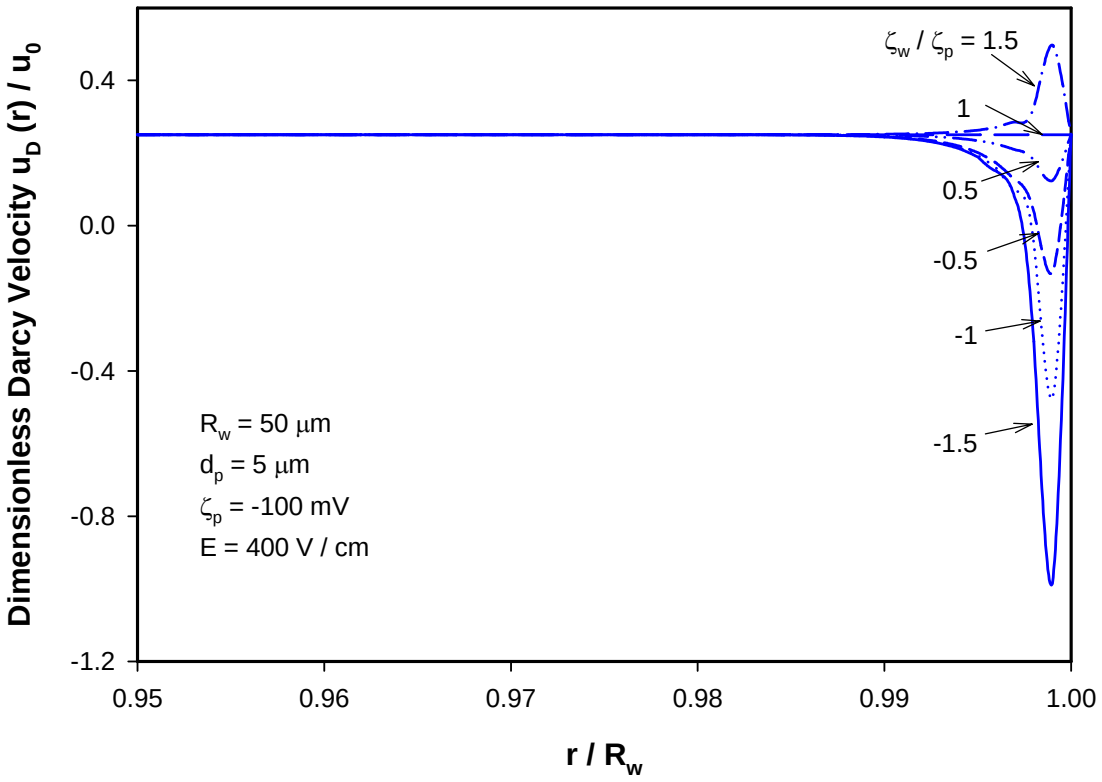

Figure 4-3 (a)

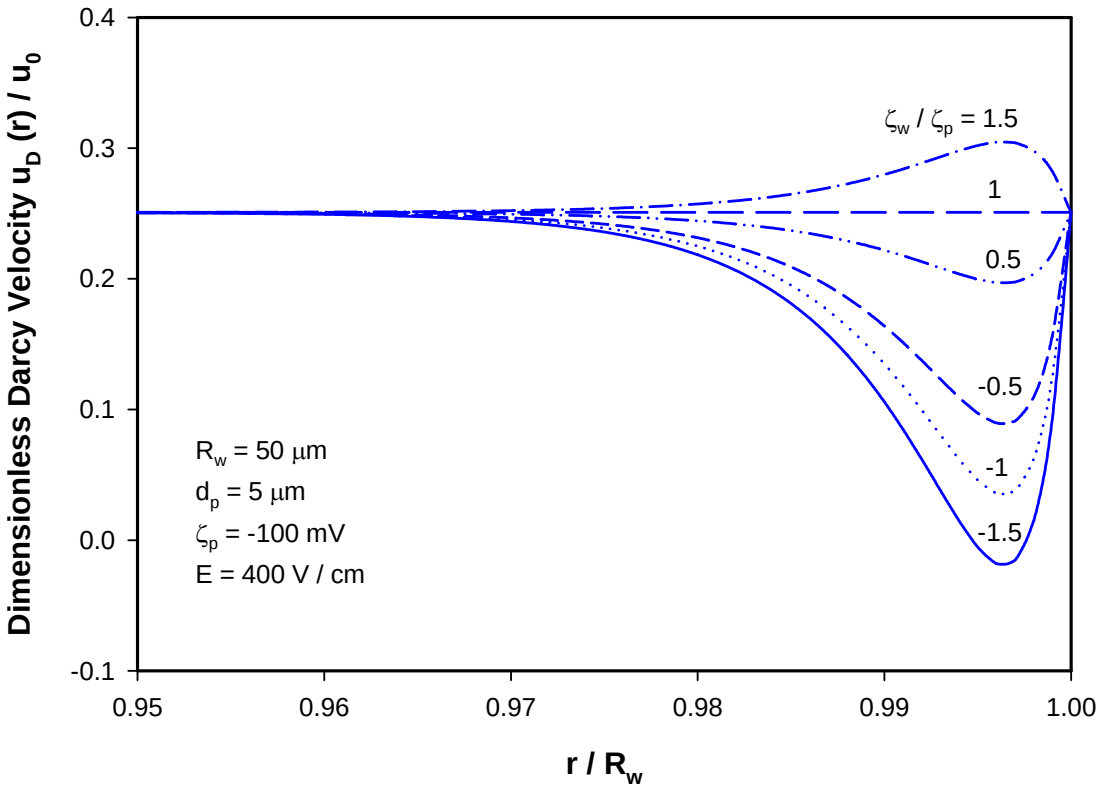

Figure 4-3 (b)

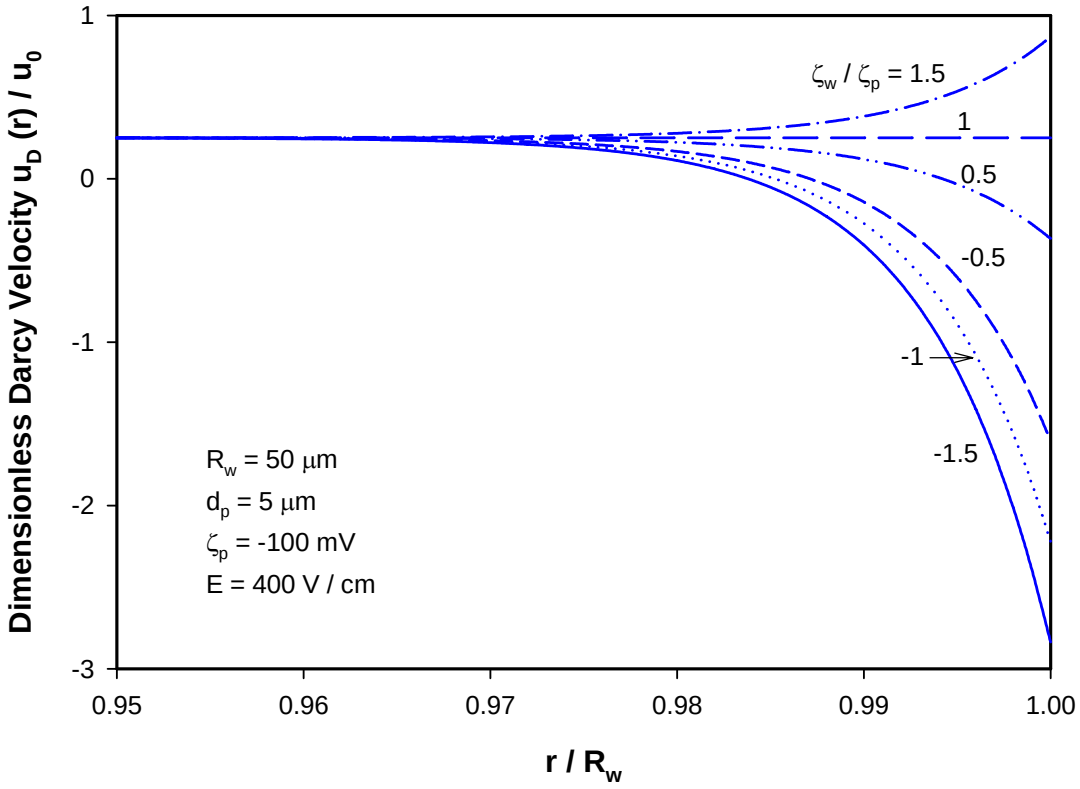

Figure 4-3 (c)

Figure 4-3 Electroosmotic flow velocity distributions in a charged microcapillary packed with charged microspheres, for different values of zeta potential ratio, ζ_w/ζ_p. The results are obtained on the basis of a) the numerical solution of Eq. (4.12); b) the analytical solution based on Eq. (4.28); c) the slip velocity approximation based on Eq. (4.31). Reference velocity $u_0 = -\frac{\varepsilon_r \varepsilon_0}{\mu} E_0 \zeta_0$, where E_0 = 300 V/cm and ζ_0 = -100 mV.

Comparison of Figure 4-3(a-c) shows that at the center region of the capillary, the three methods give nearly the same results for velocity distributions, while adjacent to the charged channel wall the discrepancy is observed. It is demonstrated that the enhanced regime under the analytical solution (i.e., Eq. (4.28)) or the slip velocity approximation (i.e., Eq. (4.31)) is wider than that under the complete numerical solution of Eq. (4.12). The discrepancy is due to the Debye-Hückel approximation used in derivation of the solutions given by Eq. (4.28) and Eq. (4.31). It has been shown (Kang *et al.*, 2002) that use of the Debye-Hückel approximation usually over-estimates the EDL region nearby the charged wall, and thus the affected area by the excessive zeta potential becomes larger. Further, the difference between the result of the slip velocity approximation (i.e., Eq. (4.31)) and that obtained from either the numerical method (Eq. (4.12)) or the analytical solution (i.e., Eq. (4.28)) is resulted from the assumption of the moving boundary condition. In the slip velocity approximation, the boundary velocity is assumed to be proportional to the electric field (refer to Eq. (4.30b)), while the zero (no-slip) boundary velocities are used in both the numerical solution of Eq. (4.12) and the analytical solution based on Eq. (4.28). Nonetheless, evaluation of Figure 4-3(a-c) indicates that compared to the complete numerical solution of Eq. (4.12), the analytical solution (Eq. (4.28)) under-estimates the electrokinetic wall effect while the slip velocity approximation (Eq. (4.31)) over-estimates the electrokinetic wall effect.

Figure 4-4 shows the size effect of the packing particles on the EOF in a packed capillary. In calculation, three different sizes of spherical particles with diameter of 2, 5, and 8 μm are considered. Two typical conditions are presented: with wall effect (ζ_w/ζ_p=1.5) and no wall effect (ζ_w/ζ_p=1). As discussed earlier, if there is no wall effect, the velocity exhibits a uniform profile along the channel radius. In this situation, use of larger packing particles can

generate a higher uniform velocity u_{Di}. This is because, according to Eq. (4.2), the intraparticle pore size increases with increasing the packing particle size. Moreover, the value of G in Eq. (4.7), which denotes the average EDL potential inside the intraparticle pore, decreases with increasing the pore size. Thus the EOF velocity inside larger packing particles is higher. In terms of the wall effect, larger packing particles can generate stronger enhancement of local EOF velocity in the vicinity of the capillary wall. This can be explained that the void space between the particles is larger for larger particle sizes. Thus the drag force of the packing particles should be smaller.

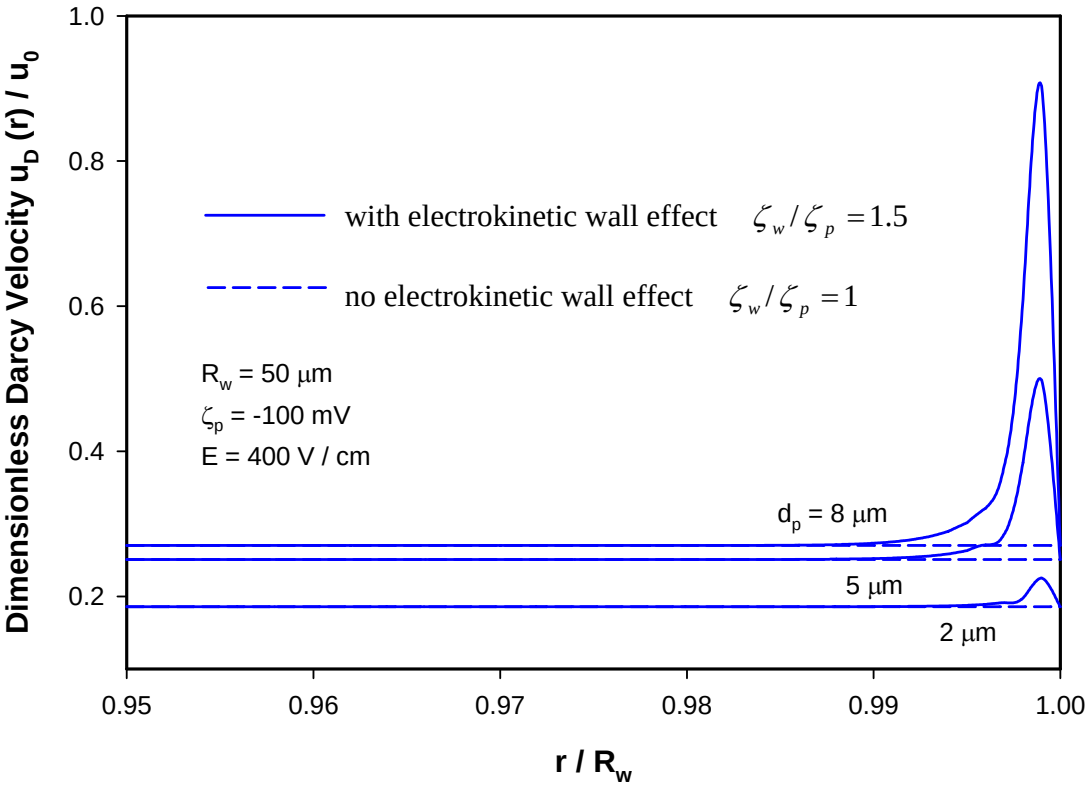

Figure 4-4 (a)

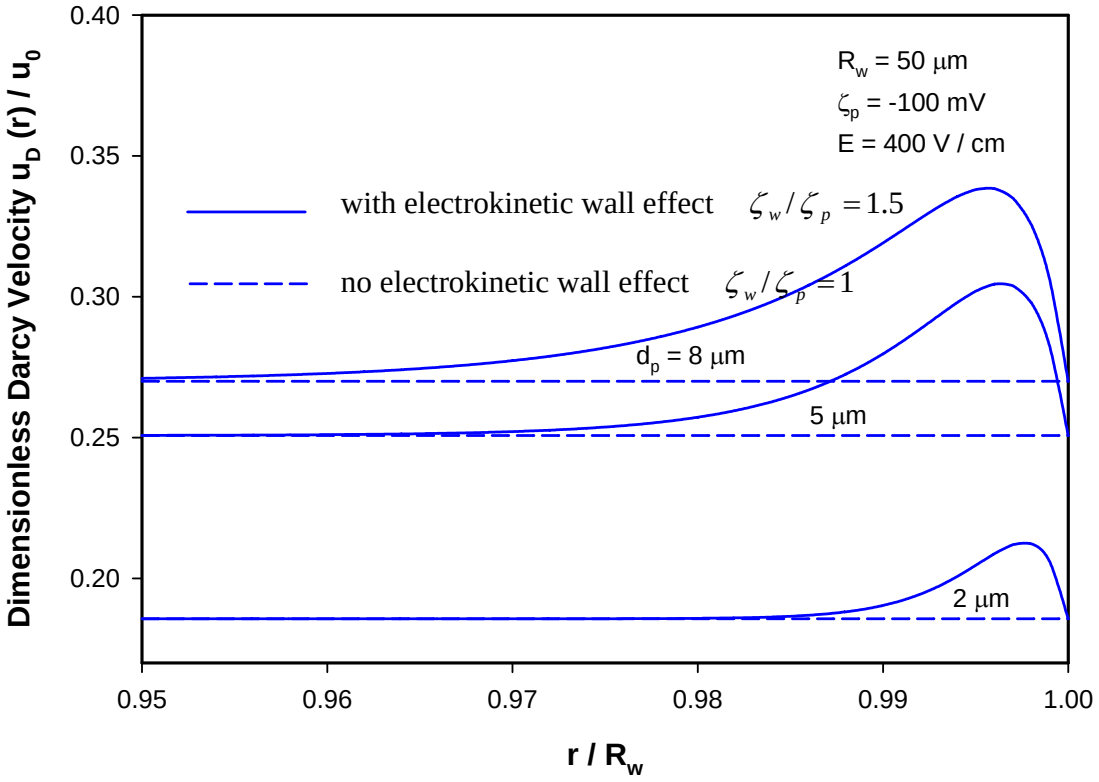

Figure 4-4 (b)

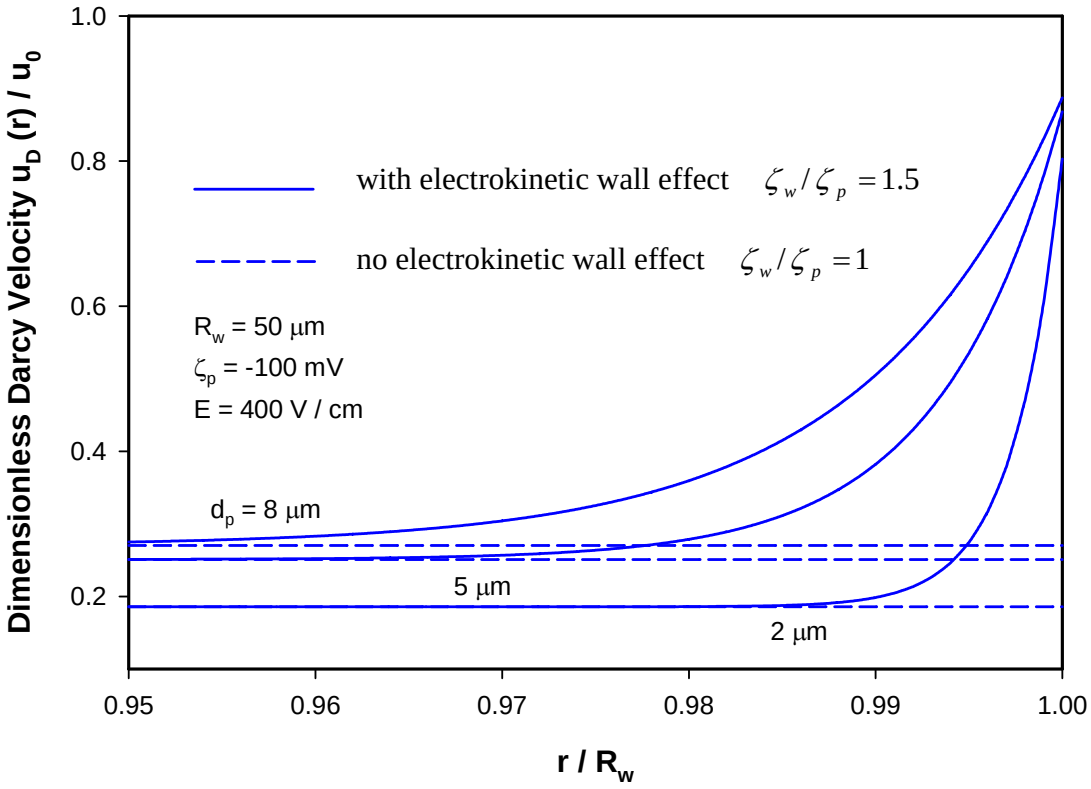

Figure 4-4 (c)

Figure 4-4 Electroosmotic flow velocity distributions in a charged microcapillary packed with charged microspheres, for different sizes of packing particles, d_p. The results are obtained on the basis of a) the numerical solution of Eq. (4.12); b) the analytical solution based on Eq. (4.28); c) the slip velocity approximation based on Eq. (4.31). Reference velocity is the same as in Figure 4-3.

In Figure 4-5 the EOF velocity in charged porous media is demonstrated under different applied voltages. It is noted that the velocity increases linearly with increasing voltage. This is due to the presence of the local EDL of the charged particle surface. In the middle portion of the channel where no electrokinetic wall effect is present, we can infer from Eq. (4.32) that the local Darcy velocity should be u_{Di}, which is proportional to the external electric field according to Eq. (4.7). However close to the channel wall, both the numerical solution of Eq. (4.12) and the analytical solution (Eq. (4.28)) show that the EOF velocity increases to a maximum and then decreases to the original value at the wall. This is because in the EDL region close to the wall, the excessive wall zeta potential further enhances the electroosmosis.

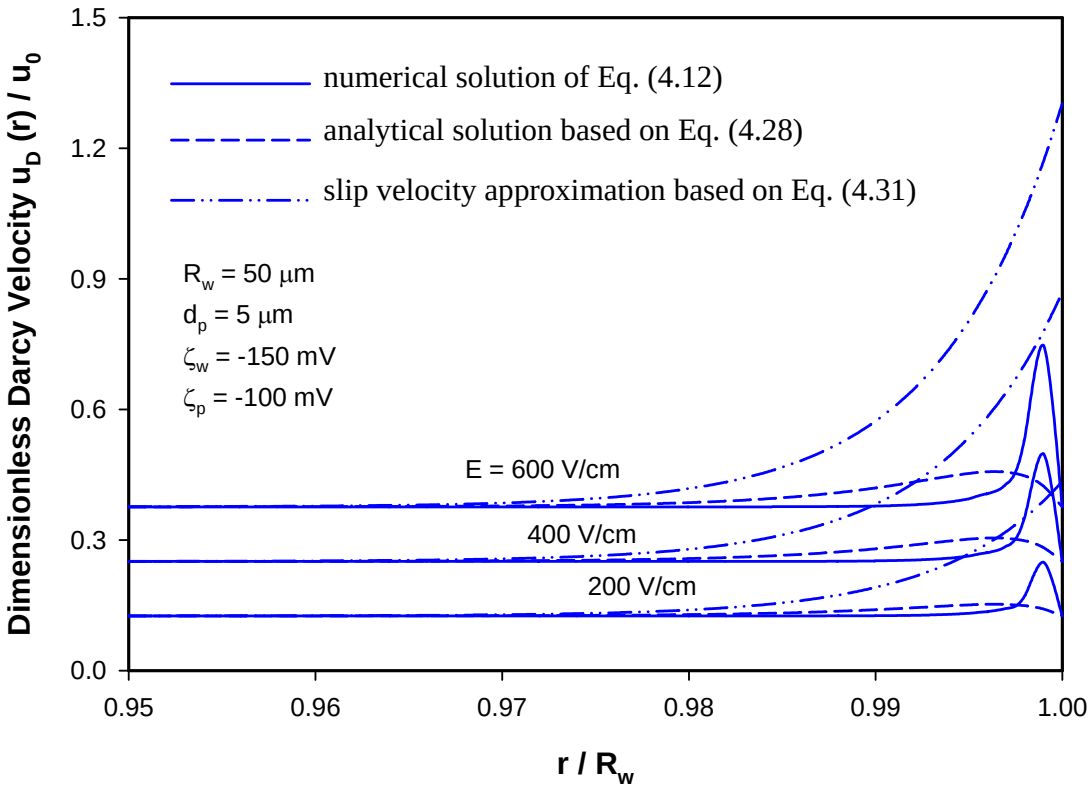

Figure 4-5 Electroosmotic flow velocity distributions in a charged microcapillary packed with charged microspheres, for different electric field strengths, *E*. Reference velocity is the same as in Figure 4-3.

Otherwise we can expect the velocity to be uniform throughout the entire cross-section of the channel if the zeta potential of the wall is the same as that of the particle surface. For the same reason discussed above, the slip velocity approximation (Eq. (4.31)) gives different results because the moving boundary velocity is used.

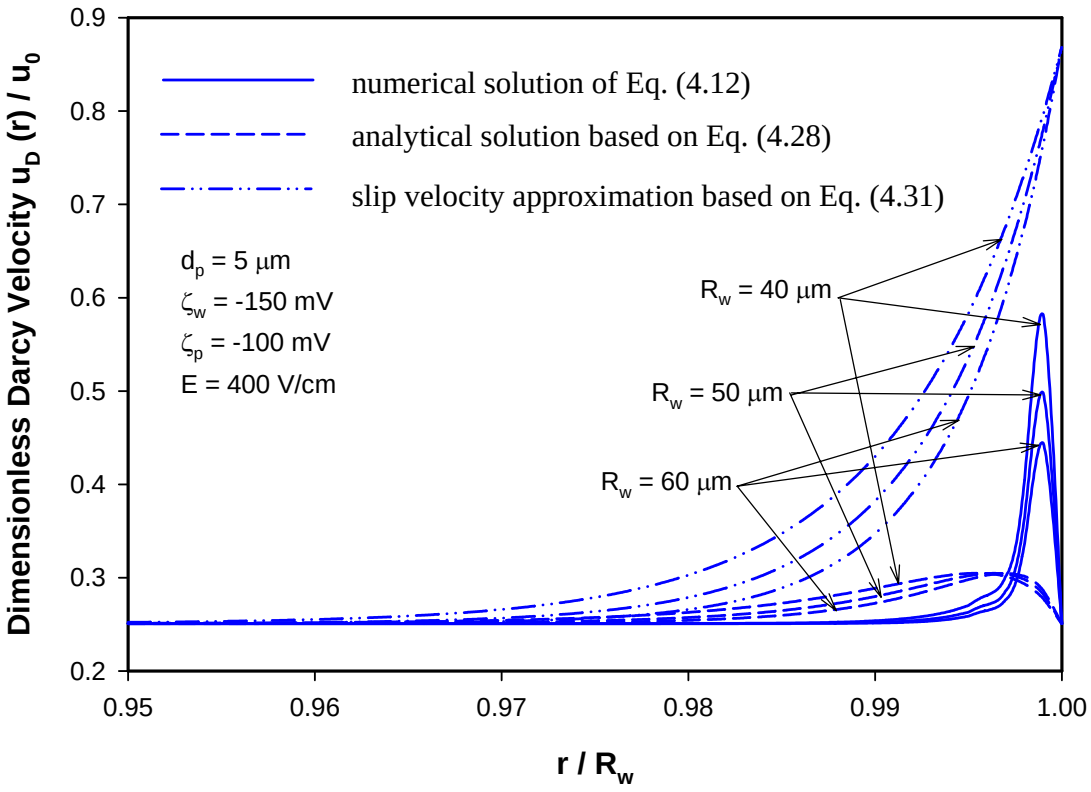

Figure 4-6 Electroosmotic flow velocity distributions in a charged microcapillary packed with charged microspheres, for different channel sizes, R_w. Reference velocity is the same as in Figure 4-3.

The velocity distributions for the same packing particles in different channel sizes are shown in Figure 4-6. It is clear that the channel size dose not affect the velocity magnitude in center region of the channel. This is expected because the EOF velocity is only dependent on the pore size at the channel center where the packing condition is homogeneous and no

electrokinetic wall effect is present. Since the size of the packing particles is the same, the pore size is also the same, and hence the homogeneous velocity should keep unchanged. The channel size effect due to the excessive zeta potential only exists in the excessive EDL region close to the wall. In calculation the Debye length, λ_D, which measures thickness of the excessive EDL potential, keeps constant, and thus for a smaller channel, the region where enhanced EOF is observed extends relatively further away from the wall.

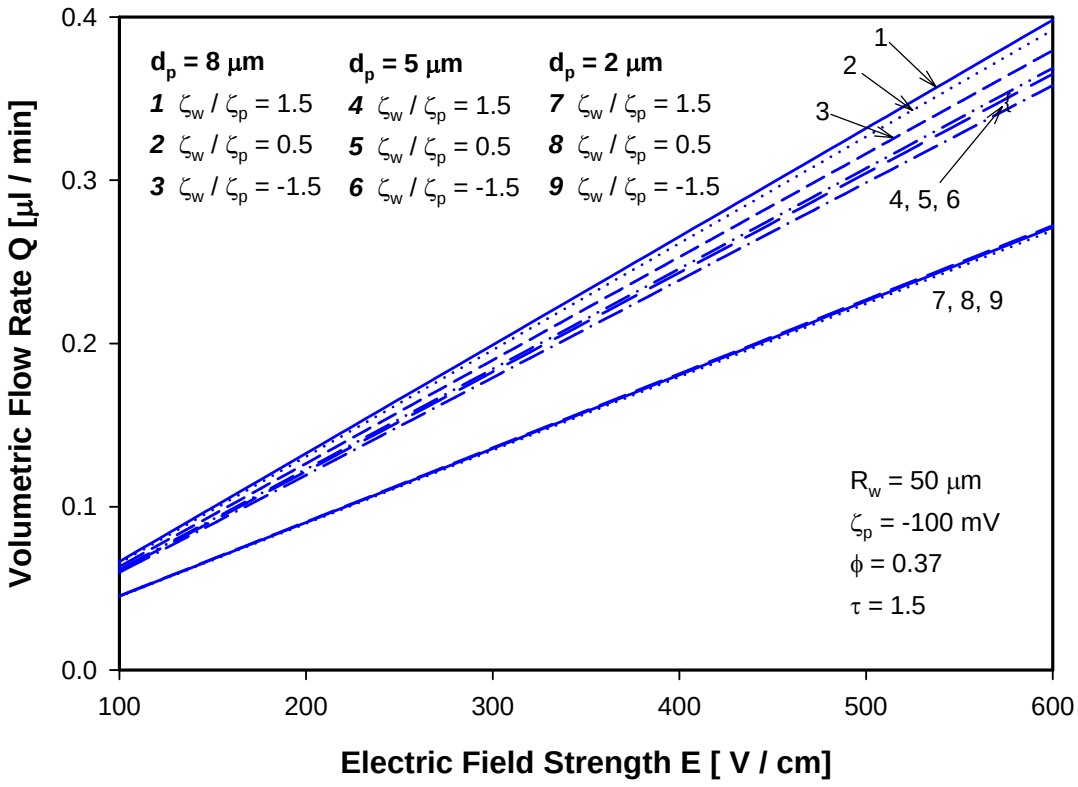

Figure 4-7 Electroosmotic flow rate versus applied electric field for different values of particle diameter, d_p, and zeta potential ratio, ζ_w / ζ_p.

Of practical interest for micropumps, we also study the effect of the channel wall and packing particles on the overall electroosmotic flow rate in a microcapillary. Flow rate versus applied external electric field, for different packing particle size and the zeta potential ratio,

ζ_w/ζ_p is plotted in Figure 4-7. It is noted that the flow rate increases linearly with increasing applied voltage. For larger packing particles the flow rate is always higher. This is because of the same reason that larger packing particles can generate higher velocity as shown in Figure 4-4. For a given packing structure, the flow rate slightly increases when $\zeta_w/\zeta_p > 1$, and decreases when $\zeta_w/\zeta_p < 1$, which is due to the electrokinetic wall effect.

4.7 Summary

A mathematical model has been developed to quantitatively describe the electroosmotic flow in a charged microcapillary packed with charged microspheres. The model is based on the *Carman-Kozeny theory*, which assumes the porous medium to be equivalent to a series of parallel tortuous tubules. The interstitial tubular velocity is obtained by solving the Navier-Stokes equation and the Poisson-Boltzmann equation. The Brinkman macroscopic momentum equation is modified for describing electroosmotic flow in a porous medium, and it is solved using three different methods: (i) the numerical method, (ii) the analytical solution, and (iii) the slip velocity approximation to take into account the electrokinetic wall effect. It is demonstrated that the enhanced regime under the analytical solution (i.e., Eq. (4.28)) or the slip velocity approximation (i.e., Eq. (4.31)) is wider than that under the complete numerical solution of Eq. (4.12). It is also found that compared to the complete numerical solution of Eq. (4.12), the analytical solution (Eq. (4.28)) under-estimates the electrokinetic wall effect while the slip velocity approximation (Eq. (4.31)) over-estimates the electrokinetic wall effect.

It is shown that the EOF in a charged microcapillary packed with charged microparticles is

affected by several parameters: the property of the working fluid, which determines the thickness of the EDL; the porosity and tortuosity of the porous packing; the size of the capillary and packing particles; the charge condition of the particle and capillary surfaces. The electrokinetic wall effect is stronger if the size of packing particles is comparable to that of the microcapillary. Furthermore, when the capillary wall is more negatively charged than the particles ($\zeta_w / \zeta_p > 1$), the EOF close to the capillary wall gets enhanced; otherwise, when the capillary wall is less negatively charged than the particles ($0 < \zeta_w / \zeta_p < 1$), neutral ($\zeta_w = 0$), or positively charged ($\zeta_w > 0$), the EOF close to the capillary wall becomes weakened, even leading to a change of flow direction.

Chapter 5

AC Electroosmotic Flow in a Microchannel Packed with Microspheres

5.1 Introduction

The interest to the AC electroosmosis lies in its potential application in microfluidic devices for mixing (Oddy *et al*., 2001)) and sample manipulation (Minerick *et al*., 2003). Some studies have been reported on the AC electroosmosis in non-packed microcapillaries. However, no study has been done on the AC electroosmosis in a microcapillary packed with a porous medium. This chapter serves as an attempt to investigate the dynamic response of the EOF in a cylindrical microcapillary packed with microspheres to AC electric field. Two different conditions regarding the openness of channel ends are considered. When the channel is open, i.e., both ends are connected to two reservoirs and subject to the ambient pressure, the oscillating electroosmotic flow is analyzed using the capillary flow model as employed in chapter 4. When the two capillary ends are closed, the AC electroosmotic flow is balanced by the oscillating counter-flow, resulting in zero net flow rate. The counter-flow is due to the generated backpressure. The dynamic aspect of the induced backpressure is analyzed by solving the modified Brinkman momentum equation.

Consider a cylindrical microcapillary densely packed with charged spherical microparticles of diameter, d_p, as illustrated in Figure 5-1. The zeta potential of microparticles is ζ_p. The

liquid flowing through the porous structure is assumed to be an incompressible, Newtonian, monovalence electrolyte of density, ρ, and viscosity, μ. In normal applications for electroosmotic pumping, the ratio of the capillary diameter to the packing particles' diameter is larger than 50, i.e., $d_c/d_p \geq 50$ (Zeng *et al.*, 2001). Thus according to Tallarek *et al*. (2001), the entire porous medium can be assumed to be homogeneous and the capillary wall effects can be safely neglected. The AC electroosmotic flow in both open-end and closed-end microcapillaries will be discussed.

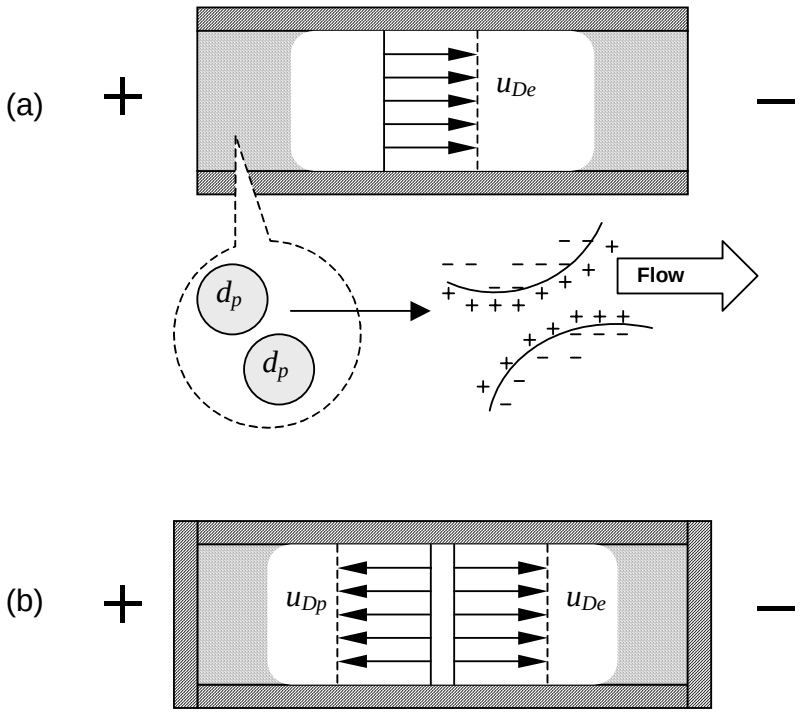

Figure 5-1 Schematic illustrations of the AC electroosmotic flow in a porous medium. (a) flow in a packed microcapillary connected with two reservoirs. (b) flow in a packed microcapillary with two closed ends. Where u_{De} is the filter (Darcy) velocity due to electroosmosis, and u_{Dp} is the filter (Darcy) velocity due to backpressure.

5.2 Flow in a Packed Microchannel Connected to Two Open Reservoirs

In this situation, the flow is sorely electroosmosis-driven and no pressure gradient is present. We use the so-called capillary model, also known as the *Carman-Kozeny theory* (Kaviany, 1995), in which the porous medium is assumed to be equivalent to a series of parallel tortuous tubules with an effective pore size $d_{pore} = 2R_{pore} = \frac{2\phi}{3(1-\phi)} d_p$, where ϕ is the porosity of the porous medium. The motion of liquid through the cylindrical tubules is governed by the Navier-Stokes equation (Probstein, 1994)

$$\rho \frac{\partial u(r,t)}{\partial t} - \mu \frac{1}{r} \frac{\partial}{\partial r} \left[r \frac{\partial u(r,t)}{\partial r} \right] = E(t) \rho_e(r) \qquad (0 \le r \le R_{pore}) \tag{5.1}$$

where $u(r, t)$ is the transient velocity field. $\rho_e(r)$ is the local volumetric net charge density due to the presence of the EDL, and is assumed to be governed by the Boltzmann distribution (Hunter, 1981),

$$\rho_e(r) = -2 n_0 e_0 \sinh \left[\frac{e_0 \psi(r)}{k_b T} \right] \qquad (0 \le r \le R_{pore}) \tag{5.2}$$

where e_0 is the elementary charge, n_0 is the ionic concentration in the bulk liquid phase (i.e., far from the charged surfaces), k_b is the Boltzmann constant, T is the absolute temperature, and $\psi(r)$ is the electrostatic potential of the EDL.

Introducing the following dimensionless parameters:

$$\bar{u} = \frac{u}{u_s} \qquad \bar{t} = \frac{t}{t_{diff}} \qquad \bar{r} = \frac{r}{R_{pore}} \qquad \Psi = \frac{e_0 \psi}{k_b T} \tag{5.3}$$

(where the reference time $t_{diff} = \rho R_{pore}^2 / \mu$ is the time scale of viscous diffusion across a length of R_{pore}), we can nondimensionlize Eq. (5.1) and Eq. (5.2) respectively as

$$\frac{\partial \bar{u}}{\partial \bar{t}} - \frac{1}{\bar{r}}\frac{\partial}{\partial \bar{r}}\left(\bar{r}\frac{\partial \bar{u}}{\partial \bar{r}}\right) = \frac{R_{pore}^2}{\mu u_s}\rho_e(\bar{r})E(\bar{t}) \tag{5.4}$$

and

$$\rho_e(\bar{r}) = -2n_0 e_0 \sinh[\Psi(\bar{r})] \tag{5.5}$$

Here u_s is the reference velocity defined as

$$u_s = -\frac{\varepsilon_r \varepsilon_0}{\mu} E_0 \zeta_p \tag{5.6}$$

where ε_r is the dielectric constant of the electrolyte and ε_0 is the permittivity of vacuum.

Substituting Eq. (5.5) into Eq. (5.4), we obtain

$$\frac{\partial \bar{u}}{\partial \bar{t}} - \frac{1}{\bar{r}}\frac{\partial}{\partial \bar{r}}\left(\bar{r}\frac{\partial \bar{u}}{\partial \bar{r}}\right) = \frac{(\kappa R_{pore})^2}{\Psi_s E_0}\sinh\left[\Psi(\bar{r})\right]E(\bar{t}) \tag{5.7}$$

where $\Psi_s = \dfrac{e_0\zeta_p}{k_b T}$ and $\kappa = \sqrt{\dfrac{2n_0 e_0^2}{\varepsilon_r \varepsilon_0 k_b T}}$. κ is the Debye-Hückel parameter, and $1/\kappa$ denotes the characteristic thickness of the EDL. Eq. (5.7) is subject to the initial and boundary conditions

$$\bar{u}(\bar{t}=0) = 0 \tag{5.8a}$$

$$\left.\frac{\partial \bar{u}}{\partial \bar{r}}\right|_{\bar{r}=0} = 0 \qquad\qquad \bar{u}(\bar{r}=1) = 0 \tag{5.8b}$$

Using the Green's function method as detailed in chapter 2, we can obtain the solution to Eq. (5.7), subject to the homogeneous boundary condition specified in Eq. (5.8b), as

$$\bar{u}(\bar{r},\bar{t}) = \int_{\tau=0}^{\bar{t}}\int_{\xi=0}^{1} G(\bar{r},\bar{t}\,|\,\xi,\tau)\left\{\frac{(\kappa R_{pore})^2}{\Psi_s E_0}\sinh\left[\Psi(\xi)\right]E(\tau)\right\}d\xi\, d\tau \tag{5.9}$$

where $G(\bar{x},\bar{t};\xi,\tau)$ is the specified Green's function which can be expressed as (Kang *et al.*, 2002),

$$G(\bar{r},\bar{t}\,|\,\xi,\tau) = H(\bar{t}-\tau)\sum_{n=1}^{\infty}\frac{2\,J_0(\lambda_n\bar{r})}{J_1^2(\lambda_n)}\xi\,J_0(\lambda_n\,\xi)\exp[-\lambda_n^2(\bar{t}-\tau)] \tag{5.10}$$

where λ_n is the positive root of the zero-order Bessel function $J_0(\lambda_n) = 0$, and $H(\bar{t}-\tau)$ is the Heaviside step function. Substituting Eq. (5.10) into Eq. (5.9) gives

$$\bar{u}(\bar{r},\bar{t}) = \frac{2(\kappa R_{pore})^2}{\Psi_s}\sum_{n=1}^{\infty}C_n\frac{J_0(\lambda_n\bar{r})}{J_1^2(\lambda_n)}\int_{\tau=0}^{\bar{t}}\frac{1}{E_0}E(\tau)\exp[-\lambda_n^2(\bar{t}-\tau)]d\tau \tag{5.11}$$

where $C_n = \int_{\xi=0}^{1}\xi\,J_0(\lambda_n\xi)\sinh\left[\Psi(\xi)\right]d\xi$. Integrating Eq. (5.11) along the radius of the cylindrical tubule, we obtain the non-dimensional mean velocity in each tubule

$$\bar{u}_m(\bar{t}) = 2\int_{\bar{r}=0}^{1}\bar{r}\,\bar{u}(\bar{r},\bar{t})\,d\bar{r} = \frac{4(\kappa R_{pore})^2}{\Psi_s}\sum_{n=1}^{\infty}\frac{C_n}{\lambda_n J_1(\lambda_n)}\int_{\tau=0}^{\bar{t}}\frac{1}{E_0}E(\tau)\exp[-\lambda_n^2(\bar{t}-\tau)]d\tau \tag{5.12}$$

Consider the application of a sinusoidally alternating electric field with an angle frequency ω

$$E(t) = E_0 e^{i\omega t} \tag{5.13}$$

Substituting Eq. (5.13) into Eq. (5.11), we can show next

$$\begin{aligned}\bar{u}(\bar{r},\bar{t}) &= REAL\left[\frac{2(\kappa R_{pore})^2}{\Psi_s}\sum_{n=1}^{\infty}C_n\frac{J_0(\lambda_n\bar{r})}{J_1^2(\lambda_n)}\frac{\exp(i\beta^2\bar{t})-\exp(-\lambda_n^2\bar{t})}{\lambda_n^2+i\beta^2}\right]\\ &= \frac{2(\kappa R_{pore})^2}{\Psi_s}\sum_{n=1}^{\infty}C_n\frac{J_0(\lambda_n\bar{r})}{J_1^2(\lambda_n)}\frac{\lambda_n^2\cos(\beta^2\bar{t})+\beta^2\sin(\beta^2\bar{t})-\lambda_n^2\exp(-\lambda_n^2\bar{t})}{\lambda_n^4+\beta^4}\end{aligned} \tag{5.14}$$

where i is the unit imaginary number. "*REAL*" denotes the real part of the solution. Here a new parameter β is defined as (Kang *et al.*, 2002)

$$\beta = \frac{R_{pore}}{\delta_s} \tag{5.15}$$

β represents the aspect ratio of the tubule radius R_{pore} to the Stokes penetration depth δ_s, defined as

$$\delta_s = \sqrt{\frac{\mu}{\rho\omega}} = \sqrt{\frac{\mu}{2\pi\rho f}} \tag{5.16}$$

where $f = \omega / 2\pi$ is the frequency of the applied electric field.

Accordingly, the mean velocity can be obtained from Eq. (5.14) as

$$\bar{u}_m(\bar{t}) = \frac{4(\kappa R_{pore})^2}{\Psi_s} \sum_{n=1}^{\infty} \frac{C_n}{\lambda_n J_1(\lambda_n)} \frac{\lambda_n^2 \cos(\beta^2 \bar{t}) + \beta^2 \sin(\beta^2 \bar{t}) - \lambda_n^2 \exp(-\lambda_n^2 \bar{t})}{\lambda_n^4 + \beta^4} \tag{5.17}$$

Under the volume averaging method as described in chapter 4, the macroscopic filter velocity (the Darcy velocity) of the fluid due to electroosmosis can be expressed as the mean velocity in each tubule taking into account of the tortuosity τ and the porosity ϕ, as

$$\begin{aligned} \bar{u}_{De}(\bar{t}) &= \frac{\phi}{\tau} \bar{u}_m(\bar{t}) \\ &= \frac{\phi}{\tau} \frac{4(\kappa R_{pore})^2}{\Psi_s} \sum_{n=1}^{\infty} \frac{C_n}{\lambda_n J_1(\lambda_n)} \frac{\lambda_n^2 \cos(\beta^2 \bar{t}) + \beta^2 \sin(\beta^2 \bar{t}) - \lambda_n^2 \exp(-\lambda_n^2 \bar{t})}{\lambda_n^4 + \beta^4} \end{aligned} \tag{5.18}$$

Combining Eqs. (5.15), (5.16), and (5.18), we can further obtain the expression of the frequency-dependent maximum Darcy velocity,

$$\left|\bar{u}_{De}\right|_{\max}(f) = \frac{\phi}{\tau} \frac{4(\kappa R_{pore})^2}{\Psi_s} \sum_{n=1}^{\infty} \frac{C_n}{\lambda_n J_1(\lambda_n)} \frac{1}{\sqrt{\lambda_n^4 + \beta^4}} \tag{5.19}$$

According to Eqs. (5.18) and (5.19), it shows that the electroosmotic Darcy velocity is proportional to the porosity and inversely proportional to the tortuosity of a porous medium.

In case of an applied DC electric field, i.e., $f = 0$, thus $\beta = 0$, Eq. (5.18) reduces to

$$\bar{u}_{De}(\bar{t}) = \frac{\phi}{\tau} \frac{4(\kappa R_{pore})^2}{\Psi_s} \sum_{n=1}^{\infty} \frac{C_n}{\lambda_n^3 J_1(\lambda_n)} \left[1 - \exp(-\lambda_n^2 \bar{t})\right] \tag{5.20}$$

Physically Eq. (5.20) denotes the time developing of the transient electroosmotic flow after application of a DC electric field.

5.3 Flow in a Packed Microchannel with Closed Ends

In a closed-end microcapillary, the electroosmotic flow induces a backpressure gradient. The backpressure gradient in turn generates a counter-flow to balance the electroosmotic volume flow, resulting in a zero flow rate. In porous media, no matter the flow is pressure-driven or electroosmosis-driven, the fluid velocity is represented by a uniform filter (Darcy) velocity u_D. Thus to balance the volumetric electroosmosis-driven flow, the back flow velocity, u_{Dp}, which is driven by the backpressure, must equal in magnitude to the flow velocity, u_{De} driven by electroosmosis (illustrated in Figure 5-1(b)), i.e.,

$$\bar{u}_{Dp}(\bar{t}) = \bar{u}_{De}(\bar{t}) \tag{5.21}$$

Using the Brinkman's momentum equation (Kaviany, 1995) for general pressure-driven flow in porous media, and neglecting the inertial forces and the channel wall effect, we can obtain the modified Brinkman's momentum equation for an electroosmotic flow

$$\frac{\rho}{\phi}\frac{du_{Dp}(t)}{dt} = -\frac{\partial p(t)}{\partial z} - \frac{\mu}{K}u_{Dp}(t) \tag{5.22}$$

Here $u_{Dp}(t)$ is the pressure-driven Darcy velocity through the porous medium packed inside the microcapillary. ϕ is the porosity of the porous medium. The Darcy permeability K is defined in the *Carman-Kozeny* equation (Kaviany, 1995), $K = \phi^3 d_p^2 / a(1-\phi)^2$, with a = 150 being the Ergun constant (Hsu and Cheng, 1990). The rearranged form of Eq. (5.22) is

$$\frac{\partial p(\bar{t})}{\partial z} = -\frac{\mu}{K}u_s\left[\bar{u}_{Dp}(\bar{t}) + \frac{K}{\phi R_{pore}^2}\frac{d\bar{u}_{Dp}(\bar{t})}{d\bar{t}}\right] \tag{5.23}$$

Substitute Eqs. (5.18) and (5.21) into Eq. (5.23), we obtain the time-periodic oscillating pressure gradient

$$\frac{\partial p(\bar{t})}{\partial z} = -\frac{\phi}{\tau}\frac{\mu}{K}u_s\frac{4(\kappa R_{pore})^2}{\Psi_s}\left[\sum_{n=1}^{\infty}\frac{C_n}{\lambda_n J_1(\lambda_n)}\frac{\lambda_n^2\cos(\beta^2\bar{t})+\beta^2\sin(\beta^2\bar{t})-\lambda_n^2\exp(-\lambda_n^2\bar{t})}{\lambda_n^4+\beta^4}\right.$$
$$\left.+\frac{K}{\phi R_{pore}^2}\sum_{n=1}^{\infty}\frac{C_n}{\lambda_n J_1(\lambda_n)}\frac{\beta^4\cos(\beta^2\bar{t})-\beta^2\lambda_n^2\sin(\beta^2\bar{t})+\lambda_n^4\exp(-\lambda_n^2\bar{t})}{\lambda_n^4+\beta^4}\right] \tag{5.24}$$

At time-periodic steady state, i.e., $\bar{t}\to\infty$, combining Eqs. (5.15-5.16), Eq. (5.24) is reduced to

$$\frac{\partial p(\bar{t})}{\partial z} = -\frac{\phi}{\tau}\frac{\mu}{K}u_s\frac{4(\kappa R_{pore})^2}{\Psi_s}\sum_{n=1}^{\infty}\frac{C_n}{\lambda_n J_1(\lambda_n)}\frac{\left(\lambda_n^2+\frac{K\rho\omega}{\mu\phi}\beta^2\right)\cos(\beta^2\bar{t})+\left(\beta^2-\frac{K\rho\omega}{\mu\phi}\lambda_n^2\right)\sin(\beta^2\bar{t})}{\lambda_n^4+\beta^4} \tag{5.25}$$

From Eq. (5.25), we obtain frequency-dependent maximum pressure gradient, expressed as

$$\left|\frac{\partial p}{\partial z}\right|_{\max}(f) = -\frac{\phi}{\tau}\frac{\mu}{K}u_s\frac{4(\kappa R_{pore})^2}{\Psi_s}\sum_{n=1}^{\infty}\frac{C_n}{\lambda_n J_1(\lambda_n)}\frac{\sqrt{\left(\lambda_n^2+\frac{K\rho\omega}{\mu\phi}\beta^2\right)^2+\left(\beta^2-\frac{K\rho\omega}{\mu\phi}\lambda_n^2\right)^2}}{\lambda_n^4+\beta^4}$$
$$= -\frac{\phi}{\tau}\frac{\mu}{K}u_s\frac{4(\kappa R_{pore})^2}{\Psi_s}\sum_{n=1}^{\infty}\frac{C_n}{\lambda_n J_1(\lambda_n)}\frac{\sqrt{1+\left(\frac{K\rho\omega}{\mu\phi}\right)^2}}{\sqrt{\lambda_n^4+\beta^4}} \tag{5.26}$$

In case of an applied DC electric field, i.e., $f = 0$, thus $\beta = 0$, Eq. (5.24) reduces to

$$\frac{\partial p(\bar{t})}{\partial z} = -\frac{\phi}{\tau}\frac{\mu}{K}u_s\frac{4(\kappa R_{pore})^2}{\Psi_s}\sum_{n=1}^{\infty}\frac{C_n}{\lambda_n^3 J_1(\lambda_n)}\left[1-\left(1-\frac{\lambda_n^2 K}{\phi R_{pore}^2}\right)\exp(-\lambda_n^2\bar{t})\right] \tag{5.27}$$

When the fluid flow becomes steady state, i.e., $\bar{t}\to\infty$, the pressure gradient becomes constant

$$\frac{\partial p}{\partial z} = -\frac{\phi}{\tau}\frac{\mu}{K}u_s \frac{4(\kappa R_{pore})^2}{\Psi_s}\sum_{n=1}^{\infty}\frac{C_n}{\lambda_n^3 J_1(\lambda_n)} \tag{5.28}$$

Since the electroosmotic flow velocity is coupled with the EDL potential distribution by the factor C_n in Eqs. (5.11-5.12), the EDL potential field should be obtained independently before we solve the flow field. An analytical solution of the EDL potential is provided in appendix B.

5.4 Results and Discussion

In the parametric study in this section, the calculations are based on the values reported by Zeng *et al.* (2001). The properties of the working solution were reported as: ionic strength 7.5 μM, the Debye length 0.11 μm, fluid viscosity 1.0×10^{-3} kg $m^{-1}s^{-1}$, density 998 kg m^{-3}, and dielectric constant 6.9×10^{-10} $CV^{-1}m^{-1}$. Three different packing particles of size d_p, 1.35 μm, 2.7 μm, and 5.6 μm are considered in calculations. The corresponding pore sizes, R_{pore} are 0.264 μm, 0.528 μm, and 1.1 μm, respectively. Other fixed parameters measured by experiments are: zeta potential –95 mV, porosity 0.37, and tortuosity 1.5.

Several important parameters are also highlighted before discussion. The characteristic viscous diffusion time scale is denoted by the reference time $t_{diff} = \rho R_{pore}^2 / \mu$. The time period for excitation electric field is denoted by $t_E = 1/f$. From the exponential term in Eq. (5.18), we can further estimate the characteristic time scale for an AC electroosmotic flow to reach its time-periodic steady state by choosing $\lambda_1^2 t^* = \lambda_1^2 \frac{\mu}{\rho R_{pore}^2} t^* = 1$. Then we can obtain $t^* = \frac{\rho R_{pore}^2}{\mu \lambda_1^2}$, where $\lambda_1 = 2.405$ determined form $J_0(\lambda_n) = 0$. The corresponding characteristic

frequency of the system is defined as $f^* = \frac{1}{t^*} = \frac{\mu\lambda_1^2}{\rho R_{pore}^2}$. The factor β present in all the analytical expressions, defined by Eq. (5.15), denotes the aspect ratio of the tubule radius R_{pore} to the Stokes penetration depth δ_s. And we can further infer that β also represents the square root of the aspect ratio of the viscous diffusion time scale to the period of electric field, i.e., $\beta = \sqrt{2\pi t_{diff} / t_E}$.

5.4.1 Oscillating flow velocity in a packed microchannel connected to two reservoirs

The steadily time-periodic AC electroosmotic flow velocity for two-cycle periods in a packed microchannel with open ends are shown in Figure 5-2. It is clearly shown that the flow presents a harmonic sinusoidal oscillation only with different magnitudes and phase lags. Figure 5-2(a) gives a comparison of the effects of three different excitation frequencies for a fixed pore size. It is obvious that, under the same packing condition, using an AC field of higher frequency decreases the EOF velocity. This is anticipated because under high frequency, the electric field changes its direction so fast that the flow can never get fully developed across the bulk intraparticle domain. In case of very high frequency, corresponding to a large value of β, the diffusion time scale is much greater than the oscillation time period, i.e., $t_{diff} > t_E$. Therefore there is no sufficient time for the flow momentum to diffuse far into the intraparticle bulk phase. Consequently the perturbed area is restricted only within a thin layer near the particle surface, while the fluid in the bulk phase remains stationary. This typical length scale of the oscillatory laminar viscous flow in response to a harmonic external excitation is represented by the frequency-dependent Stokes

penetration depth, δ_s, as defined by Eq. (5.16). Furthermore, it can be observed that as increasing frequency the flow lags behind the excitation field with a larger phase lag. From Eq. (5.18) and Eqs. (5.15-5.16), we can show that the phase lag of the oscillating velocity to the excitation field is expressed as $\theta = \tan^{-1}\left(\frac{\beta^2}{\lambda_n^2}\right) = \tan^{-1}\left(\frac{2\pi\rho}{\mu\lambda_n^2} f R_{pore}^2\right) = \tan^{-1}\left(2\pi \frac{f}{f^*}\right)$, indicating that the phase lag θ increases with increasing the excitation frequency f. These results are in accord with the findings by Dutta and Beskok (2001) and Kang *et al*. (2002) in their studies on AC electroosmosis in non-packed microchannels.

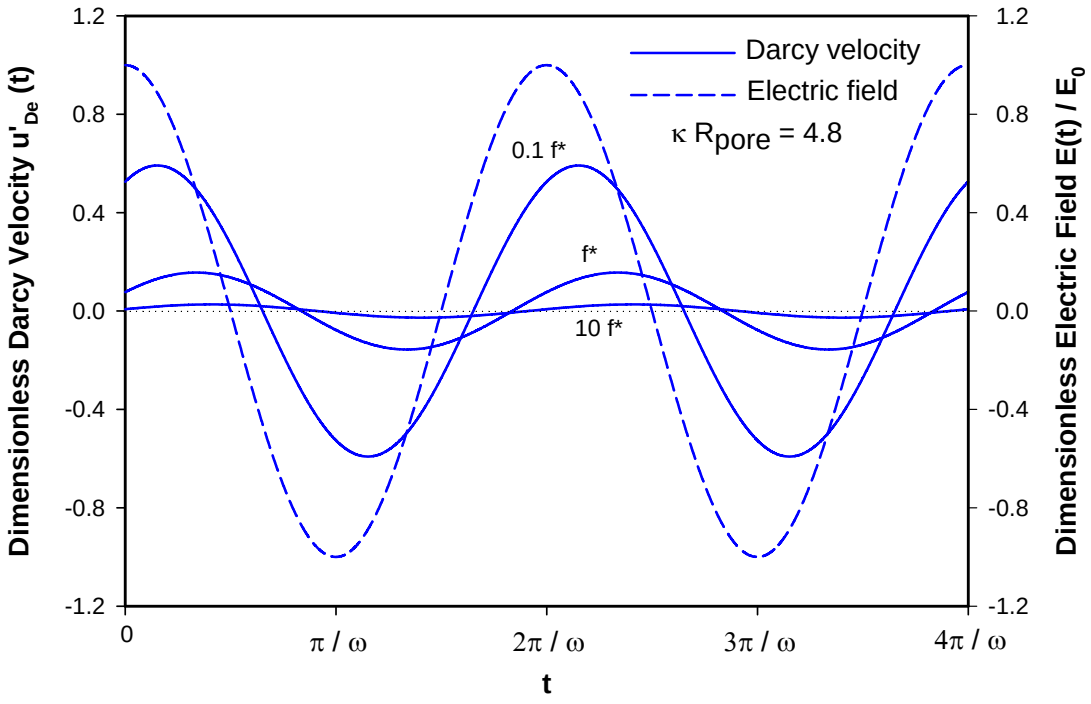

Figure 5-2 (a)

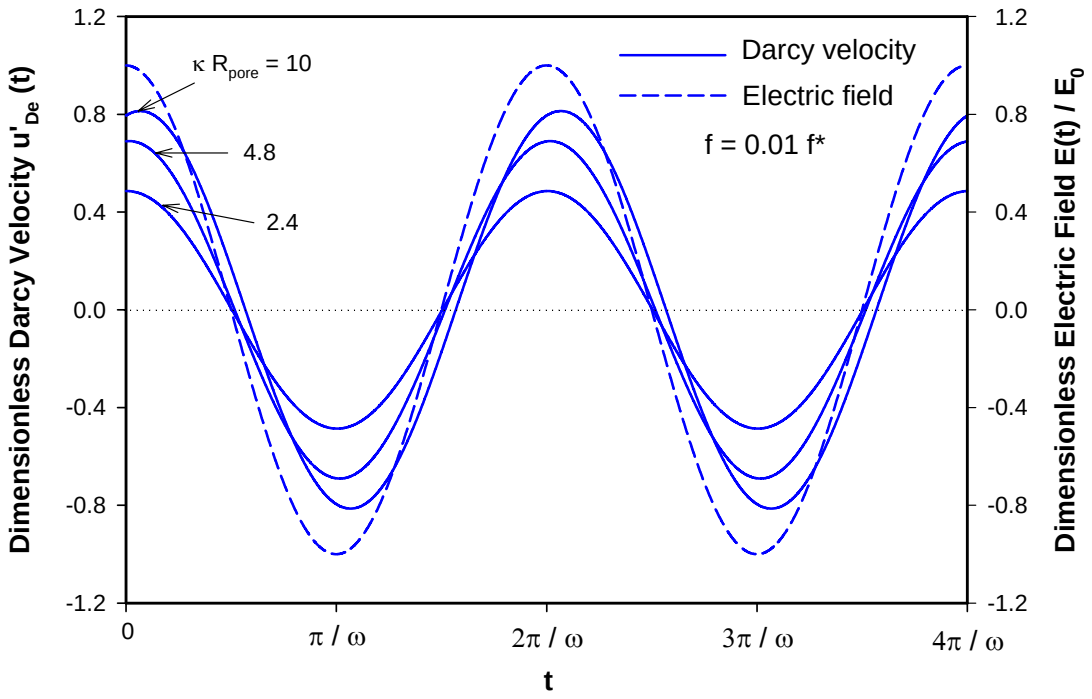

Figure 5-2 (b)

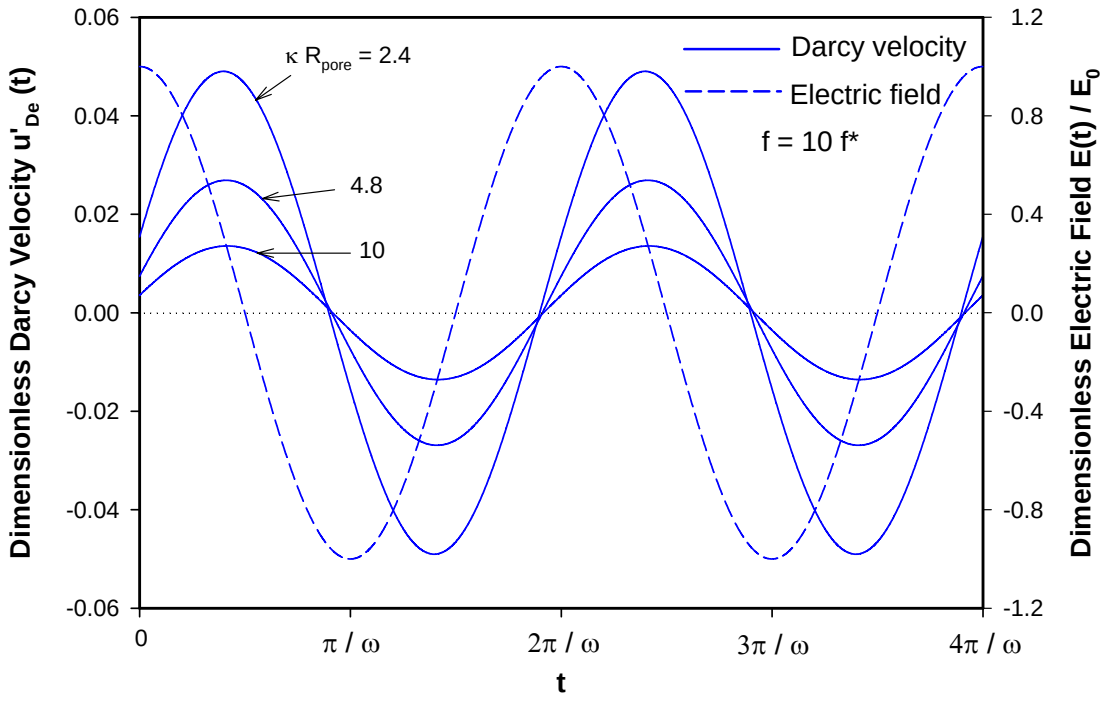

Figure 5-2 (c)

Figure 5-2 Dimensionless time-periodic oscillating Darcy electroosmotic flow velocity versus time. (a) steadily oscillating Darcy velocity for three different excitation frequencies, 0.1*f, *f** and 10*f** at a fixed pore size, κR_{pore} =4.8. (b-c) steadily oscillating Darcy velocity for three different pore sizes, 2.4, 4.8 and 10 at a fixed excitation frequency, (b) 0.01*f** and (c) 10 *f**, respectively. Reference velocity is chosen as $u_{ref} = \frac{\phi}{\tau}\frac{\varepsilon_r \varepsilon_0}{\mu} E_0 \zeta_p$.**

The effects of porous pore sizes are presented in Figure 5-2 (b-c) for low and high excitation frequencies, respectively. In case of low frequency, e.g., *f=0.01f** shown in Figure 5-2(b), t_{diff} is smaller than t_E, thus the momentum diffusion is faster than the period of oscillation. The flow momentum has enough time to diffuse far to bulk intraparticle domain, and thus the Darcy velocity (i.e., the mean velocity averaged over the pore cross-section) is higher for larger pore sizes. However the phase lag becomes larger for large pore sizes. Physically this is because a large pore size denotes more time needed for momentum diffusion. It also can be interpreted by using the mathematical expression for the phase lag, $\theta = \tan^{-1}\left(\frac{2\pi\rho}{\mu\lambda_n^2} f R_{pore}^2\right)$. Apparently, the phase lag increases with the square of pore radius (cross-sectional area of pore). It therefore can be expected that at very low frequencies the phase lag is proportional to the pore cross-sectional area. In contrast, for a high excitation frequency, e.g., *f=10f** shown in Figure 5-2(c), there is insufficient time for flow momentum diffusion. Hence the Darcy velocity is lower for larger pore sizes. In this situation, the fluid inertial effect predominates and the pore size effect diminishes. Mathematically, when the excitation frequency f approaches to infinity, the phase lag θ approaches to $\frac{\pi}{2}$. The pore size has no effect on the phase lag. Thus the phase lags for various sizes are almost the same and close to $\frac{\pi}{2}$, as shown in Figure 5-2(c).

To achieve a better understanding of the frequency-dependent velocity, in Figure 5-3 we compare the magnitude of the oscillating velocity versus frequency for three different pore sizes. In accord with above analysis, for a fixed pore size, the magnitude of maximum velocity decreases with increasing excitation frequency. With increasing pore size, the

magnitude of the maximum velocity gets higher in case of low frequency domain (lower than about 0.02*f**), and gets lower in case of high frequency domain (higher than about 0.2 *f**).

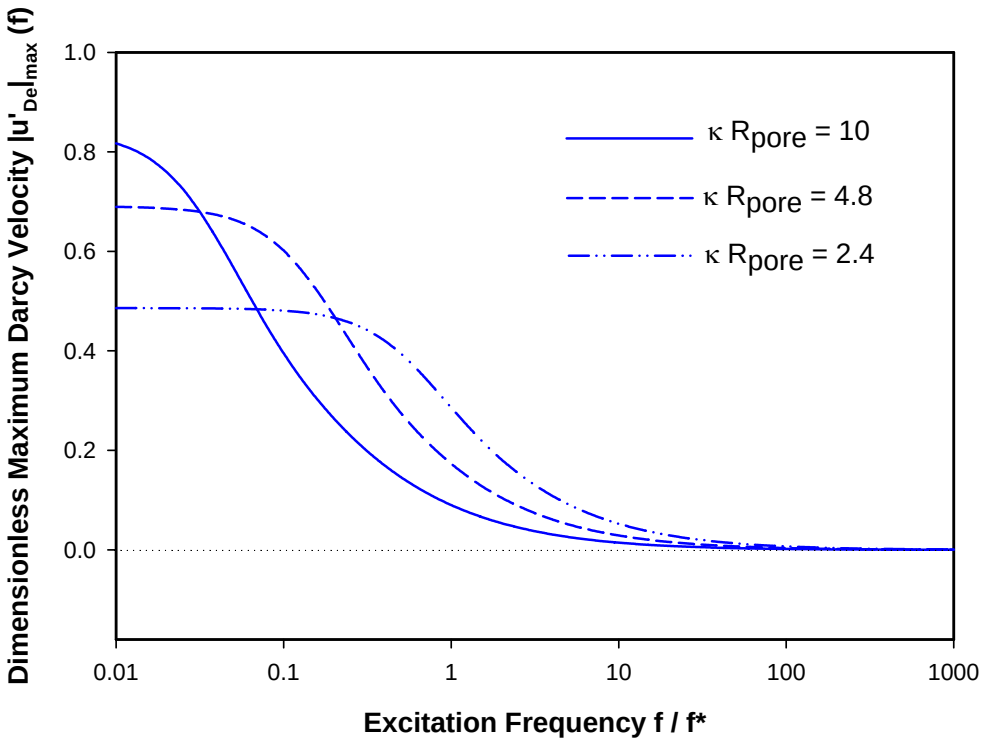

Figure 5-3 Dimensionless maximum Darcy electroosmotic flow velocity versus excitation frequency for three different pore sizes, 2.4, 4.8 and 10. Reference velocity is the same as in Figure 5-2.

In Figure 5-4 we study the time evolution of the transient electroosmotic flow for a special case of an applied DC electric field for three different pore sizes. It is apparent that the flow develops rapidly after imposing electric field. It takes a time period of around diffusion time scale, t_{diff} for the flow to get fully developed into a steady state, at which the larger pore size corresponds to a larger velocity.

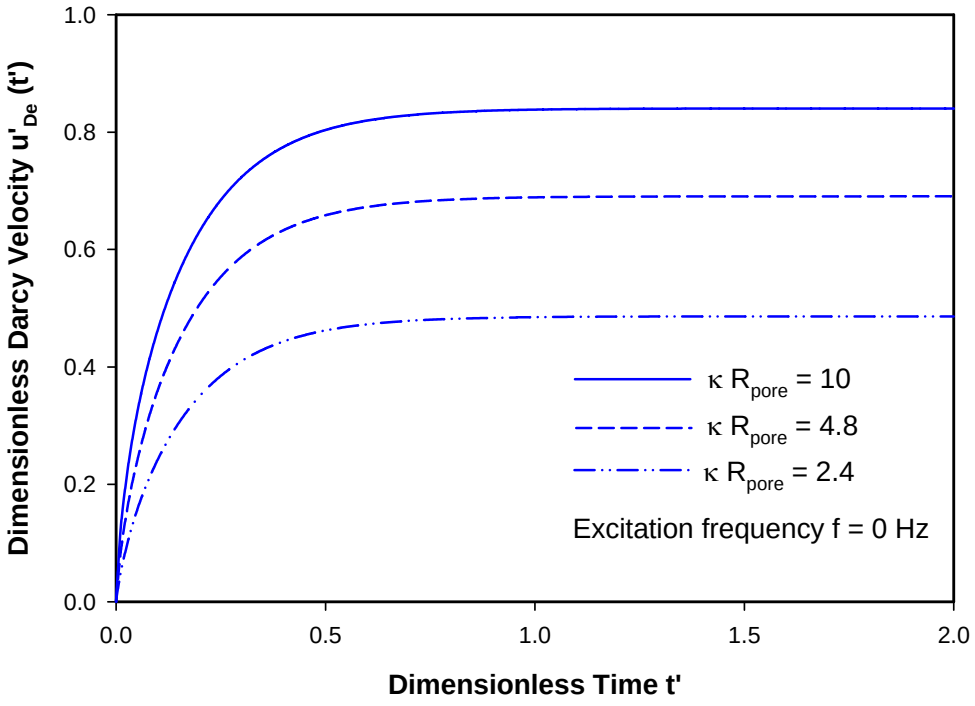

Figure 5-4 Time evolution of the DC electroosmotic flow velocity for three different pore sizes, 2.4, 4.8 and 10. Reference velocity is the same as in Figure 5-2.

5.4.2 Oscillating backpressure in a packed microchannel with two closed ends

Figure 5-5 presents the steadily time-periodic oscillation of the backpressure in a capillary of closed ends. It is shown that the backpressure associated with the counter-flow to balance the AC electroosmotic flow after application of the alternating voltage also presents a harmonic oscillation.

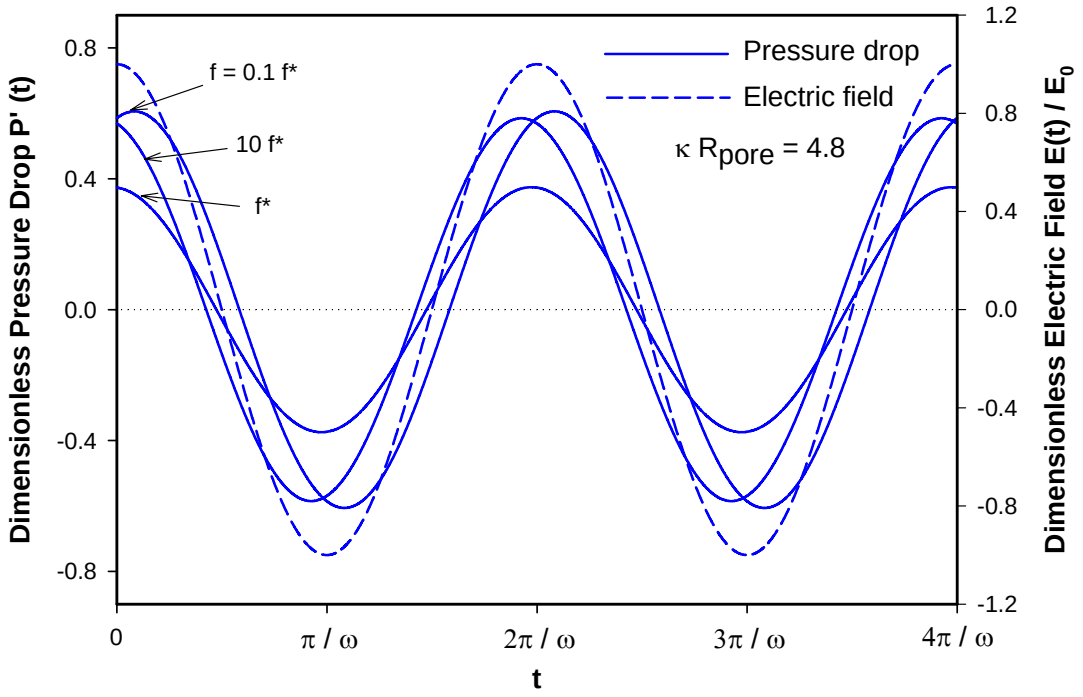

Figure 5-5 Dimensionless time-periodic oscillating backpressure drop versus time for three different excitation frequencies, 0.1*f, *f** and 10*f** at a fixed pore size, κR_{pore} =4.8. Reference pressure is chosen as** $p_{ref} = \left| \frac{\mu}{K} \frac{\phi}{\tau} \frac{\varepsilon_r \varepsilon_0}{\mu} E_0 \zeta_p \right|_{\kappa R_{pore}=4.8}$.

The magnitude of the maximum pressure drop versus excitation frequency for three different pore sizes is shown in Figure 5-6. The maximum pressure drop generated by a small pore size (corresponding to a smaller packing particle size) is always greater than that generated by a large pore size (corresponding to a large packing particle size), for the entire domain of the excitation frequency. This agrees with the experimental results reported by Paul *et al.*

(1998) in their study on the generation of high pressures using DC electroosmosis in porous structures. They reported that the pressure generated per applied volt increases with packing beads of smaller diameters. It is also noted in Figure 5-6 that, for a fixed pore size, the backpressure decreases with increasing excitation frequency, until it reaches its system characteristic frequency *f**, after which the backpressure increases with increasing excitation frequency.

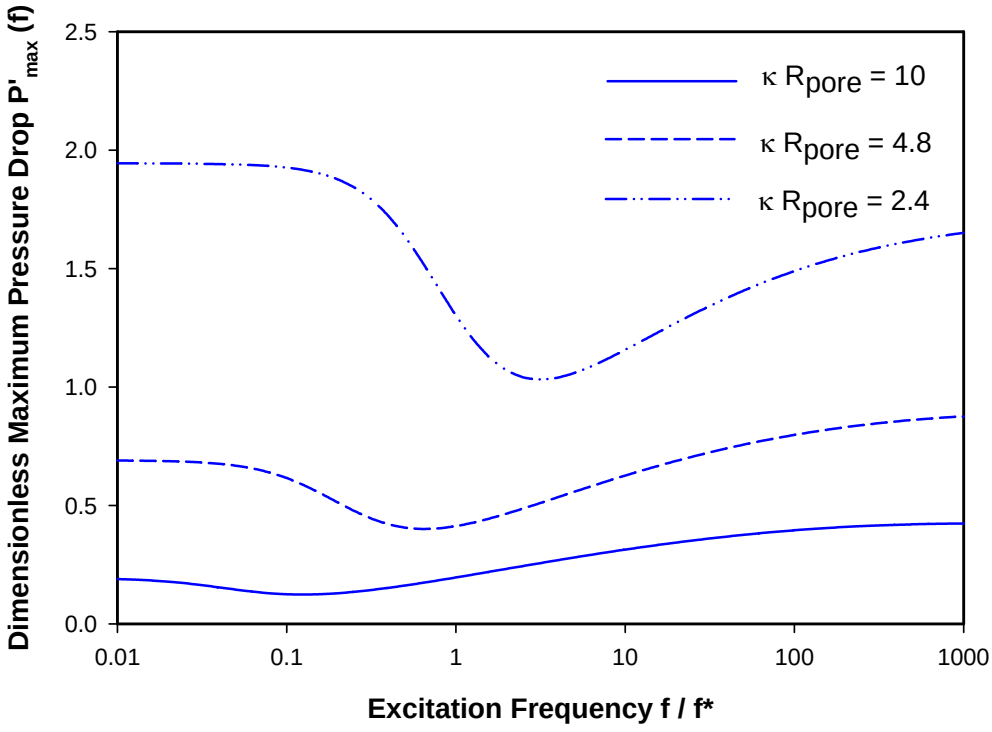

Figure 5-6 Dimensionless maximum backpressure drop versus excitation frequency for three different pore sizes, 2.4, 4.8 and 10. Reference pressure is the same as in Figure 5-5.

In Figure 5-7 we also study the special case of time evolution of the backpressure after application of a DC electric field. Similar to the transient flow velocity in the open-end capillary, the backpressure attains a constant value when the time period reaches to the viscous diffusion time scale, t_E. At the steady state, use of smaller packing particles can generate a higher backpressure. The results also reveal that there is a suddenly fall of magnitude of the backpressure immediately after the application of an electric field. This phenomenon can be interpreted by examining Eq. (5.23). Before the development of the counter-flow, the magnitude of the flow velocity, u_{Dp} is zero, however, the time derivative of the flow velocity, du_{Dp} / dt is not zero. As counter-flow quickly develops, du_{Dp} / dt decreases in magnitude while velocity increases. Therefore the backpressure presents a profile that the magnitude first deceases and then increases to a constant.

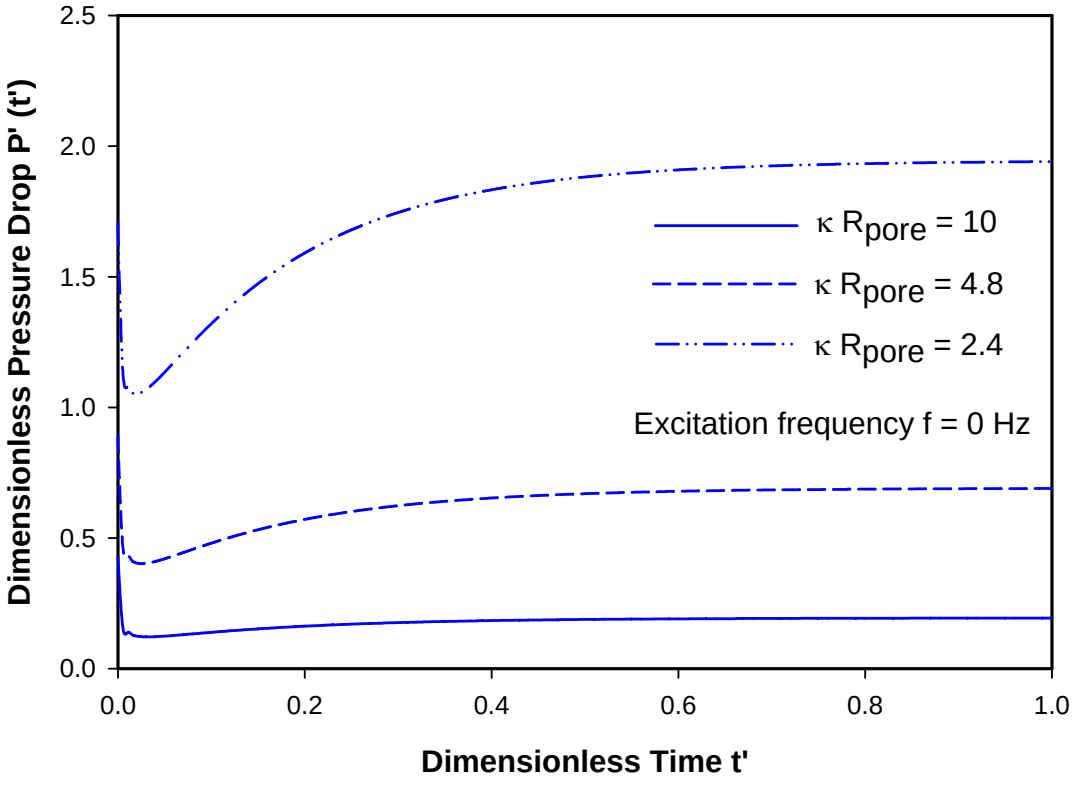

Figure 5-7 Time evolution of the backpressure drop due to DC electroosmosis in a closed-end microcapillary for three different pore sizes, 2.4, 4.8 and 10. Reference pressure is the same as in Figure 5-5.

5.5 Summary

An analytical model has been developed for the AC electroosmotic flow in both open-end and closed-end cylindrical microcapillaries packed with uniform spherical particles. The time-periodic oscillating electroosmotic flow in an open-end capillary is obtained using the Green's function approach. The analysis is based on the *Carman-Kozeny theory*. And the backpressure in a closed-end capillary is also analytically solved using the modified Brinkman's momentum equation. It is found that in a capillary with open ends (connected to two reservoirs and subject to the ambient pressure), the oscillating Darcy velocity profile depends on both the pore size and the excitation frequency; such effects are coupled through an important aspect ratio of the tubule pore radius to the Stokes penetration depth. For a fixed pore size, the magnitude of the AC electroosmotic flow decreases with increasing frequency. With increasing pore size, however, the magnitude of the maximum velocity shows two different trends with respect to the excitation frequency: it gets higher in low frequency domain, and gets lower in high frequency domain. Similarly, the backpressure associated with the counter-flow in a closed capillary (with closed ends), also presents a harmonic oscillation. Generally for a fixed excitation frequency, use of smaller packing particles can generate higher backpressure. For a fixed pore size, there exist two different trends of the backpressure magnitude versus the excitation frequency. When the excitation frequency is lower than the system characteristic frequency, the backpressure decreases with increasing excitation frequency. Whereas the excitation frequency is higher than the system characteristic frequency, the backpressure increases with increasing excitation frequency.

Chapter 6

Joule Heating Effect on the Electroosmotic Flow in a Microchannel Packed with Microspheres

6.1 Introduction

Since the electroosmotic flow is electric field induced, the Joule heating of the conductive electrolyte solution is inevitable. As pointed out in chapter 1, it is a major disadvantage in the application of electroosmotic flow, especially for large capillary size or high electrolyte concentration. The Joule heating effect on the electroosmotic flow in a non-packed microchannel has been studied in the literature (Tang, *et al.*, 2004a, b). It is also reported that magnificent temperature rise occurs due to Joule heating in the application of electrochromatography (Keim and Ladisch, 2003), in which the electroosmotic flow through porous media is the driving mechanism for separation purpose. Knox (1988) pointed out that the Joule heating effect can cause peak dispersion and thus greatly reduce the separation efficiency. In addition, a significant temperature elevation of the electrolyte solution may change the chemical properties or even lead to the degradation of the biochemical molecules (Xuan *et al.*, 2004a). Therefore it is important to control the temperature within the microfluidic system. Some popular measures to reduce the heating effect include using materials with rapid heat conduction and thermal inertia, and using cooling jacket around the microfluidic system.

The objective of this chapter is to numerically analyze the transient Joule heating effect on the electroosmotic flow in a microcapillary packed with microspheres. The influences of the electric field, the ionic concentration, the capillary size, the packing particle size, and the convection heat transfer coefficient outside the capillary will be discussed. The temperature dependent viscosity, dielectric constant, and electric conductivity of the electrolyte solution are taken into account. Specifically, the non-uniform electric field strength, which is due to variation of temperature-dependent local electric conductivity, will be taken into consideration. As far as the author knows, there is still no published literature which presents such a systematic study on the Joule heating effect of the electroosmotic flow through porous media. A complete numerical model will be developed which includes the coupled equations of the energy, momentum, mass and electric current continuity. The model is solved numerically using finite difference method.

6.2 Problem Formulation

Consider a cylindrical microcapillary densely packed with charged microspheres of diameter, d_p. The zeta potential of microparticles is ζ_p. The liquid flowing through the porous structure is assumed to be an incompressible, Newtonian, monovalence electrolyte of density, ρ_f, and viscosity, μ_f. In normal applications for electroosmotic pumping, the diameter ratio of the capillary to the packing particles is larger than 50, i.e., $d_c/d_p \geq 50$ (Zeng *et al.*, 2001). Thus according to Tallarek *et al*. (2001), the entire porous medium can be assumed to be homogeneous and the capillary wall effects can be safely neglected.

6.2.1 Equations of energy

In the following, we will derive the governing equation that expresses the first law of thermodynamics in electroosmotic flow in a microcapillary packed with microspheres. For modeling purpose, we divide the packed capillary into two distinct subsystems (as shown in Figure 6-1). The fluid and stationary phases (packing particles) forms the first subsystem, with axial boundaries consisting of the capillary inlet and outlet. The outer radial boundary of the first system is the capillary inner wall. The second subsystem is the capillary wall itself and is subject to the free convection on the outer surface, and heat conduction through the solid wall.

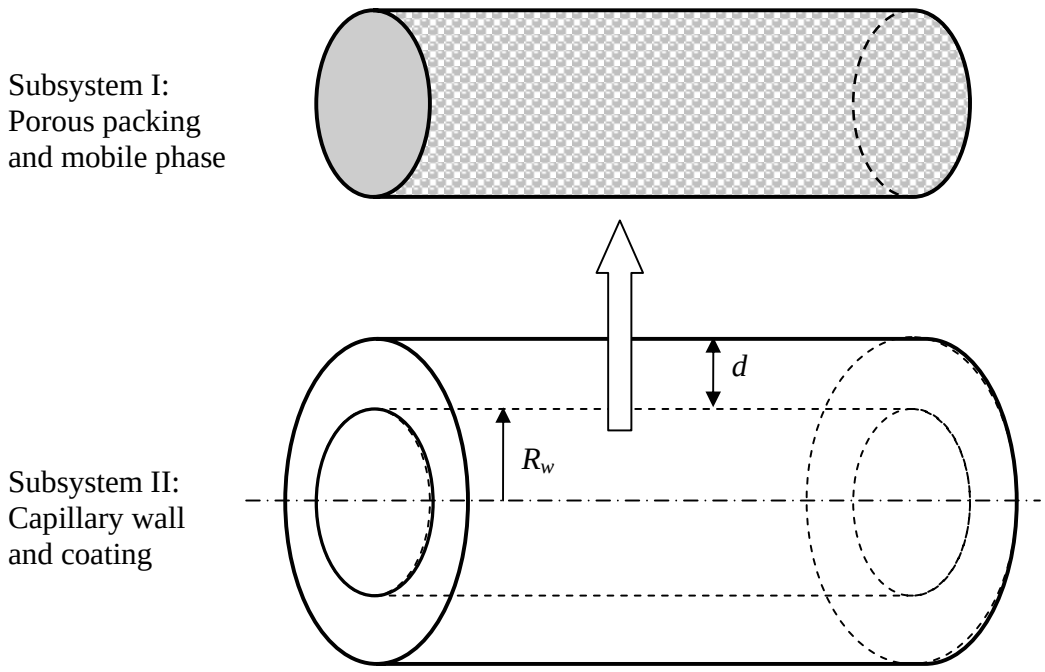

Figure 6-1 Schematic illustration of the two modeling subsystems of the packed microcapillary.

Subsystem I – homogeneous porous media

We start with a simple situation in which the medium is homogeneous, and where radiative effect and thermal dispersion effect are negligible. Very shortly we shall assume that there is local thermal equilibrium so that $T_s = T_f = T$, where T_s and T_f are the temperatures of the solid and fluid phases, respectively. When system dimension L is much longer than particles d_p ($L/d_p >> 1$) and when the variation of temperature across d_p is negligible compared to that across L for both the solid and fluid phases, then we can assume that within a distance d_p both phases are in local thermal equilibrium (LTE) (Kaviany, 1995). Here we also assume that heat conduction in the solid and fluid phases take place in parallel so that there is no net heat transfer from one phase to the other.

In a representative elementary volume (REV) of the medium we have, for the solid phase,

$$(\rho c_p)_s \frac{\partial T_s}{\partial t} = \nabla \cdot (k_s \nabla T_s) + \dot{q}_s \tag{6.1}$$

and, for the fluid phase,

$$(\rho c_p)_f \left(\frac{\partial T_f}{\partial t} + \vec{U}_p \cdot \nabla T_f \right) = \nabla \cdot (k_f \nabla T_f) + \mu_f \Omega + \dot{q}_f \tag{6.2}$$

Here the subscript s and f refer to the solid and fluid phases, respectively; $(\rho c_p)_s$ and $(\rho c_p)_f$ are the heat capacities of the solid and fluid phases at constant pressure, respectively; k is the thermal conductivity, and $\dot{q}$ is the heat production per unit volume. μ_f is the fluid viscosity. The term Ω refers to the viscous dissipation function of the fluid, which is proportional to the square of the velocity. Due to the low Reynolds number nature of electroosmosis in porous media, the viscous dissipation term can be neglected in current study. $\vec{U}_p$ is the local pore velocity vector.

Taking averages over the REV of the porous medium, we have, for the solid phase,

$$(1-\phi)(\rho c_p)_s \frac{\partial T_s}{\partial t} = (1-\phi)\nabla\cdot(k_s \nabla T_s) + (1-\phi)\dot{q}_s \tag{6.3}$$

and, for the fluid phase,

$$\phi(\rho c_p)_f \frac{\partial T_f}{\partial t} + (\rho c_p)_f \vec{U}_D \cdot \nabla T_f = \phi\nabla\cdot(k_f \nabla T_f) + \phi\dot{q}_f \tag{6.4}$$

where we have used the space-averaged velocity, i.e., Darcy velocity vector is defined as

$$\vec{U}_D = \frac{1}{V_p}\iint_{V_p} \vec{U}_p dV_p \tag{6.5}$$

where V_p is the void space (which is also called pore where the fluid phase can pass through) of the elementary volume, V_e is the total space of the elementary volume. From the definition of porosity, we can infer $V_p/V_e = V_f/V = \phi$.

Setting $T_s = T_f = T$ as above discussion and adding Eq. (6.3) and (6.4) we have

$$(\rho c_p)_m \frac{\partial T}{\partial t} + (\rho c_p)_f \vec{U}_D \cdot \nabla T = \nabla\cdot(k_m \nabla T) + \dot{q}_m \tag{6.6}$$

where we define the thermal capacity, thermal conductivity, and heat generation of the porous medium, respectively, as

$$(\rho c_p)_m = (1-\phi)(\rho c_p)_s + \phi(\rho c_p)_f \tag{6.7a}$$

$$k_m = (1-\phi)k_s + \phi k_f \tag{6.7b}$$

$$\dot{q}_m = (1-\phi)\dot{q}_s + \phi\dot{q}_f \tag{6.7c}$$

with further arrangement and using $\dot{q}_s = 0$, and assuming constant heat capacities, we have

$$\frac{\partial T}{\partial t} + \frac{1}{\sigma}\vec{U}_D \cdot \nabla T = \nabla\cdot(\alpha_m \nabla T) + \frac{\phi\dot{q}_f}{(\rho c_p)_m} \tag{6.8}$$

where we introduce the capacity ratio

$$\sigma = \frac{(\rho c_p)_m}{(\rho c_p)_f} \tag{6.9}$$

and the thermal diffusivity of the porous medium

$$\alpha_m = \frac{k_m}{(\rho c_p)_m} \tag{6.10}$$

The Joule heat generation in the fluid phase can be obtained using Ohm's law

$$\dot{q}_f = \frac{I^2}{\lambda_f} \tag{6.11}$$

where λ_f is the electric conductivity of the electrolyte which is given by

$$\lambda_f(T) = \lambda_+(T)C_+ + \lambda_-(T)C_- \tag{6.12}$$

Here $\lambda_+(T) = \lambda_{+0} + 0.025\lambda_{+0}(T - 298.13)$ and $\lambda_-(T) = \lambda_{-0} + 0.025\lambda_{-0}(T - 298.13)$ are ionic conductivity of the cation and anion of the electrolyte, respectively; C_+ and C_- respectively denote the mole concentration of cations and anions of the electrolyte. For sodium chloride (NaCl) solution, $\lambda_{+0} = 50.08\times10^{-4} m^2 S/mol$ and $\lambda_{+0} = 76.31\times10^{-4} m^2 S/mol$ (Tang, *et al.*, 2004a). In reality, the electric current density *I* should be the summation of two parts. One is due to the external electric field applied on the conductive solution $E_p\lambda$, the other is due to the movement of the net charge within the double layer $u_p\rho_e$, also known as surface conductance (Li, 2002). Due to the higher electrolyte concentration in the double layer, current density going through the double layer is significantly higher than that in Ohmic bulk liquid. Especially when the double layer thickness exceeds 10% of the capillary radius, the surface conduction becomes so strong that its contribution to the total current should be considered (Li, 2004). However, the non-neutral double layer inside the inter-particulate space is significantly thin compared with the pore size (less than 10% of the pore size in

present study), and the electroosmotic flow velocity in the porous media is very low (about 0.2 mm/s). The total current by bulk conduction is several orders of magnitude larger than that by surface conduction. Thus the electric current due to the surface conduction can be safely neglected. Considering the tortuosity effect in the porous media, the local electric field strength is $E_p = E_z / \sqrt{\tau}$ (Figure 4-1). Therefore, the Joule heat generation is expressed as

$$\dot{q}_f = \frac{(E_p \lambda)^2}{\lambda} = \frac{E_z^2 \lambda}{\tau} = \frac{\lambda}{\tau}\left(\frac{\partial \Phi}{\partial z}\right)^2 \tag{6.13}$$

$E_z = -\partial\Phi / \partial z$ is the axial electric field strength, where Φ is the applied electric field potential. It is assumed that $\frac{\partial T}{\partial r} \ll \frac{\partial T}{\partial z}$ and the thermal conductivity *k* is constant, Eq. (6.8) can be expanded as

$$\frac{\partial T}{\partial t} + \frac{u_z}{\sigma}\frac{\partial T}{\partial z} = \alpha_m \left[\frac{\partial^2 T}{\partial z^2} + \frac{1}{r}\frac{\partial}{\partial r}\left(r\frac{\partial T}{\partial r}\right)\right] + \frac{\phi}{\tau}\frac{\lambda}{(\rho c_p)_m}\left(\frac{\partial \Phi}{\partial z}\right)^2 \tag{6.14}$$

Subsystem II – capillary wall

Generally, the temperature boundary condition at the inner capillary wall is unknown. Since the heat generated by Joule heating in the electrolyte solution is primarily dissipated through the capillary wall to the surrounding environment, a conjugate heat transfer problem has to be solved to simultaneously account for heat transfer in both the solution and the capillary wall. The governing equation for heat conduction in the capillary wall, in cylindrical coordinates, is

$$\frac{\partial T}{\partial t} = \alpha_w \left[\frac{\partial^2 T}{\partial z^2} + \frac{1}{r}\frac{\partial}{\partial r}\left(r\frac{\partial T}{\partial r}\right)\right] \tag{6.15}$$

the thermal diffusivity of the capillary wall is defined as

$$\alpha_w = \frac{k_w}{(\rho c_p)_w} \tag{6.16}$$

where k_w is the thermal conductivity of the capillary wall, and $(\rho c_p)_w$ is the heat capacity of the capillary wall, all of which are assumed as constant.

The governing equations (6.14-6.15) are subject to following boundary conditions

$$T(r,z)\big|_{z=0} = T_0 \qquad \left.\frac{\partial T}{\partial z}\right|_{z=L} = 0 \tag{6.17a}$$

$$\left.\frac{\partial T}{\partial r}\right|_{r=0} = 0 \qquad k_w \left.\frac{\partial T}{\partial r}\right|_{r=R_w+d} = h(T - T_\infty) \tag{6.17b}$$

where h is the convection heat transfer coefficient at the outer capillary wall. R_w is the inner radius of the capillary and d is the thickness of the capillary wall.

6.2.2 Equations of continuity and momentum

The equation of continuity of the fluid flow in the porous media is (Bejan, 1995)

$$\frac{\partial \rho}{\partial t} + \nabla \cdot (\rho \vec{U}_D) = 0 \tag{6.18}$$

Since the fluid is assumed incompressible, Eq. (6.18) reduces to

$$\frac{1}{r}\frac{\partial (r u_r)}{\partial r} + \frac{\partial u_z}{\partial z} = 0 \tag{6.19}$$

Since the electroosmotic flow is strongly coupled with temperature field by the temperature-dependent viscosity and dielectric constant, it is can be infer that the velocity field is not uniform if temperature gradient is present. In this case, a pressure field should be induced to satisfy the mass conservation, i.e., constant flow rate. Therefore a pressure-driven flow component through porous media is introduced in present model. According to the well-known Darcy's law which describes the pressure-driven flow in porous media and the

derivation of the electroosmotic flow inside porous media in chapter 4, the Darcy velocity due to electroosmosis and induced pressure can be determined by

$$\bar{U}_D = \frac{\phi}{\tau}\frac{\varepsilon_r \varepsilon_0}{\mu_f}\zeta_p(1-G)\bar{\mathrm{E}} - \frac{K}{\mu_f}\bar{\mathrm{P}} \tag{6.20}$$

where the electric field strength $\bar{\mathrm{E}} = -\nabla\Phi$ and the reassure gradient $\bar{\mathrm{P}} = \nabla p$. K is the permeability of the porous medium, as defined in chapter 4. Neglecting the radial gradient of the electric potential field, $\partial\Phi/\partial r$, Eq. (6.20) can be re-written as

$$u_r = -\frac{K}{\mu_f}\frac{\partial p}{\partial r} \tag{6.21a}$$

$$u_z = -\frac{\phi}{\tau}\frac{\varepsilon_r \varepsilon_0}{\mu_f}\zeta_p(1-G)\frac{\partial\Phi}{\partial \mathrm{z}} - \frac{K}{\mu_f}\frac{\partial p}{\partial \mathrm{z}} \tag{6.21b}$$

where ε_r is the dielectric constant of the electrolyte and is considered as a function of temperature, expressed by $\varepsilon_r(T) = 305.7\exp\left(-\frac{T}{219}\right)$ (Tang, et al., 2004a). ε_0 is the permittivity of vacuum. μ_f is the viscosity of the electrolyte solution and its variation with the temperature is given by $\mu_f(T) = 2.761\times10^{-6}\exp\left(\frac{1713}{T}\right)$ (Tang, et al., 2004a). ζ_p is the zeta potential at the surface of the packing particles. G is defined as

$$G = \frac{2}{\zeta_p R_{pore}^2}\int_0^{R_{pore}} r\psi_i(r)dr \tag{6.22}$$

According to the capillary model, $\psi_i(r)$ is the interstitial EDL field inside the imaginary tubules, and it is governed by Poisson-Boltzmann equation (Probstein, 1994)

$$\frac{1}{r}\frac{d}{dr}\left[r\frac{d\psi_i(r)}{dr}\right] = -\frac{2n_0 z e_0}{\varepsilon_r \varepsilon_0}\sinh\left[\frac{z e_0 \psi_i(r)}{k_b T}\right] \qquad (0 \le r \le R_{pore}) \tag{6.23}$$

subject to the following boundary conditions

$$\left.\frac{d\psi_i}{dr}\right|_{r=0} = 0 \qquad \psi_i\big|_{r=R_{pore}} = \zeta_p \tag{6.24}$$

where the pore size is defined as

$$d_{pore} = 2R_{pore} = \frac{2\phi}{3(1-\phi)} d_p \tag{6.25}$$

6.2.3 Continuity of electric current

Since the capillary wall is non-conducting, the conservation of the electric current density, neglecting the convection current as in above discussion, gives

$$\nabla \cdot \left(\lambda_f \nabla \Phi\right) = 0 \tag{6.26}$$

Neglecting the radial gradient of the electric potential field, $\partial\Phi/\partial r$, Eq. (6.26) is reduced to

$$\frac{\partial}{\partial z}\left(\lambda_f \frac{\partial \Phi}{\partial z}\right) = 0 \tag{6.27}$$

where the electric potential field Φ is subject to

$$\Phi\big|_{z=0} = \Phi_0 \qquad \Phi\big|_{z=L} = 0 \tag{6.28}$$

Since the fluid electric conductivity λ_f, dielectric constant ε_r, and viscosity μ_f are temperature dependent, it is necessary to solve the coupled energy equation (6.14-6.15), mass continuity equation (6.19), momentum equation (6.21), and the electric current continuity equation (6.27) simultaneously.

6.3 Numerical Method

The complete set of coupled equations is solved numerically using the finite difference method. For which purpose, an in-house code is developed to solve the disretized equations. For this transient problem, at each time step, the physical parameters are evaluated by the current temperature field (initially at room temperature), to determine the electric potential field, induced pressure field, and thus the velocity field. Next, the known velocity and potential field are used to solve the new temperature field. These steps are iterated until the temperature variation between two consecutive time-steps are less than a tolerance, i.e., the temperature reaches a steady state.

In order to verify the code, we compared results under the present model with two published works on the Joule heating in electrochromatography. One is the improved formulae derived by Knox (1988) on the steady state temperature excess across both the porous and the capillary wall subsystems. The other is the numerical and experimental study by Keim and Ladisch (2003). It is found that the numerical prediction of this study is in good agreement with the analytical solution by Knox (1988) and the experimental data reported by Keim and Ladisch (2003). The details will be shown in the following section.

6.4 Results and Discussion

In this section, the joule heating effect on the transient electroosmotic flow in a microcapillary packed with microspheres will be presented. Influences of electric field, electrolyte solution, channel and packing sizes, and heat exchange with ambient atmosphere will be discussed. In simulation, NaCl solution of concentration 10^{-4}~10^{-3} M is chosen as the fluid phase; stationary phase is Octyldecyl silica (ODS) particles. The packing columns are

fused silica capillaries with polyimide coating. According to the product specifications (Polymicro Technologies, USA), the ratio of capillary radius to wall thickness is chosen as 3:1. Accordingly the ratio of the wall thickness to the coating layer thickness is chosen as 3:1. The physical properties of the capillary and particles are listed in Table. 1. Since the electrokinetic boundary wall effect is neglected due to large column-particle ratio, the porosity and tortuosity factors of the packed capillary are fixed as 0.4 and 1.5, respectively.

Table 6-1 Material property in simulation

Properties	Electrolyte solution (NaCl)	Packing particles (ODS)	Capillary wall (Fused Silica)	Coating
Density, ρ [kg m^{-3}]	1000	2600	2202	1420
Heat capacity, C_p [J kg^{-1} K^{-1}]	4180	750	743	1100
Thermal conductivity, k [W m^{-1} K^{-1}]	0.61	1.2	1.38	0.15
Molar conductivity, λ_0 [m^2 S mol^{-1}]	$126.4[1+0.025(T-298)]\times10^{-4}$			
Dynamic viscosity, μ [kg m^{-1} s^{-1}]	$2.761\exp(1713/T)\times10^{-6}$			
Dielectric constant, ε_r	$305.7\exp(-T/219)$			

6.4.1 Transient developing temperature field and its effect on EOF

The transient time development of the temperature field induced by Joule heating is shown in Figure 6-2. It is demonstrated that there exists a thermal entrance region where the temperature distribution varies not only along the capillary radius but also along the capillary axis. Figure 6-2(a) is the axial distribution of the temperature at the capillary centerline. The temperature of the fluid starts to increase from the room temperature (25 ^{o}C) and finally

reaches a steady temperature at a distance along the downstream direction. The length of the distance is traditionally called *thermal entrance length* (Bejan, 1995). The axial temperature gradient is highest at the inlet and decreases to zero at the end of the thermal entrance region. It is noted that the thermal entrance length for the electroosmotic flow in a packed microcapillary extends about 250 times of channel diameter, which is exceptionally longer than the traditional thermal entrance problem of Newtonian fluid in a non-packed channel (5-10 D_h) (Tang *et al.*, 2004a). The traditional thermal entrance problem has been well investigated. It is reported that the thermal entrance length is proportional to the Peclet number (product of Reynolds number and Prandtl number), $x_{fd,t} \approx 0.05 D \,\mathrm{Re}_D \,\mathrm{Pr}$. However, the thermal entrance length for the EOF in packed channel has never been reported as far as the authors know. Obviously the thermal entrance length in this case doesn't follow this simple relationship. Since the thermal entrance length is significant, it is deserved for a further study to include the entrance effect when designing a practical electrokinetic micropump system. It will be shown in next section that the thermal entrance length will be affected by different working parameters.

Figure 6-2(b) shows the time development of radial temperature distributions at the thermal fully-developed region. It is demonstrated that the radial temperature gradient inside the porous packing and the channel wall is insignificant compared with the transient temperature increase with time. This phenomenon is due to the low Biot number of the whole system (as a rough estimation, $Bi = \mathrm{O}(10^{-3})$). Because the Reynolds number of the macroscopic electroosmotic flow is very small ($\mathrm{Re}_{D_c} = \mathrm{O}(10^{-1})$), the heat generated in the packed region is dissipated mainly by radial conduction through the channel wall and then by convection with the surrounding air, rather than by axial advection of the fluid flow. If $Bi \ll 1$, the

resistance to heat conduction within the capillary system is much less than the resistance to thermal convection across the channel wall-surrounding air boundary layer (Incropera and DeWitt, 2002). Hence virtually the temperature variation is only the difference between the outer wall and the surrounding air, whereas the temperature within the whole capillary system remains nearly uniform. However, with a close examination of the steady state radial temperature distribution ($t > 600\text{s}$) as in the inset of Figure 6-2(b), the temperature distribution in the porous packing shows a parabolic profile. The highest temperature occurs at the channel centerline. This result confirms the findings by Knox (1988) in a study on the thermal effects in capillary electrochromatography. Further quantitative comparison between the current results and the Knox's formulae will be shown in the following section.

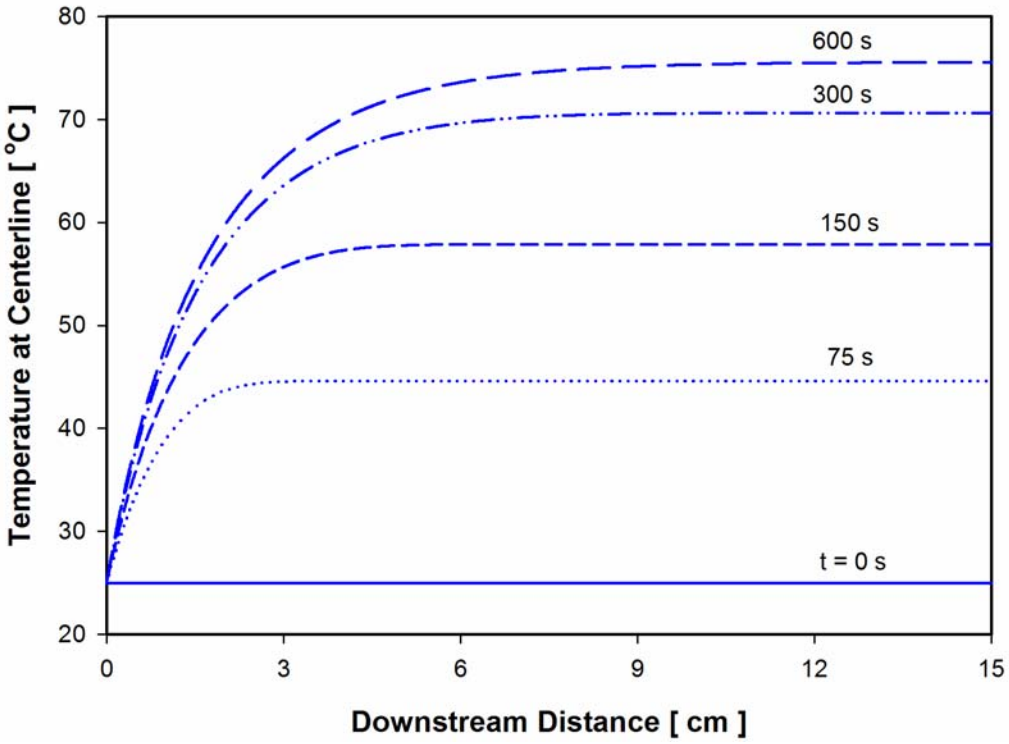

Figure 6-2(a)

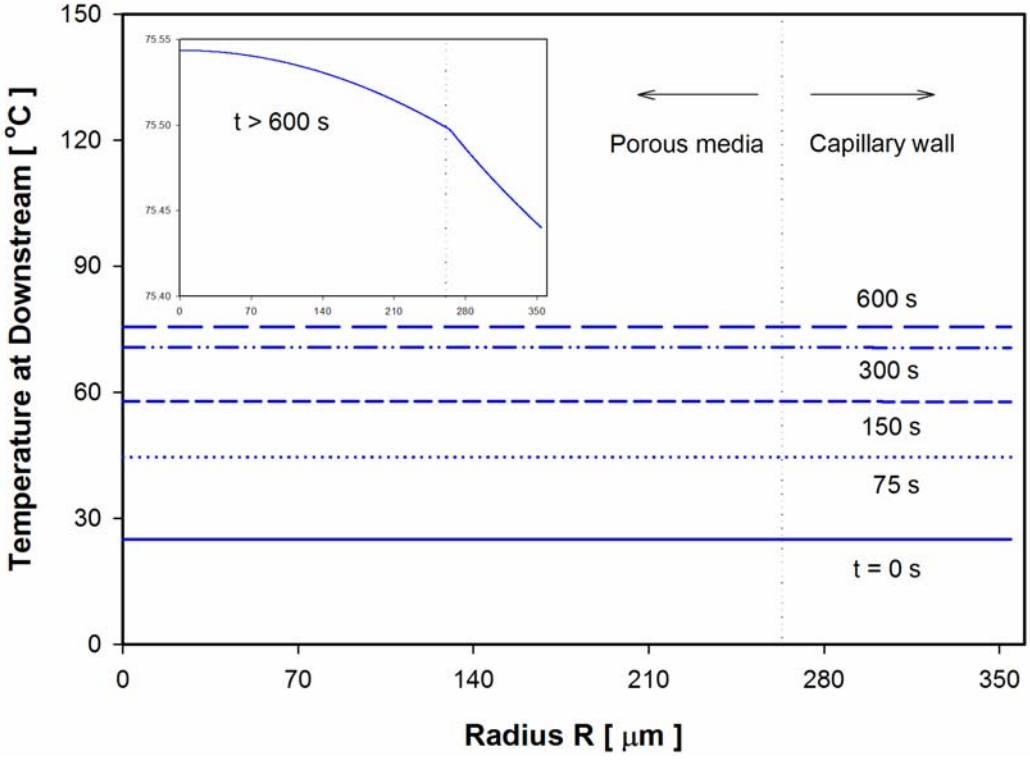

Figure 6-2 (b)

Figure 6-2 Transient development of the temperature field: (a) along the axis, (b) radial distribution at downstream. Working parameters: capillary inner diameter d_w = 530 μm, capillary length L = 15 cm, packing particle size d_p = 6 μm, porosity ϕ = 0.4, tortuosity τ = 1.5, electrolyte concentration C = 10^{-3} M, zeta potential at particle surface ζ_p = 50 mV, applied electric field Φ = 3000 V, and convection heat transfer coefficient at the capillary outer surface h = 5 W/m^2 K.

The most direct effect of the temperature rise is that it causes variation of the fluid electric conductivity. The local electric conductivity increases proportionally with temperature elevation. Since the total electric current density along the capillary is constant, as determined by Eq. (6.27), higher local electric conductivity leads to lower local electric field strength. Therefore the electric field strength becomes much higher at the entrance region where the temperature is under development, and it becomes lower and constant in the thermally developed region, as shown in Figure 6-3.

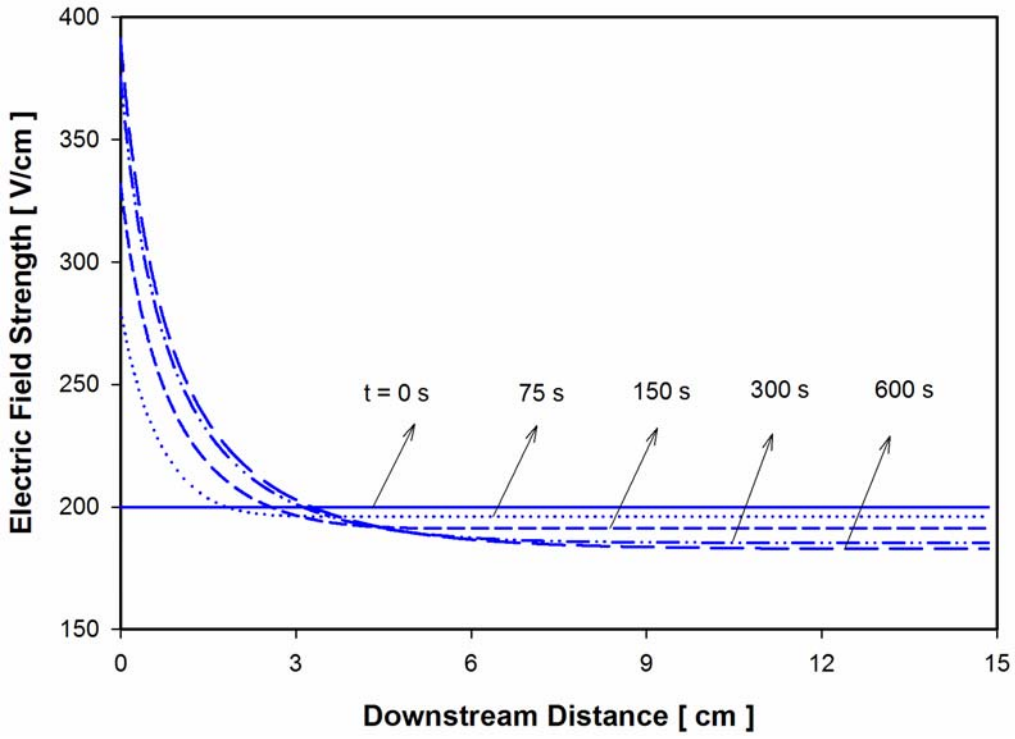

Figure 6-3 Transient development of the electric field strength. Working parameters are identical to those in Figure 6-2.

According to Eq. (6.21), the EOF velocity field is coupled with the temperature field by the temperature-dependent dielectric constant, ε_r, viscosity, μ_f, and electric field strength, $\partial\Phi/\partial z$. The transient development of the axial and radial velocity distributions is shown in Figure 6-4. Although both viscosity and the dielectric constant decrease with increasing temperature (Table 6-1), the effect on viscosity is much more significant thus resulting in an increase in EOF velocity. Further, as shown in Figure 6-4(a), the high local electric field strength greatly increases the local velocity at the entrance.

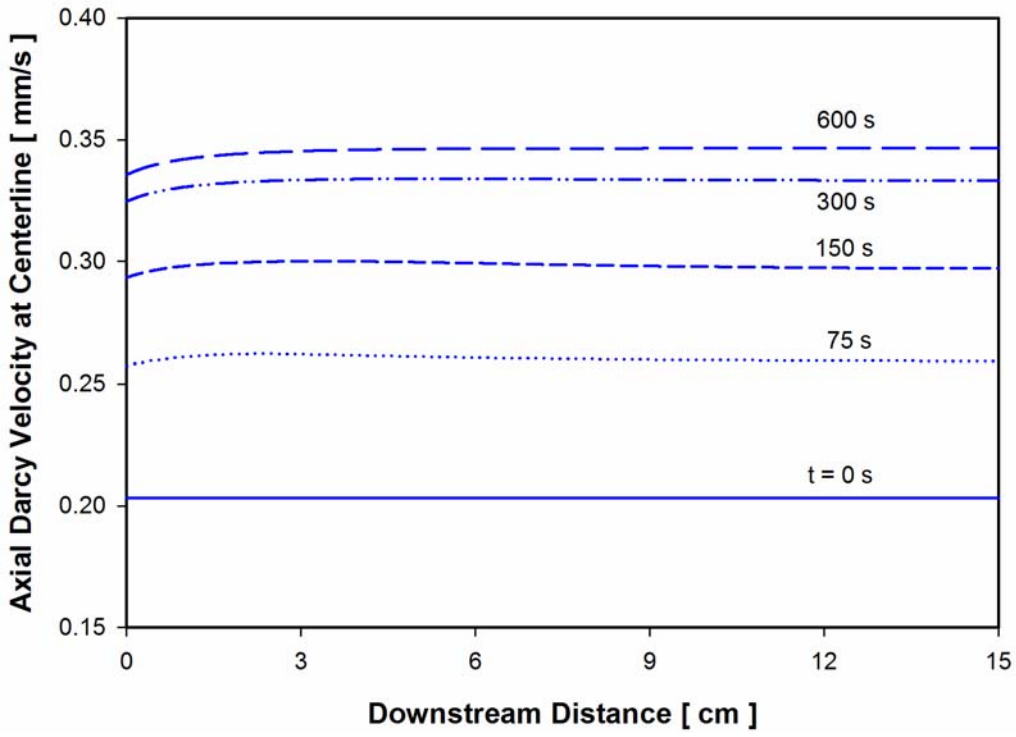

Figure 6-4(a)

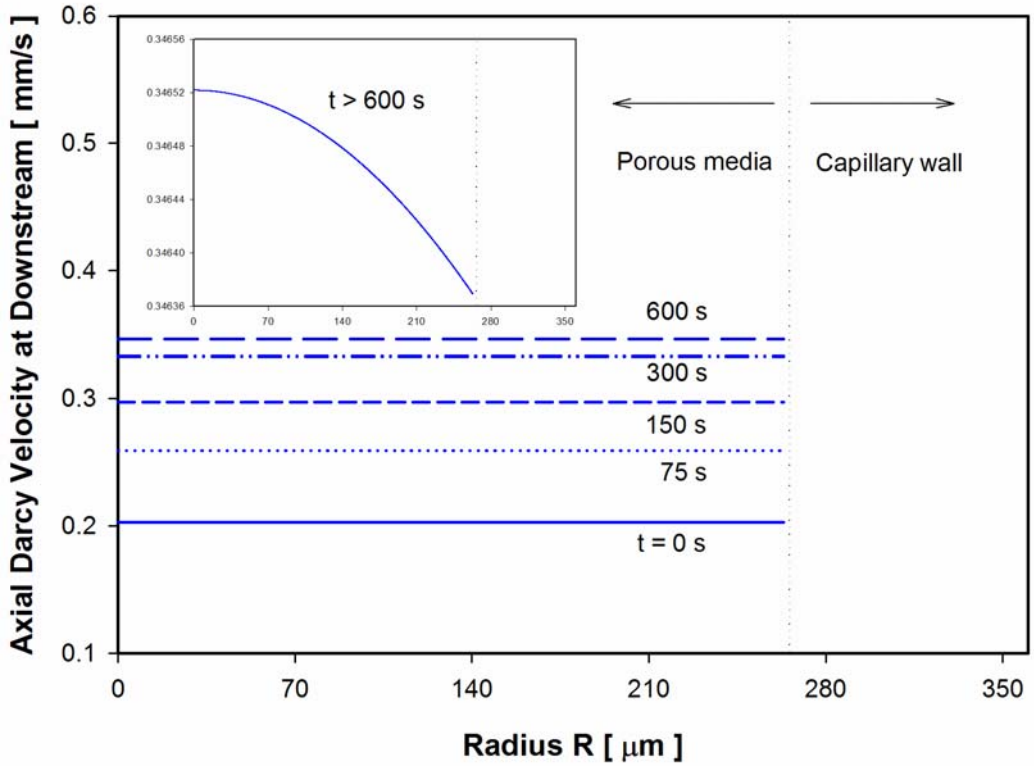

Figure 6-4(b)

Figure 6-4 Transient development of the electroosmotic velocity: (a) axial distribution, (b) radial distribution at downstream. Working parameters are identical to those in Figure 6-2.

In Figure 6-4(b), it is noted that the EOF velocity begins to increase gradually over the time until it reaches a steady state. The time for this velocity developing process is the same as that for temperature field. Actually, if there is no Joule heating effect, the velocity field will remain uniform in the porous domain. From Eq. (5.20), we can infer the time scale for the EOF velocity in porous media to reach its steady state after application of electric field, $t^* = \rho R_{pore}^2 / \mu = \mathrm{O}(10^{-6}\mathrm{s})$, (without considering Joule heating). This time scale is very small

due to the small inter-particulate pore size, which is about 1 micron in this case. However, when the Joule heating effect is present, the time for velocity to be fully developed becomes almost eight times of order of magnitude higher ($O(10^2 s)$), depending on the size of the capillary. Also the fully developed velocity increases to about 60% higher than its initial magnitude. Therefore the Joule heating effect is significant and should be taken into account under the conditions of high ionic concentration, large channel size, or high electric field strength. Furthermore, the steady state velocity distribution in Figure 6-4(b) also shows a parabolic profile with the highest velocity in channel center. This is because the highest temperature rise occurs at the center. But the radial temperature difference is so small that the radial velocity is virtually uniform in its transient development.

It is interesting to note that the present model predicts an induced pressure field along the flow direction, as shown in Figure 6-5. As mentioned above, the variation of the temperature along the flow direction causes the non-uniform flow velocity. The presence of the induced pressure field inside the capillary is to adjust the flow velocity to satisfy the mass conservation (i.e., a constant flow rate). Similar to the finding by Xuan *et al.* (2004a) on the Joule heating in non-packed capillaries, the induced pressure gradient is positive at the entrance region to decrease the flow rate, whereas it becomes negative at the fully developed region to increase the flow rate. However, the velocity profile at the entrance in this study is in convex shape, which is contrary to the concave profile in non-packed capillary reported by Xuan *et al*. (2004a). This inconsistency is due to the different nature of the pressure-driven flow in packed and non-packed capillaries. In non-packed capillaries, the flow profile is parabolic (Poiseuille flow). However in packed capillaries, according to Darcy's law, the

flow profile is flat (plug flow). Therefore the positive pressure gradient (back pressure) at the entrance can generate a concave shape in case of a non-packed capillary.

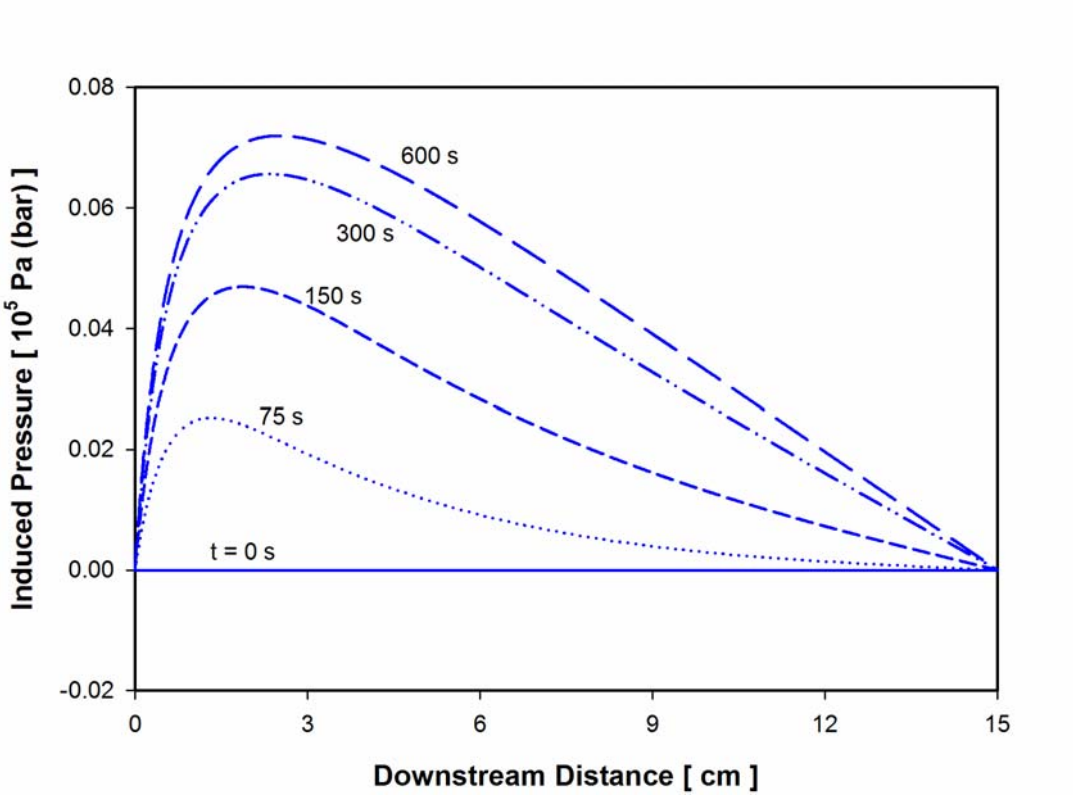

Figure 6-5 Transient development of the induced pressure. Working parameters are identical to those in Figure 6-2.

6.4.2 Comparison with published works

To verify the current numerical model, case studies compared with Knox's formulae and the numerical and experimental work by Keim and Ladisch (2003) will be shown in the following, respectively.

Knox (1988) presented simple formulae to estimate the temperature difference between the channel axis and its inner wall, $\theta_{core} = \frac{E^2 \lambda C \phi D_c^2}{16 k_m}$ and temperature excess across the channel

wall, $\theta_{wall} = \frac{E^2 \lambda C \phi D_c^2}{8k_w} \ln\left(\frac{D_o}{D_c}\right)$. With simple modification including the tortuosity factor of the porous packing, Knox's formulae can give $\theta_{core} = \frac{\phi}{\tau} \frac{E^2 \lambda C D_c^2}{16k_m} = 0.046\ ^{o}\mathrm{C}$ and $\theta_{wall} = \frac{\phi}{\tau} \frac{E^2 \lambda C D_c^2}{8k_w} \ln\left(\frac{D_o}{D_c}\right) = 0.057\ ^{o}\mathrm{C}$. The numerical model in this study (inset of Figure 6-2(b)) gives quantitatively the same predictions as that by Knox's formulae, respectively.

Keim and Ladisch (2003) developed a numerical model to investigate the temperature profiles in large diameter electrochromatography. In addition they measured the transient temperature elevation at the center of the column outlet. Their experiment data is compared with the result by numerical modeling in this study in Figure 6-6(a). When the electric field is present, the temperature rise in their experiment is higher than that predicted by this model. Whereas during the cooling down process (electric field is turned off after 3 hours and 35 minutes), the temperature drop in the experiment is faster than that predicted by this model. This scenario is due to the special situation applied in their experiment, i.e., the flow rate was kept constant during the course of their experiment, although they did not mention how to keep a constant flow rate. However in this study the electroosmotic flow velocity is strongly coupled with the temperature field, i.e., the flow rate may change over the time. As discussed in the previous section, during the heating up session, the high axial temperature gradient at the entrance greatly enhances the local electric field strength resulting in an increased flow field. Therefore the increased axial flow convection has a better heat dissipation effect which keeps the temperature rise at a relatively low level. During the cooling session, there is no driving force due to the absence of electric field. Thus the flow velocity will decrease until the fluid comes to a full stop. In this situation, the heat dissipation is mainly dependent on the

heat conduction in radial direction. No wonder that the temperature drop is faster in their experiment in which the flow rate was not affected.

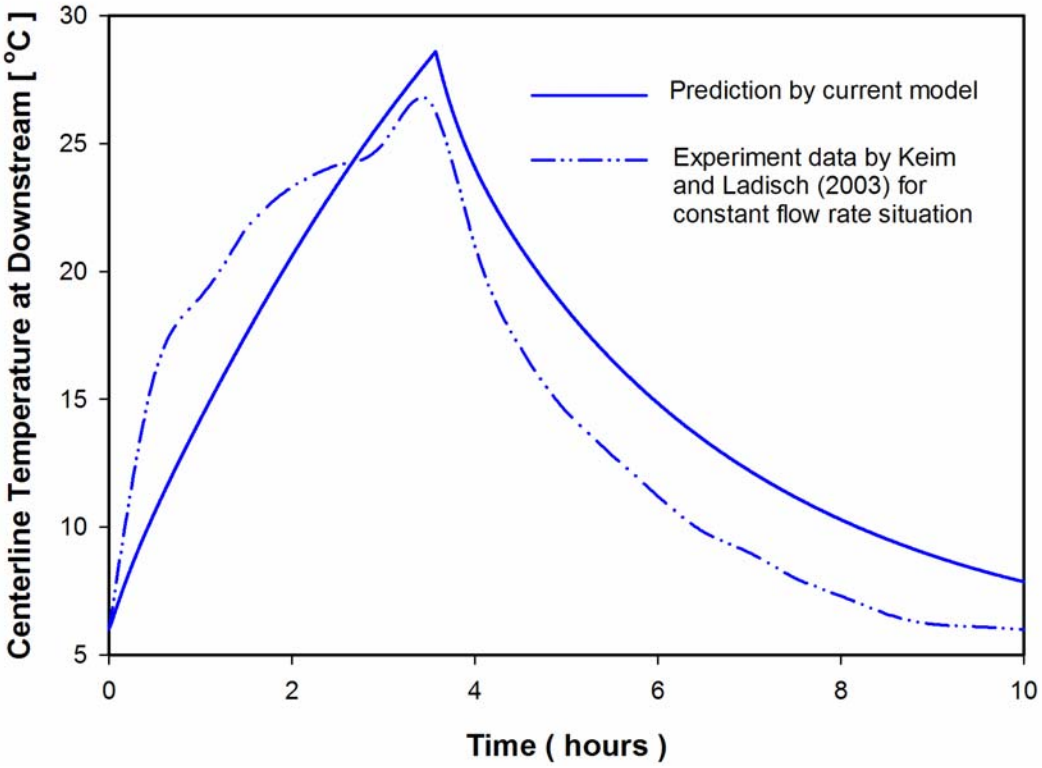

Figure 6-6(a)

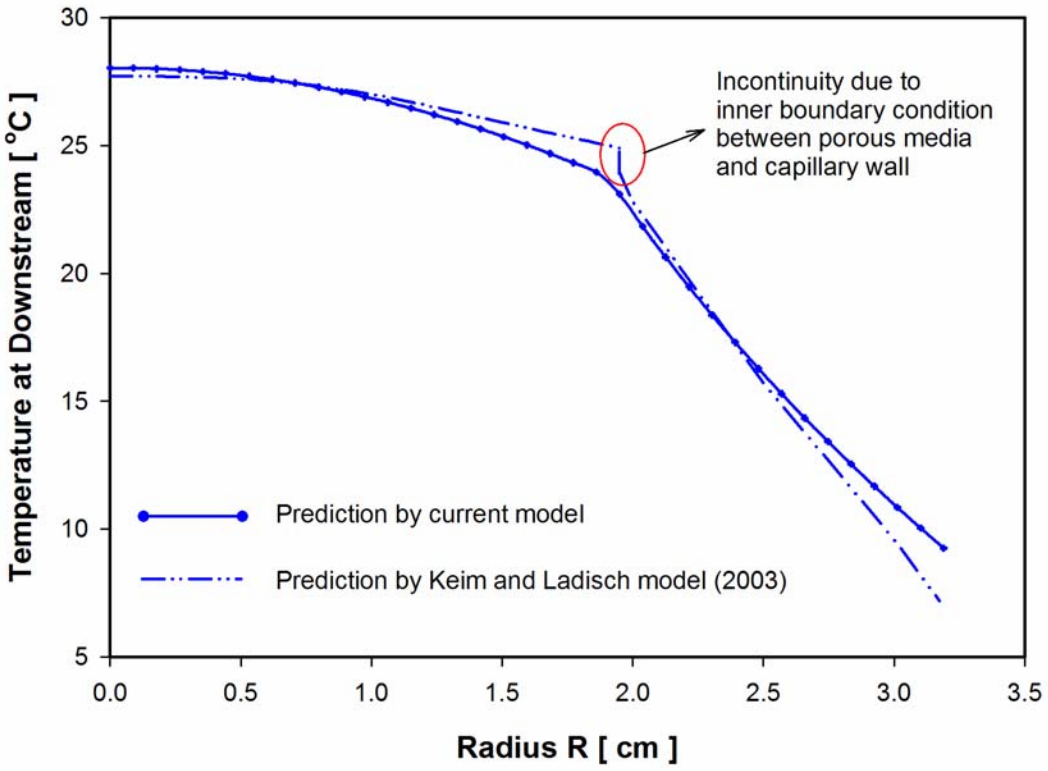

Figure 6-6(b)

Figure 6-6 Results comparison with published works by Keim and Ladisch (2003): (a) experiment data of transient temperature rise at the center of the column outlet, (b) modeling of the radial temperature profile at column outlet. Working parameters: capillary inner diameter d_w = 3.81 cm, capillary length L = 38.1 cm, packing particle size d_p = 5 μm, porosity ϕ = 0.36, tortuosity τ = 1.5, electrolyte concentration C = 3.9×10^{-3} M, zeta potential at particle surface ζ_p = 60 mV, applied electric field Φ = 419 V, and convection heat transfer coefficient at the capillary outer surface h = 5 W/m^2 K.

Figure 6-6(b) shows the comparison of the radial temperature profile predicted by Keim and Ladisch's numerical model and the model developed in this study. It can be seen the two models give close results. The major discrepancy lies at the boundary between the porous

packing (subsystem I) and the capillary wall (subsystem II) where their model presented a non-continuous temperature distribution. This is because an empirical boundary condition between the two subsystems was used in their numerical model. However the temperature at this boundary is unknown. In contrast, the conjugated heat transfer equations within the two subsystems are solved simultaneously in this study. The unknown boundary problem is avoided and the temperature distribution is continuous between the two subsystems.

6.4.3 Effects of working parameters

Electric field

The Joule heat is generated mainly by the electric conduction current in the electrolyte solution, and it is proportional to the square of the electric field strength $\partial\Phi/\partial z$ according to Eq. (6.13). Therefore it is anticipated that the magnitude of the electric field will greatly influence the Joule heating. It is shown that, under the condition specified in Figure 6-7, the temperature at the thermally developed region increases to above 70 ^{o}C for electric field of 3000 V. This temperature rise is significant and may cause some disastrous problems in applications of electrokinetic micropump systems. For instance, the operating temperature in the capillary may easily increase beyond the boiling point of the liquid phase under very high electric field strength. The vapor bubble will be generated, which will block the flow path of the liquid phase through the porous packing and finally stop the entire flow. In addition, the thermal entrance region extends much longer as increasing electric field, as shown in Figure 6-7(a).

The electroosmotic velocity is also determined by the electric field. From Eq. (20) it can be inferred that the EOF velocity is proportional to the electric field strength and uniform inside

the capillary if there is no Joule heating effect. However, from Figure 6-7(b), the presence of temperature rise changes the velocity distribution through the temperature-dependent viscosity and dielectric constant of the fluid phase, as well as the local electric field strength as discussed in the previous section.

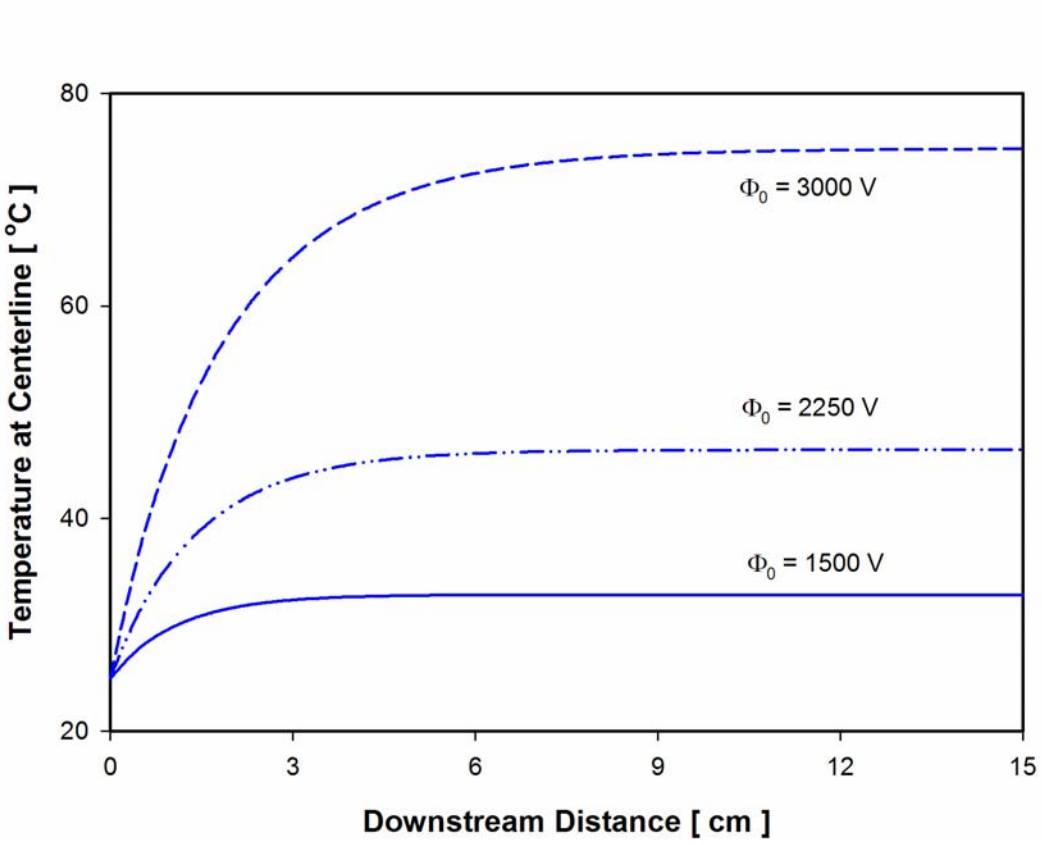

Figure 6-7(a)

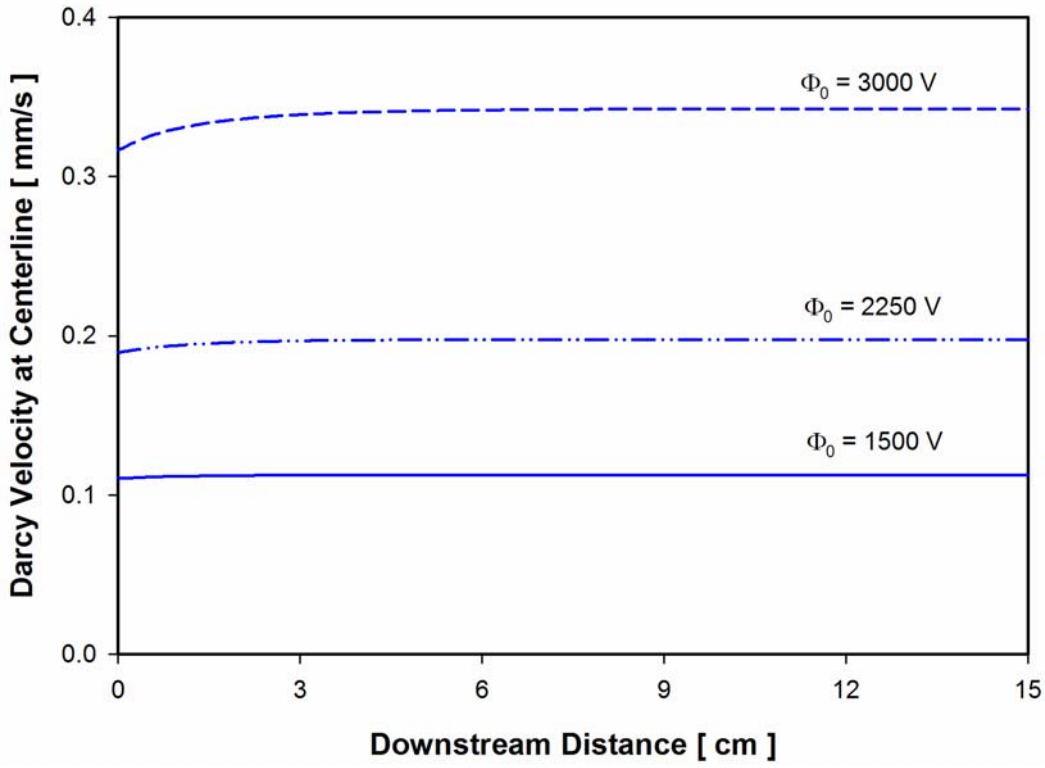

Figure 6-7(b)

Figure 6-7 Effect of applied electric field: (a) axial temperature distribution, (b) axial electroosmotic velocity distribution. Working parameters: capillary inner diameter d_w = 530 μm, capillary length L = 15 cm, packing particle size d_p = 6 μm, porosity ϕ = 0.4, tortuosity τ = 1.5, electrolyte concentration C = 10^{-3} M, zeta potential at particle surface ζ_p = 50 mV, and convection heat transfer coefficient at the capillary outer surface h = 5 W/m^2 K.

Ionic concentration

Ionic concentration is an intrinsic factor which has a strong effect on the Joule heat generation by influencing the electric conductivity of the fluid phase. It can be inferred that, from Eqs. (6.12-13), the electric conductivity λ and hence corresponding Joule heat

generation are proportional to the ionic strength *C*. Furthermore, the zeta potential of the solid phase usually decreases with increasing the ionic concentration of the electrolyte (Hunter, 1984). The effect of varying ionic strength and zeta potential is shown in Figure 6-8(a). It is apparent that use of electrolyte of high ionic strength will generate significant Joule heating. For instance the temperature rise in concentrated solution of 10^{-3} M is about 50 degree while the temperature rise in dilute solution of 10^{-4} M is about 1 degree only. When the temperature rise increases, the thermal entrance length increases accordingly for solution of higher ionic strength.

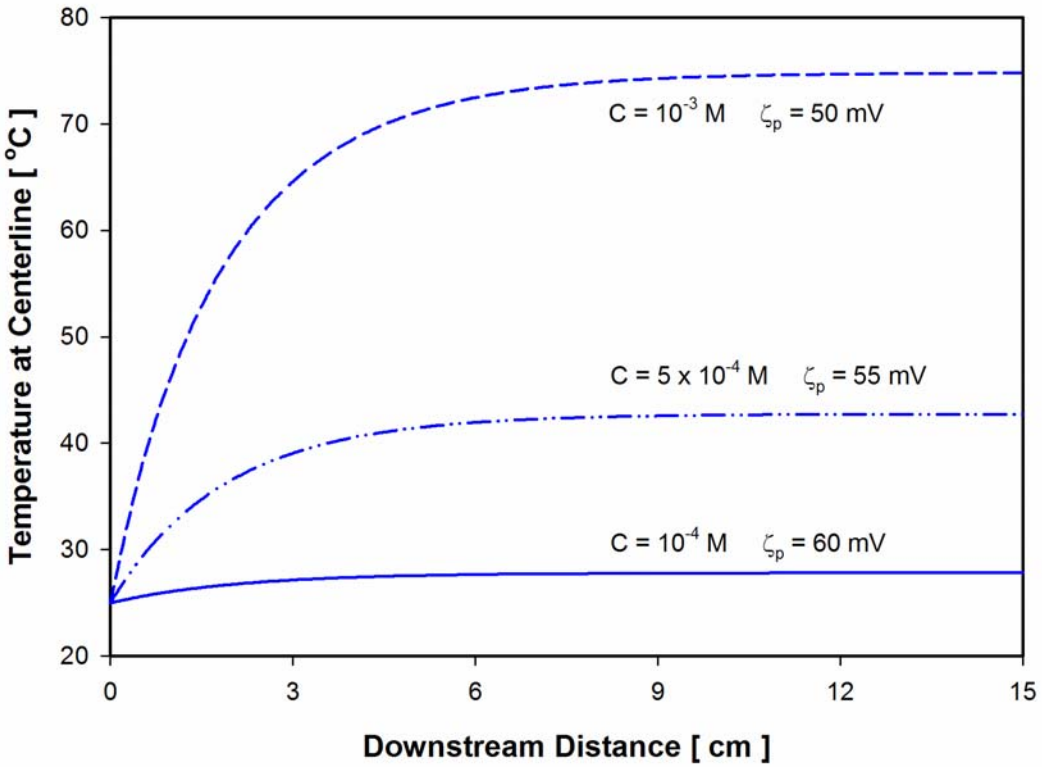

Figure 6-8(a)

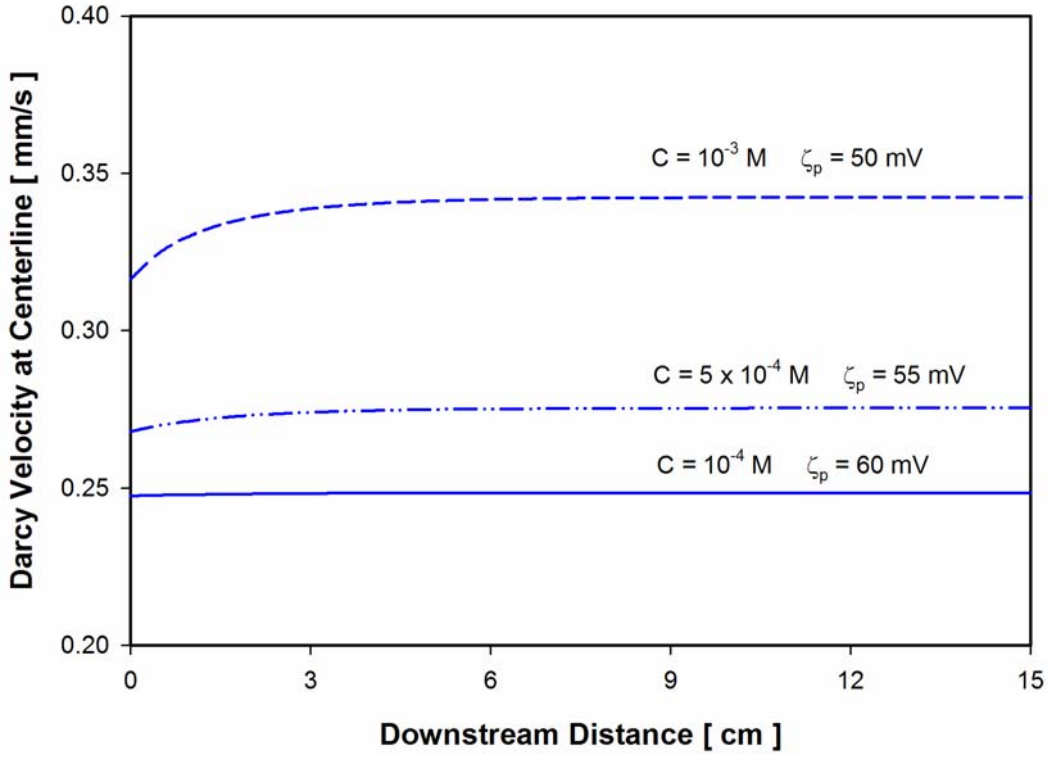

Figure 6-8(b)

Figure 6-8 Effect of electrolyte concentration and zeta potential at particle surface: (a) axial temperature distribution, (b) axial electroosmotic velocity distribution. Working parameters: capillary inner diameter d_w = 530 μm, capillary length L = 15 cm, packing particle size d_p = 6 μm, porosity ϕ = 0.4, tortuosity τ = 1.5, applied electric field Φ = 3000 V, and convection heat transfer coefficient at the capillary outer surface h = 5 W/m^2 K.

The large temperature rise has a great impact on the electroosmotic velocity as shown in Figure 6-8(b). Normally, the EOF velocity, which is proportional to the zeta potential ζ_p without considering the Joule heating effect, should be higher for lower electrolyte concentration due to the higher zeta potential. However, high ionic concentration can

generate magnificent temperature elevation when Joule heating presents. Since the high temperature rise reduces the fluid viscosity dramatically, the EOF velocity in more concentrated solution (10^{-3} M) is greater than that in dilute solution (10^{-4} M), which is in an opposite trend for the case without Joule heating.

Convection heat transfer coefficient

As discussed above, the Joule heat is transferred to the ambient mainly by radial conduction through the channel wall and then by convection with the surrounding air. Therefore it is expected that the heat transfer condition outside the channel wall will affect the temperature and velocity field inside the capillary. From the results shown in Figure 6-9(a), the cooling condition outside wall changes from natural convection (h = 5 W/m^2 K) to forced convection (h = 50 W/m^2 K), the centerline temperature drops by over 40 degree. And the thermal entrance length is reduced from 14 cm to 1 cm. The velocity field in Figure 6-9(b) basically follows the change of temperature with decreased magnitude for strong cooling condition. This cooling effect is important to reduce the Joule heating and improve the performance of the electrokinetic pump when using high electric field strength or high ionic concentration.

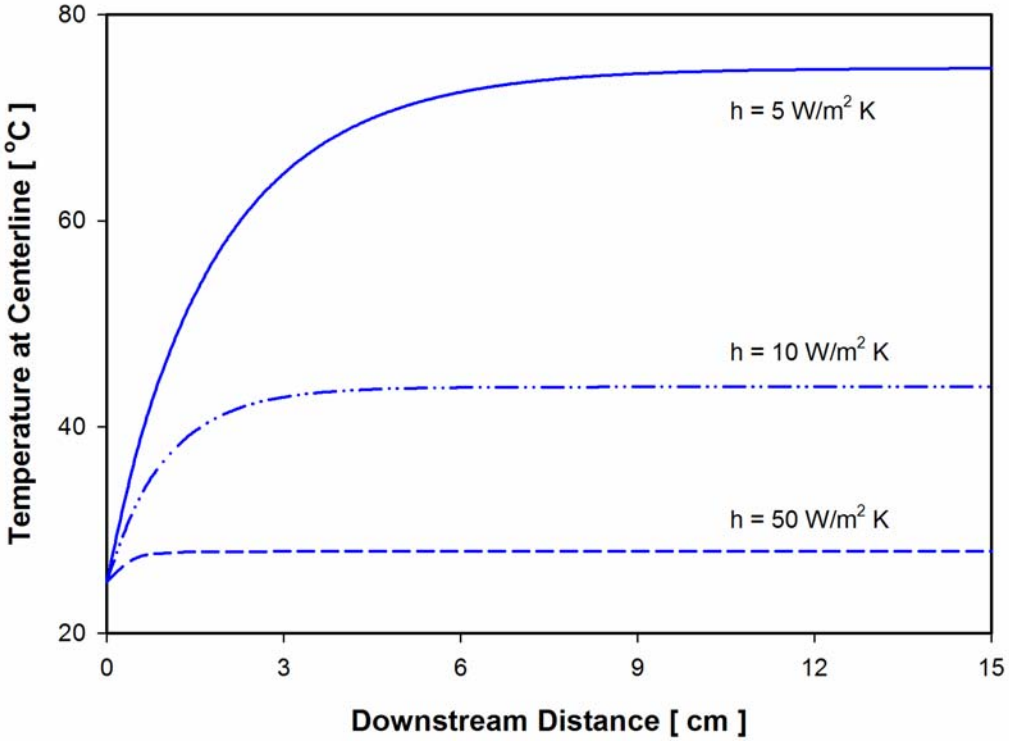

Figure 6-9(a)

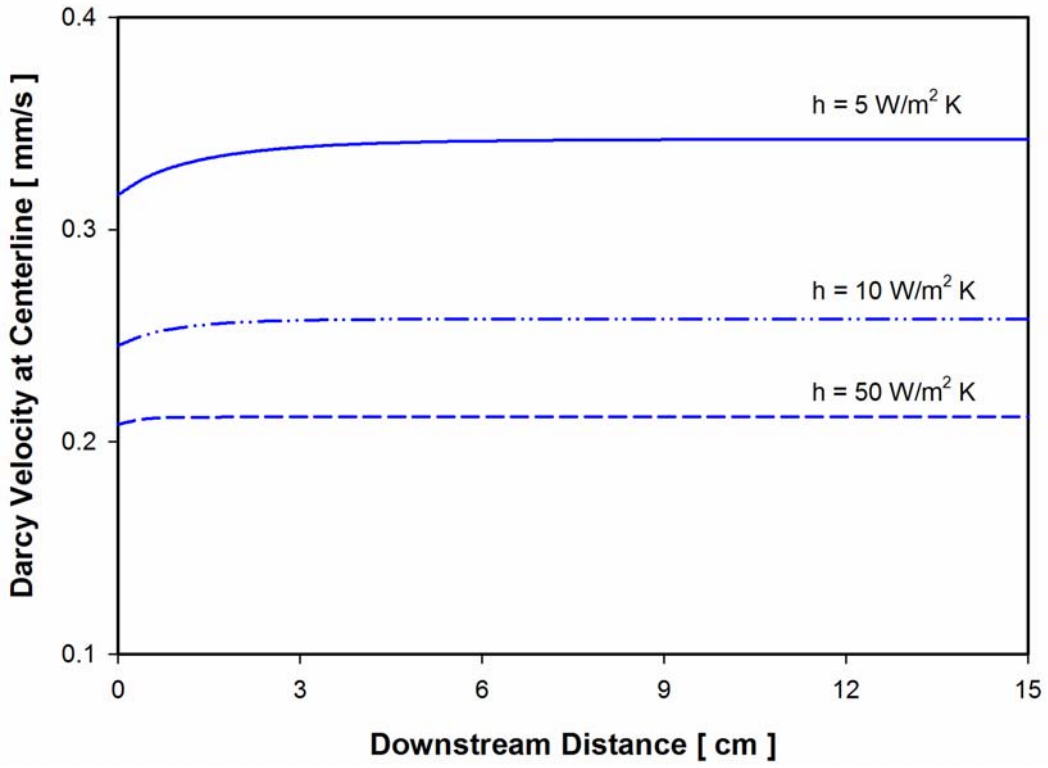

Figure 6-9(b)

Figure 6-9 Effect of the convection heat transfer coefficient at the capillary outer surface: (a) axial temperature distribution, (b) axial electroosmotic velocity distribution. Working parameters: capillary inner diameter d_w = 530 μm, capillary length L = 15 cm, packing particle size d_p = 6 μm, porosity ϕ = 0.4, tortuosity τ = 1.5, electrolyte concentration C = 10^{-3} M, zeta potential at particle surface ζ_p = 50 mV, and applied electric field Φ = 3000 V.

Capillary size

Figure 6-10(a) demonstrates the temperature distributions for three different capillary sizes. It is seen that the temperature rise is greater for larger capillaries. This is due to the fact that as the capillary size becomes larger the surface-area-to-volume ratio of the system becomes smaller, resulting in a lower ratio of the heat dissipation (measured by surface) to the Joule heat generation (measured by volume). This phenomenon is similar to the findings on Joule heating of the EOF in empty channels reported by Tang *et al*. (2004a) and Xuan *et al*. (2004a). Furthermore the thermal entrance region and the time needed for temperature to reach the steady state become greater for larger capillaries. Due to the low Reynolds number, the diffusion (conduction) effect predominates over the convection effect in current heat transfer process. Thus the time scale for the temperature to reach its steady state can be roughly estimated by letting the product of Biot number and Fourier number of the system equal to 1, i.e., $Bi \cdot Fo = \frac{hR}{k}\frac{kt^*}{\rho C_p R^2} = 1$ (Incropera and DeWitt, 2002). Hence the characteristic time is expressed as $t^* = \frac{\rho C_p}{h} R$, which predicts that the time scale for temperature development is proportional to the channel radius, *R*. In Figure 6-10 the time for the temperature to reach the steady state are about 400s, 600s, and 800s for capillaries of diameters 320 micron, 530 micron, and 700 micron, respectively.

It is well known that, in the absence of Joule heating, the EOF velocity is independent of capillary size according to Eq. (6.20). However in the presence of Joule heating, the fluid temperature increases with increasing capillary size as discussed above. This leads to a reduced liquid viscosity and in turn results in a greater EOF velocity as shown in Figure 6-10(b).

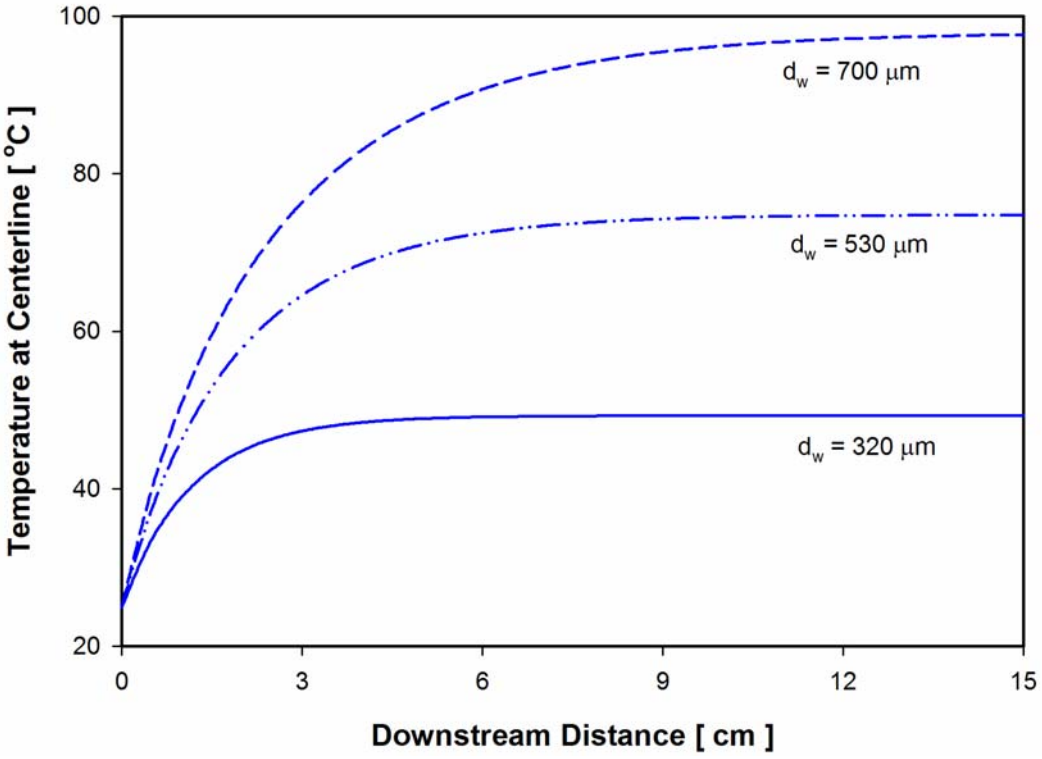

Figure 6-10(a)

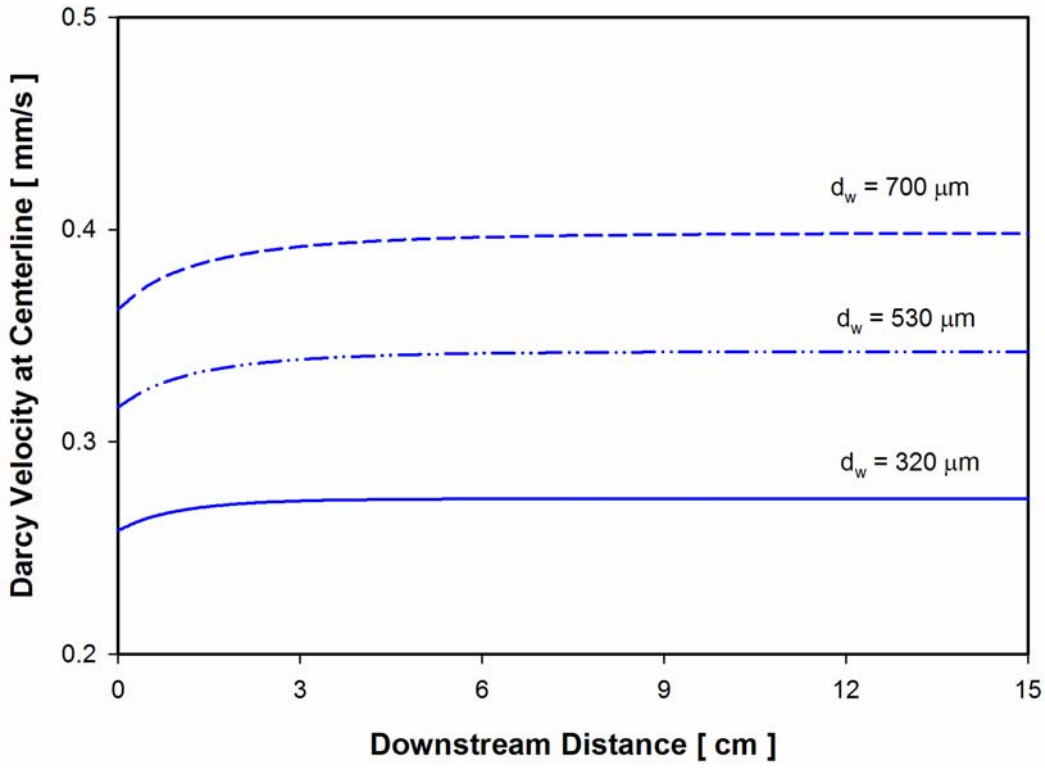

Figure 6-10(b)

Figure 6-10 Effect of the capillary diameter: (a) axial temperature distribution, (b) axial electroosmotic velocity distribution. Working parameters: capillary length L = 15 cm, packing particle size d_p = 6 μm, porosity ϕ = 0.4, tortuosity τ = 1.5, electrolyte concentration C = 10^{-3} M, zeta potential at particle surface ζ_p = 50 mV, applied electric field Φ = 3000 V, and convection heat transfer coefficient at the capillary outer surface h = 5 W/m^2 K.

Size of packing particles

Figure 6-11 presents the temperature and velocity fields for three different packing particles. It is seen that the influence of the packing particles on the Joule heating is insignificant. The temperature difference between 3 micron and 8 micron packing systems are almost indistinguishable. This is because of that variation of the particle size dose not change any thermophysical property of the system. In contrast the EOF velocity in 8 micron packing system is slightly higher than that in 3 micron packing system. This scenario is attributed to the fact that the pore size of the packed capillary R_{pore} increases proportionally to the particle diameter d_p (from Eq. (6.25)) and the increased pore size will enlarge the correction factor 1-G in Eq. (6.20) thus resulting in a higher EOF velocity. The dimensionless factor G, as defined in Eq. (6.22), physically denotes the ratio of the average EDL potential ψ_i over the pore cross-sectional area to the zeta potential ζ_p. For the same zeta potential, increasing the pore size leads to a reduced average EDL potential and hence a larger correction factor 1-G. However the change of the EOF velocity due to the particle size is small because the inter-particulate EDL potential only occupies very small fraction of the pore cross-sectional area, e.g., less than 10%. This small increment of velocity will in turn slightly enhance the advection of the flow inside the porous packing, resulting in a reduced temperature for 8 micron packing system as shown in Figure 6-11(a). But the Reynolds number is so small that the cooling effect due to the slightly enhanced advection is indistinguishable for different particle sizes.

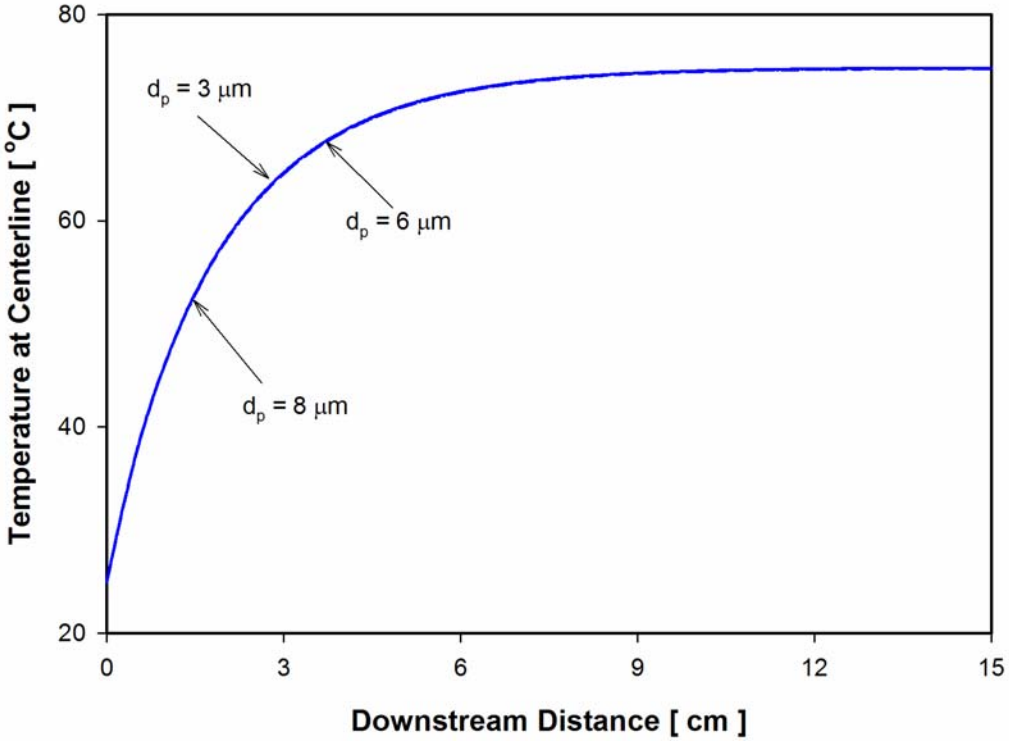

Figure 6-11(a)

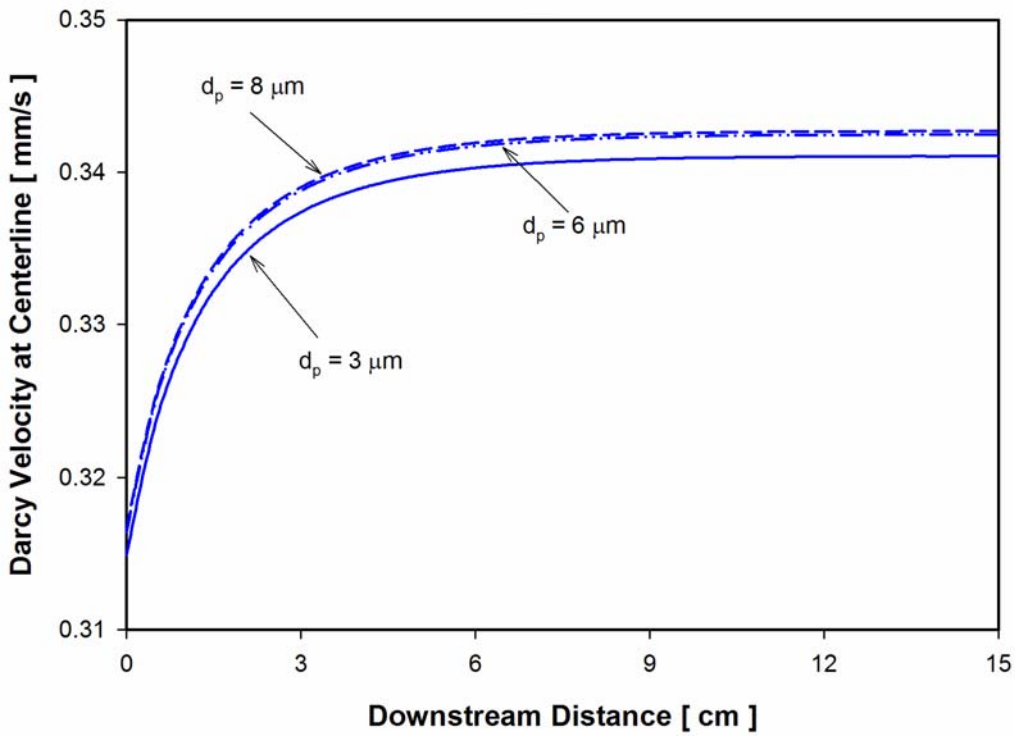

Figure 6-11(b)

Figure 6-11 Effect of the particle size: (a) axial temperature distribution, (b) axial electroosmotic velocity distribution. Working parameters: capillary inner diameter d_w = 530 μm, capillary length L = 15 cm, porosity ϕ = 0.4, tortuosity τ = 1.5, electrolyte concentration C = 10^{-3} M, zeta potential at particle surface ζ_p = 50 mV, applied electric field Φ = 3000 V, and convection heat transfer coefficient at the capillary outer surface h = 5 W/m^2 K.

6.5 Summary

A numerical model for evaluating the Joule heating effect on the electroosmotic flow in a capillary packed with microspheres is developed in this chapter. The model incorporates the momentum equation for the electroosmotic velocity derived in chapter 4, the energy equation for Joule heating induced temperature distributions in both porous packing and the capillary wall, and the mass and electric current continuity equations. The temperature-dependent physical properties of the electrolyte solution, including the viscosity, dielectric constant, and the electric conductivity, are taken into consideration. The coupled governing equations are numerically solved by the finite difference method.

The simulation predicts that, in the presence of Joule heating, there exists a significant axial temperature gradient in the thermal entrance region. This high temperature gradient strongly enhances the local electric field at the entrance, resulting in a non-uniform distribution along the flow direction. The radial temperature profile shows a parabolic distribution but the gradient is very small due to the small system Biot number. It is found that the Joule heating effect is significantly strong for high electric field strength, high ionic concentration of the solution, large capillary size, and weak cooling condition outside the capillary. All those factors have a great impact on the Joule heating by determining magnitude of temperature rise and the thermal entrance length. The capillary size and the heat transfer coefficient outside the capillary determine the time scale for transient development of the temperature field. The non-uniform temperature distribution in turn greatly affects the EOF velocity by means of changing the local viscosity and the dielectric constant of the fluid phase, and the local electric field strength. The results by this model are compared with available analytical and experimental works in the literature. And the

temperature difference between the capillary centerline and the inner wall as well as the temperature excess across the capillary wall is accurately in an agreement with the results predicted by Knox's formulae. The discrepancy of the transient temperature rise with Keim and Ladisch's experiment data is analyzed.

Chapter 7

Experimental Studies of the Electroosmotic Flow in Microcapillaries Packed with Microspheres

7.1 Introduction

In this chapter, an effort to fabricate and characterize a prototype of the electrokinetic pump is made. The entire experiment contains two main stages: column fabrication and flow measurement. The fabricated micropump is characterized under the influences of different working parameters, such as the size of the capillary and the packing particles, the working electrolyte and its ionic strength, the capillary length etc. And the experimental results will be compared with the theoretical model developed in chapter 4.

7.2 Column Fabrication

The packed capillaries used in current experiment are fabricated by using high pressure slurry packing technique (Zeng et al., 2001) as illustrated in Figure 7-1. Slurry pressure packing is the most widely used method to pack capillary columns for Capillary Electro-Chromatography (CEC) (Maloney, 2002). In this experiment, the unpacked capillary is connected to an in-house designed acrylic slurry reservoir, and the slurry reservoir is connected to a High Performance Liquid Chromatography (HPLC) pump. During the packing process, deionised (DI) water is continuously pumped under high pressure into the slurry reservoir to drive the particle slurry into the silica capillary until

the entire capillary is filled with packing particles. In the following every step in the packing process will be presented in details.

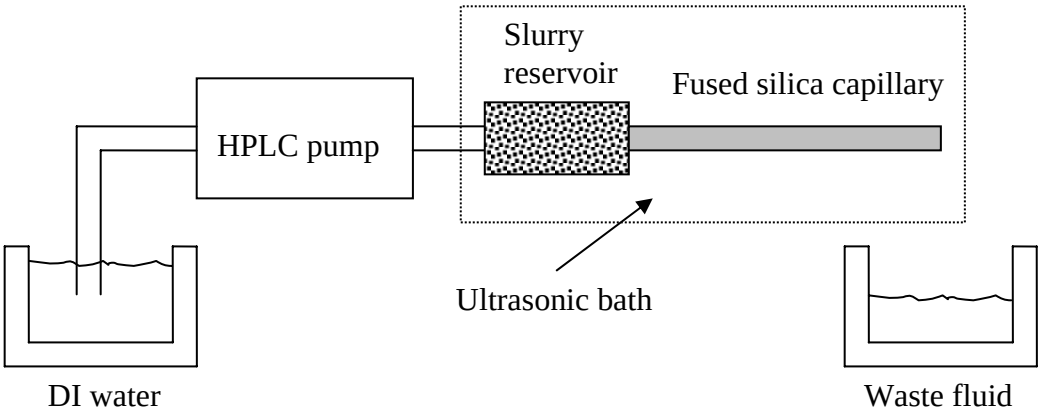

Figure 7-1 Schematic illustration of the experimental setup for column packing.

7.2.1 Preparation of the materials

Column preparation Fused silica capillaries (Polymicro Technologies Inc.) of inner diameter 320 μm, 530 μm, 700 μm are used as empty column. The capillaries are cut into pieces of a desired length (e.g., 5 cm long) from the capillary roll carefully and rinsed with acetone and DI water. After that the cleaned capillaries should be dried and kept in a dry place. This is because the bare fused silica material without polyimide coating at both ends will become fragile and easy to be broken in the moist air.

Slurry composition The packing material Inertsil C18 octyldecyl silica (ODS) particles (HPLC grade, GL Sciences Inc.) can provide the functional silanol groups which produce a negative surface charge when in contact with electrolyte solution. This surface charge is necessary to generate the electroosmotic flow. The behavior of the packing material depends on the type of the solvent and the density of the packing material in the slurry solvent. For the Inertsil ODS particles used in current experiment, it is found that Acetone or methanol alcohols are suitable solvent for better mixing. The concentration of

the particle is dependent on the desired length of packing. The longer the packing length, the higher the particle concentration. For packing length of about 5 cm in current experiment, 50-80 mg of particle mixed with l ml of methanol is recommended. For homogeneous mixing, the slurry is put in an ultrasonic bath prior use.

Slurry reservoir A slurry reservoir of inner diameter 3.9 mm and length 7 cm is fabricated using acrylic Perspex. The slurry reservoir is subject to a significantly high pressure in the slurry packing process, which requires the reservoir material be strong. Acrylic Perspex is good choice because it can withstand high pressure and also can be easily machined into desired size and shape.

7.2.2 Packing procedure

Retaining frit A retaining frit must be fabricated at one end of the empty column before column packing. The function of the retaining frit is to hold the packing material and resist the high pressure due to packing, flushing, or EOF. So it must be mechanically strong. Meanwhile the frit has to be highly permeable for the solvent flow; otherwise the EOF generated will be reduced at the outlet. The most common approach is the sintering method, in which the frit is constructed by sintering a plug of silica gel wetted with sodium silicate solution. Frit fabricated in this way can provide the best mechanical stability. The ODS particles are mixed with sodium silicate solution (14% NaOH solution, Sigma-Aldrich) with a ratio of 3:1 by weight. Only the gel or paste like substances in the mixing should be used. A gel plug of 2 mm long is packed into one end of the empty column by tapping (as in figure 7-2a). Then the capillaries with the gel plug are heated in an oven at 350 ^{o}C for about 30 minutes. This sintering process hardens the paste and allows the silica-sodium silicate mixing to adhere strongly to the capillary wall. Thus the retaining frit is formed.

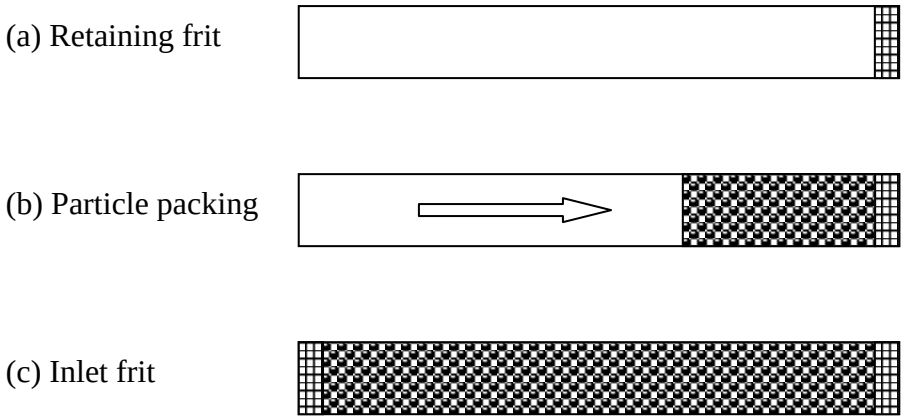

Figure 7-2 Schematic illustration of the packing procedure.

Slurry packing Once the retaining frit is ready, the other end of the capillary was connected to a pressure-driven slurry packing system, which includes a slurry reservoir and a high-pressure liquid chromatography (HPLC) pump (PU-2080, Jasco). PEEK fitting and tubing (Upchurch Scientific) are used for all connections. The particle-methanol slurry is sonicated for about 10 minutes before being loaded into the slurry reservoir. DI water is used as working fluid to drive the slurry into the capillary. The HPLC pump provides a constant pressure of 6 MPa to force the particles and the fluids into the capillary. The particles will accumulate beginning from the retaining frit (as illustrated in figure 7-2(b)), while the fluids pass through the interparticulate space and the frit into the waste reservoir. Due to the parabolic profile of the pressure driven flow, the particles tend to accumulate at the center of the capillary and the particle close to the capillary wall will be loosely distributed. To reduce this effect, the packed capillary is kept in an ultrasonic bath during the entire packing process. Around 5-10 minutes, the capillary is fully packed with ODS particle. DI water is still pumped into the packed

capillary (still in ultrasonic bath) at 5 MPa for 30 minutes to ensure the particles are densely and homogeneously packed.

Inlet frit After the capillary is firmly packed and rinsed, an inlet frit should be constructed to hold the other end of the packing. The sintering method of the inlet frit is different from that for the retaining frit which needs a long time in high temperature. The inlet frit doesn't need to be as mechanically strong as the retaining frit because it is not subject to high pressure. Therefore a local sintering method using a hot copper wire connected with a soldering iron is used to heat the particles at capillary inlet (as illustrated in figure 7-2(c)). This method can prevent the rapid evaporation of water inside the packing. After sintering for 5-10 minutes, the inlet the frit is constructed. Till now the micropump using packed capillary is finished, and it is ready for characterization.

7.3 Characterization and Flow Measurement

7.3.1 Porosity and tortuosity

Porosity and tortuosity are two important geometric factors characterizing of the packed EOF micropump. Porosity can be directly measured while tortuosity factor can only be measured indirectly.

Porosity According to the definition, the porosity denotes the ratio of the void space to the total space of the porous packing. One method to calculate the void space is by measuring the weight of the fluid inside the fully saturated porous packing. In current experiment, the porosity is calculate by

$$\phi = \frac{V_{\text{void}}}{V_{\text{total}}} = \frac{\left(\text{weight}_{\text{wet}} - \text{weight}_{\text{dry}}\right)/\rho}{AL} \tag{7.1}$$

where $\text{weight}_{\text{wet}}$ and $\text{weight}_{\text{dry}}$ denote the wet weight (saturated with DI water) and dry weight of the micropump, respectively. ρ is the density of the DI water. A is the inner

cross-sectional area of the pump and L is the physical length of the pump. It should be noted that the weigh of the pump, wet or dry, is corrected by excluding the weight of the frit

$$\text{weight}_{\text{frit, wet}} = \text{weight}_{\text{fritted column, wet}} - \text{weight}_{\text{unfritted column, wet}} \tag{7.2a}$$

$$\text{weight}_{\text{frit, dry}} = \text{weight}_{\text{fritted column, dry}} - \text{weight}_{\text{unfritted column, dry}} \tag{7.2b}$$

Tortuosity As discussed in chapter 4, the tortuosity factor, defined by $\tau = 1/\cos^2\theta = (L_e / L)^2$, denotes the non-alignment of most flow channels with the electric field, which is applied along the capillary axis. It was suggested by Rathore *et al.* (1999) that the tortuosity of the porous packing can be evaluated by measuring the resistances of the packed and unpacked capillaries. The effective cross-sectional area of the tortuous tubules is then (as illustrated in Fig. 4-1b-c)

$$A_e = \sum A_{\text{pore}} \cos\theta = \phi A / \sqrt{\tau} \tag{7.3}$$

The resistances of the empty and packed capillaries are $\varsigma L/A$ and $\varsigma L_e/A_e$, respectively, where ς is the resistivity of the working fluid. Thus the ratio of the resistances gives

$$\frac{R_{\text{empty}}}{R_{\text{packed}}} = \frac{\varsigma L / A}{\varsigma L_e / A_e} = \frac{\phi}{\tau} \tag{7.4}$$

Thus using the porosity value measured in previous step, we can calculate the value of the tortuosity by measuring the resistances of the empty and packed capillaries.

7.3.2 Test column method

One direct method to measure the electroosmotic flow velocity is by observing the movement of the fluid-air interface in a test column connected at the outlet of the micropump. Figure 7-3 demonstrates a setup of the test column method. Platinum wire is used as electrode and connected with a high-voltage power supply (Stanford Research Systems Inc.). To prevent the bubble generated by electrolysis from entering the

micropump, the electrode connected to the cathode is made into mesh-like shape, and kept in an open solution reservoir to let the bubble escape to the ambient. The micropump is primed with the working fluid with a HPLC pump for about 15 minutes before each run. The test column should also be primed with the working fluid and an air bubble is specially trapped inside the test column to prevent the retreat of the upstream fluid-air interface due to evaporation (as illustrated in Figure 7-3). The average volumetric electroosmotic flow rate Q_{av} can be calculated by measuring the time spent t for the fluid-air interface to travel a defined distance l inside the test column of inner diameter D_{test}, ie.,

$$Q_{av} = \frac{l}{t}\frac{\pi D_{test}^2}{4} \tag{7.5}$$

and the average velocity inside the micropump is determined by

$$U_{av} = \frac{Q_{av}}{A} = \frac{l}{t}\left(\frac{D_{test}}{D}\right)^2 \tag{7.6}$$

where A is the inner cross-sectional area of the packed capillary, D is the inner diameter of the packed capillary.

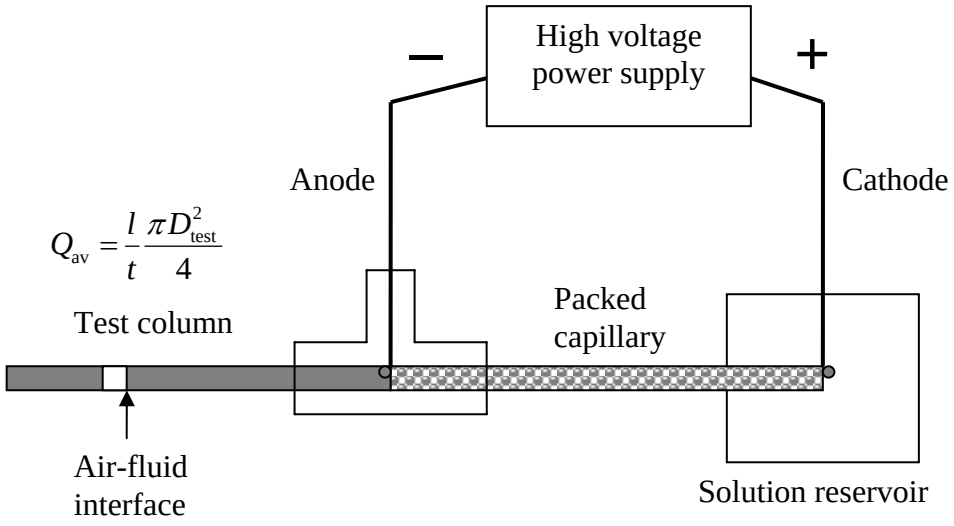

Figure 7-3 Schematic illustration of the experimental setup using the test column method.

7.3.3 Current monitoring method

An alternative method is also used to determine electroosmotic flow velocity by monitoring the electric current change when an electrolyte solution displaces the same but slightly more concentrated solution (or vice versa) inside the packed capillary (Arulanandam and Li, 2000b, and Sze *et al.*, 2003). Decrease in the solution concentration will increase the electric resistance of the micropump, resulting in a reduced electric current. As the solution of higher concentration inside the packed capillary is completely replaced by that of lower concentration due to the electroosmotic flow, the current will stop dropping and reach a constant value. The time taken t for the current to reach this constant value is regarded as the time for the electroosmotic flow to pass a distance of the capillary length L. Therefore the average electroosmotic flow velocity can be calculated as

$$U_{\text{av}} = L/t \tag{7.7}$$

A typical result for the current-time relationship is shown in Figure 7-4. In this case, the initial current upon application of an electric field at 200 V/cm is around 80 mA. As the time goes by, the current drops until it reaches a constant value at 23.5 mA. The time for the current change is about 240 seconds. Therefore, the estimated average velocity of the electroosmotic flow through a packed capillary of 50 mm long is calculated as 50/240 = 0.208 mm/s.

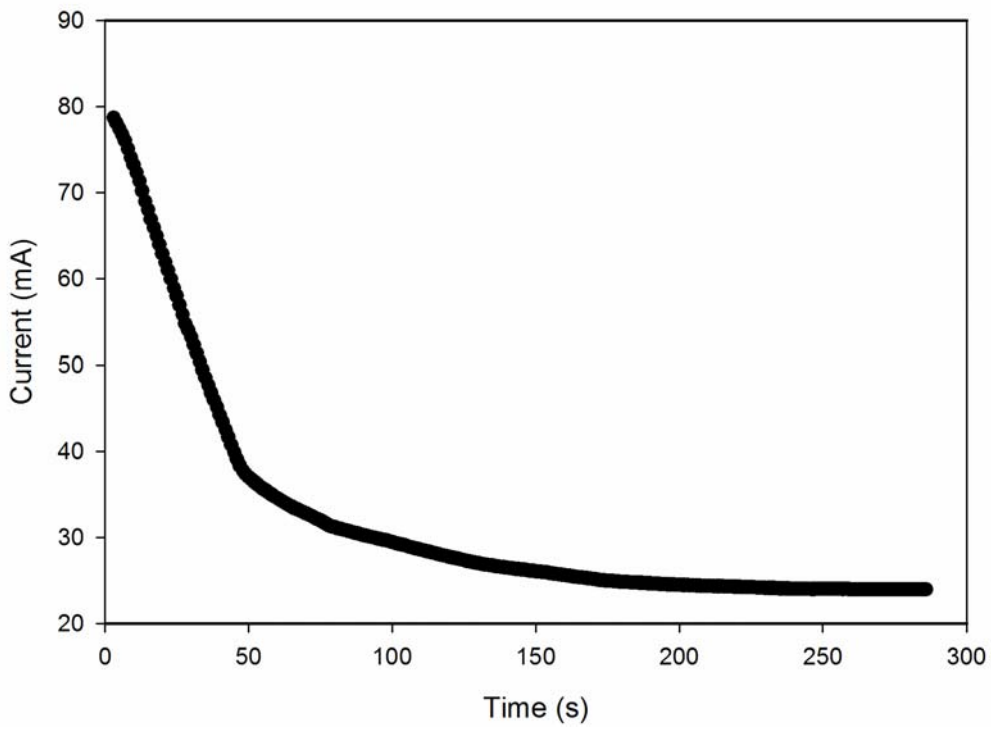

Figure 7-4 A typical relationship of current-time using current monitoring method.

The setup for the current monitoring method is shown in Figure 7-5. Both ends of the packed capillary are connected with the electrodes and kept in two open electrolyte reservoirs. The ionic strength of the solution in the upstream open reservoir is controlled at 80% of that of the more concentrated solution in the downstream open reservoir. Before being connected with the reservoirs, the packed capillary is primed with electrolyte of higher concentration. The high-voltage power supply and the current data acquisition are controlled by using Labview software (National Instrument Inc.).

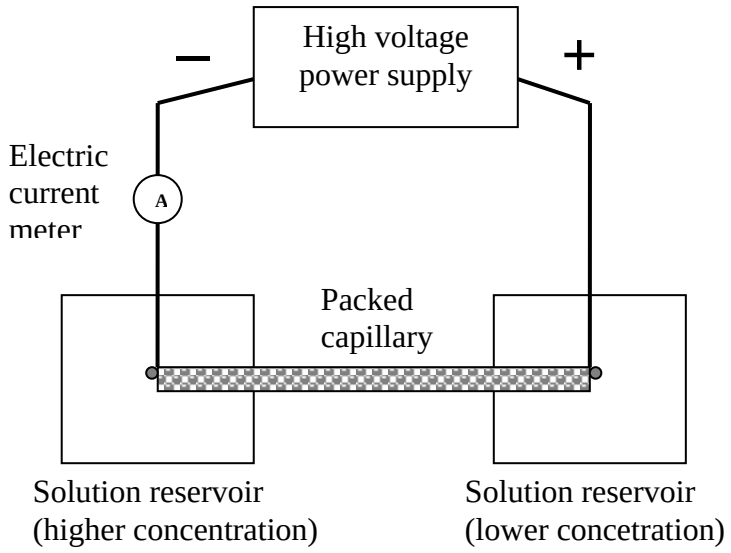

Figure 7-5 Schematic illustration of the experimental setup using the current monitoring method.

7.3.4 EOF velocity and zeta potential

Based on the discussion in chapter 4, if ignoring the boundary channel wall effects, the electroosmotic flow velocity can be estimated, from Eq. (4.7), as,

$$U_{\text{av}} = -\frac{\varepsilon_r \varepsilon_0}{\mu} E_0 \zeta_p \frac{\phi}{\tau}(1-G) \tag{7.8}$$

where

$$G = \frac{2}{\zeta_p R_{pore}^2} \int_0^{R_{pore}} r \psi_i(r) dr \tag{7.9}$$

If the Debye-Hückel linear approximation is used to solve the Poisson-Boltzmann equation, the EDL potential field inside the interparticulate tubules can be solved, from Eq. (B.20) as

$$\psi_i(r) = \zeta_p \frac{I_0(\kappa r)}{I_0(\kappa R_{pore})} \tag{7.10}$$

Substituting eq. (7.9) and Eq. (7.10) into Eq. (7.8), we can obtain

$$U_{\text{av}} = \frac{\phi}{\tau}\frac{\varepsilon_r \varepsilon_0}{\mu} E_0 \zeta_p \left[1 - \frac{2I_1(\kappa R_{pore})}{\kappa R_{pore} I_0(\kappa R_{pore})}\right] \tag{7.11}$$

where the pore size R_{pore} can be determined as $R_{pore} = \frac{\phi_\infty}{3(1-\phi_\infty)} d_p$ (Chapter 4). Hence from the porosity, tortuosity, and average EOF velocity measured in this study, the zeta potential at the particle surface can be evaluated by Eq. (7.11).

7.4 Results and Error Analysis

7.4.1 Scanning electron microscopy

Scanning electron micrograph (SEM) of a fabricated retaining frit is illustrated in Figure 7-6. The inner diameter of the fused silica capillary is 700 μm in inner diameter. It can be seen from Figure 7-6(a) that the solid matrix formed by dried sodium silicate strongly adheres the inner surface of the capillary wall and the particles. The micro-filaments of solid sodium silicate provide void space which is small enough to entrap the packing particles but large enough to let the fluid pass through, as shown in Figure 7-6(b). In this way, the frit can hold the porous packing inside the capillary without reducing the permeability of the micropump. In fact, DI water was flushed through an unpacked capillary with a retaining frit using a HPLC pump. The backpressure recorded is slightly greater (less than 0.003 MPa) than that needed to flush an unpacked capillary without frit, indicating that the frit does not significantly increase the flow resistance of the system. In addition, the frit fabricated using this method can withstand high packing pressure up to 150 MPa in this experiment, showing a good mechanical stability.

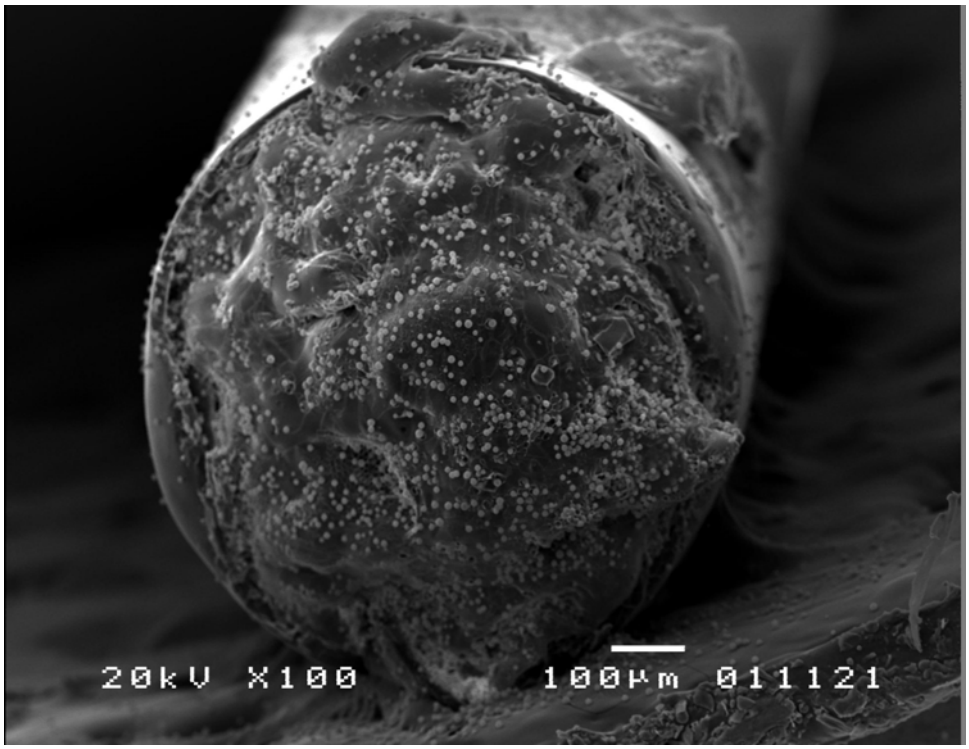

(a)

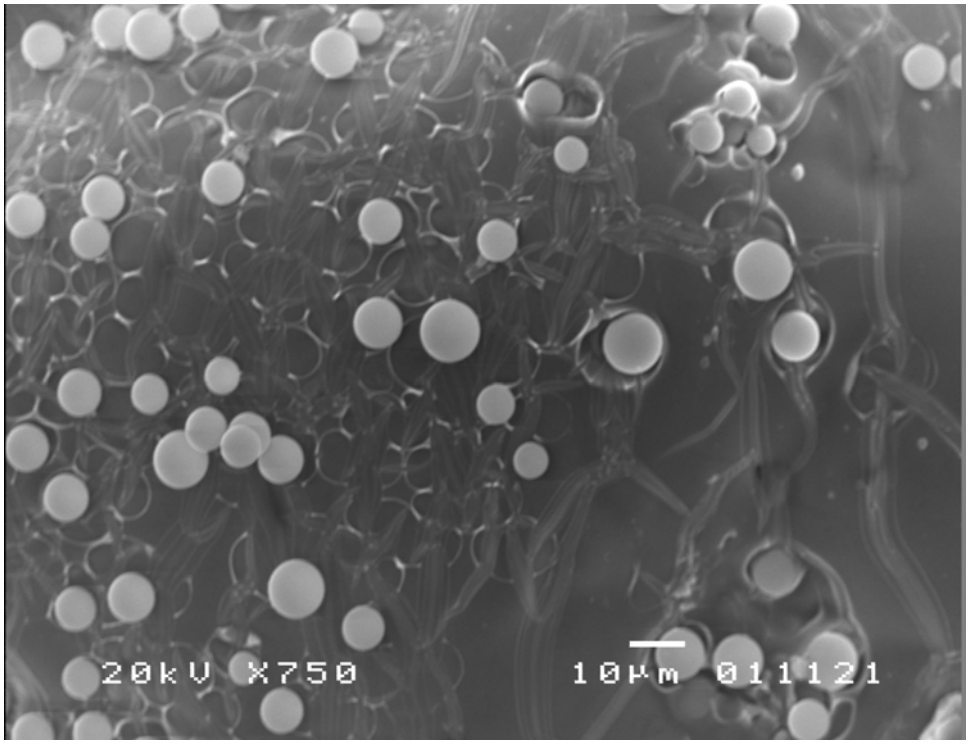

(b)

Figure 7-6 Scanning electron microscopic image of the retaining frit. (a) overall view of the frit in fused silica capillary of ID 700 μm, OD 850 μm. (b) a magnified portion of the frit.

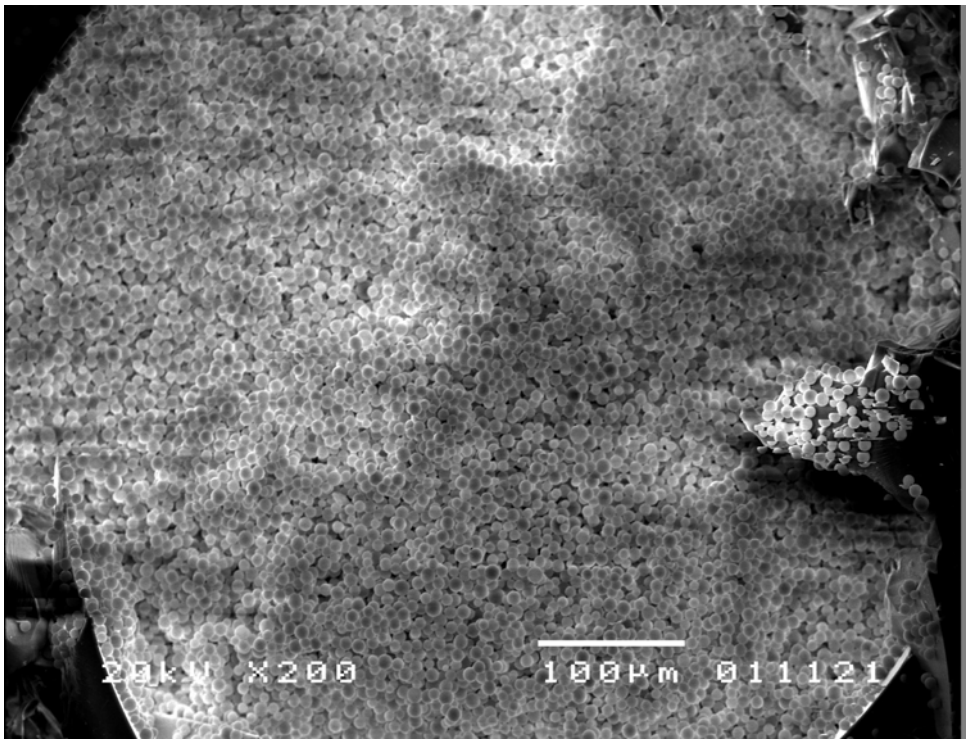

(a)

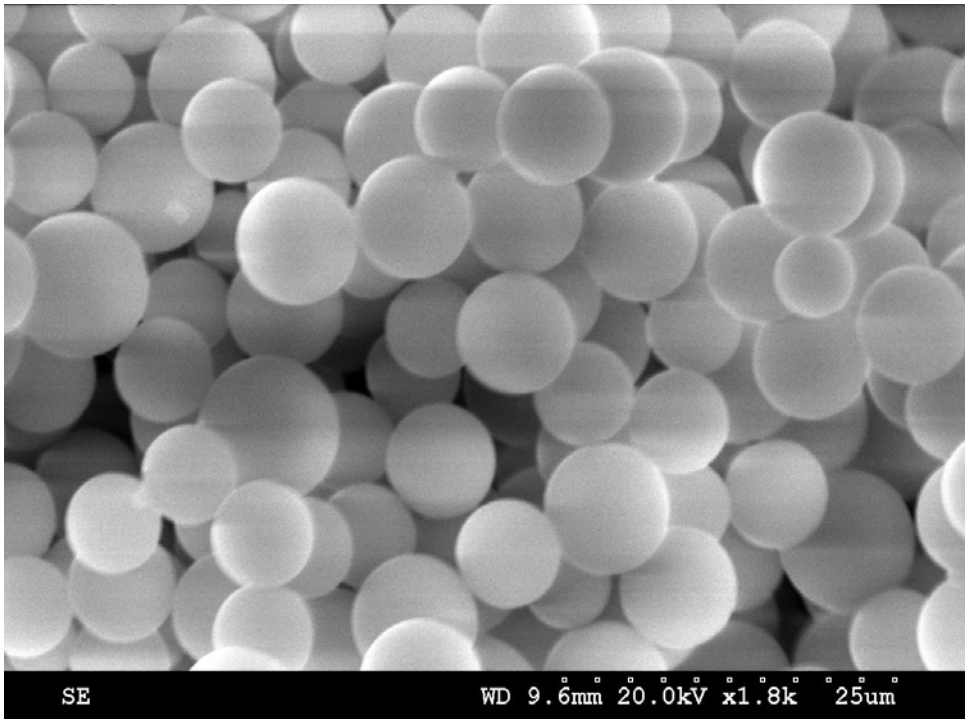

(b)

Figure 7-7 Scanning electron microscopic image of the middle cross-section of the microcapillary. (a) overall view of the cross-section in fused silica capillary of ID 700 µm OD 850 µm. (b) a magnified portion of the packed beds with ODS particles of 6 µm.

Figure 7-7 shows the SEM image of the bulk porous packing inside the capillary. This is the cross-section of a truncated capillary from the middle of the packed portion. It can be observed from that the particles are randomly and densely distributed inside the capillary. However, from a close view in Figure 7-7(b), it is found that the size of the packing particles is not uniform. Strictly speaking, there is a size distribution of the ODS particles. The size provided by the manufacturer, 6 μm in this case, is the average diameter of the particles.

7.4.2 Porosity and tortuosity

Porosity The porosity of three different packing conditions in terms of capillary size and particle size are measured as shown in Table 7-1. For uniform-size spheres, the smallest porosity is for the rhombohedral (or face-centered cubic) arrangement, which gives a porosity of 0.259. The random packing of uniformly sized spheres gives the porosity of 0.37 to 0.43 (Kaviany, 1995). The porosity values measured in this experiment, 0.39 to 0.43, are within the reported range. It is observed that the porosity changes monotonically with the ratio of the capillary diameter to the particle diameter d_c/d_p. This finding confirms the geometrical capillary wall effect predicted by the porosity distribution equation (4.9). According to Eq. (4.9), the local porosity close to the capillary wall increases with decreasing size ratio d_c/d_p, thus resulting in a higher average porosity.

Table 7-1 Results for porosity measurement

Capillary inner diameter d_c (μm)	Particle diameter d_p (μm)	Size ratio d_c / d_p	Average porosity ϕ
320	8	40	0.4325
530	6	88	0.4102
700	6	117	0.3866
530 (Zeng et al., 2001)	3.5	151	0.37

Table 7-2 Results for tortuosity measurement

Capillary inner diameter d_c (μm)	Resistance ratio $R_{empty} / R_{packed} = \phi / \tau$	Average porosity ϕ	Calculated tortuosity τ
320	0.312	0.4325	1.388
530	0.295	0.4102	1.391
700	0.277	0.3866	1.396
530 (Zeng et al., 2001)	0.247	0.37	1.5

Tortuosity Figure 7-8 shows the electric current change with applied voltage for microcapillaries filled with saturated NaCl solution (25 ^{o}C). Both capillaries are of the same size (700μm in inner diameter, and 5cm in length). One is unpacked. The other is packed with 6 μm ODS particles. At such high ionic strength and low voltage gradient, the double layer is so thin and the EOF is so weak that the conduction current predominates and the advection current due to electroosmotic flow can be ignored. Using the measured resistance ratio and the porosity, we can obtain the tortuosity. For instance, from Figure 7-8, we can obtain the resistance ratio of empty capillary to packed capillary is 0.277. This value is slightly higher than the value 0.24 reported by Zeng *et al.* (2001) for packing of 3.5 μm particles, but it is very close to the value 0.28 obtained by Rathore *et al.* (1999) for packing of 6 μm particles. According to Eq. (7.4) and the measured porosity value 0.3866, the tortuosity can be calculated as 1.396. The tortuosity measured in this experiment is between 1.388 and 1.396, which is close to the reported values: 1.5 (Zeng *et al.*, 2001) and 1.45 (Yao, *et al.*, 2003b). And it is also found from the experiment that the tortuosity values do not change greatly with the packing conditions. However, the correlation between the porosity and the porosity is apparent in Table 7-2, in which the tortuosity decreases with increasing the porosity. This correlation qualitatively agrees with the theoretical finding by Koponen *et al.* (1996), who numerically simulated the Newtonian incompressible fluid in a two-dimensional porous medium.

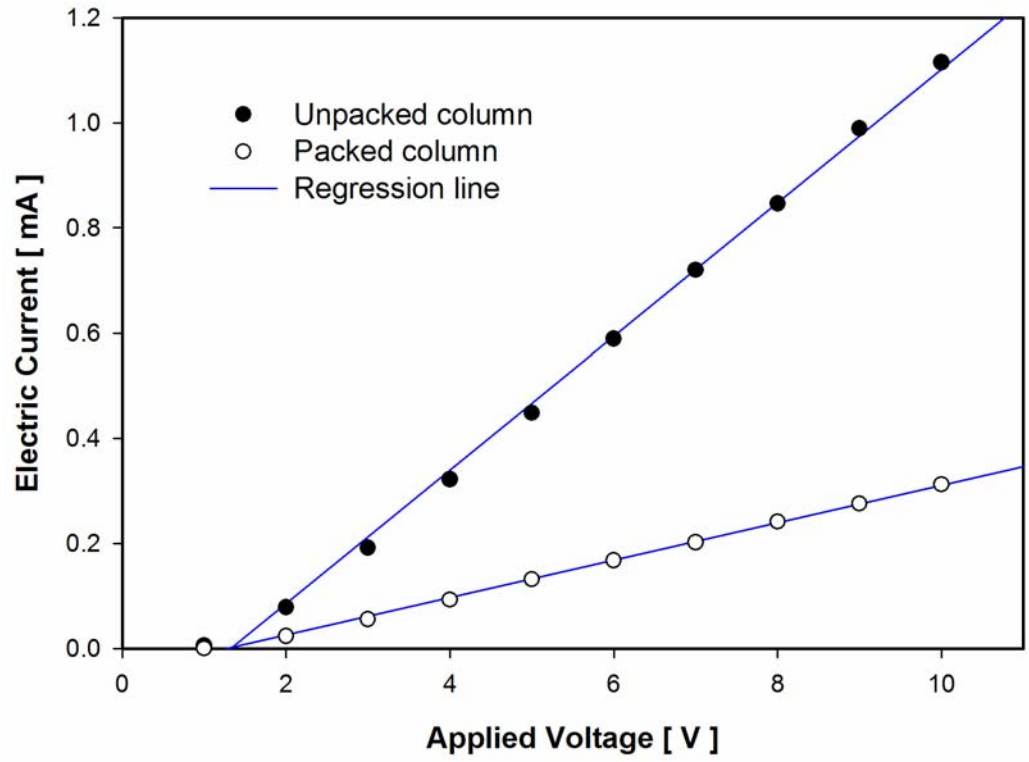

Figure 7-8 Electric current change with applied voltage for packed and unpacked capillaries (700μm in inner diameter, 5cm in length) filled with saturated NaCl solution at 25 °C.

7.4.3 Error analysis – the current monitoring method vs. the test column method

Current monitoring method According to Eq. (7.7), the uncertainty involved in the EOF velocity measurement using the current monitoring method is given by (Figliola and Beasley, 2000)

$$\Delta U = \pm\left[\left(\frac{\partial U}{\partial L}\Delta L\right)^2 + \left(\frac{\partial U}{\partial t}\Delta t\right)^2\right]^{\frac{1}{2}} \tag{7.12}$$

or expressed in ratio,

$$\frac{\Delta U}{U} = \pm\left[\left(\frac{1}{L}\Delta L\right)^2 + \left(\frac{1}{t}\Delta t\right)^2\right]^{\frac{1}{2}} \tag{7.13}$$

where ΔL is taken as half of the standard ruler's accuracy (ΔL=0.5mm). It can be seen in Figure 7-4 that the current change is not very sharp when the solution of higher concentration is totally replaced by the solution of lower concentration. Therefore, Δt is chosen as 10% of the total time measured. This treatment can include the human error caused by subjective estimation of the total time for the complete replacement of different solutions.

Test column method Similarly, from Eq. (7.6) the uncertainty for the EOF velocity using the test column method is given by

$$\frac{\Delta U}{U} = \pm\left[\left(\frac{1}{l}\Delta l\right)^2 + \left(\frac{1}{t}\Delta t\right)^2\right]^{\frac{1}{2}} \tag{7.14}$$

where Δl is taken as half of the standard ruler's accuracy (ΔL=0.5mm). Δt is chosen as 0.1 second to include the human response error when using a stop watch.

The test results of the average EOF velocity using two different measurement methods are shown in Figure 7-9. The electroosmotic flow velocity increases linearly with increasing electric field strength. However, the measurement error in the test column method is much larger due to the small displacement of the air-fluid interface (2 mm compared with 5 cm in the current monitoring method) and the short time duration for one test (several seconds compared with several hundred seconds in the current monitoring method). The small values for distance and time increase the uncertainty in the test column method. It is also observed that the results using the current monitoring method follows a linear regression line, while the results using the test column method deviate from the linear regression line, especially under condition of high electric field strength. This deviation may be due to the Joule heating effect under high electric field

strength. As discussed in previous chapters, the Joule heating effect becomes significant for the EOF in capillaries of large size due to the reduced heat dissipation capacity (i.e., lower surface-area-to-volume ratio). The temperature rise due to Joule heating will decrease the viscosity of the fluid, resulting in an increased velocity.

However, the drawback of using the current monitoring method is that the EOF velocity under high voltages (e.g., higher than 240 V/cm in Figure 7-9) cannot be measured. When using the current monitoring method under high voltages, the packed capillary will dry up around 20 seconds, which causes complete termination of the EOF. Small bubbles were observed inside packed capillary and the recorded current drops dramatically. The reason is also suspected to be the Joule heating effect due to the prolonged time for application of high voltage. But this effect can be reduced in the test column method, in which the measurement is taken for short time (several seconds) upon application of electric field. In this situation the temperature rise due to the Joule heating has not become strong enough to stop the flow. Thus the velocity can be measured before the capillary dries up. The other disadvantage of the current monitoring method is that the current-time relationship obtained by this method is highly non-linear if the concentration difference of the electrolyte is too large (say larger than 10%). Thus the time needed for the complete solution displacement cannot be accurately determined. Therefore it causes a relatively larger error in measuring the average EOF velocity. The non-linear relationship is caused by variation of the EOF velocity during the displacing process due to the change of the zeta potential in solutions of large concentration gradient (Ren et al., 2001). Actually smaller ionic concentration differences, such as 10% and 15%, were tried during the initial testing. However no apparent current change was observed for smaller ionic concentration difference. The apparent current drop was observed only when the concentration difference increases to 20%. This is different from the observation by Ren

et al using the current monitoring method in unpacked microcapillaries (Ren *et al.*, 2001), in which the current-time relationship is highly linear under small concentration difference (5%). We speculate that this phenomenon is because the porous structure greatly changes the way of the electric current going through the whole system. However the underlying mechanism of this discrepancy remains misty and requires further investigations.Therefore in this experiment both methods are employed in velocity measurement for different voltage ranges.

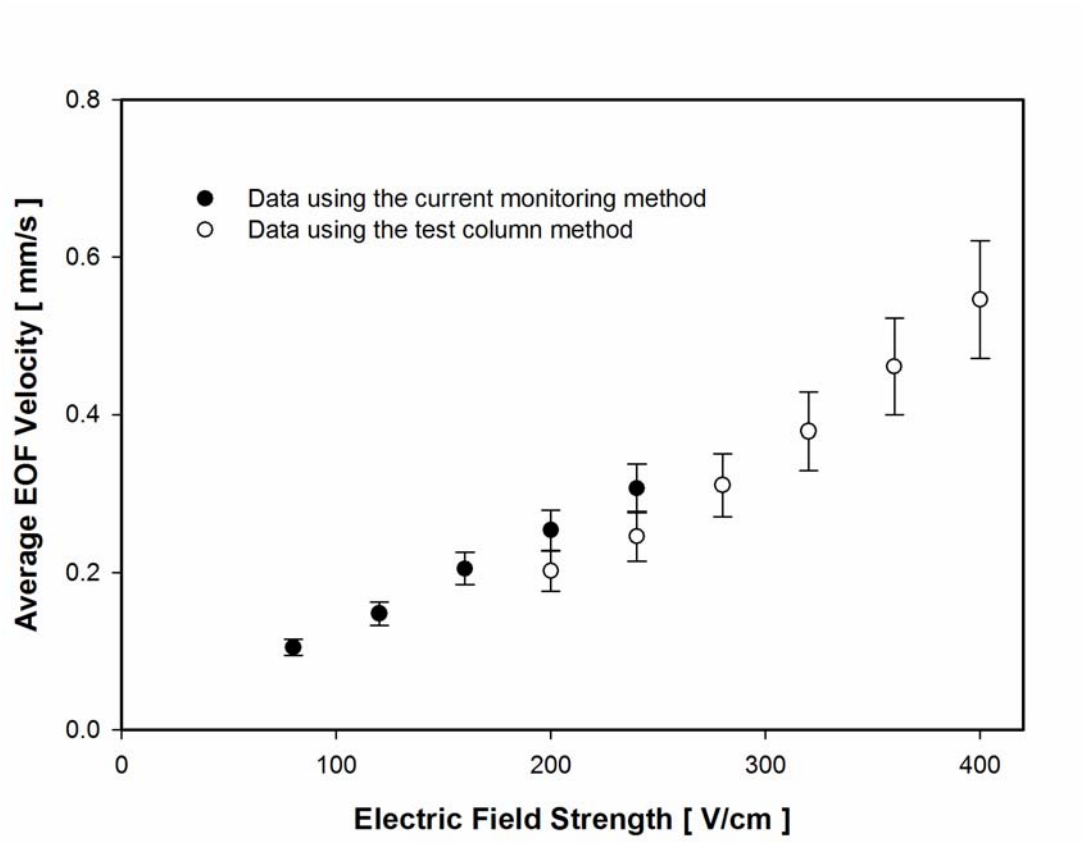

Figure 7-9 Comparison of the average electroosmotic velocity using the current monitoring method and the test column method. The working fluid is 10^{-5} M NaCl solution in capillary of inner diameter 700 μm.

7.4.4 Effects of working parameters

Capillary diameter

Theoretically if we ignore the boundary capillary wall effect, the EOF velocity should be independent of the capillary size. However, the wall effect should be included when the ratio of the capillary diameter to the particle diameter d_c/d_p is small (for instance less than 50). And this geometrical wall effect is demonstrated in figure 7-10 in which the velocity for three different capillary sizes are presented. As discussed in the previous section, the size ratio d_c/d_p affects the average porosity ϕ of the packed capillary. For the same particle size, the porosity increases with decreasing capillary diameter (in table 7-1), resulting in a higher EOF velocity according to Eq. (11).

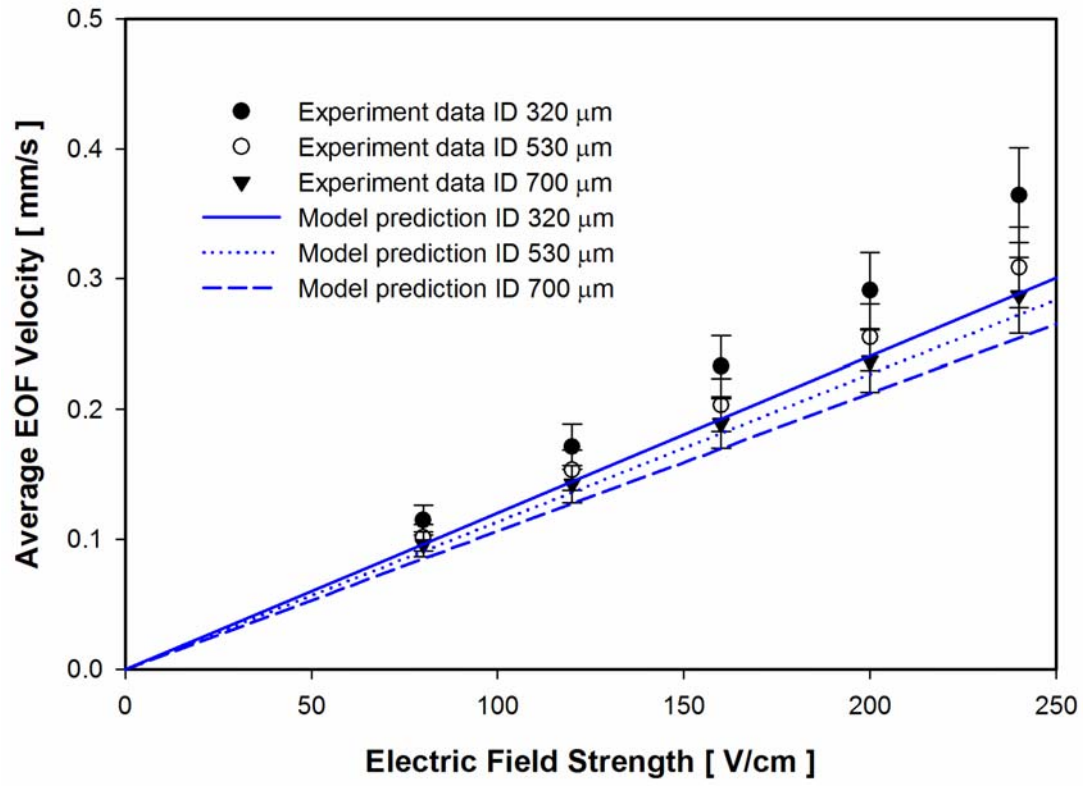

Figure 7-10 Average EOF velocity for different capillary inner diameters using the current monitoring method. Working solution is 10^{-4} M NaCl solution. Capillary length 5 cm. Packing particle size 6 μm. Frit length 1 mm.

The results predicted by the theoretical model (Eq. (4.32)) developed in chapter 4 is also presented as a comparison with the experimental data obtained from the current monitoring method. The values of the porosity and tortuosity are taken from the measurement in this study. However, the values of the zeta potential for silica particles in specified NaCl solutions cannot be found from the literature. So we chose to estimate the zeta potentials from the experimental results (Eq. (7.11)) using the test column method. It can be seen that the theoretical model underestimate the actual EOF velocity. At least part of this discrepancy is due to the value input of the particle zeta potential. Thus some other more accurate methods for measuring the particle zeta potential should be applied. Nonetheless, the theoretical model can reasonably predict the performance trend of the packed electroosmotic micropump.

Ionic strength

It is well known that the zeta potential is dependent on the ionic strength of the electrolyte solution (Hunter, 1984). The experimental results of the zeta potential for three different types of electrolyte solution at various concentrations are presented in Table 7-3. It is apparent that the magnitude of the zeta potential decreases with increasing ionic strength. However the zeta potential measured by using Eq. (7.11) is only a rough estimation because this equation is based on the simplified model and all the experimental errors will be passed to the measured zeta potential. Strictly speaking the zeta potential of the silica particle surface should be measured independently using other methods, such as electroacoustic approach (O'Brien et al., 1995), by determining the particle electrophoretic mobility.

Table 7-3 Zeta potentials at the particles surface for different electrolyte concentrations

	10^{-3} M	10^{-4} M	10^{-5} M
NaCl	45.12	56.12	67.18
Boric Acid	-	48.26	66.06
Acetic Acid	-	47.83	-
NaOH	32.96	40.54	-

Since the electroosmotic flow velocity is proportional to the particle zeta potential, a change in electrolyte concentration has an impact on the average EOF velocity by changing the particle zeta potential. The EOF velocity for different NaCl concentration measured by the current monitoring method has been shown in Figure 7-11. As anticipated, the EOF velocity for low concentration (10^{-5} M) is greater than that for high concentration (10^{-3} M) because the zeta potential at concentrated solution is lower than that in dilute solution.

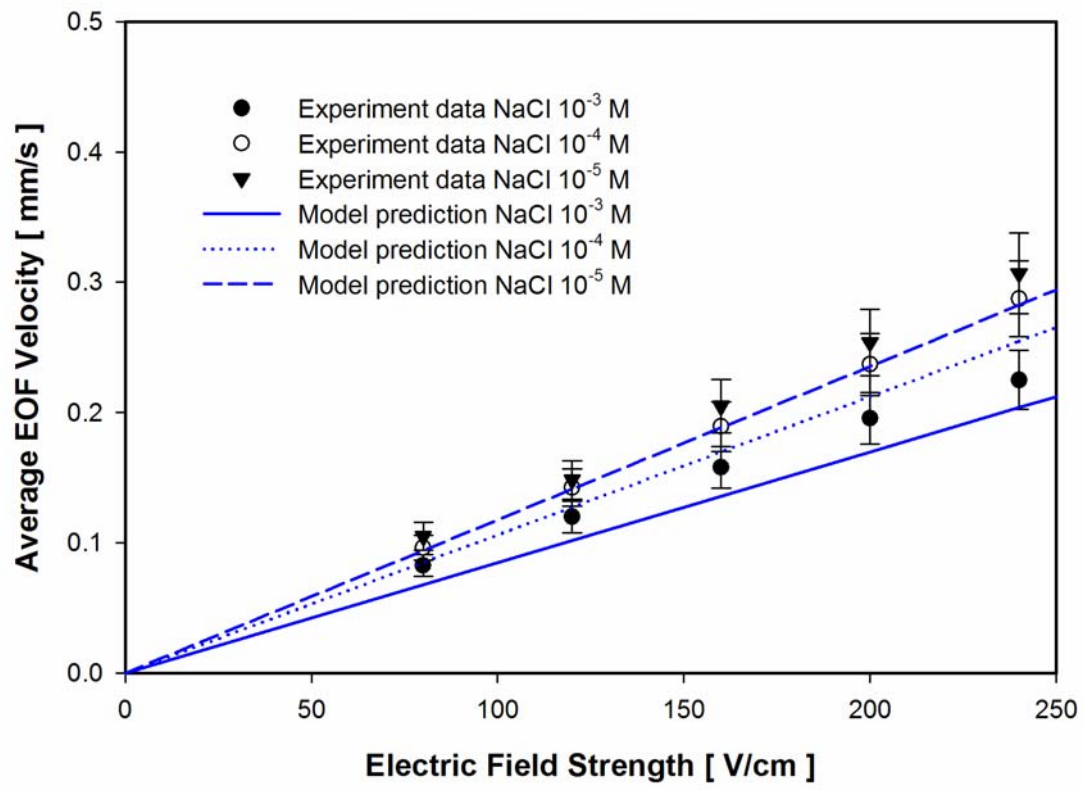

Figure 7-11 Average EOF velocity for different NaCl solution concentrations using the current monitoring method. Capillary length 5 cm. Capillary inner diameter 700 μm. Packing particle size 6 μm. Frit length 1 mm.

Particle size

Obviously, variation of the packing particle size also changes the size ratio d_c/d_p. The average porosity will be higher for the packing of larger particles. Furthermore the pore size R_{pore} also increases monotonically with increasing particle diameter d_p. From Eq. (7.9) we can infer that for a larger pore size the dimensionless average EDL potential G is smaller and the factor 1-G is greater. Thus it can be predicted by Eq. (7.8) that the EOF velocity is greater for larger particle size, which has been proved by the experimental results in Figure 7-12.

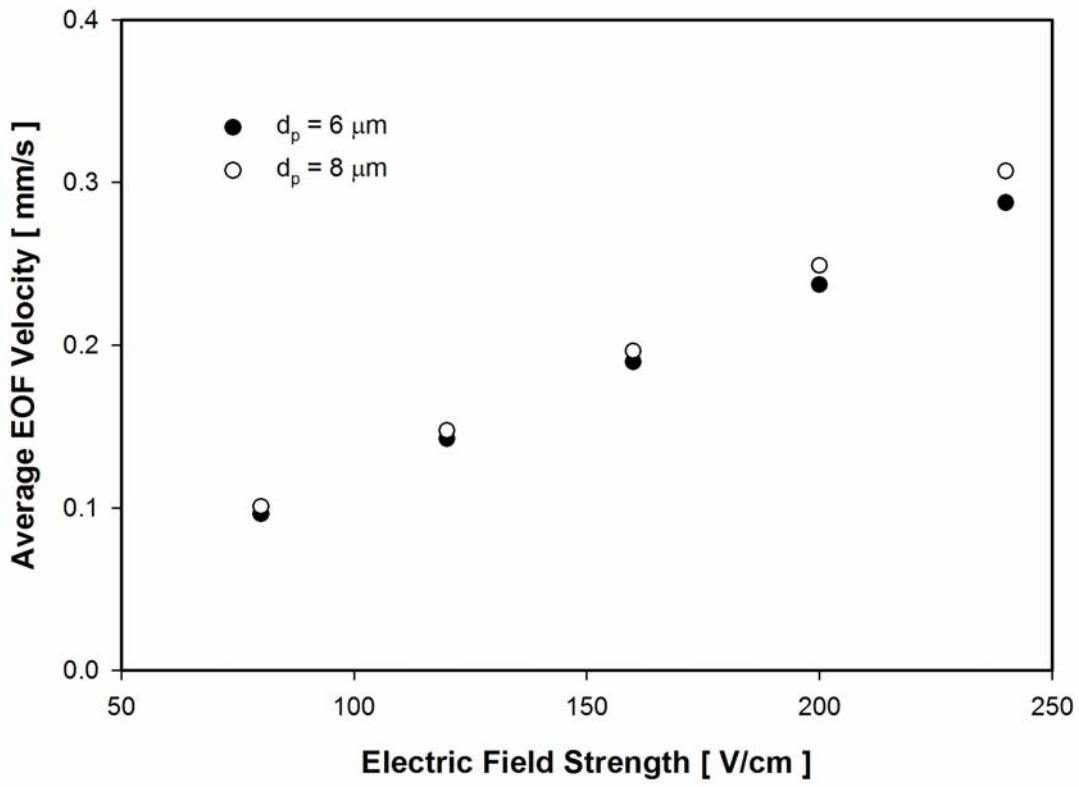

Figure 7-12 Average EOF velocity for different packing particles. Working solution is 10^{-4} M NaCl solution using the current monitoring method. Capillary length 5 cm. Capillary inner diameter 700 μm. Frit length 1 mm.

Type of electrolyte solution

The EOF velocity generated using four different kinds of electrolyte solutions at the same ionic strength is compared in Figure 7-13. It can be seen that at the same ionic

strength use of NaCl solution can generate highest EOF velocity, while use of NaOH generate the lowest EOF velocity. According to Eq. (7.11), the EOF velocity is dependent on the physicochemical parameters, which include zeta potential ζ_p, dielectric constant ε_r, viscosity μ, and Debye parameter κ. Since the electrolyte solutions are dilute and of the same concentration, the values of the dielectric constant, viscosity, and Debye parameter do not differ much from those of water. However, the zeta potentials for the varied types of solutions are different. From this experiment, the measured zeta potentials for these four solutions are shown in Table 7-3. Therefore the EOF velocity values are different for the four types of solutions.

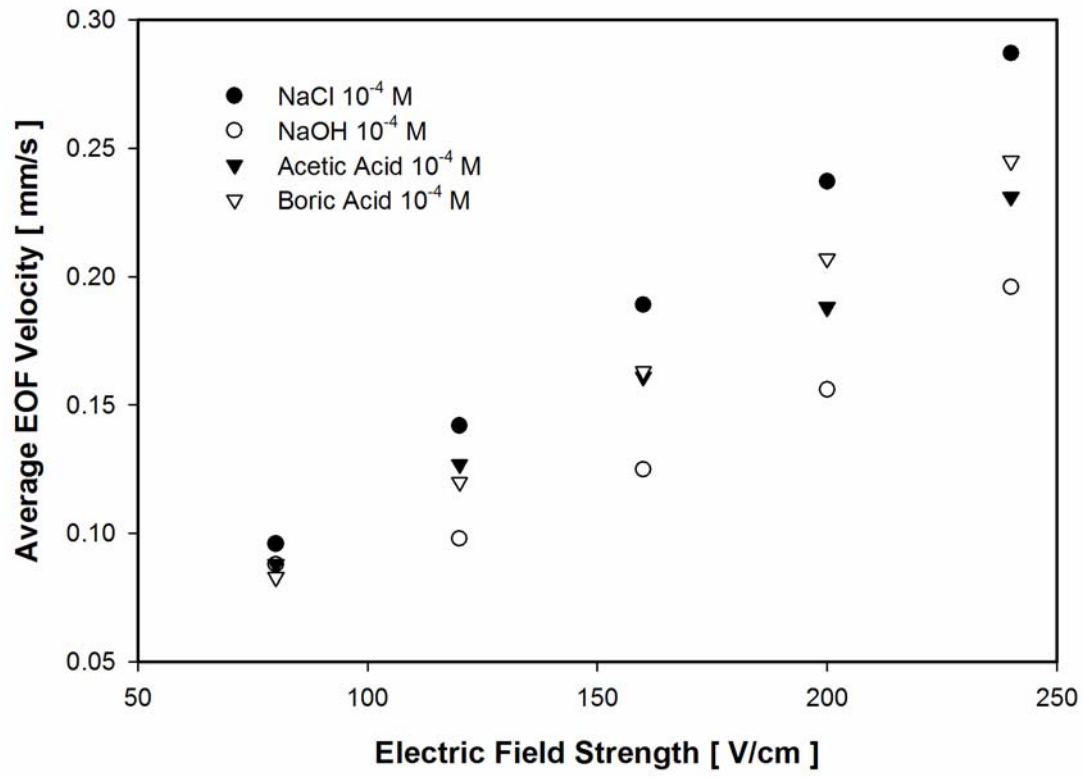

Figure 7-13 Average EOF velocity for different electrolyte solutions using the current monitoring method. Capillary length 5 cm. Capillary inner diameter 700 μm. Packing particle size 6 μm. Frit length 1 mm.

Capillary length

Theoretically the generated EOF velocity is independent of the length of the packed capillary. To confirm this prediction, three packed capillaries of different length are tested. The results are shown in Figure 7-14. It is can be seen that the EOF velocities for different packed lengths are apparently the same.

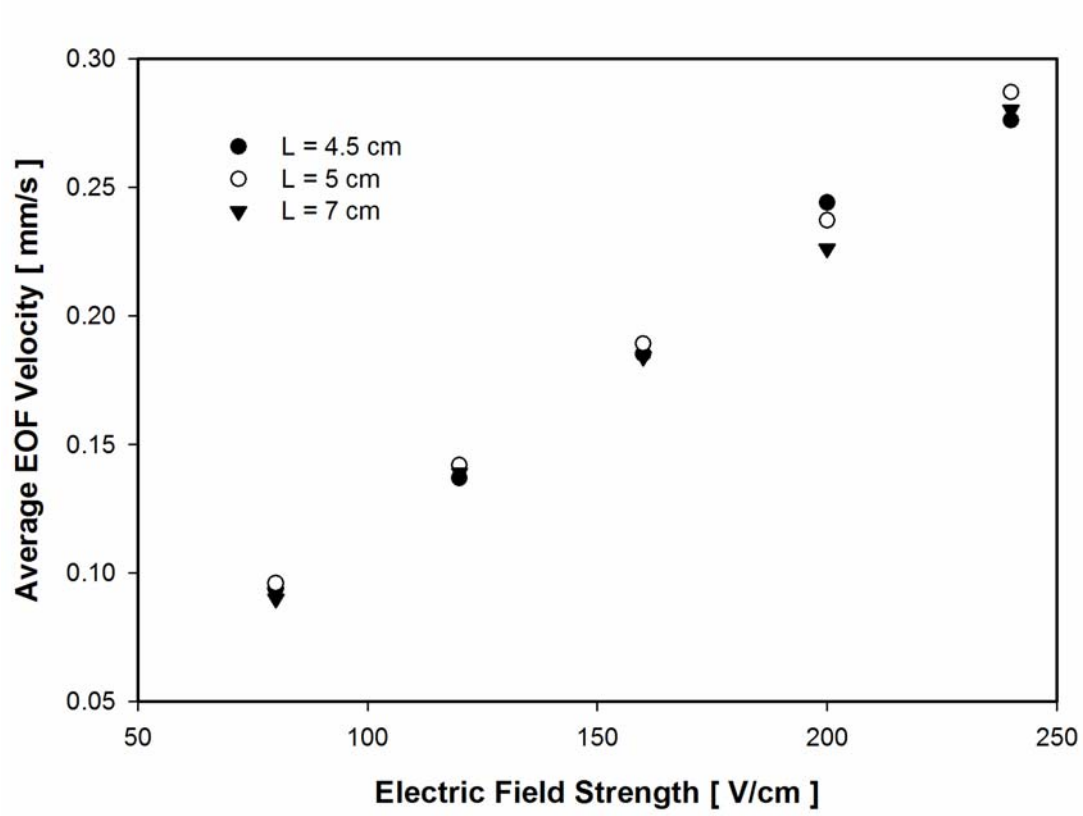

Figure 7-14 Average EOF velocity for different capillary lengths using the current monitoring method. Working solution is 10^{-4} M NaCl. Capillary inner diameter 700 μm. Packing particle size 6 μm. Frit length 1 mm.

7.5 Summary

Electrokinetic micropumps using electroosmotic flow in microcapillary packed with spherical silica microparticles are fabricated. Two methods, the test column method and the current monitoring method, are used to characterize the fabricated EK micropump under the influences of the capillary size, particle size, the capillary length, and concentration and type of the electrolyte solutions. It is found that the porosity of the packed capillary increases with increasing the ratio of the capillary diameter to the particle diameter. This is due to the geometrical boundary wall effect. The change of porosity due to variation of the size ratio affects the generated electroosmotic velocity inside the micropump. The ionic concentration and the type of the electrolyte solution also have a great impact on the velocity by determining the magnitude of the zeta potential at the surface of the silica particles. However the length of the packed capillary does not have any effect on the flow velocity. It is noted that the current monitoring method can give a more stable and consistent results than test column method which is subject to a much larger error scale. And the deviation of the results from the average regression line under high electric field strength may due to the Joule heating effects. But the test column method is advantageous to measure the EOF velocity under high electric field strength. The experimental data is compared with the theoretical model developed in chapter 4, and a reasonable agreement is found. The theoretical model is useful to the design and optimization of the micropump.

Chapter 8

Conclusion and Future Studies

8.1 Contributions Made by This Study

Following the objectives of this thesis, extensive and rigorous modeling on the dynamic electroosmotic flow in microcapillary packed with a porous medium has been developed and analyzed under varied physicochemical conditions. An experiment on the fabrication and characterization of an electrokinetic micropump has been conducted and extensive experimental data have been obtained. An in-depth understanding of the electrokinetic transport phenomenon through porous media has been achieved. The major contributions made during the course of this study can be summarized as follows:

1. ***Dynamic aspects of electroosmosis in microcapillary*** Transient electroosmotic flow in response to the application of time-dependent electric field is obtained by using Green's function method. The benefit of using Green's function method is obvious that mathematically the Green's function represents the basic solution for the disturbance from a point source. In this study, once the Green's function the electroosmotic flow has been derived, the solutions to the perturbation of varied kinds of time-dependent electric fields can be obtained easily from the integration of the specified Green's function. In the modeling of charge distribution within the electric double layer (EDL), the Boltzmann distribution is assumed, which, strictly speaking, is applicable only when the system is in the thermodynamic equilibrium state. Therefore a validation to this assumption is provided. An analytical scheme regarding the non-linear term is applied to solve the complete Poisson-Boltzmann (P-B) equation for electrostatic potential of the double layer.

This treatment avoids the limitations, such as low zeta potential or large electrokinetic diameter, of other linearization methods. The results show virtually no difference from numerical solution. The characteristic time for the flow to reach its steady state is proportional to the square of the channel radius. The evolution of the electroosmotic flow upon application of a constant electric field exhibits a unique flow profile, which is resulted from the contributions due to the electric body force and hydrodynamic viscous stress. On the other hand, the flow devolution after the external electric field is switched off follows a flow pattern solely controlled by hydrodynamic friction due to liquid viscosity. In addition, it is found that the oscillating electroosmotic flow is strongly dependent on the modulation frequency of the applied sinusoidally alternating electric field, which determines the thickness of unstable Stokes layer, and thus governs the extent of the harmonic oscillation and the velocity distributions of the oscillating electroosmotic flow.

2. ***Electroosmosis in annular microcapillary*** The interest to an annular model lies in its generality over cylindrical or parallel plates geometry. And the annular model may have potential applications in micromixing or simulation of the fluid flow in porous structures. Following the same approximation for the hyperbolic sine function in P-B equation, we obtain the analytical solutions for the electric potential profile in the annulus with high zeta potentials. A mathematical expression for the average electroosmotic velocity is derived in a fashion similar to the Smoluchowski equation. Hence a correction formula is introduced to modify the Smoluchowski equation, taking into account of contributions due to the finite thickness of the EDL and the geometry ratio-dependent correction. Specifically, under a circumstance when the two annular walls are oppositely charged, the flow direction can be determined from the sign of such correction formula,

and there exists a zero-velocity plane inside the annulus. With the assumption of large electrokinetic diameters, the location of such a zero-velocity plane can be estimated from the analytical expression for the velocity distribution. In addition, the oscillating electroosmotic flow inside an annulus under an AC electric field is analytically solved using Green's function formulation. The generality of annulus capillary model is also discussed.

3. ***DC electroosmosis in a packed microcapillary*** A mathematical model is developed to quantitatively describe the electroosmotic flow in a charged microcapillary packed with mono-sized charged microspheres. The model is based on the *Carman-Kozeny theory*, also known as capillary model, which assumes the porous medium to be equivalent to a series of parallel tortuous tubules. The overall velocity within the packed capillary comprises two components. One is the interstitial tubular velocity which is subject to volume averaging. The other is the velocity correction due to the charged capillary wall. The former is obtained by solving the Navier-Stokes equation and the Poisson-Boltzmann equation within an imaginary tubule, for which part of the results in chapter 2 and 3 can be directly used. The latter is obtained by solving the modified Brinkman's macroscopic momentum equation. The equation is solved using three different methods: (i) the numerical method, (ii) the analytical solution, and (iii) the slip velocity approximation. Parametric studies are carried out for the electroosmotic flow in the charged microcapillary packed with charged microparticles under the influences of the working fluid property, the channel and particle size, and the zeta potential of charged surfaces. Specifically, the electrokinetic wall effects are discussed for several typical cases.

4. ***AC electroosmosis in a packed microcapillary*** As another major contribution of this study, this thesis presents a theoretical investigation on AC-driven electroosmotic flow in both open-end and closed-end microchannels packed with charged microspheres. Since the AC electroosmosis in porous media has potential applications in the development of electrokinetic micro-actuator for its pressure-building ability, it deserves to make a research input. The modeling is also based on the capillary model applied in chapter 4. The time-periodic oscillating electroosmotic flow in an open-end capillary in response to the application of an AC electric field is obtained by using the Green's function approach (results derived in chapter 2). The backpressure associated with the counter-flow in a closed-end capillary is obtained by analytically solving the modified Brinkman's momentum equation. It is demonstrated that in a microchannel with its two ends connected to reservoir and subject to the ambient pressure, the oscillating Darcy velocity profile depends on both the pore size and the excitation frequency; such effects are coupled through an important aspect ratio of the tubule radius to the Stokes penetration depth. An important finding is that, in a microchannel with closed ends, use of smaller packing particles can generate higher backpressure at a fixed excitation frequency. And it is also found that there is a system frequency beside which the pressure response shows two opposite variation trends.

5. ***Joule heating effect of electroosmosis in a packed microcapillary*** Joule heating effect is a side effect coming with all the electric field induced flow. Electroosmosis is not an exception. The problem is getting worse in case of high electric field, large capillary size, or high electrolyte concentration. It may damage the performance the electrokinetic micropump or even to make it break down. Recently some works on the Joule heating effect of the electroosmotic flow in a non-packed

microcapillary have been reported. However, there is still no study on Joule heating of electroosmotic flow in porous media reported. In order to quantitatively evaluate the Joule heating effect on the electroosmotic flow in a packed microcapillary, a systematic numerical analysis is presented in this thesis. This model incorporates the momentum equation developed in preceding chapters, the conjugate energy equations for the porous packing and the capillary wall, and the continuity equations for mass and current density conservation. The temperature dependent fluid viscosity, dielectric constant, and the electric conductivity are taken into consideration. Finite difference method is used to numerically solve the temperature and velocity fields. A detailed parametric study is carried out to evaluate the Joule heating and its effect under the influences of electric field strength, the ionic concentration, the capillary size, the packing particle size, and the convection heat transfer coefficient outside the capillary. Specifically, the non-uniform electric field caused by the temperature gradient is evaluated and discussed. It is also found that there is an induced pressure field inside capillary due to the velocity variation caused by the temperature gradient.

6. ***Experimental study on electroosmosis in a packed microcapillary*** In the experiment, electrokinetic micropumps using electroosmotic flow in microcapillary packed with spherical silica microparticles are fabricated and characterized under the influences of the capillary size, particle size, concentration and type of the electrolyte solutions, and the capillary length. It is found that the porosity of the packed capillary increases with increasing the ratio of the capillary diameter to the particle diameter. This is due to the geometrical boundary wall effect. The change of porosity due to variation of the size ratio affects the generated electroosmotic velocity inside the micropump. The ionic concentration and the type of the electrolyte solution also have great influence on

the velocity by determining the magnitude of the zeta potential at the surface of the silica particles. However the length of the packed capillary dose not have any effect on the flow velocity. The experimental data is compared with the prediction by the theoretical model developed in this study, and a reasonable agreement is found.

8.2 Recommendations for Future Studies

Based on the results presented in this study, some comments and recommendations are made as following for future research in order to achieve a better and more complete understanding of the electroosmotic flow in microcapillaries.

1. The driving force for the electroosmotic flow in microchannels is determined by the local net charge density distribution and the strength of the applied electric field. The net charge density is dependent on the EDL field and hence on the zeta potential; the magnitude of the electroosmotic flow in turn is governed by the zeta potential. Generally the zeta potential is a function of the ionic valence, the ionic concentration of the electrolyte solution, and the surface properties of the microchannel wall. For a system with a simple electrolyte solution and a homogeneous channel wall, zeta potential is considered constant, such as the analyses in this report. However, in practice, the liquid involved in various biochips using the electroosmotic pumping to transport liquid and or perform other operations are solutions containing biological particles (e.g., DNA or proteins). The adhesion of these particles to the channel wall will cause the non-uniform zeta potential distribution along the channel, depending on the distribution and extent of the adhered particles. Therefore, the understanding of the flow behavior in such a situation is also important for manipulating the flow in biochip devices. To study the

effect of channel wall heterogeneity, a model on stochastic zeta potential distribution is suggested to be developed.

2. The capillary model is simple and empirical in nature. It cannot take into account of the contact area of the particles, where the local electric double layers overlap thus reducing the local electroosmotic velocity. In addition all of the particles cannot be exactly the same in size and shape. There is a size distribution of the particles. Variation of particle size will affect the local pore size. As discussed in previous chapters. The pore size is an important parameter for a porous packing. The electroosmotic flow is independent of the pore size only when the pore size is large compared with the Debye length of the solution. However, when the pore size is small enough (for submicron sized particles or nano-particles), the overlap of the double layer has to be considered. Furthermore like in recommendation 1, in analysis of the electroosmotic flow containing bio-molecules, the zeta potential on the particles may become non-uniformly distributed. The surface heterogeneity of the particles surface should be considered by applying a stochastic zeta potential distribution in modeling.

3. The experiment conducted in this study is an attempt to explore the mechanism of the EOF in porous media. However, as discussed in chapter 7, the method for measurement of the EOF velocity inside the porous media is subject to further improvement. The current monitoring method cannot measure the EOF velocity under high electric field strength. And the test column method can generate large error. It is suggested that a real-time camera recording system be used to measure the displacement of the air-liquid interface in the test column to obtain more accurate velocity values. The other important concern is the bubble generation and drying up of the channel due to the Joule heating inside the packed capillaries. One possible reason is that there are microbubbles in the particle slurry and the DI water used in the packing procedure. The

microbubbles are invisible to naked eyes. But they are very sensitive to the temperature change. When the electric field is on for prolonged period of time, the volume of the microbubbles is greatly enlarged which makes the porous packing dry up quickly. One option is using a degasser to reduce the amount of micro-bubbles in the working fluids prior to each test. The other possible reason is that the surface of the ODS particle in use is hydrophobic, which makes it more difficult to remove the microbubbles trapped in the porous packing. It is suggested to use ODS particles with hydrophilic surfaces or use appropriate chemicals to change the particle surface property. Other than the test column method and current monitoring method employed in this study, some other advanced visualization methods, e.g., Particle Image Velocimetry (PIV) technique, or laser induced fluorescent dye (Sinton et al., 2003), are expected to be developed to measure the EOF velocity field in porous media.

4. The microchannels used in this work are commercial fused silica capillaries, which may be difficult to be integrated into a microsystem. In practical application using the electroosmotic flow in microsystems, the microchannels are made by different micro-fabrication methods, such as soft lithography using PDMS, etching on a glass substrate, or hot embossed channel on thermoplastic materials. These microfabrication methods definitely determine the methodology of the modeling and experimentation on the electroosmotic flow in microsystems. Three important affected aspects are highlighted as following: Firstly, most of the microchannels made by these techniques are in rectangular or trapezoidal cross-sectional shapes. Thus the rectangular or trapezoidal geometry (other than the cylindrical geometry in this thesis) should be applied in analytical modeling. Secondly, because the zeta potential is dependent on the surface property, it is expected that the zeta potentials for different materials are different and should be determined independently and timely. Even for the same material (e.g., PDMS), the zeta potential

may change with the time after the microchannel is fabricated and in use. Thirdly, in this study, the microcapillary was packed using pressure-driven slurry packing approach in which the microchannel is subject to substantially high (e.g., 6 MPa) pressure. It may be difficult to apply the same approach to pack the microchannels fabricated by above popular microfabrication methods due to their weak sealing or bonding. However, other beads packing techniques, such as electrokinetic packing (using electrokinetically driven flows) or using centripetal forces may be applied (Maloney 2002).

Appendix A

Validation of Boltzmann Distribution under Dynamic Electroosmotic Flow

The ionic distribution in the electric double layer (EDL) is assumed to follow the Boltzmann distribution in this study. Strictly speaking, the Boltzmann distribution is applicable only when the system is in the thermodynamic equilibrium state (Masliyah, 1994). If a liquid flow exists, the ionic distribution may be affected by the presence of the fluid motion (Yang *et al.*, 1998). Therefore a validation of the Boltzmann distribution under the dynamic electroosmotic flow is presented in the following. As clearly shown in Eq. (2.2), it is through the electrical body force term that the Navier-Stokes equation is coupled with the governing equation for the EDL field, which in turn is associated with ionic number concentration distribution, n_i. Generally, rigorous mathematical modeling of ion transport in the EDL region under an electroosmotic flow generated by sinusoidally alternating electric fields should take into account of unsteady effects. According to the literature, the time scale related to electromigration in the EDL is of order 10^{-8}-10^{-7} second (Hsu *et al*., 1997); this value is at least two orders smaller than the characteristic time associated with the evolution of the electroosmotic flow, which is of order 10^{-5}-10^{-3} second (Yang *et al*., 2002). In the present study, we consider the sinusoidally alternating electric field of the highest frequency as 500 KHz (see the discussion part), corresponding to a characteristic time of 2×10^{-6} second. Therefore, the transient effect of the EDL "relaxation" can safely be neglected, and

the ionic concentration distribution $n_i(\underline{r})$ in the microchannel electroosmotic flow follows the Nernst-Planck equation (van de Ven, 1989), which in the absence of chemical reactions takes the convective-diffusion form

$$\nabla \cdot (D_i \nabla n_i) - \nabla \cdot (\underline{V}_i \cdot n_i) = 0 \tag{A.1}$$

where D_i is the diffusion coefficient of the type-*i* ion and $\underline{V}_i$ is the velocity of the type-i ion. Under such a situation, the ion velocity, $\underline{V}_i$, can be decomposed into contributions from liquid hydrodynamic velocity, $\underline{V}$, and a velocity, $\underline{U}_i$, due to electromigration (caused by the presence of the electric field). Then we can write

$$\underline{V}_i = \underline{V} + \underline{U}_i \tag{A.2}$$

The velocity, $\underline{U}_i$, is related to the electric forces exerting on the ions through the following equation

$$\underline{F}_{ei} = z_i e_0 \underline{E} = f_i \underline{U}_i \tag{A.3}$$

where z_i is the valence of the type-i ion, e_0 is the elementary charge, and f_i is the hydrodynamic resistance coefficient which can be determined from the Stokes-Einstein equation (Yang *et al*., 1998)

$$f_i = \frac{k_b T}{D_i} \tag{A.4}$$

The local electric field, $\underline{E}$ is assumed to be decoupled as the summation of the applied electric field and the EDL field due to the charged channel wall, and thus $\underline{E}$ can be expressed as

$$\underline{E} = E(t)\,\underline{e}_z - \nabla \psi \tag{A.5}$$

where $E(t)$ is the applied electric field and exists only along the flowing axial direction, $\underline{e}_z$. ψ is the electrical potential of the EDL field. Then from Eqs. (A.3) – (A.5), we can readily obtain an expression for $\underline{U}_i$

$$\underline{U}_i = \left[E(t)\,\underline{e}_z - \nabla\psi\right]\frac{z_i e_0 D_i}{k_b T} \tag{A.6}$$

Substituting Eqs. (A.2) and (A.6), and making use of continuity equation $\nabla\cdot\underline{V}=0$, according to Eq. (A.1) we can show next

$$D_i\nabla^2 n_i + \nabla\cdot\left(\frac{z_i e_0 D_i n_i}{k_b T}\nabla\psi\right) - \underline{V}\cdot\nabla n_i - \frac{z_i e_0 D_i}{k_b T}E(t)\nabla n_i\cdot\underline{e}_z = 0 \tag{A.7}$$

When the microchannel electroosmotic flow is fully developed, the components of fluid velocity $\underline{V}$ satisfy $u_z = u_z(r,t)$ and $u_r = u_\theta = 0$ in terms of cylindrical coordinates. Eq. (A.7) can reduce to

$$D_i\nabla^2 n_i + \nabla\cdot\left(\frac{z_i e_0 D_i n_i}{k_b T}\nabla\psi\right) - \left(u_z + \frac{z_i e_0 D_i}{k_b T}E(t)\right)\frac{\partial n_i}{\partial z} = 0 \tag{A.8}$$

Note that the ionic number concentration is time-independent and the flow is fully-developed, implying no appreciable ionic concentration gradient is established along the flow direction, i.e., $\frac{\partial n_i}{\partial z}=0$. Then Eq. (A.8) becomes

$$D_i\nabla^2 n_i + \nabla\cdot\left(\frac{z_i e_0 D_i n_i}{k_b T}\nabla\psi\right) = 0 \tag{A.9}$$

We can readily solve Eq. (A.9), and obtain its solution, which is (Hunter, 1981)

$$n_i = n_{i0}\exp\left(-\frac{z_i e_0\psi}{k_b T}\right) \tag{A.10}$$

Here n_{i0} is the ionic number concentration of the type-*i* ions in the bulk phase where $\psi = 0$. Eq. (A.10) is the well-known Boltzmann distribution. Therefore, it can be concluded that for a microchannel electroosmotic flow in a fully developed condition, the equilibrium Boltzmann distribution is still valid if the frequency of the external electric field is not very high, (e.g., less than 1 MHz).

Appendix B

Electric Double Layer Potential Distribution in a Capillary Cylinder

From the discussion of Chapter 2, the EDL potential distribution, $\psi(r)$ within the capillary region can be described by Poisson-Boltzmann equation (2.6) which, in polar coordinates, takes the non-dimensional form (Hunter, 1981)

$$\frac{1}{R}\frac{d}{dR}\left[R\frac{d\Psi(R)}{dR}\right]=\sinh\Psi(R) \tag{B.1}$$

Eq. (B.1) is subject to the boundary conditions specified by

$$\Psi(\kappa a)=\Psi_s \qquad \left.\frac{d\Psi(R)}{dR}\right|_{R=0}=0 \tag{B.2}$$

where $R=\kappa r$. $\kappa=\sqrt{\dfrac{2n_0e_0^2}{\varepsilon_r\varepsilon_0k_bT}}$ is the Debye-Hückel parameter.

However, no exact solution to Eq. (B.1) is available because of non-linearity. Here three methods to solve the above P-B equation are presented as following.

Analytical scheme proposed by Philip and Wooding (1970)

In this work, we follow Philip and Wooding (1970) to approximate the hyperbolic sine function $\sinh\Psi$ as (see Figure B-1)

$$\sinh\Psi \approx \begin{cases} -\frac{1}{2}\exp(-\Psi) & \Psi < -1 \\ \Psi & -1 \le \Psi \le 1 \\ \frac{1}{2}\exp(\Psi) & \Psi > 1 \end{cases} \tag{B.3}$$

Such an analytical scheme was successfully used by Philip and Wooding (1970) in their study concerning the electrical potential distribution outside a charged cylindrical particle immersed in an electrolyte. They found that the obtained potential profile differs only slightly from that by using numerical integration of the complete P-B equation.

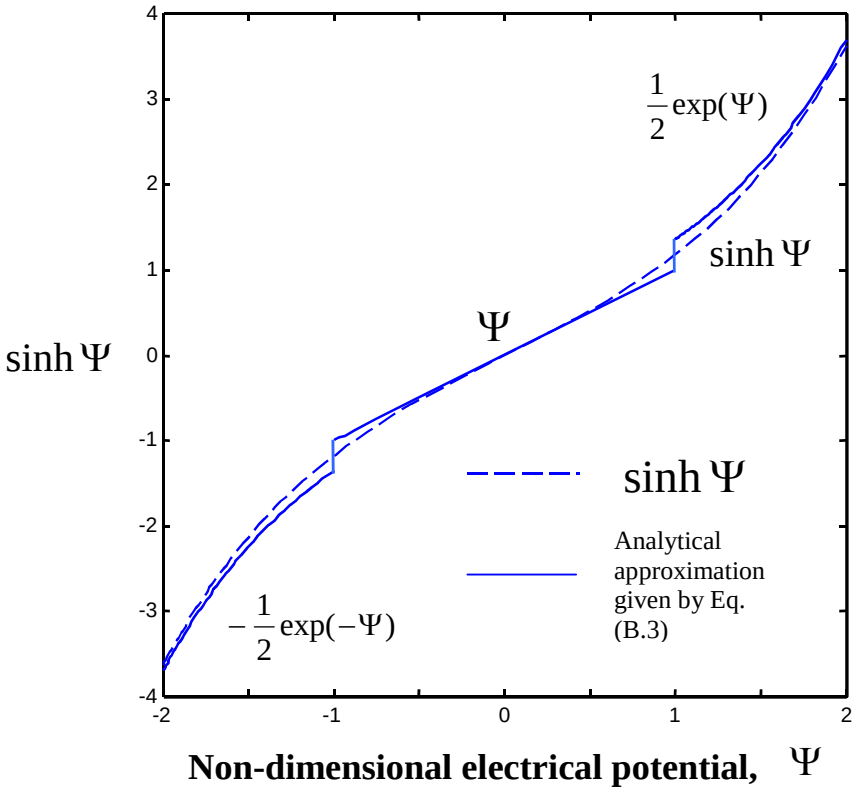

Figure B-1 Analytical approximation for the hyperbolic sine function as defined in Eq. (B.3).

Based on the approximation given in Eq. (B.3), we envisage the entire cylindrical region as comprising two hypothetical concentric regimes (L and H) so that at their junctions (i.e., $R = R^*$), we have $\Psi = 1$ (see Figure B-2). Hence we propose to solve the following equations (Levine *et al.*, 1975)

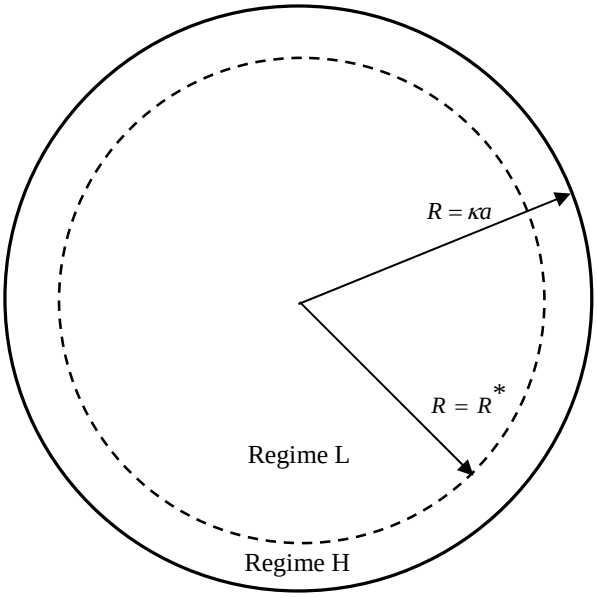

Figure B-2 Essential geometry of capillary cylinder for solving the Poisson-Boltzmann equation with high zeta potentials.

Low potential regime L $(0 \le R \le R^*)$

$$\frac{1}{R}\frac{d}{dR}\left[R\frac{d\Psi_L(R)}{dR}\right] = \Psi_L(R) \tag{B.4}$$

High potential regime H $(R^* \le R \le \kappa a)$

$$\frac{1}{R}\frac{d}{dR}\left[R\frac{d\Psi_H(R)}{dR}\right]=\frac{1}{2}\exp[\Psi_H(R)] \tag{B.5}$$

subject to the coupling boundary conditions

$$\Psi_L(R^*)=\Psi_H(R^*)=1 \tag{B.6a}$$

and

$$\left.\frac{d\Psi_L(R)}{dR}\right|_{R=R^*}=\left.\frac{d\Psi_H(R)}{dR}\right|_{R=R^*} \tag{B.6b}$$

The solution of Eq. (B.4) together with the boundary conditions Eqs. (B.2), (B.6a) can be given as

$$\Psi_L(R)=\frac{I_0(R)}{I_0(R^*)} \qquad (0\le R\le R^*) \tag{B.7}$$

where I_0 is the zero-order modified Bessel function of the first kind.

To get the solution for Eq. (B.5), we introduce the new variables

$$m=\ln R \qquad w=\Psi_H(R)+2\ln R \tag{B.8}$$

Then we can replace Eq. (B.5) with

$$\frac{d}{dm}\left(\frac{dw}{dm}\right)^2=\frac{d}{dm}[\exp(w)] \tag{B.9}$$

A first integration of Eq. (B.9) gives

$$\left(\frac{dw}{dm}\right)^2=\exp(w)+C \tag{B.10}$$

or

$$\left[R\frac{d\Psi_H(R)}{dR}+2\right]^2=R^2\exp[\Psi_H(R)]+C \tag{B.11}$$

where C is a constant of integration. Making use of Eqs. (B.6) – (B.7), we can obtain

$$C = \left[2 + R^* \frac{I_1(R^*)}{I_0(R^*)} \right]^2 - eR^{*2} \tag{B.12}$$

$C = 0$ at $R^* = R_0^* = 2.158$; $0 < C < 4$ for $R^* < R_0^*$; $C < 0$ for $R^* > R_0^*$.

The positive square root of Eq. (B.10) is chosen, and thus we have

$$\frac{dw}{dm} = \left[\exp(w) + C \right]^{\frac{1}{2}} \tag{B.13}$$

Integrating Eq. (B.13) and using Eq. (B.8), for $C < 0$, we obtain

$$\begin{aligned} \Psi_H(R) &= \ln\left\{ \frac{-C}{R^2 \cos^2\left[B_- + \frac{1}{2}\sqrt{-C}\ln\left(\frac{R}{\kappa a}\right)\right]} \right\} \\ &= \ln\left\{ \frac{-C}{R^2 \cos^2\left[A_- + \frac{1}{2}\sqrt{-C}\ln\left(\frac{R}{R^*}\right)\right]} \right\} \end{aligned} \tag{B.14}$$

where

$$B_- = \cos^{-1}\sqrt{\frac{-C}{e^{\Psi_s}(\kappa a)^2}} \tag{B.15a}$$

$$A_- = \cos^{-1}\sqrt{\frac{-C}{eR^{*2}}} = B_- + \frac{1}{2}\sqrt{-C}\ln\left(\frac{R^*}{\kappa a}\right) \tag{B.15b}$$

at $C = 0$, we have

$$\Psi_H(R) = -2\ln\left[\frac{R}{R_0^*} e^{-1/2} - \frac{R}{2}\ln\left(\frac{R}{R_0^*}\right)\right] \tag{B.16}$$

For $0 < C < 4$

$$\Psi_H(R) = \ln\left\{\frac{4B_+C\left(\frac{R}{\kappa a}\right)^{\sqrt{C}}}{R^2\left[1-B_+\left(\frac{R}{\kappa a}\right)^{\sqrt{C}}\right]^2}\right\} = \ln\left\{\frac{4A_+C\left(\frac{R}{R^*}\right)^{\sqrt{C}}}{R^2\left[1-A_+\left(\frac{R}{R^*}\right)^{\sqrt{C}}\right]^2}\right\} \tag{B.17}$$

where

$$B_+ = \frac{\sqrt{C+e^{\Psi_s}(\kappa a)^2}-\sqrt{C}}{\sqrt{C+e^{\Psi_s}(\kappa a)^2}+\sqrt{C}} \tag{B.18a}$$

$$A_+ = \frac{\sqrt{C+eR^{*2}}-\sqrt{C}}{\sqrt{C+eR^{*2}}+\sqrt{C}} = B_+\left(\frac{R^*}{\kappa a}\right)^{\sqrt{C}} \tag{B.18b}$$

Before closing this section, we realize that to calculate the electrical potential profile, $\Psi(R)$, the electroosmotic velocity distribution, we must determine R^* first. Recall that we have already obtained $R_0^* = 2.1585$. If we consider the general conditions of large κa values (say $\kappa a = 25$), it is obvious that $R^* > R_0^*$. So we can easily show that $C < 0$. Therefore we can find the values of R^* from Eqs. (B.15).

Debye-Hückel linear approximation

Under Debye-Hückel linear approximation, the P-B equation (B.1) is approximated as

$$\frac{1}{R}\frac{d}{dR}\left[R\frac{d\Psi(R)}{dR}\right] = \Psi(R) \tag{B.19}$$

The solution of Eq. (B.19) subjected to boundary condition in Eq. (B.2) can be easily obtained as

$$\Psi(R) = \Psi_s\frac{I_0(R)}{I_0(\kappa a)} \tag{B.20}$$

It should be noted that this method is accurate only when the magnitude of zeta potential is low, e.g., less than 25 mV.

Numerical method

When using the numerical method to solve P-B equation (B.1), the nonlinear source term of the Poisson-Boltzmann equation is linearized by Taylor series expansion and neglect the high-order term

$$\sinh \Psi^{n+1} = \sinh \Psi^{n} + \left(\Psi^{n+1} - \Psi^{n}\right)\cosh \Psi^{n} \tag{B.21}$$

where the superscript $(n+1)$ denotes the value for n obtained in the previous iteration. The derived algebraic equations were solved by using the Gauss-Siedel iteration.

Appendix C

Slip Velocity Approximation for the AC Electroosmosis in a Cylindrical Capillary

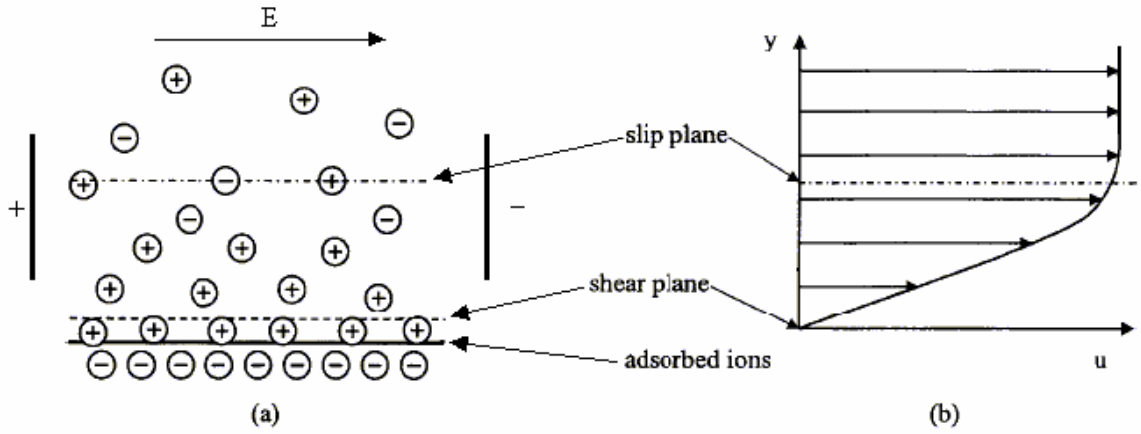

Figure C-1 Schematic representation of the slip velocity approximation

Conceptually, the steadily oscillating velocity profile induced by the application of a sinusoidally alternating electric field is similar to the fluid flow actuated by an oscillating motion of the channel wall; the latter was well documented by Telionis (1981). The basic concept of introducing the slip velocity approximation is to neglect the thin EDL region such that the entire flow is motivated by the frictional stresses originated from liquid viscosity. Here the thin EDL region can be regarded as an oscillating moving channel wall. The outer slip boundary velocity is determined by the Helmholtz-Smoluchowski equation, $u_s(t) = -\frac{\varepsilon_r \varepsilon_0}{\mu} \zeta_o E_0 e^{i\omega t}$. Hence the harmonically oscillating flow field is governed by the Navier-Stokes equation, in non-dimensional form

$$\frac{\partial \bar{u}}{\partial \bar{t}} = \frac{1}{\bar{r}} \frac{\partial}{\partial \bar{r}} \left(\bar{r} \frac{\partial \bar{u}}{\partial \bar{r}} \right) \tag{C.1}$$

subject to the boundary conditions (the reference velocity used in non-dimensionlization is chosen as $u_s = -\frac{\varepsilon_r \varepsilon_0}{\mu} E_0 \zeta_o$)

$$\bar{r} = 0 \qquad \frac{\partial \bar{u}}{\partial \bar{r}} = 0 \tag{C.2a}$$

$$\bar{r} = 1 \qquad \bar{u} = \exp(i\beta^2 \bar{t}) \tag{C.2b}$$

Solution to Eq. (C.1) can be readily obtained by using the classical method of separation of variables, and it is given as

$$\bar{u}(\bar{r}, \bar{t}) = REAL\left[\frac{I_0(\sqrt{i}\beta \bar{r})}{I_0(\sqrt{i}\beta)} \exp(i\beta^2 \bar{t}) \right] \tag{C.3}$$

where I_0 is the zero-order modified Bessel function of the first kind. i is the unit imaginary number. “REAL” denotes the real part of the solution.

Appendix D

Validation of Onsager Relationship for Transient and Frequency-dependent EOF in a Capillary with Closed-ends

In chapter 2, the transient and frequency-dependent AC EOF in an open cylindrical microchannel has been presented. However, the AC EOF in a microchannel with closed ends is also interesting. Since the two ends of the channel are closed, the AC electroosmosis exhibits a different frequency response due to the superposition of the viscous waves generated by the electroosmotic flow and the induced counter-flow. It not only is relevant to the development of new microelectrophoretic method (Minor *et al.*, 1997) but also can provide theoretical insight into novel electrokinetic micropumps and microactuators (Paul *et al.*, 1998). Further, the underlying mathematical modeling and solution pose more challenge and complexity. In the present study, The Navier-Stokes equation governing AC electroosmosis is solved analytically using the Green's function formulation. The exact solutions for the frequency responses of electroosmotic flow and the induced pressure gradient are obtained. Further, the valid Onsager's principle of reciprocity is demonstrated.

1. Transient and frequency dependent EOF in capillary with closed-ends

In this study, the liquid is assumed to be incompressible, Newtonian and symmetric electrolyte. Under a negligible Joule heating effect, the electrolyte is considered to have constant density, ρ, and viscosity, μ. The channel wall is uniformly charged with a zeta potential, ζ. The motion of liquid in a laminar, fully-developed electroosmotic flow through

a cylindrical microchannel of radius *a* can be described by the Navier-Stokes equation (Probstein, 1994).

$$\rho\frac{\partial u(r,t)}{\partial t}-\mu\frac{1}{r}\frac{\partial}{\partial r}\left(r\frac{\partial u(r,t)}{\partial r}\right)=-\frac{dP(t)}{dz}+E(t)\rho_e(r) \tag{D.1}$$

where $u(r,t)$ is the transient velocity field, $P(t)$ is the induced back-pressure, $E(t)$ is the externally applied electric field, and $\rho_e(r)$ is the local net charge density due to the presence of the electric double layer (*EDL*).

The externally applied electric field and the induced backpressure are sinusoidal with an alternating frequency of ω. Mathematically, they can be expressed as

$$E(t)=E_0e^{i\omega t} \tag{D.2a}$$

$$P(t)=P_0e^{i(\omega t+\phi)} \tag{D.2b}$$

where E_0 is the amplitude of the electric field, i is the unit of imaginary number, P_0 is the amplitude of the backpressure, and ϕ is the phase lag due to fluid inertia.

For a symmetric electrolyte, the net charge density is expressed using the Boltzmann distribution (Hunter, 1981),

$$\rho_e(r)=z_ve_0(n_+-n_-)=-2z_ve_0n_0\sinh\left(\frac{z_ve_0}{k_bT}\psi(r)\right) \tag{D.3}$$

where z_v is the electrolyte valence, e_0 is the elementary charge, n_0 is the ionic number concentration in the bulk solution, k_b is the Boltzmann constant, T is the absolute temperature, and $\psi(r)$ is the local electric potential of the *EDL* governed by the well-known Poisson-Boltzmann equation (2.6), which is rewritten as

$$\frac{1}{r}\frac{d}{dr}\left(r\frac{d\psi}{dr}\right)=\frac{2z_ve_0n_0}{\varepsilon_r\varepsilon_0}\sinh\left(\frac{z_ve_0\psi}{k_bT}\right) \tag{D.4}$$

This equation can be solved using the same method presented in appendix B.
The following dimensionless parameters are introduced:

$$\bar{u} = \frac{u}{U} \qquad \bar{t} = \frac{\nu}{a^2} t \qquad Z = \frac{z}{a\,\mathrm{Re}_0} \tag{D.5a}$$

$$\bar{P}_0 = \frac{P_0}{\rho U^2} \qquad \bar{E}_0 = \frac{E_0 a\,\mathrm{Re}_0}{\zeta} \qquad \overline{G} = \frac{2 z_\nu e_0 n_0 \zeta}{\rho U^2} \tag{D.5b}$$

where U is the reference velocity, $\nu = \frac{\mu}{\rho}$ is the liquid kinematic viscosity, $\mathrm{Re}_0 = \frac{\rho a U}{\mu}$ is the reference Reynolds number, and $\overline{G}$ represents a measure of the ability to convert the electrical energy, $z_\nu e_0 n_0 \zeta$ to the fluid kinetic energy, $\rho U^2/2$.

Substituting equations (D.2) and (D.3) into equation (D.1) and using the non-dimensional parameters, we can obtain

$$\frac{\partial \bar{u}}{\partial \bar{t}} - \frac{1}{\bar{r}} \frac{\partial}{\partial \bar{r}} \left(\bar{r} \frac{\partial \bar{u}}{\partial \bar{r}} \right) = -\frac{d\bar{P}_0}{dZ} e^{i\left(\frac{\omega a^2 \bar{t}}{\nu} + \phi\right)} - \overline{G}\bar{E}_0 e^{\frac{i\omega a^2 \bar{t}}{\nu}} \sinh \Psi(\bar{r}) \tag{D.6}$$

Equation (D.6) is subjected to the following initial and boundary conditions:

$$\bar{u}(\bar{r}, \bar{t})\big|_{\bar{t}=0} = 0 \tag{D.7a}$$

$$\left.\frac{\partial \bar{u}}{\partial \bar{r}}\right|_{\bar{r}=0} = 0 \qquad \bar{u}\big|_{\bar{r}=1} = 0 \tag{D.7b}$$

The analytical solution to equation (D.6), subjected to the initial and boundary conditions described in equations (D.7a) and (D.7b), can be obtained by using the Green's function formulation approach and is given as

$$\bar{u}(\bar{r}, \bar{t}) = REAL\left\{ -\int_{\tau=0}^{\bar{t}} d\tau \int_{r'=0}^{1} r' G(\bar{r}, \bar{t}\,|r', \tau) \left[\frac{d\bar{P}_0}{dZ} e^{i\left(\frac{\omega a^2 \tau}{\nu} + \phi\right)} + \overline{G}\bar{E}_0 e^{\frac{i\omega a^2 \tau}{\nu}} \sinh \Psi(r') \right] dr' \right\} \tag{D.8}$$

where $G(\bar{r}, \bar{t}\,|r', \tau)$ is the Green's function, and its expression is given by

$$G(\bar{r},\bar{t}\,|r',\tau) = 2\sum_{n=1}^{\infty}\frac{e^{-\lambda_n^2(\bar{t}-\tau)}J_0(\lambda_n r')J_0(\lambda_n \bar{r})}{J_1^2(\lambda_n)} \tag{D.9}$$

where λ_n is the positive roots of $J_0(\lambda_n) = 0$.

Substituting equation (D.9) to equation (D.8) and carrying out the integration, we can obtain the non-dimensional fluid velocity distribution in the microchannel as

$$\bar{u}(\bar{r},\bar{t}) = REAL\left[-2\frac{d\bar{P}_0}{dZ}\sum_{n=1}^{\infty}\frac{J_0(\lambda_n\bar{r})}{J_1(\lambda_n)}\frac{e^{i\left(\frac{\omega a^2}{\nu}\bar{t}+\phi\right)}-e^{-\lambda_n^2\bar{t}+i\phi}}{\lambda_n\left(\lambda_n^2+i\frac{\omega a^2}{\nu}\right)}-2\bar{G}\bar{E}_0\sum_{n=1}^{\infty}C_n\frac{J_0(\lambda_n\bar{r})}{J_1^2(\lambda_n)}\frac{e^{i\frac{\omega a^2}{\nu}\bar{t}}-e^{-\lambda_n^2\bar{t}}}{\lambda_n^2+i\frac{\omega a^2}{\nu}}\right] \tag{D.10}$$

where

$$C_n = \int_{r'=0}^{1} r' J_0(\lambda_n r')\sinh\left[\Psi(r')\right]dr' \tag{D.11}$$

Equation (D.10) shows that electroosmotic flow in a closed-end cylindrical microchannel is a linear superposition of: (i) the flow due to the applied electric field, and (ii) the flow due to the induced backpressure gradient. In this study, two cases are being considered here:

Case 1: Transient electroosmotic flow field under DC electric field ($\omega = 0$)

In this case, the phase-lag is zero (ϕ = 0) and the expression for the velocity field is simplified to

$$\bar{u}(\bar{r},\bar{t}) = -2\frac{d\bar{P}_0}{dZ}\sum_{n=1}^{\infty}\frac{J_0(\lambda_n\bar{r})}{J_1(\lambda_n)}\frac{1-e^{-\lambda_n^2\bar{t}}}{\lambda_n^3}-2\bar{G}\bar{E}_0\sum_{n=1}^{\infty}C_n\frac{J_0(\lambda_n\bar{r})}{J_1^2(\lambda_n)}\frac{1-e^{-\lambda_n^2\bar{t}}}{\lambda_n^2} \tag{D.12}$$

For a closed-end electroosmotic system, the net flow rate is equal to zero, or mathematically the system fulfills the following condition,

$$\int_{\bar{r}=0}^{1} \bar{r}\,\bar{u}(\bar{r},\bar{t})\,d\bar{r} = 0 \tag{D.13}$$

Substituting equation (D.12) into equation (D.13) and performing the integration, we can show that the induced backpressure gradient can be expressed as

$$\frac{d\bar{P}_0}{dZ} = -\bar{G}\bar{E}_0 \frac{\sum_{n=1}^{\infty} \frac{C_n}{J_1(\lambda_n)} \frac{1-e^{-\lambda_n^2 \bar{t}}}{\lambda_n^3}}{\sum_{n=1}^{\infty} \frac{1-e^{-\lambda_n^2 \bar{t}}}{\lambda_n^4}} \tag{D.14}$$

(i) For a small time elapsed, i.e., $\bar{t} << 1$, $e^{-\lambda_n^2 \bar{t}} \approx 1 - \lambda_n^2 \bar{t}$, the velocity distribution can therefore be expressed as

$$\bar{u}(\bar{r},\bar{t}) = -2\frac{d\bar{P}_0}{dZ}\bar{t}\sum_{n=1}^{\infty}\frac{J_0(\lambda_n \bar{r})}{\lambda_n J_1(\lambda_n)} - 2\bar{G}\bar{E}_0\bar{t}\sum_{n=1}^{\infty} C_n \frac{J_0(\lambda_n \bar{r})}{J_1^2(\lambda_n)} \tag{D.15a}$$

and the pressure gradient is

$$\frac{d\bar{P}_0}{dZ} = -\bar{G}\bar{E}_0 \frac{\sum_{n=1}^{\infty} \frac{C_n}{\lambda_n J_1(\lambda_n)}}{\sum_{n=1}^{\infty} \frac{1}{\lambda_n^2}} \tag{D.15b}$$

indicating that the velocity is linearly proportional to time at the initial moment.

(ii) For a large time, i.e., $\bar{t} \to \infty$, $e^{-\lambda_n^2 \bar{t}} \approx 0$, the velocity field becomes

$$\bar{u}(\bar{r},\bar{t}) = -2\frac{d\bar{P}_0}{dZ}\sum_{n=1}^{\infty}\frac{J_0(\lambda_n \bar{r})}{\lambda_n^3 J_1(\lambda_n)} - 2\bar{G}\bar{E}_0\sum_{n=1}^{\infty} C_n \frac{J_0(\lambda_n \bar{r})}{\lambda_n^2 J_1^2(\lambda_n)} \tag{D.16a}$$

and the pressure gradient is given by

$$\frac{d\bar{P}_0}{dZ} = -\bar{G}\bar{E}_0 \frac{\sum_{n=1}^{\infty} \frac{C_n}{\lambda_n^3 J_1(\lambda_n)}}{\sum_{n=1}^{\infty} \frac{1}{\lambda_n^4}} \tag{D.16b}$$

which is the formulation for the velocity distribution under the steady-state situation.

Case 2: Oscillating electroosmotic flow field under alternating AC electric field

In this situation, the exponential term on the right-hand side of equation (D.10) decays, and hence it reduces to

$$\bar{u}(\bar{r},\bar{t}) = REAL\left[-2\frac{d\bar{P}(\bar{t})}{dZ}\sum_{n=1}^{\infty}\frac{J_0(\lambda_n \bar{r})}{\lambda_n J_1(\lambda_n)\left(\lambda_n^2 + i\frac{\omega a^2}{\nu}\right)} - 2\bar{G}\bar{E}(\bar{t})\sum_{n=1}^{\infty}\frac{J_0(\lambda_n \bar{r})}{J_1^2(\lambda_n)}\frac{C_n}{\lambda_n^2 + i\frac{\omega a^2}{\nu}}\right] \quad \text{(D.17)}$$

where

$$\frac{d\bar{P}(\bar{t})}{dZ} = \frac{d\bar{P}_0}{dZ}e^{i\left(\frac{\omega a^2 \bar{t}}{\nu}+\phi\right)} \quad \text{(D.18a)}$$

$$\bar{E}(\bar{t}) = \bar{E}_0 e^{\frac{i\omega a^2}{\nu}\bar{t}} \quad \text{(D.18b)}$$

The induced backpressure gradient can be expressed as

$$\frac{d\bar{P}(\bar{t})}{dZ} = -\bar{G}\bar{E}(\bar{t})\frac{\sum_{n=1}^{\infty}\frac{C_n}{\lambda_n J_1(\lambda_n)\left(\lambda_n^2 + i\frac{\omega a^2}{\nu}\right)}}{\sum_{n=1}^{\infty}\frac{1}{\lambda_n^2\left(\lambda_n^2 + i\frac{\omega a^2}{\nu}\right)}} \quad \text{(D.19)}$$

According to equation (D.14) and equation (D.19), the induced pressure gradient for both DC and AC electric fields is linearly proportional to the strength of an applied electric field, and the parameter $\bar{G}$. Moreover, equation (D.19) can be reduced to equation (D.15b) in a limiting situation as $\omega \to \infty$, suggesting that the induced pressure gradient under extremely

high applied frequencies is identical to that at the initial moment under a DC electric field because in both cases, the flow only occurs within the *EDL* region.

2. Onsager's Principle of Reciprocity

Equation (D.10) shows that the flow field in a closed-end microchannel is linearly proportional to the driving electric field and the induced backpressure gradient. The linear relationship of the flow field, the driving electric field and the induced backpressure gradient suggests a possible constitution of the Onsager principle of reciprocity familiar in the theory of non-equilibrium thermodynamics. In the literature, the Onsager reciprocal relations for electrokinetic flows *under a steady-state situation* were demonstrated by Burgreen and Nakache (1964) for a parallel slit and by Rice and Whitehead (1965) and Levine *et al.* (1975) for a cylindrical capillary. The demonstration of valid Onsager's reciprocity relations for both transient electroosmotic flow and AC oscillating electroosmotic flow in a closed-end cylindrical microchannel is presented here.

The flow rate $Q(t)$ in the microchannel can be obtained by

$$Q(t) = 2\pi \int_0^a r\, u(r,t)\, dr \tag{D.20a}$$

Because of the symmetry, the flow rate is further expressed as

$$Q(t) = 2\pi U a^2 \int_0^1 \bar{r}\, \bar{u}(\bar{r},\bar{t})\, d\bar{r} \tag{D.20b}$$

Case 1: Transient electroosmotic flow under DC electric field ($\omega = 0$)

In the case of DC applied electric field, substituting equation (D.12) into equation (D.20b), we can express the flow rate in terms of the dimensional induced pressure gradient and the dimensional electric field as

$$Q(t) = L_{11}\frac{dP_0}{dz} + L_{12}E_0 \tag{D.21}$$

where the Onsager transport coefficients are

$$L_{11} = -\frac{4\pi\, a^4}{\mu}\sum_{n=1}^{\infty}\frac{1-e^{-\lambda_n^2\bar{t}}}{\lambda_n^4} \tag{D.22a}$$

$$L_{12} = -\frac{8\pi\, z_v e_0 n_0 a^4}{\mu}\sum_{n=1}^{\infty}C_n\frac{1-e^{-\lambda_n^2\bar{t}}}{\lambda_n^3 J_1(\lambda_n)} \tag{D.22b}$$

In general, the axial component of the electric current density is expressed as (Masliyah, 1994)

$$i_z(t) = u z_v e_0\,(n_+ - n_-) - z_v\, e_0\,(D_+\frac{\partial n_+}{\partial z} + D_-\frac{\partial n_-}{\partial z}) + \lambda_0\, E_z \tag{D.23}$$

where λ_0 is the electric conductivity of the fluid, and $D_\pm$ are the mass diffusivity of cations and anions, respectively. Since no ionic concentration gradient is built up along the axial direction, the second term on the right-hand side of equation (D.23) drops off. Therefore, the electric current across a straight cylindrical channel can be expressed as

$$I(t) = 2\pi U a^2\int_0^1 \bar{r}\rho_e u(\bar{r},t)d\bar{r} + \pi\lambda_0 E_0 a^2 \tag{D.24}$$

Substituting equation (D.2) and equation (D.12) into equation (D.24) and performing the integration, we can obtain the electrical current expressed in the Onsager form as

$$I(t) = L_{21}\frac{dP_0}{dz} + L_{22}E_0 \tag{D.25}$$

where the Onsager transport coefficients are

$$L_{21} = \frac{8\pi\, z_v e_0 n_0 a^4}{\mu} \sum_{n=1}^{\infty} C_n \frac{1 - e^{-\lambda_n^2 \bar{t}}}{\lambda_n^3 J_1(\lambda_n)} \tag{D.26a}$$

$$L_{22} = \frac{16\pi\, z_v^2 e_0^2 n_0^2 a^4}{\mu} \sum_{n=1}^{\infty} C_n^2 \frac{1 - e^{-\lambda_n^2 \bar{t}}}{\lambda_n^2 J_1^2(\lambda_n)} + \pi \lambda_0 a^2 \tag{D.26b}$$

From equation (D.22) and equation (D.26), it can be noted that $L_{12} = -L_{21}$, which suggests the validity of the Onsager principle of reciprocity for transient electroosmotic flow in a closed-end cylindrical microchannel.

Case 2: Oscillating electroosmotic flow under alternating AC electric field

Similarly, for the sinusoidally alternating applied electric field, we can obtain the expression for the flow rate by substituting equation (D.17) into equation (D.20b),

$$Q(t) = J_{11} \frac{dP(t)}{dz} + J_{12} E(t) \tag{D.27}$$

where the Onsager transport coefficients are

$$J_{11} = -\frac{4\pi\, a^4}{\mu} \sum_{n=1}^{\infty} \frac{1}{\lambda_n^2 \left(\lambda_n^2 + \frac{i\omega a^2}{\nu} \right)} \tag{D.28a}$$

$$J_{12} = -\frac{8\pi\, z_v e_0 n_0 a^4}{\mu} \sum_{n=1}^{\infty} \frac{C_n}{\lambda_n J_1(\lambda_n) \left(\lambda_n^2 + \frac{i\omega a^2}{\nu} \right)} \tag{D.28b}$$

and the electrical current is given by

$$I(t) = J_{21} \frac{dP(t)}{dz} + J_{22} E(t) \tag{D.29}$$

where the Onsager transport coefficients are

$$J_{21} = \frac{8\pi\, z_v e_0 n_0 a^4}{\mu} \sum_{n=1}^{\infty} \frac{C_n}{\lambda_n J_1(\lambda_n)\left(\lambda_n^2 + \frac{i\omega a^2}{\nu}\right)} \tag{D.30a}$$

$$J_{22} = \frac{16\pi\, z_v^2 e_0^2 n_0^2 a^4}{\mu} \sum_{n=1}^{\infty} \frac{C_n^2}{J_1^2(\lambda_n)\left(\lambda_n^2 + \frac{i\omega a^2}{\nu}\right)} + \pi\lambda_0 a^2 \tag{D.30b}$$

From equations (D.28) and (D.30), it is noted that $J_{12} = -J_{21}$, which fulfills the Onsager's principle of reciprocity for oscillating electroosmotic flow in a closed-end cylindrical microchannel.

Appendix E

Electric Double Layer Potential Distribution in a Capillary Annulus

As indicated by Eq. (3.15), the fluid velocity field is coupled with electric potential field, $\psi(r)$. When the EDL deformation is negligible, the electrical potential profile (i.e., the EDL field) in the annulus region is governed by the Poisson-Boltzmann equation, which can be expressed in a non-dimensional form as (Hunter, 1981)

$$\frac{1}{R}\frac{d}{dR}\left[R\frac{d\Psi(R)}{dR}\right]=\sinh\Psi(R) \tag{E.1}$$

where $R=\kappa r$ and $\kappa=\sqrt{\frac{2n_0e_0^2}{\varepsilon_r\varepsilon_0k_bT}}$.

Here κ is the Debye-Hückel parameter, and $1/\kappa$ denotes the characteristic thickness of the EDL (Hunter, 1981). e_0 is the elementary charge. n_0 is the number concentration of cations or anions in the neutral electrolyte (i.e., far from charged surfaces). k_b is the Boltzmann constant. T is the absolute temperature.

Rewrite the boundary conditions, Eqs. (3.7), as

$$\Psi(\kappa a)=\Psi_s \qquad\qquad \Psi(\alpha\kappa a)=\beta\Psi_s \tag{E.2}$$

The factor G, defined in Eq. (3.19), can also be non-dimensionalized as

$$G=\frac{2}{\Psi_s(\kappa a)^2(1-\alpha^2)}\int_{\alpha\kappa a}^{\kappa a}R\Psi(R)dR \tag{E.3}$$

It has been demonstrated by Philip and Wooding (1970) that the mathematical approximations,

$$\sinh\Psi \approx \begin{cases} -\frac{1}{2}\exp(-\Psi) & \Psi < -1 \\ \Psi & -1 \le \Psi \le 1 \\ \frac{1}{2}\exp(\Psi) & \Psi > 1 \end{cases} \qquad \text{(E.4)}$$

can constitute a good representation of the $\sinh\Psi$ function throughout the region of $-\infty < \Psi < +\infty$ (see Figure B-1).

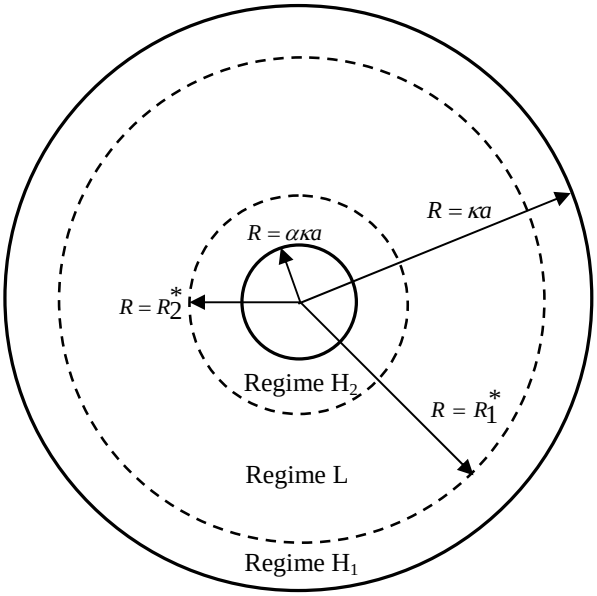

Figure E-1 Essential geometry of an annulus for solving the Poisson-Boltzmann equation with high zeta potentials.

We envisage the entire annular region as comprising three hypothetical concentric regions (L, H_1 and H_2) so that at their junctions (i.e., $R = R_1^*$ and $R = R_2^*$), we have $\Psi = 1$ (see Figure E-1). Hence we propose to solve, instead of Eq. (E.1), the following equations

High Potential Regime H_2 $(\alpha\kappa a \le R \le R_2^*)$

$$\frac{1}{R}\frac{d}{dR}\left[R\frac{d\Psi_{H2}(R)}{dR}\right] = \frac{1}{2}\exp[\Psi_{H2}(R)] \tag{E.5}$$

subject to the boundary conditions

$$\Psi_{H2}(R_2^*) = \Psi_L(R_2^*) = 1 \tag{E.6a}$$

$$\left.\frac{d\Psi_{H2}(R)}{dR}\right|_{R=R_2^*} = \left.\frac{d\Psi_L(R)}{dR}\right|_{R=R_2^*} \tag{E.6b}$$

Low Potential Regime L $(R_2^* \le R \le R_1^*)$

$$\frac{1}{R}\frac{d}{dR}\left[R\frac{d\Psi_L(R)}{dR}\right] = \Psi_L(R) \tag{E.7}$$

subject to the boundary conditions

$$\Psi_L(R_2^*) = \Psi_L(R_1^*) = 1 \tag{E.8}$$

High Potential Regime H_1 $(R_1^* \le R \le \kappa a)$

$$\frac{1}{R}\frac{d}{dR}\left[R\frac{d\Psi_{H1}(R)}{dR}\right] = \frac{1}{2}\exp[\Psi_{H1}(R)] \tag{E.9}$$

subject to the boundary conditions

$$\Psi_{H1}(R_1^*) = \Psi_L(R_1^*) = 1 \tag{E.10a}$$

$$\left.\frac{d\Psi_{H1}(R)}{dR}\right|_{R=R_1^*} = \left.\frac{d\Psi_L(R)}{dR}\right|_{R=R_1^*} \tag{E.10b}$$

In above mathematical equations, the subscript L designates the lower potential

region while H represents the higher potential region. The mathematical treatment ensures that the calculated $\Psi(R)$ profile, under the approximation as shown in Figure 3-1, would be a smooth, continuous function in the neighbourhood of R_1^* and R_2^*.

The solution of Eq. (E.7) together with the boundary conditions Eq. (E.8) is given by

$$\Psi_L(R) = AI_0(R) + BK_0(R) \tag{E.11}$$

where

$$A = \frac{K_0(R_2^*) - K_0(R_1^*)}{I_0(R_1^*)K_0(R_2^*) - I_0(R_2^*)K_0(R_1^*)} \tag{E.12a}$$

$$B = \frac{I_0(R_1^*) - I_0(R_2^*)}{I_0(R_1^*)K_0(R_2^*) - I_0(R_2^*)K_0(R_1^*)} \tag{E.12b}$$

I_0 and K_0 are the zero-order modified Bessel function of the first and second kind, respectively.

Introducing the new variables

$$m = \ln R \qquad\qquad w = \Psi_{H1}(R) + 2\ln R \tag{E.13}$$

Then we can replace Eq. (E.9) with

$$\frac{d}{dm}\left(\frac{dw}{dm}\right)^2 = \frac{d}{dm}(e^w) \tag{E.14}$$

A first integration of Eq. (E.14) gives

$$\left(\frac{dw}{dm}\right)^2 = e^w + C_1 \tag{E.15}$$

or

$$\left[R\frac{d\Psi_{H1}(R)}{dR} + 2\right]^2 = R^2 e^{\Psi_{H1}(R)} + C_1 \tag{E.16}$$

where C_1 is a constant of integration. Making use of Eqs. (E.10) and (E.11), we can obtain an expression for C_1,

$$C_1 = \{2 + R_1^*[AI_1(R_1^*) - BK_1(R_1^*)]\}^2 - eR_1^{*2} \tag{E.17}$$

The modified Bessel functions change exponentially. When R_1^* and R_2^* are not close to each other, there is a great difference in the magnitude of the values for the functions of I_0, I_1, K_0 and K_1, i.e., $I_0(R_1^*) >> I_0(R_2^*)$, $I_1(R_1^*) >> I_1(R_2^*)$, $K_0(R_1^*) << K_0(R_2^*)$, and $K_1(R_1^*) << K_1(R_2^*)$). As such, we can neglect small value terms in Eq. (E.17), and approximate it as

$$C_1 = \left[2 + R_1^* \frac{I_1(R_1^*)}{I_0(R_1^*)}\right]^2 - eR_1^{*2} \tag{E.18}$$

From which, we can readily show the following: $C_1 < 0$ for $R_1^* > R_{10}^*$, $C_1 = 0$ when $R_1^* = R_{10}^* = 2.1585$, and $4 > C_1 > 0$ for $R_1^* < R_{10}^*$.

From the conditions at $R = R_1^*$, the positive square root of Eq. (E.15) is chosen, and thus we have

$$\frac{dw}{dm} = (e^w + C_1)^{\frac{1}{2}} \tag{E.19}$$

Integrating Eq. (E.19) and using Eq. (E.13), for $C_1 < 0$, we obtain

$$\Psi_{H1}(R) = \ln\left\{\frac{-C_1}{R^2\cos^2\left[B_- + \frac{1}{2}\sqrt{-C_1}\ln\left(\frac{R}{\kappa a}\right)\right]}\right\} = \ln\left\{\frac{-C_1}{R^2\cos^2\left[A_- + \frac{1}{2}\sqrt{-C_1}\ln\left(\frac{R}{R_1^*}\right)\right]}\right\} \tag{E.20}$$

where

$$B_- = \cos^{-1}\sqrt{\frac{-C_1}{(\kappa a)^2 e^{\Psi_s}}} \tag{E.21a}$$

$$A_- = \cos^{-1}\sqrt{\frac{-C_1}{eR_1^{*2}}} = B_- + \frac{1}{2}\sqrt{-C_1}\ln\left(\frac{R_1^*}{\kappa a}\right) \tag{E.21b}$$

When $C_1 = 0$,

$$\Psi_{H1}(R) = -2\ln\left[\frac{R}{R_{10}^*}e^{-1/2} - \frac{R}{2}\ln\left(\frac{R}{R_{10}^*}\right)\right] \tag{E.22}$$

When $0 < C_1 \le 4$,

$$\Psi_{H1}(R) = \ln\left\{\frac{4B_+C_1\left(\frac{R}{\kappa a}\right)^{\sqrt{C_1}}}{R^2\left[1 - B_+\left(\frac{R}{\kappa a}\right)^{\sqrt{C_1}}\right]^2}\right\} = \ln\left\{\frac{4A_+C_1\left(\frac{R}{R_1^*}\right)^{\sqrt{C_1}}}{R^2\left[1 - A_+\left(\frac{R}{R_1^*}\right)^{\sqrt{C_1}}\right]^2}\right\} \tag{E.23}$$

where

$$B_+ = \frac{\sqrt{(\kappa a)^2 e^{\Psi_s} + C_1} - \sqrt{C_1}}{\sqrt{(\kappa a)^2 e^{\Psi_s} + C_1} + \sqrt{C_1}} \tag{E.24a}$$

$$A_{+} = \frac{\sqrt{eR_1^{*2} + C_1} - \sqrt{C_1}}{\sqrt{eR_1^{*2} + C_1} + \sqrt{C_2}} = B_{+}\left(\frac{R_1^{*}}{\kappa a}\right)^{\sqrt{C_1}} \tag{E.24b}$$

Follow the same procedure we can obtain the solution of Eq. (E.5) through

$$C_2 = \{2 + R_2^{*}[AI_1(R_2^{*}) - BK_1(R_2^{*})]\}^2 - eR_2^{*2} \tag{E.25}$$

With approximation, C_2 is simplified to

$$C_2 = \left[2 - R_2^{*}\frac{K_1(R_2^{*})}{K_0(R_2^{*})}\right]^2 - eR_2^{*2} \tag{E.26}$$

From which, we can show that $C_2 = 0$ when $R_2^{*} = R_{20}^{*} = 0.602$, $4 > C_2 > 0$ for $R_2^{*} < R_{20}^{*}$, and $C_2 < 0$ for $R_2^{*} > R_{20}^{*}$.

From the condition at $R = R_2^{*}$, the negative square root of Eq. (E.15) is chosen, and thus we have

$$\frac{dw}{dm} = -(e^{w} + C_2)^{\frac{1}{2}} \tag{E.27}$$

Integrating Eq. (E.27), for $C_2 < 0$, we obtain

$$\begin{aligned}\Psi_{H2}(R) &= \ln\left\{\frac{-C_2}{R^2\cos^2\left[B_{-} - \frac{1}{2}\sqrt{-C_2}\ln\left(\frac{R}{\alpha\kappa a}\right)\right]}\right\} \\ &= \ln\left\{\frac{-C_2}{R^2\cos^2\left[A_{-} - \frac{1}{2}\sqrt{-C_2}\ln\left(\frac{R}{R_2^{*}}\right)\right]}\right\}\end{aligned} \tag{E.28}$$

where

$$B_{-} = \cos^{-1}\sqrt{\frac{-C_2}{(\alpha\kappa a)^2 e^{\beta\Psi_s}}} \tag{E.29a}$$

$$A_{-} = \cos^{-1}\sqrt{\frac{-C_2}{eR_2^{*2}}} = B_{-} - \frac{1}{2}\sqrt{-C_2}\ln\left(\frac{R_2^*}{\alpha\kappa a}\right) \tag{E.29b}$$

When $C_2 = 0$,

$$\Psi_{H2}(R) = -2\ln\left[\frac{R}{R_{20}^*}e^{-1/2} + \frac{R}{2}\ln\left(\frac{R}{R_{20}^*}\right)\right] \tag{E.30}$$

When $4 > C_2 > 0$,

$$\Psi_{H2}(R) = \ln\left\{\frac{4B_{+}C_2\left(\frac{R}{\alpha\kappa a}\right)^{-\sqrt{C_2}}}{R^2\left[1 - B_{+}\left(\frac{R}{\alpha\kappa a}\right)^{-\sqrt{C_2}}\right]^2}\right\} = \ln\left\{\frac{4A_{+}C_2\left(\frac{R}{R_2^*}\right)^{-\sqrt{C_2}}}{R^2\left[1 - A_{+}\left(\frac{R}{R_2^*}\right)^{-\sqrt{C_2}}\right]^2}\right\} \tag{E.31}$$

where

$$B_{+} = \frac{\sqrt{(\alpha\kappa a)^2 e^{\beta\Psi_s} + C_2} - \sqrt{C_2}}{\sqrt{(\alpha\kappa a)^2 e^{\beta\Psi_s} + C_2} + \sqrt{C_2}} \tag{E.32a}$$

$$A_{+} = \frac{\sqrt{eR_2^{*2} + C_2} - \sqrt{C_2}}{\sqrt{eR_2^{*2} + C_2} + \sqrt{C_2}} = B_{+}\left(\frac{R_2^*}{\alpha\kappa a}\right)^{-\sqrt{C_2}} \tag{E.32b}$$

In the above derivations, we assume that both the inner and the outer walls are positively charged, i.e., $\beta > 0$. If one wall carries a different charge sign from the other, for example, the outer wall is negatively charged and the inner wall has a positive charge, then $\beta < 0$. We therefore should modify the boundary conditions in Eq. (E.6a) and Eq. (E.8) as $\Psi_{H2}(R_2^*) = \Psi_L(R_2^*) = -1$, $\Psi_L(R_2^*) = -1$ and $\Psi_L(R_1^*) = 1$, and rewrite Eq. (E.5) as

$$\frac{1}{R}\frac{d}{dR}\left[R\frac{d\Psi_{H2}(R)}{dR}\right]=-\frac{1}{2}\exp[-\Psi_{H2}(R)].$$

Before closing this section, we realise that to calculate the electrical potential profile, $\Psi(R)$, the electroosmotic velocity distribution, $u(r)$, and the correction factor to the Smoluchowski equation, J, we must determine R_1^* and R_2^* first. Recall that we have already obtained $R_{10}^*=2.1585$ and $R_{20}^*=0.602$. If we consider the general conditions of large κa values (say $\kappa a=25$), it is obvious that $R_1^*>R_{10}^*$ and $R_2^*>R_{20}^*$. So we can easily show that $C_1<0$ and $C_2<0$. Therefore we can find the values of R_1^* and R_2^* from Eq. (E.21) and Eq. (E.29), respectively.

The evaluation of G from Eq. (E.3) is as follows.

$$\begin{aligned}G&=G_{H2}+G_L+G_{H1}\\&=\frac{2}{\Psi_s(\kappa a)^2(1-\alpha^2)}[\int_{\alpha\kappa a}^{R_2^*}R\Psi_{H2}(R)dR+\int_{R_2^*}^{R_1^*}R\Psi_L(R)dR+\int_{R_1^*}^{\kappa a}R\Psi_{H1}(R)dR]\end{aligned}\qquad\text{(E.33)}$$

In Eq. (E.33), the integral for G_L can be expressed analytically. We can show that

$$G_L=\frac{2}{\Psi_s(\kappa a)^2(1-\alpha^2)}\{A[R_1^*I_1(R_1^*)-R_2^*I_1(R_2^*)]-B[R_1^*K_1(R_1^*)-R_2^*K_1(R_2^*)]\}\qquad\text{(E.34)}$$

While the integrals for G_{H2} and G_{H1} will be evaluated numerically.

Appendix F

Frequency-dependent Electroosmotic Flow Using Green's Function Formulation

Consider the electroosmotic flow in an annular capillary with infinite length between two coaxial circular cylinders of radii, αa and a, as shown in Figure 3-1 (α is the ratio of the inner radius to the outer radius). The annulus is filled with an incompressible, Newtonian, symmetric monovalence electrolyte of uniform dielectric constant, ε_r, viscosity, μ and density, ρ. The inner and outer capillary walls are uniformly charged with the zeta-potentials ζ_i and ζ_o, respectively. When an external electric field, $E(t)$ is applied along the axis of the capillary, the liquid starts to move as result of the interaction between the net charge density in the electric double layer (EDL) and the applied electric field. The motion of liquid through the cylindrical microcapillary under time-dependent electric field is governed by the Navier-Stokes equation (Probstein, 1994)

$$\rho \frac{\partial u(r,t)}{\partial t} - \mu \frac{1}{r} \frac{\partial}{\partial r}\left[r \frac{\partial u(r,t)}{\partial r} \right] = E(t)\rho_e(r) \tag{F.1}$$

where $u(r,t)$ is the transient velocity field. $\rho_e(r)$ is the local volumetric net charge density of the electrolyte due to the presence of the EDL, and in combination of the Boltzmann distribution, it is expressed as (Hunter, 1981)

$$\rho_e(r) = e_0 (n_+ - n_-) = -2n_0 e_0 \sinh\left[\frac{e_0 \psi(r)}{k_b T} \right] \tag{F.2}$$

where e_0 is the elementary charge, n_0 is the ionic concentration in the bulk phase (i.e., far from the charged surfaces), k_b is the Boltzmann constant, T is the absolute temperature, and $\psi(r)$ is the electric potential of the EDL.

We can nondimensionlize Eq. (F.2) and Eq. (F.1) respectively as

$$\frac{\partial \bar{u}}{\partial \bar{t}} - \frac{1}{\bar{r}}\frac{\partial}{\partial \bar{r}}\left(\bar{r}\frac{\partial \bar{u}}{\partial \bar{r}}\right) = \frac{a^2}{\mu u_s}\rho_e(\bar{r})E(\bar{t}) \tag{F.3}$$

and

$$\rho_e(\bar{r}) = -2n_0 e_0 \sinh[\Psi(\bar{r})] \tag{F.4}$$

where ε_r is the dielectric constant of the electrolyte and ε_0 is the permittivity of vacuum. Substituting Eq. (F.4) into Eq. (F.3), we obtain an inhomogeneous diffusion equation

$$\frac{\partial \bar{u}}{\partial \bar{t}} - \frac{1}{\bar{r}}\frac{\partial}{\partial \bar{r}}\left(\bar{r}\frac{\partial \bar{u}}{\partial \bar{r}}\right) = \frac{(\kappa a)^2}{\Psi_s E_0}\sinh\left[\Psi(\bar{r})\right]E(\bar{t}) \tag{F.5}$$

where $\Psi_s = \frac{e_0\zeta_o}{k_b T}$ and $\kappa = (\frac{2n_0 e_0^2}{\varepsilon_r \varepsilon_0 k_b T})^{\frac{1}{2}}$. κ is the Debye-Hückel parameter, and $1/\kappa$ denotes the characteristic thickness of the EDL. Eq. (F.5) is subject to the initial and boundary conditions

$$\bar{t} = 0 \qquad \bar{u} = 0 \tag{F.6a}$$

$$\bar{r} = \alpha \qquad \bar{u} = 0 \qquad \Psi = \beta\Psi_s \tag{F.6b}$$

$$\bar{r} = 1 \qquad \bar{u} = 0 \qquad \Psi = \Psi_s \tag{F.6c}$$

where $\beta = \zeta_i / \zeta_o$ denotes the ratio between the zeta potential of the inner and outer radii. Following the same Green's function formulation in chapter 2, the specified Green's function can be solved, and it takes the form

$$G(\bar{r},\bar{t}\,|\,\xi,\tau) = H(\bar{t}-\tau)\cdot \sum_{n=1}^{\infty}\frac{2\lambda_n^2 J_0^2(\lambda_n)\left[J_0(\lambda_n\bar{r})N_0(\lambda_n\alpha) - J_0(\lambda_n\alpha)N_0(\lambda_n\bar{r})\right]}{J_0^2(\lambda_n\alpha) - J_0^2(\lambda_n)}\xi\left[J_0(\lambda_n\xi)N_0(\lambda_n\alpha) - J_0(\lambda_n\alpha)N_0(\lambda_n\xi)\right]e^{-\lambda_n^2(\bar{t}-\tau)} \tag{F.7}$$

where λ_n are the positive roots of the zero-order Bessel function

$$J_0(\lambda_n)N_0(\lambda_n\alpha) - J_0(\lambda_n\alpha)N_0(\lambda_n) = 0 \tag{F.8}$$

Using the initial and boundary conditions in Eqs. (F.6), we can show that the solution to Eq. (F.5) is expressed as

$$\bar{u}(\bar{r},\bar{t}) = \int_{\tau=0}^{\bar{t}} \int_{\xi=\alpha}^{1} G(\bar{r},\bar{t}\,|\,\xi,\tau)\left\{\frac{(\kappa a)^2}{\Psi_s E_0}\sinh[\Psi(\xi)]E(\tau)\right\} d\xi d\tau \tag{F.9}$$

Substituting Eq. (F.7) into Eq. (F.9) leads to

$$\bar{u}(\bar{r},\bar{t}) = \frac{2(\kappa a)^2}{\Psi_s}\sum_{n=1}^{\infty} C_n \frac{\lambda_n^2 J_0^2(\lambda_n)}{J_0^2(\lambda_n\alpha) - J_0^2(\lambda_n)}\left[J_0(\lambda_n\bar{r})N_0(\lambda_n\alpha) - J_0(\lambda_n\alpha)N_0(\lambda_n\bar{r})\right]\int_{\tau=0}^{\bar{t}} \frac{1}{E_0}E(\tau)e^{-\lambda_n^2(\bar{t}-\tau)}d\tau \tag{F.10}$$

where

$$C_n = \int_{\xi=\alpha}^{1} \xi\left[J_0(\lambda_n\xi)N_0(\lambda_n\alpha) - J_0(\lambda_n\alpha)N_0(\lambda_n\xi)\right]\sinh[\Psi(\xi)]d\xi \tag{F.11}$$

Consider the application of a sinusoidally alternating electric field with an angle frequency ω

$$E(t) = E_0 e^{i\omega t} \tag{F.12}$$

Substituting Eq. (F.12) into Eq. (F.10), we can show next

$$\begin{aligned}\bar{u}(\bar{r},\bar{t}) &= REAL\left\{\frac{2(\kappa a)^2}{\Psi_s}\sum_{n=1}^{\infty} C_n \frac{\lambda_n^2 J_0^2(\lambda_n)}{J_0^2(\lambda_n\alpha) - J_0^2(\lambda_n)}\left[J_0(\lambda_n\bar{r})N_0(\lambda_n\alpha) - J_0(\lambda_n\alpha)N_0(\lambda_n\bar{r})\right]\frac{e^{i\eta^2\bar{t}} - e^{-\lambda_n^2\bar{t}}}{\lambda_n^2 + i\eta^2}\right\} \\ &= \frac{2(\kappa a)^2}{\Psi_s}\sum_{n=1}^{\infty} C_n \frac{\lambda_n^2 J_0^2(\lambda_n)\left[J_0(\lambda_n\bar{r})N_0(\lambda_n\alpha) - J_0(\lambda_n\alpha)N_0(\lambda_n\bar{r})\right]}{J_0^2(\lambda_n\alpha) - J_0^2(\lambda_n)}\frac{\lambda_n^2\cos(\eta^2\bar{t}) + \eta^2\sin(\eta^2\bar{t}) - \lambda_n^2\exp(-\lambda_n^2\bar{t})}{\lambda_n^4 + \eta^4}\end{aligned} \tag{F.13}$$

where i is the unit imaginary number. "*REAL*" denotes the real part of the solution. Here a new parameter η is defined as (Telionis, 1981)

$$\eta = \frac{a}{\sqrt{\mu/(\rho\omega)}} \tag{F.14}$$

η represents the aspect ratio of the capillary radius a to the Stokes penetration depth δ_s, defined as (Telionis, 1981)

$$\delta_s = \sqrt{\frac{\mu}{\rho\omega}} = \sqrt{\frac{\mu}{2\pi\rho f}} \tag{F.15}$$

where $f = \frac{\omega}{2\pi}$ is the driving frequency of the applied electric field.

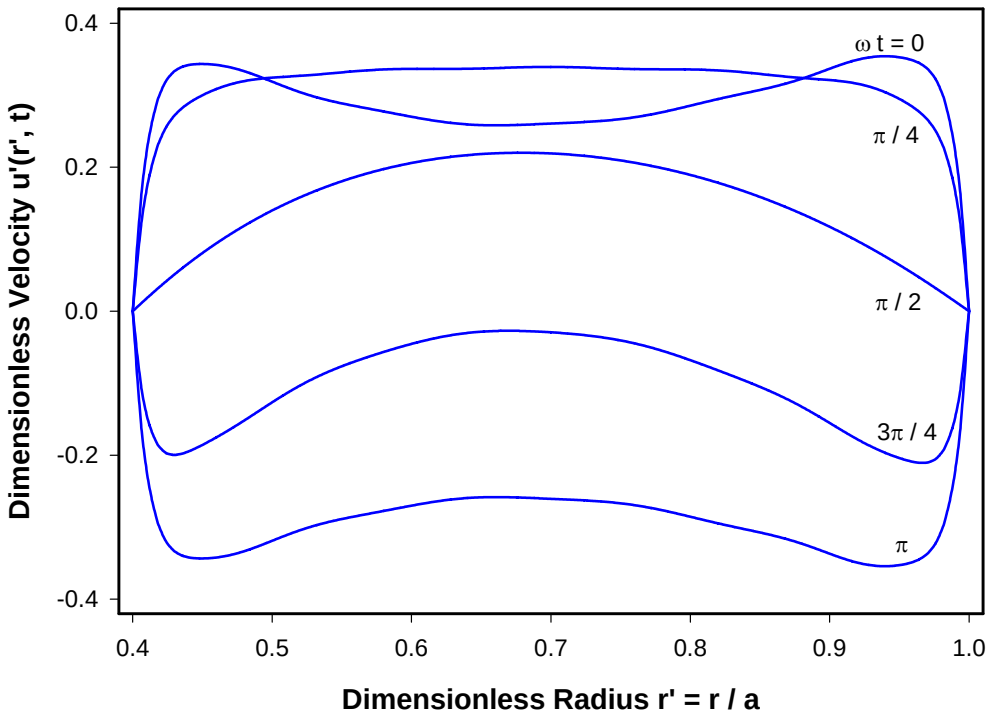

Figure F-1(a) Low frequency of the external field, $f = 0.1\ f^*$.

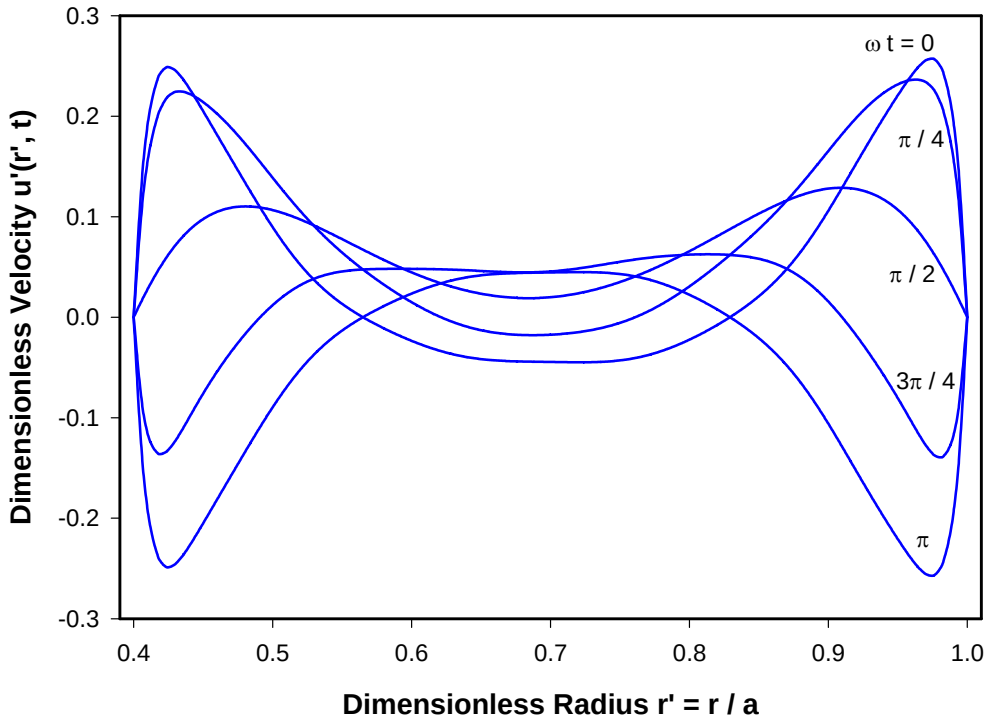

Figure F-1(b) The eigenfrequency of the external field, $f = f^*$.

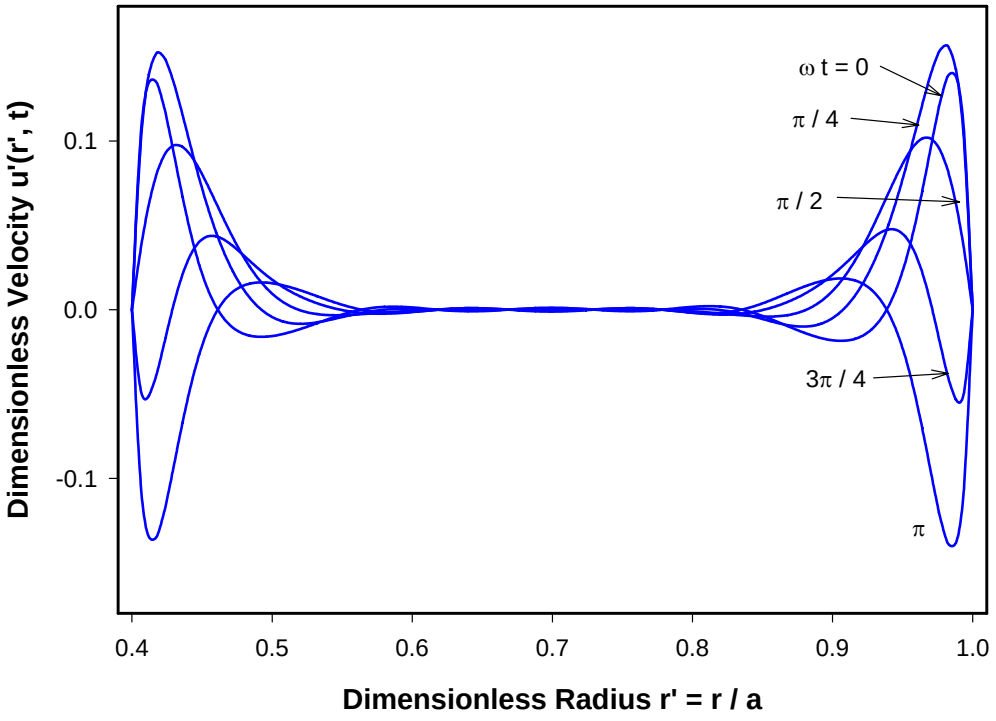

Figure F-1(c) High frequency of the external field, $f = 10\, f^*$.

Figure F-1 Steadily oscillating velocity distributions along the dimensionless radius for three different aspect frequencies of the external field, 0.1 f^*, f^* and 10 f^*, with the electrokinetic diameter, κa = 65.14, the zeta potential, Ψ_s = 4 and eigenfrequency, f^*=60.566 KHz. Snapshots are presented at five different characteristic moments: ωt = 0, π/4, π/2, 3π/4, π. Reference velocity is chosen as $u_s = -\dfrac{\varepsilon_r \varepsilon_0}{\mu} E_0 \zeta_o$.

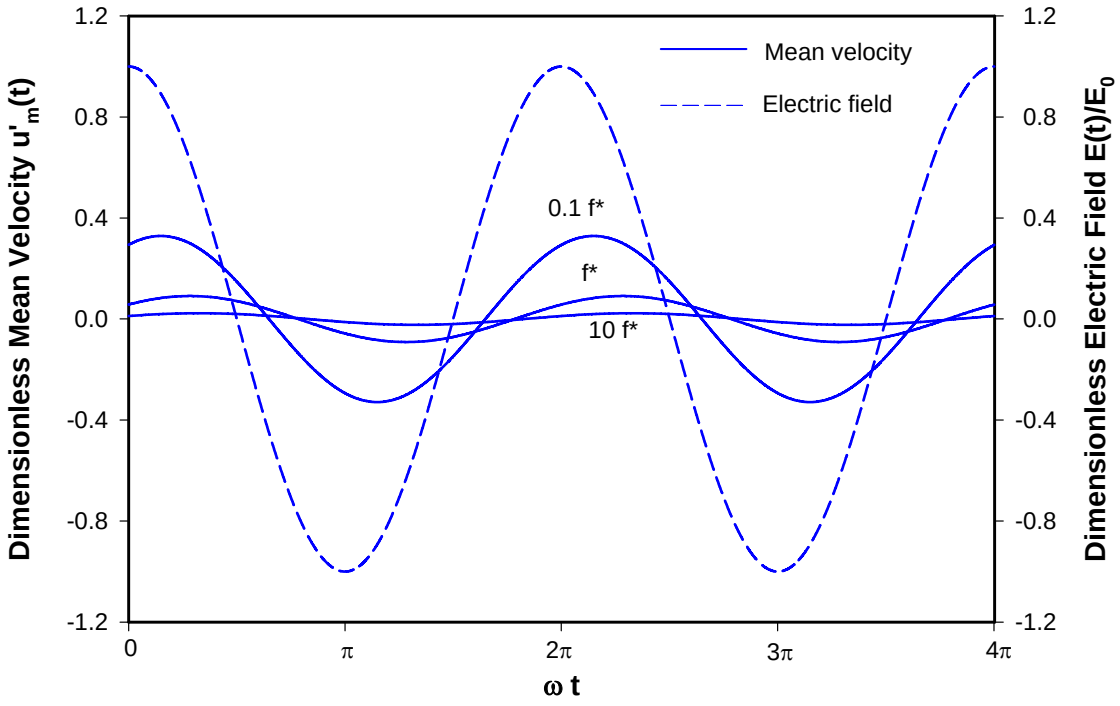

Figure F-2 Dimensionless mean velocity versus time with fixed the electrokinetic diameter, κa = 65.14 and the zeta potential, Ψ_s = 4. Reference velocity is chosen as $u_s = -\frac{\varepsilon_r \varepsilon_0}{\mu} E_0 \zeta_o$. Steadily oscillating mean velocity for three different aspect frequencies of the external field, 0.1 f^*, f^* and 10 f^*, with the system eigenfrequency of f^*=60.566 KHz.

Appendix G

Numerical Scheme for Solving the Temperature Fields in the Joule Heating Effect

The finite difference analysis based control volume method is applied to derive the partial differential equations into discretised linear equations. Using full implicit scheme, the energy equations Eq. (6.14-6.15) can be discretised as

$$a_P T_P^{n+1} - a_E T_E^{n+1} - a_W T_W^{n+1} - a_N T_N^{n+1} - a_S T_S^{n+1} = b \tag{G.1}$$

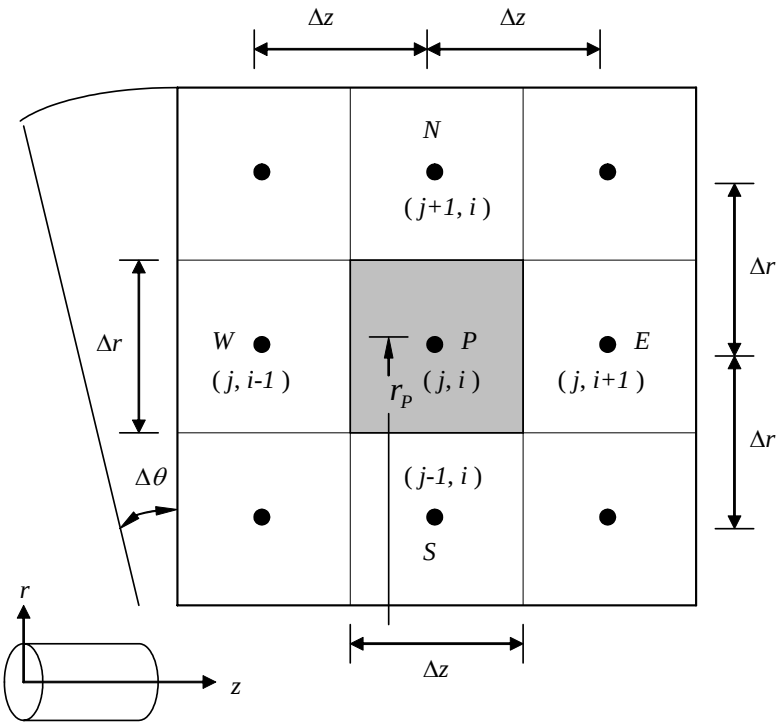

Figure G-1 Control volume used for the discretisation of the energy equation.

The corresponding coefficients in porous media subsystem are defined as

$$
\begin{aligned}
a_P &= 1+\frac{2\alpha_m \Delta t}{(\Delta z)^2}+\frac{2\alpha_m \Delta t}{(\Delta r)^2}-S_P \Delta t \\
a_E &= \frac{\alpha_m \Delta t}{(\Delta z)^2}-\frac{u_z \Delta t}{2\sigma \Delta z} \\
a_W &= \frac{\alpha_m \Delta t}{(\Delta z)^2}+\frac{u_z \Delta t}{2\sigma \Delta z} \\
a_N &= \frac{\alpha_m \Delta t}{(\Delta r)^2}\left(1+\frac{\Delta r}{2r_P}\right) \\
a_S &= \frac{\alpha_m \Delta t}{(\Delta r)^2}\left(1-\frac{\Delta r}{2r_P}\right) \\
b &= T_P^n + S_C \Delta t
\end{aligned}
\qquad \text{(G.2)}
$$

The corresponding coefficients in channel wall subsystem are defined as

$$
\begin{aligned}
a_P &= 1+\frac{2\alpha_w \Delta t}{(\Delta z)^2}+\frac{2\alpha_w \Delta t}{(\Delta r)^2} \\
a_E &= \frac{\alpha_w \Delta t}{(\Delta z)^2} \\
a_W &= \frac{\alpha_w \Delta t}{(\Delta z)^2} \\
a_N &= \frac{\alpha_w \Delta t}{(\Delta r)^2}\left(1+\frac{\Delta r}{2r_P}\right) \\
a_S &= \frac{\alpha_w \Delta t}{(\Delta r)^2}\left(1-\frac{\Delta r}{2r_P}\right) \\
b &= T_P^n
\end{aligned}
\qquad \text{(G.3)}
$$

The corresponding coefficients at boundary in porous media side are defined as:

$$
\begin{aligned}
a_P &= 1+\frac{2\alpha_m \Delta t}{(\Delta z)^2}+\frac{2k_w}{k_m+k_w}\frac{\alpha_m \Delta t}{(\Delta r)^2}\left(1+\frac{\Delta r}{2r_P}\right)+\frac{\alpha_m \Delta t}{(\Delta r)^2}\left(1-\frac{\Delta r}{2r_P}\right)-S_P \Delta t \\
a_E &= \frac{\alpha_m \Delta t}{(\Delta z)^2}-\frac{u_z \Delta t}{2\sigma \Delta z} \\
a_W &= \frac{\alpha_m \Delta t}{(\Delta z)^2}+\frac{u_z \Delta t}{2\sigma \Delta z} \\
a_N &= \frac{2k_w}{k_m+k_w}\frac{\alpha_m \Delta t}{(\Delta r)^2}\left(1+\frac{\Delta r}{2r_P}\right) \\
a_S &= \frac{\alpha_m \Delta t}{(\Delta r)^2}\left(1-\frac{\Delta r}{2r_P}\right) \\
b &= T_P^n + S_C \Delta t
\end{aligned}
\qquad \text{(G.4)}
$$

The corresponding coefficients at boundary in capillary side are defined as:

$$
\begin{aligned}
a_P &= 1+\frac{2\alpha_w \Delta t}{(\Delta z)^2}+\frac{\alpha_w \Delta t}{(\Delta r)^2}\left(1+\frac{\Delta r}{2r_P}\right)+\frac{2k_m}{k_m+k_w}\frac{\alpha_w \Delta t}{(\Delta r)^2}\left(1-\frac{\Delta r}{2r_P}\right) \\
a_E &= \frac{\alpha_w \Delta t}{(\Delta z)^2} \\
a_W &= \frac{\alpha_w \Delta t}{(\Delta z)^2} \\
a_N &= \frac{\alpha_w \Delta t}{(\Delta r)^2}\left(1+\frac{\Delta r}{2r_P}\right) \\
a_S &= \frac{2k_m}{k_m+k_w}\frac{\alpha_w \Delta t}{(\Delta r)^2}\left(1-\frac{\Delta r}{2r_P}\right) \\
b &= T_P^n
\end{aligned}
\qquad \text{(G.5)}
$$

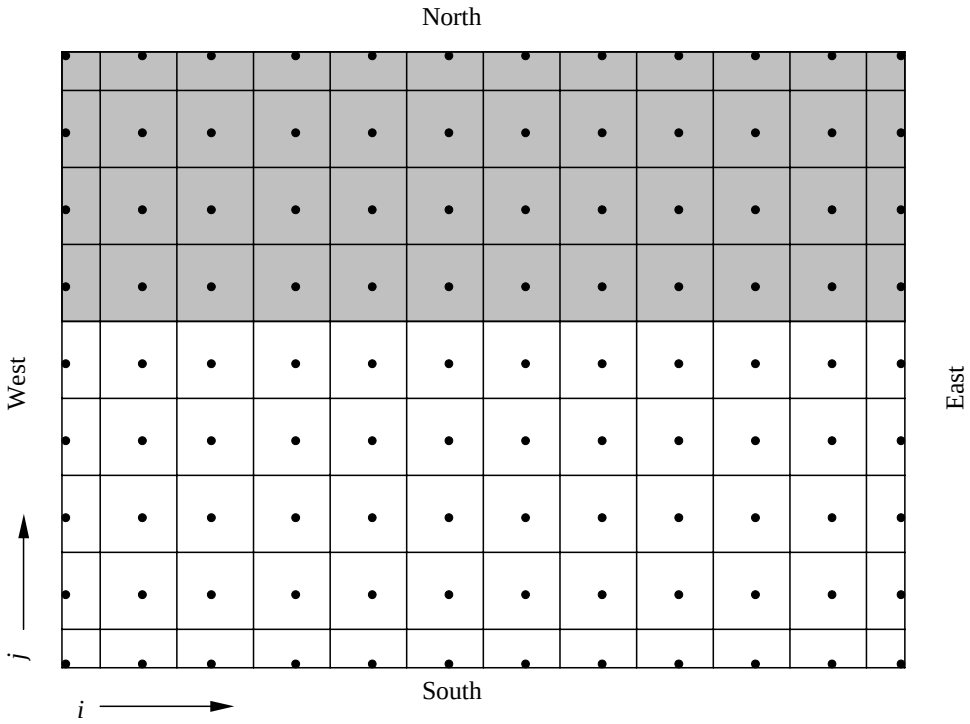

Figure G-2 Line-by-line application of the TDMA method.

To solve the equation system, we chose first along the south-north line at the west side (i =2). The discretised equation is re-arranged in the form

$$-a_S T_S^{n+1} + a_P T_P^{n+1} - a_N T_N^{n+1} = a_W T_W^{n+1} + a_E T_E^{n+1} + b \qquad \text{(G.6)}$$

The right side of Eq. (G.6) is assumed to be temporarily known. Subsequently the calculation is moved on towards east to the next south-north line. The sequence in which lines are chosen is known as the sweep direction (Versteeg and Malalasekera, 1995). Since we sweep from west to east the values of T_W to the west of the point P are known from the calculations on the previous line. Values of T_E to the east however are unknown so the calculation process must be iterative. At each iteration cycle T_E is taken to have its value at the end of previous iteration or a given initial value at the first iteration. The line-by-line calculation procedure is repeated several times until a converged solution is obtained.

References

1. Andreeev, V.P., Koleshko, S.B., Holman, D.A., Scampavia, L.D., and Christian, G.D. (1999) Hydrodynamics and Mass Transfer of the Coaxial Jet Mixer in Flow Injection Analysis. *Anal*. *Chem*. **71**, 2199-2204.

2. Arulanandam, S. and Li, D. (2000a) Liquid Transport in Rectangular Microchannels by Electroosmotic Pumping. *Colloids Surface.* A **161**, 89-102.

3. Arulanandam, S. and Li, D. (2000b) Determining ζ Potential and Surface Conductance by Monitoring the Current in Electro-osmotic Flow. *J. Colloids Interface Sci.*, **225**, 421-428.

4. Bejan, A. (1995) Convection heat transfer. John Wiley & Sons, New York.

5. Barragán, V.M. and Bauzá, C.R. (2000) Electroosmosis through a Cation-Exchange Membrane: Effect of an ac Perturbation on the Electroosmotic Flow. *J. Colloid Interface Sci.* **230**, 359-366.

6. Ben, Y. and Chang, H.-C. (2002) Nonlinear Smoluchowski Slip Velocity and Vortex Generation. *J. Fluid Mech.* **461**, 229-238.

7. Bianchi, F., Ferrigno, R., and Girault, H.H. (2000) Finite Element Simulation of an Electroosmotic-Driven Flow Division at a T-junction of Microscale Dimensions. *Anal*. *Chem*. **72**, 1987-1993.

8. Blokhra, R.L., and Joshi, J. (1999) Flow through Porous Media XVI: Electrokinetic Transport Coefficients of Aqueous Solutions of Mercuric Chloride and Glycine through a Sintered Disc Impregnated with a Cellulose Acetate Membrane under a Magnetic Field. *J. Colloid Interface Sci.* **220**, 458-464.

9. Boer, G., Dodge, A., Fluri, K., van der Schoot, B.H., Verpoorte, E., and de Rooji, N.F. (1998) Studies of Hydrostatic Pressure Effects in Electrokinetically Driven μTAS, in: Proceedings of the Micro Total Analysis System '98 Workshop, Banff, Canada, 1998, pp.53-56.

10. Bousse, L., Cohen, C., Nikiforov, T., Chow, A., Kopf-Sill, A.R., Dubrow, R., and Parce, J.W. (2000) Electrokinetically Controlled Microfluidic Analysis Systems. *Annu. Rev. Biophys. Biomol. Struct.* **29**, 155-181.

11. Burgreen, D., and Nakache, F.R. (1964) Electrokinetic Flow in Ultrafine Capillary Slits, *J. Phys. Chem.* **68**, 1084-1091.

12. Butkov, E. (1968) Mathematical Physics, Addison-Wesley Publishing Company, New York.

13. Chen, C.-H., Zeng, S., Mikkelsen, Jr., J.C., and Santiago, J.G. (2000) Development of a Planar Electrokinetic Micropump, in: Proceedings of 2000 ASME International Mechanical Engineering Congress and Exposition, Orlando, Florida, November 5-10, 2000.

14. Chen, L., Ma, J., Tan, F., and Guan, Y. (2003) Generating high-pressure sub-microliter flow rate in packed microchannel by electroosmotic force: potential application in microfluidic systems. *Sensors and Actuators B*, **88**, 260-265.

15. Coelho, D., Shapiro, M., Thovert, J.F., and Adler, P.M. (1996) Electroosmotic Phenomena in Porous Media. *J. Colloid Interface Sci.* **181**, 169-190.

16. Dukhin, S.S. (1991) Electrophoresis at Large Peclet Numbers. *Adv. Colloid Interface Sci.* **36**, 219-248.

17. Dutta, P., and Beskok, A. (2001) Analytical solution of time periodic electroosmotic flows: Analogies to Stokes second problem *Anal. Chem.* **73** 5097-5102.

18. Erickson, D. and Li, D. (2002) Influence of Surface Heterogeneity on Electrokinetically Driven Microfluidic Mixing. *Langmuir* **18**, 1883-1892.

19. Fan, Z.H., and Harrison, D.J. (1994) Micromachining of capillary electrophoresis injectors and separators on glass chips and evaluation of flow at capillary intersections. *Anal. Chem.* **66**, 177-184.

20. Figliola, R.S. and Beasley, D.E. (2000) Theory and Design for Mechanical Measurements. John Wiley & Sons, New York.

21. Gleeson, J.P. (2001) Electroosmotic Microfluidic Flows with Random Zeta Potential. *Modeling and Simulation of Microsystems*. 190-193.

22. Gleeson, J.P. (2002) Electroosmotic Flows with Random Zeta Potential. *J. Colloid Interface Sci.* **249**, 217-226.

23. Grimes, B.A., Meyers, J.J., and Liapis, A.I. (2000) Determination of the Intraparticle Electroosmotic Volumetric Flow Rate, Velocity and Peclet Number in Capillary Electrochromatography From Pore Network Theory. *J. Chromatogr.* A, **890**, 61-72.

24. Herr, A.E., Molho, J.I., Santiago, J.G., Mungal, M.G., and Kenny, T.W. (2000) Electroosmotic Capillary Flow with Nonuniform Zeta Potential. *Anal. Chem.* **72**, 1053-1057.

25. Hiemenz, P.C. (1986) Principles of Colloid and Surface Chemistry. 2nd ed. Marcel Dekker, New York.

26. Hsu, C.T., and Cheng, P. (1990) Thermal dispersion in a porous medium, *Int. J. Heat Mass Transfer.* **33** 1587-1597.

27. Hsu, J.P., Kuo, Y.C., and Tseng, S.J. (1997) Dynamic Interactions of Two Electrical Double Layers. *J. Colloid Interface Sci.* **195** 388-394.

28. Hunter, R.J. (1981) Zeta Potential in Colloid Science: Principles and Applications, Academic Press, New York.

29. Incropera, F.P., and DeWitt, D.P. (2002) Fundamentals of heat and mass transfer. John Wiley & Sons, New York.

30. Kang, Y.J., Yang, C., and Huang, X.Y. (2002a) Electroosmotic Flow in a Capillary Annulus with High Zeta Potentials. *J. Colloid Interface Sci.* **253**, 285-294.

31. Kang, Y.J., Yang, C., and Huang, X.Y. (2002b) Dynamic Aspects of Electroosmotic Flow in a Cylindrical Microcapillary. *Int. J. Eng. Sci.* **40**, 2203-2221.

32. Kaviany, M. (1995) *Principles of Heat Transfer in Porous Media* Springer-Verlag, New York.

33. Keh, H.J., and Liu, Y.C. (1995) Electrokinetic Flow in a Circular Capillary with a Surface Charge Layer. *J. Colloid Interface Sci.* **172**, 222-229.

34. Keh, H.J. and Tseng, H.C. (2001) Transient Electrokinetic Flow in Fine Capillaries. *J. Colloid Interface Sci.* **242**, 450-459.

35. Keim, C. and Ladisch, M. (2003) Model for temperature profiles in large diameter electrochromatography columns. *AICHE Journal*, **49** (2), 402-410.

36. Knox, J.H. (1988) Thermal effects and band spreading in capillary electro-separation. *Chromatographia*, **26**, 329-337.

37. Koh, W.-H., and Anderson, J.L. (1975) Electroosmosis and Electrolyte Conductance in Charged Microcapillaries. *AICHE J*. **21**, 1176-1188.

38. Koponen, A., Kataja, M., and Timonen, J. (1996) Tortuous flow in porous media. *Physical Review E*, **54**, No. 1, 406-410.

39. Lee, E., Lee, Y.S., Yen, F.-Y., and Hsu., J.-P. (2000) Electroosmotic Flow of a General Electrolyte Solution through a Fibrous Medium. *J. Colloid Interface Sci.* **223**, 223-228.

40. Levine, S., Marriott, J.R., Neale, G., and Epstein, N. (1975) Theory of Electrokinetic Flow in Fine Cylindrical Capillaries at High Zeta-Potentials. *J. Colloid Interface Sci.* **52**, 136-149.

41. Li, D. (2002) "Measurement of Surface Conductance", *Encyclopedia of Surface and Colloid Science*, A. Hubbard, Ed., Marcel Dekker, New York.

42. Li, D. (2004) *Electrokinetics in Microfluidics*, Academic Press, Toronto.

43. Liapis, A.I., and Grimes, B.A. (2000) Modeling the velocity field of the electroosmotic flow in charged capillaries and in capillary columns packed with charged particles: interstitial and intra particle velocities in capillary electrochromatography systems. *J. Chromatogr.* A **877**, 181-215.

44. Liapis, A.I., and Grimes, B.A. (2001) Modeling the velocity field of the electroosmotic flow in charged capillaries and in capillary columns packed with charged particles: interstitial and intra particle velocities in capillary electrochromatography systems, *J. Chromatogr. A* **877** 181-215.

45. López-García, J.J., Horno, J., González-Caballero, F., Grosse, C., and Delgado, A.V. (2000) Dynamics of the Electric Double Layer: Analysis in the Frequency and Time Domains. *J. Colloid Interface Sci.* **228**, 95-104.

46. Mala, G.M., Li, D., Werner, C., Jacobasch, H.-J., and Ning, Y.B. (1997a) Flow Characteristics of Water through a Microchannel between two Parallel Plates with Electrokinetic Effects. *Int. J. Heat and Fluid Flow* **18**, 489-496.

47. Mala, G.M., Li, D., and Dale, J.D. (1997b) Heat Transfer and Fluid Flow in Microchannels. *Int. J. Heat Mass Transfer* Vol. **40**, No. 13, 3079-3088.

48. Maloney, T.D. (2002) PhD thesis: Column packing technology in capillary electrochromatography and capillary liquid chromatography. The State University of New York at Buffalo.

49. Marino, S., Coelho, D., Békri, S., and Adler, P.M. (2000) Electroosmotic Phenomena in Fractures. *J. Colloid Interface Sci.* **223**, 292-304.

50. Marino, S., Shapiro, M., and Adler, P.M. (2001) Coupled Transports in Heterogeneous Media. *J. Colloid Interface Sci.* **243**, 391-419.

51. Masliyah, J.H. (1994) Electrokinetic Transport Phenomena. AOSTRA Technical Publication Series No. 12, AOSTRA, Edmonton.

52. Meinhart, C.D., Wereley, S.T., and Santiago, J.G.(1998) Micron-Resolution Velocimetry Techniques, in: Developments in Laser Techniques and Applications to Fluid Mechanics, Adrian, R.J. *et al*. (Eds.), Springer-Verlag, Berlin, 1998.

53. Minerick, A., Takhistov, P., Zhou, R., and Chang, H.-C. (2003) Manipulation and characterization of red blood cells with AC fields in micro-devices, *Electrophoresis*, **24**, 3703-3717.

54. Minor, M., van der Linde, A.J., van Leeuwen, H.P., and Lyklema, J. (1997) Dynamic Aspects of Electrophoresis and Electroosmosis: A New Fast Method for Measuring Particle Mobilities. *J. Colloid Interface Sci.* **189**, 370-375.

55. Mitchell, M.J., Qiao, R., and Aluru, N.R. (2000) Meshless Analysis of Steady-State Electro-Osmotic Transport. *Journal of Microelectromechanical System*, **9**, 435-449.

56. Nguyen, N.-T., Huang X., and Toh, K.C. (2002) MEMS-Micropumps: A Review. *Journal of Fluids Engineering*, **124**, 384-392.

57. Nield, D.A. and Bejan, A. (1999) *Convection in Porous Media* Springer-Verlag, New York.

58. Northup, M. A., Hills, R. F., Landre, R., Lehew, H. D., Watson, R. A. (1995). A MEMS-based DNA analysis system, Transducers'95, Eighth International Conference on Solid State Sensors and Actuators, Stockholm, Sweden, June, pp. 764-767.

59. O'Brien R.W., Cannon D.W., and Rowlands W.N. (1995) Electroacoustic determination of particle size and zeta potential. *J. Colloid Interface Sci.* **173**, 406-418.

60. O'Connor, A.J., Pratt, H.R., and Stevens, G.W. (1996) Electrophoretic mobilities of proteins and protein mixtures in porous membranes. *Chem. Eng. Sci*. **51**, 3459-3477.

61. Oddy, M.H., Santiago, J.G. and Mikkelsen, J.C. (2001) Electrokinetic Instability Micromixing. *Anal. Chem.* **73**, 5822-5832.

62. J.Th.G. Overbeek (1952) Phenomenology of Lyophobic, Chapter II In: H.R. Kruyt (Ed.), Colloid Science, Amsterdam.

63. Patankar, N.A., and Hu, H.H. (1998) Numerical Simulation of Electroosmotic Flow. *Anal. Chem.* **70**, 1870-1881.

64. Paul, P.H., Arnold, D.W., and Rakestraw, D.J. (1998) Electrokinetic Generation of High Pressures Using Porous Microstructures, in: Proceedings of the Micro Total Analysis System '98 Workshop, Banff, Canada 1998, pp.49-52.

65. Peled, N. (1996) Design and implementation of a microchemistry analyzer. *Pure & Appl. Chem.*, **68**, No. 10, 1837-1841.

66. Philip, J.R., and Wooding, R.A. (1970) Solution of the Poisson-Boltzmann Equation About a Cylindrical Particle. *J. Chem. Phys.* **52,** 953.

67. Probstein, R.F. (1994) "Physicochemical Hydrodynamics: An Introduction" 2nd ed., John Wiley & Sons, New York.

68. Ramos, A., Morgan, H., Green, N.G. and Castellanos, A. (1999) AC Electric-Field-Induced Fluid Flow in Microelectrodes. *J. Colloid Interface Sci.* **217**, 420-422.

69. Rathore, A.S., and Horváth, Cs. (1997) Capillary Electrochromatography: Theories on Electroosmotic Flow in Porous Media. *J. Chromatogr.* A **781**, 185-195.

70. Rathore, A.S., Wen, E., and Horváth, Cs. (1999) Electroosmotic mobility and conductivity in columns for capillary electrochromatography. *Anal. Chem.* **71**, 2633-2641.

71. Remcho, V.T., and Vallano, P.T. (2001). Electroosmosis in Complex Media: Bulk Transport in CEC. Pages 42-62 in: Capillary Electrochromatography (RSC Chromatography Monograph Series), K.D. Bartle and P. Myers, eds., Royal Society of Chemistry Press: London.

72. Ren, L., and Li, D. (2001) Electroosmotic Flow in Heterogeneous Microchannels. *J. Colloid Interface Sci.* **243**, 255-261.

73. Ren, L., Escobedo, C., and Li, D. (2001) Electroosmotic Flow in a Microcapillary with One Solution Displacing Another Solution. *J. Colloid Interface Sci.* **242**, 264-271.

74. Reuss, F.F. (1809) Sur un nouvel effet de l'´electricit´e glavanique *M´emoires de la Societ´e Imp´eriale des Naturalistes de Moscou* **2**, 327– 337.

75. Rice, C.L., and Whitehead, R. (1965) Electrokinetic Flow in a Narrow Cylindrical Capillary. *J. Phys. Chem.* **69**, 4017-4023.

76. Santiago, J.G. (2001) Electroosmotic Flows in Microchannels with Finite Inertial and Pressure Forces. *Anal. Chem.* **73**, 2353-2365.

77. Sinton, D., Ren, L., and Li, D. (2003) Visualization and numerical modelling of microfluidic on-chip injection processes. *J. Colloid Interfacial Sci.* **260**, 431-439.

78. Söderman, O. and Jönsson, B. (1996) Electro-osmosis: Velocity Profiles in Different Geometries with Both Temporal and Spatial Resolution. *J. Chem. Phys.* **105** (23), 10300-10311.

79. Sze, A., Erickson, D., Ren, L., and Li, D. (2003) Zeta-potential measurement using the Smoluchowski equation and the slope of the current-time relationship in electroosmotic flow. *J. Colloid Interfacial Sci.* **261**, 402-410.

80. Takhistov, P., Duginova, K., and Chang, H.-C. (2003) Electrokinetic Mixing Vortices due to Electrolyte Depletion at Microchannel Junctions. *J. Colloid Interfacial Sci.* **263**, 133-143.

81. Takhistov, P.V., Indeikina, A., and Chang, H.-C. (2002). Electrokinetic displacement of air bubbles in microchannels. *Phys. Fluids* **14**, 1-14.

82. Tallarek, U., Scheenen, T.W.J., and Van As, H. (2001) Macroscopic Heterogeneities in Electroosmotic and Pressure-Driven Flow through Fixed Beds at Low Column-to-Particle Diameter Ratio. *J. Phys. Chem.* B **105**, 8591-8599.

83. Tallarek U., Scheenen T.W.J., de Jager P.A., and Van As H. (2001) Using NMR displacement imaging to characterize electroosmotic flow in porous media, *Magnetic Resonance Imaging. B* **19** 453-456.

84. Tang, G.Y., Yang, C., Chai, C.J., and Gong, H.Q. (2003) Modelling of electroosmotic flow and capillary electrophoresis with the Joule heating effect: The Nernst-Planck Equation versus the Boltzmann distribution. *Langmuir*, 19, 10975-10984.

85. Tang, G.Y., Yang, C., Chai, C.J., and Gong, H.Q. (2004a) Joule heating effect on electroosmotic flow and mass species transport in a microcapillary. *International Journal of Heat and Mass Transfer*, 47, 215-227.

86. Tang, G.Y., Yang, C., Chai, C.J., and Gong, H.Q. (2004b) Numerical analysis of the thermal effect on electroosmotic flow and electrokinetic mass transport in microchannels. *Analytica Chimica Acta*, 507, 27-37.

87. Telionis, D. P. (1981) Unsteady Viscous Flow, Springer-Verlag, New York.

88. Thamida, S. and Chang, H.-C. (2002) Nonlinear Electrokinetic Ejection and Entrainment due to Polarization at Nearly Insulated Wedges. *Phys. Fluids* **14**, 4315-4328.

89. Tsao, H.K. (2000) Electroosmotic Flow through an Annulus. *J. Colloid Interface Sci.* **225**, 247-250.

90. van de Ven, T.G.M. (1989) Colloidal Hydrodynamics, Academic Press, San Diego.

91. Versteeg, H.K. and Malalasekera, W. (1995) An introduction to computational fluid dynamics: the finite volume method. John Wiley & Sons Inc., New York.

92. Xuan, X., Sinton, D., and Li, D. (2004a) Thermal end effects on electroosmotic flow in a capillary. *International Journal of Heat and Mass Transfer*, 47, 3145-3157.

93. Xuan, X., Xu, B., Sinton, D., and Li, D. (2004b) Electroosmotic flow with Joule heating effects. *Lab on a Chip*, 4, 230-236.

94. Yang, C., and Huang, X., "Proceeding of the International MEMS Workshop 2001." 142 – 150, Singapore, 2001.

95. Yang, C., and Li, D. (1997) Electrokinetic Effects on Pressure-Driven Liquid Flows in Rectangular Microchannels. *J. Colloid Interface Sci.* **194**, 95-107.

96. Yang, C., and Li, D. (1998) Analysis of Electrokinetic Effects on the Liquid Flow in Rectangular Microchannels. *Colloids Surfaces A: Physicochem. Eng. Aspects* **143**, 339-353.

97. Yang, C., Li, D., and Masliyah, J.H. (1998) Modeling Forced Liquid Convection in Rectangular Microchannels with Electrokinetic Effects. *Int. J. Heat Mass Transfer* **41**, 4229-4249.

98. Yang, C., Ng, C.B. and Chan, V. (2002) Transient Analysis of Electroosmotic Flow in a Slit Microchannel. *J. Colloid Interface Sci.* **248**, 524-527.

99. Yang, R.-J., Fu, L.-M. and Hwang, C.-C. (2001) Electroosmotic Entry Flow in a Microchannel. *J. Colloid Interface Sci.* **244**, 173-179.

100. Yao, S., Huber, D., Mikkelsen, Jr., J.C., and Santiago, J.G. (2001) A Large Flowrate Electroosmotic Pump with Micron Pores, in: Proceedings of 2001 ASME International Mechanical Engineering Congress and Exposition, New York, NY, November 11-16, 2001.

101. Yao, S. and Santiago, J.G. (2003a) Porous glass electroosmotic pumps: theory. *J. Colloid Interface Sci.* **268**, 133-142.

102. Yao, S., Hertzog, D.E., Zeng, S., Mikkelsen, Jr., J.C., and Santiago, J.G. (2003b) Porous glass electroosmotic pumps: design and experiments. *J. Colloid Interface Sci.* **268**, 143-153.

103. Zeng, S., Chen, C.-H., Mikkelsen, Jr., J.C., and Santiago, J.G. (2001) Fabrication and Characterization of Electroosmotic Micropumps. *Sensors and Actuators B*, **79**, 107-114.

104. Zeng, S., Chen, C-H., Santiago, J.G., Chen, J.R., Zare, R.N., Tripp, J.A., Svec, F., and Fréchet, J.M.J. (2002) Electroosmotic flow pump with polymer frits. *Sensors and Actuators B*, **82**, 209-212.